UCLA
UCLA Electronic Theses and Dissertations

Title

Development of Closure for Heat Exchangers Based on Volume Averaging Theory

Permalink

https://escholarship.org/uc/item/1xh3v9g3

Author

Zhou, Feng

Publication Date

2014

Peer reviewed|Thesis/dissertation

UNIVERSITY OF CALIFORNIA

Los Angeles

Development of Closure for Heat Exchangers Based on Volume Averaging Theory

A dissertation submitted in partial satisfaction

of the requirements for the degree

Doctor of Philosophy in Mechanical Engineering

by

Feng Zhou

2014

ABSTRACT OF THE DISSERTATION

Development of Closure for Heat Exchangers Based on Volume Averaging Theory

by

Feng Zhou

Doctor of Philosophy in Mechanical Engineering

University of California, Los Angeles, 2014

Professor Ivan Catton, Chair

The design of heat exchangers, which has always been important, has become increasingly critical in today's world and has also become closely coupled with optimization. The commonly used optimization methods, such as design of experiment (DOE), genetic algorithm (GA), etc., require a large population of design points/individuals to be evaluated. To shorten the optimization process, the evaluation of these large number of design points/individuals should be fast, which has precluded the use of time-consuming evaluation methods, such as direct numerical simulations (DNS) due to the significant computational costs of performing the flow and heat transfer in such heterogeneous (and porous), hierarchical devices with conjugate effects included, nor experimental evaluation that requires a large number of different heat exchangers be fabricated which is not only time-consuming but also expensive. This makes population-based optimization quite difficult if combined with system level CFD or experimental evaluation.

To enable these optimization methods, a fast-running solver is necessary to perform an evaluation of the many needed design points/individuals. Breakthroughs in the modeling of transport phenomena in heterogeneous media with Volume Averaging Theory (VAT) have allowed engineers to fully simulate flow and heat transfer in thermal devices in seconds, in comparison with hours or days it takes to do so with system level CFD simulation over one single design of a heat exchanger.

VAT is a hierarchical modeling method that includes mathematical description on two different levels. The lower level is flow and heat transfer at the pore scale for individual subscale elementary volume, which is described by the point-wise Navier-Stokes and thermal energy equations. The upper level is for the whole heat transfer device, described by the VAT-based mass, momentum, and thermal energy transport equations. The two levels are rigorously connected by mathematical scaling procedures, yielding additional integral and differential terms which need to be evaluated.

Proper evaluation of these extra terms is called the closure problem of the VAT based model, which has been the primary measure of advancement and for measuring success in research on transport in porous media. A method to obtain closures of the VAT based governing equations by CFD evaluation is developed. The procedure of the closure evaluation consists of eight main steps: 1) select the representative elementary volume correctly, which is simply the periodic unit cell in the case of periodic media; 2) define a proper characteristic length scale; 3) select a proper numerical method according to the flow condition; 4) discretize the computational domain carefully and conduct validation and verification of the adopted numerical method; 5) determine the number of REVs needed to obtain reasonable fully developed local values; 6) conduct numerical simulation

over the selected REVs; 7) extract the macroscopic hydrodynamic and thermal characteristics from the microscopic results by evaluating the closures over the REV; 8) collect the evaluated results for friction factor and heat transfer coefficient and develop the corresponding correlations. Since the closure evaluation is conducted by carrying out direct numerical experiments at the pore scale of the representative elementary volume (REV) which usually has a quite small computational domain, therefore the computation load is much lower than simulation at the device scale. With the closure correlations, the upper-level governing equation set is relatively simple and allows a nonlocal description of transport phenomena in heterogeneous thermal devices, with the morphology directly incorporated into the field equations and conjugate effects fully treated. The simplicity of the VAT based governing equations makes it possible for them to be solved discretely and a rapid evaluation of the design points to be performed.

With a fast-running solver being developed, the population based optimization methods can be exploited to guide the design to its optimal configuration. To demonstrate how the VAT based solver can be combined with commonly used optimization methods, a fin-and-tube heat exchanger is optimized using genetic algorithm and a heat sink with scale-shaped surface roughness is optimized using design of experiment. It should be noted that the development of the optimization algorithms is not the focus of the present work. The algorithms adopted in the present study are quite basic ones, which were borrowed from other researchers.

The dissertation of Feng Zhou is approved.

Adrienne Lavine

Jeff D. Eldredge

William W-G. Yeh

Ivan Catton, Committee Chair

University of California, Los Angeles

2014

This thesis is dedicated to my parents and my wife.

TABLE OF CONTENTS

LIST OF FIGURES

LIST OF TABLES

NOMENCLATURE

A Area, [m²]

A_f Fin surface area, [m²]

A_{fr} Frontal area, [m²]

A_{min} Minimum flow area, [m²]

A_o Total surface area, [m²]

A_w Wetted surface, [m²]

A_{wp} The cross flow projected area, [m²]

c_d Drag coefficient

c_p Specific heat, [J/(kg·K)]

D Tube diameter (Outer diameter if not specified), [m]

D_i Inner diameter of the tube, [m]

D_o Outer diameter of the tube, [m]

D_c Fin collar outside diameter, $D_c = D_o + 2\delta_f$, [m]

D_h VAT based hydraulic diameter, [m]

D_h^* Hydraulic diameter defined by Wang, et al. [1], [m]

d_h Hydraulic diameter defined by Chang et al. [2], [m]

d_p Diameter of the spherical particles, [m]

e	Scale height, [m]
F	Fitness function
F_1, F_2	Blending functions
F_p	Fin pitch, [m]
f	Friction factor
f_f	Fanning friction factor
G_{min}	Mass flux of the air based on the minimum flow area, [kg/(m^{2}s)]
H	Channel height, [m]
H_b	Base thickness, [m]
h	Heat transfer coefficient, [W/(m^2·K)]
j	Colburn factor
k	Turbulence kinetic energy per unit mass, [m^2/s^2]
k_f	Thermal conductivity of the fluid, [W/(m·K)]
k_s	Thermal conductivity of the solid, [W/(m·K)]
k_T or k_t	Turbulent heat conductivity, [W/(m·K)]
L	Total length of the channel or length of a FTHX, [m]
M	$\dfrac{\sum(|\vec{U}||\nabla T|)}{n}$, parameter
M_0	The base value of M

m	$\sqrt{(2h)/(\lambda_f \delta_f)}$, parameter
$<m>$	Average porosity
$\dot{m}$	Mass flow rate, [kg/s]
n	The number of control volumes or number of parameters
N	The number of tube rows
Nu	Nusselt number
p	Pressure, [Pa]
Δp	Pressure drop, [Pa]
Pr	Prandtl number
Pr_T	Turbulent Prandtl number
P_k	Shear production of turbulence
P	Pitch of circular scales, [m]
P_t	Transverse tube/scale pitch, [m]
P_l	Longitudinal tube/scale pitch, [m]
PP	Pumping power, [W]
$\dot{Q}$	Heat transfer rate, [W]
q	Heat flux, [W/m^2]
r	Radius of tube, including collar thickness, [m]

Re_{D_c} Reynolds number based on fin collar outside diameter and maximum velocity, $\mathrm{Re}_{D_c} = \dfrac{u_{max} D_c}{v}$

Re_{D_h} Reynolds number based on hydraulic diameter and average velocity, $\mathrm{Re}_{D_h} = \dfrac{\tilde{\tilde{u}} D_h}{v}$

R_{eq} Equivalent radius for circular fin, [m]

S An invariant measure of the strain rate

S_l Non-dimensional longitudinal tube pitch, $S_l = P_l/D$

S_t Non-dimensional transverse tube pitch, $S_t = P_t/D$

S_w Specific surface of a porous media, $S_w = \partial S_w / \Delta\Omega$, [1/m]

S_{wp} The cross flow projected area per volume, [1/m]

T_f Fluid temperature, [K]

T_s Solid temperature, [K]

ΔT Logarithmic mean temperature difference, [K]

u, v, w x-, y-, z-direction velocity term, [m/s]

u_m Average velocity through the channel, [m/s]

U Velocity vector

W Width of the channel or weight, [m]

X_L Geometric parameter , [m], $\begin{cases} \dfrac{\sqrt{\left(\dfrac{P_t}{2}\right)^2 + P_l^2}}{2} & \text{staggered layout} \\[4mm] \dfrac{P_l}{2} & \text{inline or 1-row layout} \end{cases}$

X_M $P_t/2$, geometric parameter, [m]

Greek

α Scaling factor for Reynolds number, or turbulence model constant, or scale attack angle

β Scaling factor for friction factor defined by Wang [1] or turbulence model constant

β^* Turbulence model constant

γ Scaling factor for friction factor defined by Tang [3]

δ_b Fin thickness at the base, [m]

δ_d Tube thickness, [m]

δ_f Thickness of a fin, [m]

δ_t Fin thickness at the tip, [m]

ε Heat exchanger effectivenesses

η_o Surface efficiency

η_f	Fin efficiency
η_{eff}	Effectiveness factor
θ	Intersection angle, [°]
μ	Viscosity, [Pa·s]
μ_T	Turbulent eddy viscosity, [Pa·s]
ν	Kinematic viscosity, [m^2/s]
ν_T	Turbulent kinematic viscosity, [m^2/s]
ρ	Density, [kg/m^3]
σ_ε	k-ε turbulence model constant
σ_k	Turbulence model constant for the k equation
σ_ω	k-ω turbulence model constant
τ_{wL}	Laminar shear stress, [Pa]
τ_{wT}	Turbulent shear stress, [Pa]
Φ	Heat transfer rate, [W]
φ_1	Represent any constant in the original k-ω model (σ_{k1}, …)
φ_2	Represent any constant in the transformed k-ε model (σ_{k2}, …)
φ	Represent the corresponding constant in the SST model (σ_k, …)
$\Delta\Omega$	The volume of the REV, [m^3]

ω	Specific turbulence dissipation rate, [1/s]

Subscripts and Superscripts

~	A value averaged over the representative volume
–	An average of turbulent values
^	Fluctuation of a value
$\langle f \rangle_f$	Means the superficial average of the function f
$\{f\}_f$	Means the intrinsic average of the function f
E	Heat transfer enhanced channels
f	Fin surface or fluid phase
in	Air-side inlet
max	Maximum value
min	Minimum value
m	Mean value
out	Air-side outlet
s	Solid phase
t, T	Turbulent or total
w	Tube wall

1	A value on the air side
2	A value on the water side
0	Evaluated at the wall or surface
b	Evaluated at the bulk temperature

ACKNOWLEDGEMENTS

I would like to thank my supervisor, Dr. Ivan Catton, for his incredible support and guidance throughout all aspects of my research. It was an excellent privilege for me to work with him and learn from his great knowledge and experience.

I would like to thank my Committee members, Professors Lavine, Eldredge, and Yeh for supporting and helpfully guiding me academically and professionally.

I would like to thank the students and faculty members of Mechanical Engineering at UCLA. I appreciate having had the opportunity to work with such a wide range of talented students and researchers. In particular, I would like to specially thank David Geb, Nicholas Hansen, George DeMoulin, Krsto Sbutega, Sean Reilly, Qi Yao, Jake Supowit and Mike Stubblebine for their friendships and academic supports during my time as a graduate student.

I would also like to thank my parents in China, who always believe in me, for being an unending source of encouragement and inspiration throughout my academic adventures. Finally, loving thanks go to my wife, Xiaoqiao Cao, for her continuous and lovely support, her endless encouragement, and her kindly patience.

VITA

2006.6	B.S., Thermal Energy and Power Engineering
	Southeast University
	Nanjing, China
2006.7-2009.7	Researcher
	Southeast University
	Nanjing, China
2013.3-2013.8	Research Intern
	BOSCH Research and Technology Center
	Palo Alto, California
2013.9-2013.12	Electronics Research Intern
	TOYOTA Research Institute of North America
	Ann Arbor, Michigan
2009.9-2014.3	Graduate Student Researcher and Teaching Assistant
	Department of Mechanical and Aerospace Engineering
	University of California, Los Angeles
	Los Angeles, California

PUBLICATIONS

JOURNAL PUBLICATIONS

1. Zhou, F., DeMoulin, G., Geb, D., and Catton, I., 2012, "Closure for a Plane Fin Heat Sink with Scale-Roughened Surfaces for Volume Averaging Theory (VAT) Based Modeling," *International Journal of Heat and Mass Transfer* 55(25-26): 7677-7685.

2. Zhou, F. and Catton, I., 2012, "Volume Averaging Theory (VAT) based modeling and closure evaluation for fin-and-tube heat exchangers." *Heat and Mass Transfer*: 48(10): 1813-1823.1

3. Geb, D., Zhou, F., and Catton, I., 2012, "Internal Heat Transfer Coefficient Determination in A Packed Bed From The Transient Response Due to Solid Phase Induction Heating," *Journal of Heat Transfer*, 134(4): 042604.

4. Zhou, F., and Catton, I., 2011, "Numerical Evaluation of Flow and Heat Transfer in Plate-Pin Fin Heat Sinks with Various Pin Cross-Sections," *Numerical Heat Transfer, Part A*, 60(2), pp. 107-128.

5. Zhou, F., Hansen, N., Geb, D., and Catton, I., 2011, "Obtaining Closure for Fin-And-Tube Heat Exchanger Modeling Based on Volume Averaging Theory (VAT)," *Journal of Heat Transfer*, 133(11): 111802.

6. Zhou, F., Hansen, N., Geb, D., and Catton, I., 2011, "Determination of the Number of Tube Rows to Obtain Closure for Volume Averaging Theory Based Model of Fin-And-Tube Heat Exchangers," *Journal of Heat Transfer*, 133(12): 121801.

7. Zhou, F. and Catton, I., 2013, "A Numerical Investigation of Turbulent Flow and Heat Transfer in Rectangular Channels with Elliptic Scale-Roughened Walls." *Journal of Heat Transfer* 135(8): 081901-081901.

8. Zhou, F. and Catton, I., 2013, "Obtaining closure for a plane fin heat sink with elliptic scale-roughened surfaces for Volume Averaging Theory (VAT) based modeling." *International Journal of Thermal Sciences* 71(0): 264-273.

9. Geb, D., Zhou, F., DeMoulin, G. and Catton, I., 2013, "Genetic Algorithm Optimization of a Finned-Tube Heat Exchanger Modeled With Volume-Averaging Theory." *Journal of Heat Transfer* 135(8): 082602-082602.

10. Zhou, F., Li, X., Cook, D., Chumakov, S., Wu, D., and Catton, I., 2014, "Dropwise Condensation Modeling: Drop Size Distribution and Heat Transfer," *Energy*, pending.

CONFERENCE PROCEEDINGS

1. Zhou, F., Joshi, S. and Dede, E., 2014, "Visualization of bubble behavior for jet impingement cooling with phase change," in the Proceedings of The Intersociety Conference on Thermal and Thermomechanical Phenomena in Electronic Systems, ITHERM 2014, May 27 – 30, 2014, Orlando, FL, USA, Institute of Electrical and Electronics Engineers Inc.

2. Zhou, F. and Catton, I., 2012, "Numerical investigation on turbulent flow and heat transfer of rectangular channels with elliptic scale-roughened walls," in the Proceedings of the ASME 2012 International Mechanical Engineering Congress and Exposition: IMECE2012-85059, Houston, Texas, USA.

3. Zhou, F., Geb, D., DeMoulin, G., and Catton, I., 2012, "Hierarchical modeling and closure evaluation for fin-and-tube heat exchangers using 3-D numerical simulation," ASME 2012 Heat Transfer Summer Conference Collocated with the ASME 2012 Fluids Engineering Div. Summer Meeting and the ASME 2012 10th Int. Conf. on Nanochannels, Microchannels and Minichannels, HT 2012, July 8, 2012 - July 12, 2012, Rio Grande, Puerto Rico, American Society of Mechanical Engineers.

4. Geb, D., Zhou, F., DeMoulin, G., and Catton, I., 2012, "Genetic algorithm optimization of a compact heat exchanger modeled using volume averaging theory," ASME 2012 Heat Transfer Summer Conference Collocated with the ASME 2012 Fluids Engineering Div. Summer Meeting and the ASME 2012 10th Int. Conf. on Nanochannels, Microchannels and Minichannels, HT 2012, July 8, 2012 - July 12, 2012, Rio Grande, Puerto Rico, American Society of Mechanical Engineers.

5. Zhou, F., DeMoulin, G. W., Geb, D., and Catton, I., 2012, "Closure for a Plane Fin Heat Sink with Scale-Roughened Surfaces for Volume Averaging Theory (VAT) Based Modeling," Proc. GOMACTech 2012: 31-1, Las Vegas, Nevada, USA.

6. Zhou, F., Vasquez, D. DeMoulin, G. W., Geb, D., and Catton, I., 2012, "Volume Averaging Theory (VAT) based modeling and closure evaluation of scale-roughened plane fin heat sink," 28th Annual IEEE Semiconductor Thermal Measurement and Management Symposium, SEMI-THERM 2012, March 18, 2012 - March 22, 2012, San Jose, CA, United states, Institute of Electrical and Electronics Engineers Inc.

7. Zhou, F., Geb, D. and Catton, I. 2011, "Numerical investigation on air side performance of fin-and-tube heat exchangers with large diameter tubes and large number of tube rows," ASME 2011 International Mechanical Engineering Congress and Exposition, IMECE 2011, November 11, 2011 - November 17, 2011, Denver, CO, United states, American Society of Mechanical Engineers.

8. Geb, D., Chu, J., Zhou, F. and Catton, I., 2011, "Obtaining experimental closure for the VAT-based energy equations modeling a heat sink as a porous medium," ASME 2011 International Mechanical Engineering Congress and Exposition, IMECE 2011, November 11, 2011 - November 17, 2011, Denver, CO, United states, American Society of Mechanical Engineers.

9. Zhou, F., DeMoulin, G. W., Geb, D., and Catton, I., 2011, "Modeling of pin fin heat sinks based on volume averaging theory," ASME-JSME-KSME 2011 Joint Fluids

Engineering Conference, AJK 2011, July 24, 2011 - July 29, 2011, Hamamatsu, Japan, American Society of Mechanical Engineers.

10. Zhou, F., G. W., Geb, D., and Catton, I., 2011, "Cooling performance comparisons of five different plate-pin compound heat sinks based on two different length scale," ASME 2011 Pacific Rim Technical Conference and Exhibition on Packaging and Integration of Electronic and Photonic Systems, InterPACK 2011, July 6, 2011 - July 8, 2011, Portland, OR, United states, American Society of Mechanical Engineers.

11. Zhou, F., Hansen, N. and Catton, I., 2011, "Numerical predictions of thermal and hydraulic performances of heat sinks with enhanced heat transfer capability," ASME/JSME 2011 8th Thermal Engineering Joint Conference, AJTEC 2011, March 13, 2011 - March 17, 2011, Honolulu, HI, United states, American Society of Mechanical Engineers.

12. Zhou, F., Hansen, N. and Catton, I., 2011, "VAT based modeling of plate-pin fin heat sink and obtaining closure from CFD solution," ASME/JSME 2011 8th Thermal Engineering Joint Conference, AJTEC 2011, March 13, 2011 - March 17, 2011, Honolulu, HI, United states, American Society of Mechanical Engineers.

13. Zhou, F., Hansen, N. and Catton, I., 2010, "Determining the computational domain length to obtain closure for VAT based modeling by 3D numerical simulation and field synergy analysis," (IMECE 2010-37561). ASME 2010 International Mechanical Engineering Congress & Exposition, IMECE 2010, Vancouver, British Columbia, Canada.

14. Zhou, F., Hansen, N. and Catton, I., 2010, "VAT based modeling of heat exchanger and obtaining closure from CFD solution," ASME 2010 International Mechanical Engineering Congress & Exposition, IMECE 2010, November 12, 2010 - November 18, 2010, Vancouver, British Columbia, Canada.

15. Zhou, F., Hansen, N. and Catton, I., 2010, "Obtaining closure for heat exchanger modeling based on Volume Averaging Theory (VAT)," 2010 14th International Heat Transfer Conference, IHTC14, August 8, 2010 - August 13, 2010, Washington, DC, United states, American Society of Mechanical Engineers.

16. Hansen, N., Catton, I. and Zhou, F., 2010, "Heat sink optimization; A multi-parameter optimization problem," 2010 14th International Heat Transfer Conference, IHTC14, August 8, 2010 - August 13, 2010, Washington, DC, United states, American Society of Mechanical Engineers.

1. Introduction

This chapter presents the motivations and objectives of the present study and the scope of this Ph.D. thesis. First, the reason why the present study is important (motivation) and what is the goal of the present work (objective) are explained. After that, an overview of Volume Averaging Theory (VAT) based modeling and the development of closures for heat exchangers using CFD evaluation is provided. Finally, the organization of the document is described.

1.1. Motivation

With the growth of thermal systems, such as those related to materials processing, energy conversion, cooling of electronic equipment, refrigeration, pollution, aerospace, and automobiles, the need to design and optimize thermal systems has also grown. The subject of design, which had always been important, has become increasingly critical in today's world and has also become closely coupled with optimization. The heat-exchange device, such as fin-and-tube heat exchangers and heat sinks, is one of the essential components of these thermal systems. Optimization of heat sinks and heat exchangers has proven difficult due to the large number of parameters involved in describing them, and the computationally intensive nature of modeling the fluid flow and heat transfer within such heterogeneous and hierarchical structures.

Simple but complete equations fully accounting for all aspects of the configuration under consideration are the only answer if we want to find the optimum configuration for a conjugate problem. Computational fluid dynamics (CFD) or experiment by themselves

are out of the question, and simple equations are needed but they need to be made more rigorous. It is proposed that Volume Averaging Theory (VAT) [4] be used to develop the simple equations allowing clear rigorous statements to be made that define how the friction factor and heat transfer coefficient are to be determined. Modeling a heat exchanger as porous media based on Volume Averaging Theory (VAT), specific geometry can be accounted for in such a way that the details of the original structure can be replaced by their averaged counterparts and the VAT based governing equations can be solved for a wide range of heat exchanger designs. This 'porous media' model, which is a function only of porous media morphology, represented by porosity and specific surface area, and its closure, can easily be adapted to many different structures, and can pave the way for optimization of fin-and-tube heat exchangers and heat sinks.

However, the biggest hurdle in applying VAT to model heat exchangers is to obtain proper closures for the VAT based governing equations that will give the right connection between phases and is the primary measure of success in the application of VAT. Once the closures are developed, the VAT upper-level equations are simple and can easily be solved discretely.

A numerical scheme will be developed to obtain closures for the VAT based governing equations. The closure will be obtained by using the pointwise lower scale solutions of the Navier-Stokes and energy equations solved by a commercial CFD code and scaling them up to an upper scale. The closures obtained include closure for two-stream fin-and-tube heat exchangers and for plate fin heat sinks with scale-shaped surface roughness. The closure evaluation method is general and applicable to different geometries,

not limited to the two heat exchangers, which are presented in the present work as a demonstration.

1.2. Methodology

1.2.1. VAT Based Modeling

The VAT based modeling procedure is summarized as shown in Figure 1.1. First, VAT is used to scale transport phenomena from lower level to higher level and applied to the heat transfer device we are interested at. The outcome of this yields global upper-level governing equations, yet in an open form and in need of proper closure. The lower level is associated with fluid and heat transport in pore scale representative elementary volumes. Therefore, the closure terms, which are related to a local friction factor and a heat transfer coefficient, are evaluated over the REV using direct CFD simulation. Correlations of the local friction factor and heat transfer coefficient are developed from the results of evaluation and fed back to the VAT based governing equations. Now the heat transfer device is described by a closed upper-level VAT based model and the whole device could be viewed as a homogeneous media consisting of many REVs. With the closure correlations, the upper-level governing equation set is relatively simple and allows a nonlocal description of transport phenomena in heterogeneous thermal devices, with the morphology directly incorporated into the field equations and conjugate effects fully treated. The simplicity of the VAT based governing equations makes it possible for them to be solved discretely and a VAT based solver could be developed for rapid evaluation of design points. This method reduces the difficulties of modeling a hierarchical geometry to the closure allowing the closure to be obtained by CFD simulation over the REV, much

less computational expensive than CFD simulations at the system or device level but still

able to provide a good view of the whole picture.
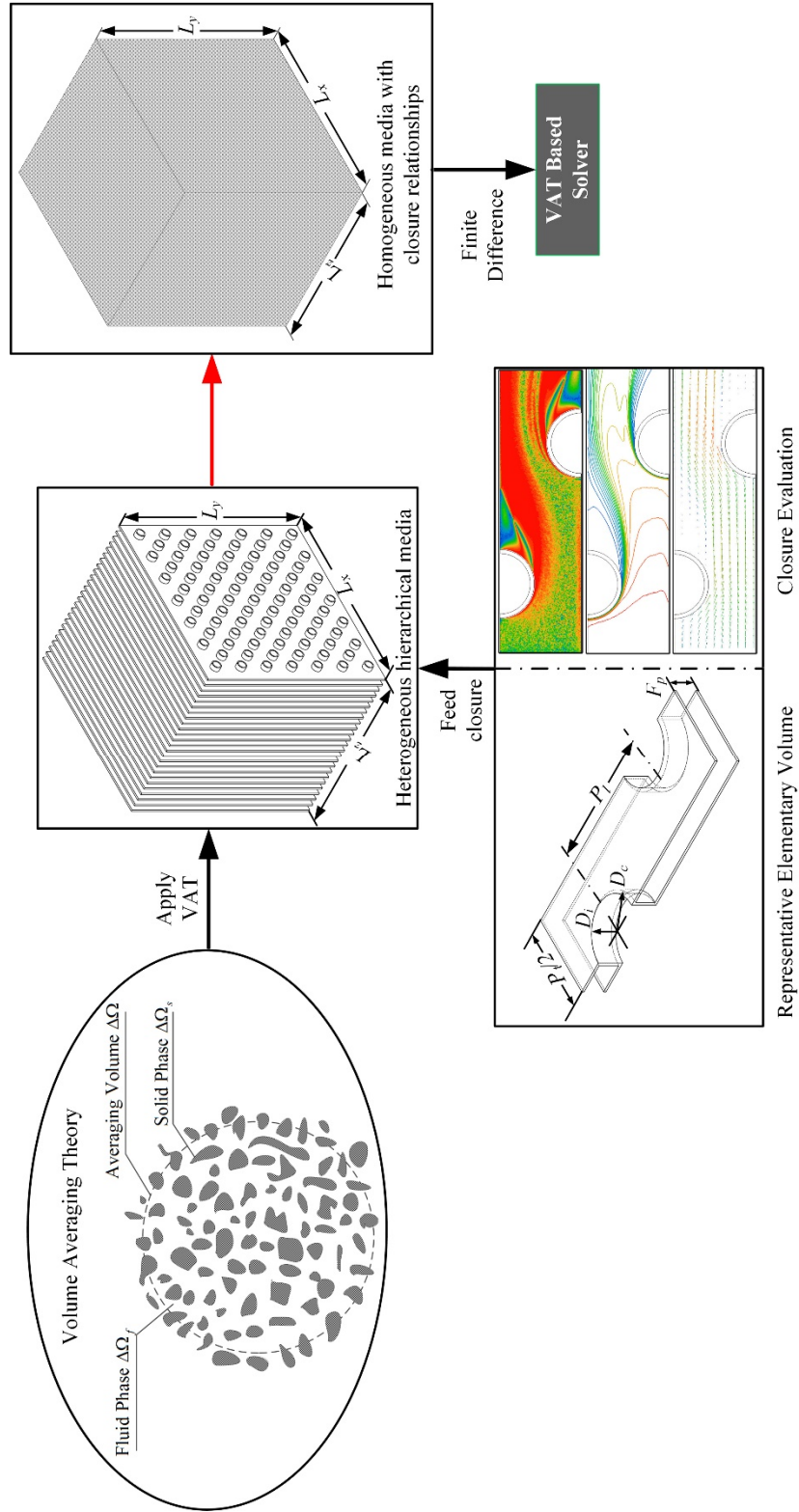
Figure 1.1: Schematic of the process of VAT based modeling and closure evaluation.

1.2.2. Closure Evaluation

As explained in the previous section, Volume Averaging Theory reduces the difficulty of properly describing the flow and heat transfer through a hierarchical and heterogeneous media to the development of closures. In the present work, a method to obtain the closures for VAT based governing equations by CFD evaluation is developed. As shown in Figure 1.2, the procedure of the closure evaluation could be summarized into the following few steps. First, a proper representative elementary volume (REV) needs to be selected correctly, which is simply the periodic unit cell in the case of periodic media, but in random media, the situation is much more complicated. After that, a proper characteristic length scale should be defined. To conduct CFD calculations accurately, an appropriate numerical method is needed, which is chosen based on the flow condition. Then the computational domain needs proper discretization, i.e. structured mesh, unstructured mesh, adaptive analysis, hybrid mesh, which is determined by the complexity of the geometry. In the meantime, validation and verification of the adopted numerical method is necessary. After that, the number of REVs needed to obtain reasonable local values is determined. Then numerical simulation over the selected REVs within proper variable ranges is conducted and the closures are evaluated over the REV. Finally, the evaluated results for friction factor and heat transfer coefficient are collected and the corresponding correlations are developed. Compared to the traditional system level optimization methods, application of VAT only requires direct numerical experiments at a pore scale representative elementary volume (REV) which usually has a much smaller computational domain than the whole system, therefore the computation load is significantly reduced.

Figure 1.2: A general prodedure to obtain closures using CFD simulations.

1.3. Organization of the Document

The organization of the present document is summarized in Figure 1.3. Specifically, Chapter 2 provides an overview of the development of volume averaging theory and its closure methods, which is the starting point of the present study. Besides some typical research work conducted on fin-and-tube heat exchangers and heat sinks are presented as an introduction to the present modeling objects.

Chapter 3 revisits and establishes the right form of governing equations and closures for hierarchical media based on volume averaging theory.

Chapter 4 shows the development of closures for heat exchangers in details which is also the most important part the thesis. How Chapter 4 is organized is shown in Figure 1.3, which is also a general procedure one should follow to use the present method to obtain closure for VAT. In the end of Chapter 4, a guideline to obtain closures by using CFD evaluation over a selected REV is provided.

Chapter 5 applies the volume averaging theory to a fin-and-tube heat exchanger and a plate fin heat sink, leading to specific VAT based models for them. Along with the closures developed in Chapter 4, the governing equations are solved discretely and can be used to conduct optimization. In addition, Chapter 5 also introduce a new plate-fin fin heat sinks which is a potential application object of the methodology presented in the current work.

Chapter 6 summarizes the key contributions of the present research and provides recommendations for future work.
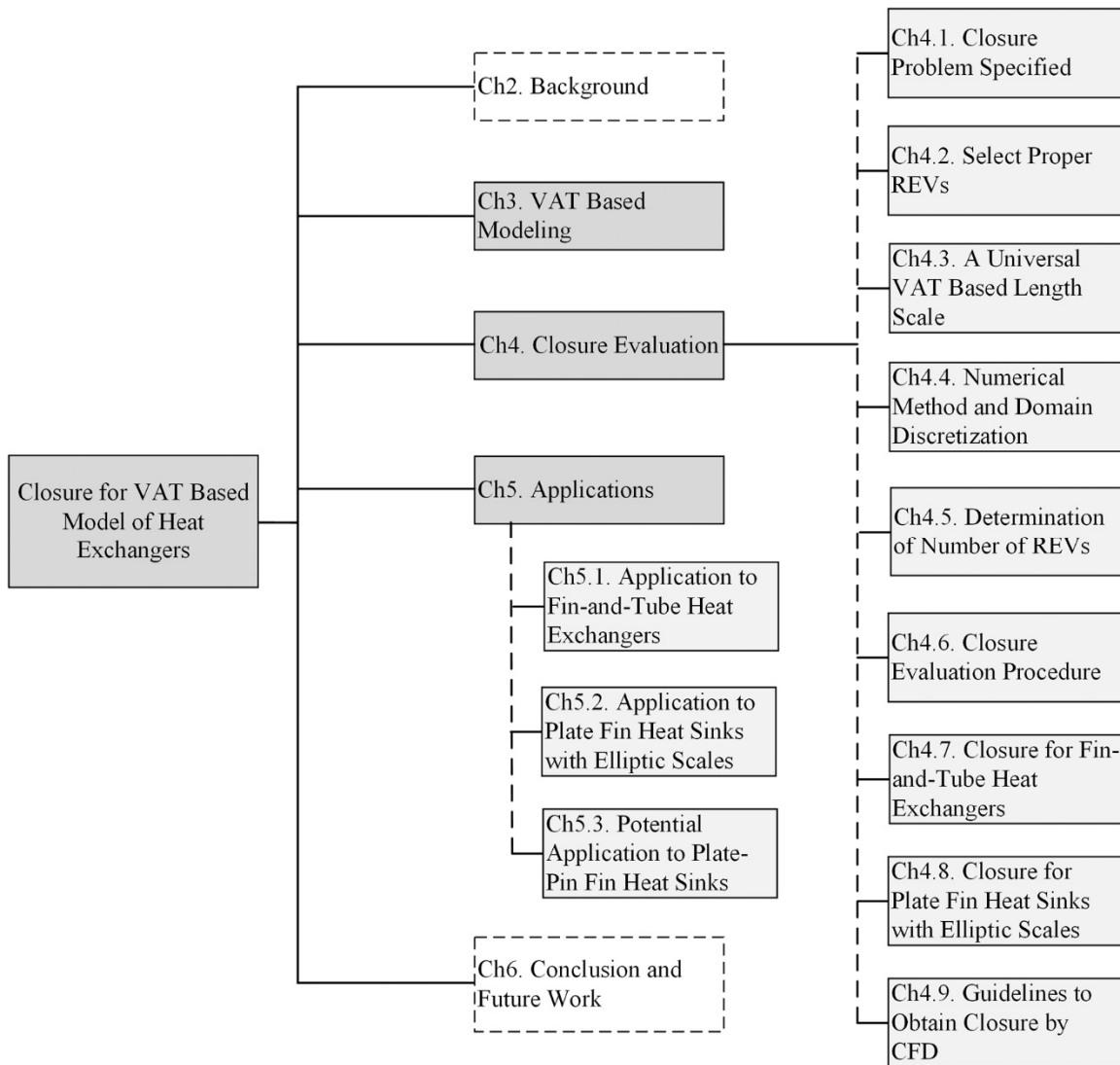
Figure 1.3: Flow chart illustrating the organization of the thesis.

2. Background

Optimization of heterogeneous and hierarchical media is a new field. It is significant for thermal engineering applications and very few references can be found in this field. Travkin and Catton [5], however, laid out a plan for optimization. Nelson and Bejan [6] tried to seek optimized solutions of transport in heterogeneous media, but the optimization given in their paper is only for a specific case. Keil and Rieckmann [7] studied structure optimization. However, that work was motivated from a morphology viewpoint, not from heat transfer viewpoint.

It is known that if rough surfaces or heterogeneous media are used, the enhanced heat transfer is accompanied by an increased pressure drop. Therefore, the key issue for the study of transport in heterogeneous media is to adjust the governing parameters and to optimize the ratio of heat transfer to pumping power, in other words to improve the heat transport efficiency of the heterogeneous media. It is believed that a systematic optimization study based on rigorously developed fundamental VAT equations will solve the problem of heat transfer optimization of heterogeneous media as well as help obtain better augmented heat transfer surfaces.

2.1. Volume Averaging Theory and the Closure Problem

Determination of flow-variables and scalar transport in a heterogeneous (or porous) media is difficult even when subject to simplifications allowing the specification of medium periodicity or regularity. Linear or linearized models fail to intrinsically account for transport phenomena, requiring dynamic coefficient models to correct for short-comings in the governing models. Allowing inhomogeneities to adopt random or stochastic

character further confounds the already daunting task of properly identifying pertinent transport mechanisms and predicting transport phenomena. Some aspects of the development of the needed theory are now well understood and have seen substantial progress in thermal physics and fluid mechanics sciences, particularly in porous media transport phenomena.

2.1.1. Volume Averaging Theory

The basis for this progress is Volume Averaging Theory (VAT), which was first proposed in the sixties by Anderson and Jackson [8], Slattery [9], Whitaker [10] and Zolotarev and Radushkevich [11]. Further advances in the use of VAT are found in the work of Slattery [12], Whitaker [13], Kaviany [14], Gray et al. [15] and Whitaker [16]. Many of the important details and examples of its application are found in books by Dullien [17] and Adler [18].

More advances in nonlinear transport phenomena in porous media was addressed by Travkin and Catton [19-24] and de Lemos's group [25-36], who developed general VAT governing equations for turbulent fluid flow and heat transfer. Nakayama and Kuwahara [37, 38] also successfully derived a set of macroscopic governing equations for turbulent heat and fluid flow through an isotropic porous media in local thermal equilibrium.

To describe transport processes in a heterogeneous media, the correct form of the governing equations remains an area where inattention to procedure by some researchers has led to significantly different equations for the same media (see discussions by Travkin and Catton [4, 19, 24]). However, the general idea is the same, which is to derive the upper-level VAT-based equations by averaging the Navier-Stokes and thermal energy equations over a specified Representative Elementary Volume (REV). Due to the averaging process,

the VAT-based governing equations yield additional integral and differential terms when compared to the homogenized or classical continuum mechanics equations.

2.1.2. The Closure Problem

In order to utilize the upper-level equations for large-scale computations, proper closure is needed to complete the VAT governing equations. In the past, there has been a great deal of work done on how to find approximate closure of coupled micro-scale flow solutions and VAT equations. The closure of the system has three basic approaches: Brenner [39, 40] developed a theory on how to find closure based on momentum methods. The work is based on particle tracking using Brownian motion theory. There are various works that do actual calculations and have demonstrated the theory to be valid for various cases. The second approach is the method of homogenization of the Navier-Stokes (N-S) equations at different scales. Mei and Auriault [41], Giorgi [42] and Chen et al. [43] applied this method to find a dispersion tensor on periodic unit cells. The third approach is the proper closure for the scalar VAT equations developed by Carbonell and Whitaker [44]. Sahraoui and Kaviany [45] solved the closure problem by lumping hydrodynamic dispersion into the effective thermal conductivity tensor. Hsiao and Advani [46, 47] used a closure that is linearly proportional to the average temperature and the average velocity and grouped intra-phase heat transfer into the thermal conduction term.

More recently, Kuwahara et al. [48], Nakayama and Kuwahara [49], Kuwahara and Nakayama [50] and Nakayama et al. [51] closed the macroscopic equations by modeling the flow resistance and heat transfer rate associated with the flowing fluid and individual subscale elements, in terms of the macroscopic velocity vector and relevant geometrical parameters. Direct numerical experiments were carried out at a pore scale for individual

subscale elements to establish such subscale models. Macroscopic hydrodynamic and thermal characteristics could be extracted from the microscopic results to determine the unknown model constants of the subscale models associated with permeability tensor, inertial tensor, and interfacial heat transfer coefficient. De Lemos and Pedras [52] and Pedras and De Lemos [53] have also conducted similar microscopic computations and close the macroscopic equations by exhaustive numerical experiments. A review on how to close the macroscopic equations by numerical computations could be found in chapter 10 of the handbook [54] and chapter 6 of the second edition of the handbook [55].

Travkin and Catton [4] rigorously derived closure terms for the VAT based model that are related to the local friction factor and the heat transfer coefficient from the lower scale governing equations. Travkin and Catton [56] also showed that choosing the correct length scale, allows one to collapse true capillary flow and flow in a bed of spheres, which spans the physical description from globular to capillary geometry with a single length scale. Furthermore, Travkin and Catton [19] found the suitable length scale as a direct result of scaling VAT equations. On a theoretical basis, this length scale is found to be a hydraulic diameter of the porous media, where the hydraulic diameter definition allows the transformation and comparison of correlation equations and experimental results obtained for wide range morphologies of the porous media.

In the present study, the closure terms rigorously derived by Travkin and Catton [4] will be evaluated using numerical computations to close the macroscopic models for fin-and-tube heat exchangers and heat sinks with scale-shaped surface roughness.

2.2. Heat Exchangers

A heat exchanger is a piece of equipment built for efficient heat transfer from one medium to another. The media may be separated by a solid wall to prevent mixing or they may be in direct contact [57]. Fin-and-Tube heat exchangers and heat sinks are the two classic examples of heat exchangers, which are also the application objects of VAT modeling in the present study.

2.2.1. Fin-and-Tube Heat Exchangers
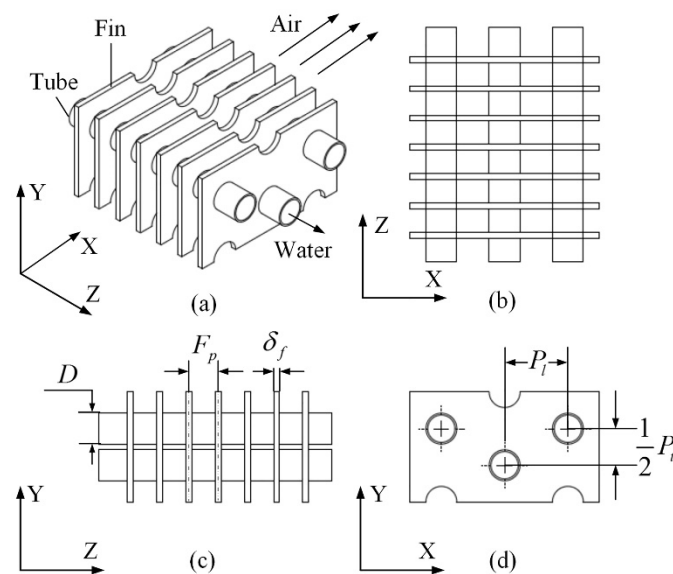
Figure 2.1: A schematic diagram of a fin-and-tube heat exchanger.

Fin-and-tube heat exchangers are widely used in thermal engineering applications, such as power stations, chemical engineering, automobiles, heating, ventilating, air conditioning and refrigeration (HVAC&R) applications, aircrafts, etc. The general geometric

arrangement of a plate fin-and-tube heat exchanger is shown in Figure 2.1. Usually, there are three or more rows of tubes which are arranged in-line or staggered. Generally, air flows through the fins perpendicular to the tubes, while water or other fluid flows through the tubes. This is a problem of conjugate heat transfer within a heterogeneous hierarchical structure.

In the past, extensive parametric studies on the performance of fin-and-tube heat exchangers have been done, either experimentally or numerically. Initially, the emphasis was on experimental work due to the absence of today's computational power. During the past 40 years, a large amount of experimental data and their resulting correlations on the air side flow and heat transfer characteristics of fin-and-tube heat exchangers have been published. Rich [58] presented experimental results for six coils, with the number of tube rows in the direction of air flow varying from 1 to 6. It was concluded that the pressure drop per row is independent of the number of tube rows. McQuiston [59] proposed the first well known correlation for plate fin-and-tube heat exchangers with tube row number being in the range of 1~4. Based on a superposition model which was initially proposed by Rich [60], Gray and Webb [61] gave an updated correlation for fin-and-tube heat exchangers, that is superior to McQuiston's [59]. It should be noted that the correlations were based on experimental data of four-row fin-and-tube heat exchangers. Kang et al. [62] presented experimental data and correlations for a 3-row fin-and-tube heat exchanger core in a wide range of Reynolds number. Most recently, Wang et al. [63] proposed the most precise correlations of friction factor and Colburn j factor for the air side of fin-and-tube heat exchangers. The correlations are based on a total of 74 samples and the proposed heat transfer correlation can describe 88.6% of the database within an error of ±15%, while the

proposed friction correlation can correlate 85.1% of the database within an error of ±15%. It is argued by some researchers [3, 64-66] that Wang's correlations [63] have certain application ranges, like $1 \leq N \leq 6$, 6.35 mm$\leq D_o \leq$12.7 mm, which are usually used in the HVAC&R engineering, and are not applicable to some applications of large industry, such as the inter-cooler of multistage compressor, in which the number of tube rows might be much larger and the outside diameter of tubes might be larger than 13 mm. As a result, investigations on the heat transfer and friction characteristics of fin-and-tube heat exchangers with large number of tube rows and large tube diameters were carried out experimentally [3, 65, 66].

In the last 20 years, CFD (Computational Fluid Dynamics) has been widely used to simulate the flow and heat transfer processes in fin-and-tube heat exchangers for design and optimization purposes. Torikoshi et al. [67] reported simulation results for 1-row and 2-row fin-and-tube heat exchangers. Jang et al. [68-70] did extensive numerical and experimental studies on fluid flow and heat transfer over a multi-row (1-6 rows) fin-and-tube heat exchanger. It was reported that the number of tube rows has a small effect on the average heat transfer coefficient when the row number was larger than 4. Xie et al. [64] tested fin-and-tube heat exchangers with a large number of large-diameter tube rows varying from 1 to 7 numerically. In addition to the literature reviewed above, there are also some other typical work on the investigation of flow and heat transfer characteristics of fin-and-tube heat exchangers being reported (refer to [71-119]).

Recently, a lot of work has been done to optimize fin-and-tube heat exchangers. Generally, previous work falls into to two different types. The first type of studies relied upon traditional methods of heat exchanger thermal modeling and correlations developed

from experimental studies. Xie et al. [120] performed optimization of a plate-fin type Compact Heat Exchanger (CHE) using a genetic algorithm as the optimization method and the traditional rating method, ε-NTU method, to evaluate the performance of the PFCHE. Experimental transfer coefficient correlations were employed for both the air and water sides, and the total weight and annual cost of the FTHX were minimized separately. Similar work was done to optimize fin-and-tube heat exchangers by Xie et al. [121]. Domanski [122] described a public-domain FTHX simulation software tool, EVAP-COND (the latest version is 3.0 released in 2010) and discussed its integration with an optimization routine [123]. Empirical correlations employed for the heat transfer coefficients and pressure drops and the heat exchanger performance is determined using a tube-by-tube segmented LMTD approach. Another design tool, CoilDesigner was described by Jiang, Aute, and Radermacher [124], that can also be integrated with optimization procedures [125]. CoilDesigner adopts a network viewpoint, and takes a segmented modeling approach using the ε-NTU method. Some other work using similar methods could be found from Ozkol and Komurgoz [126], Sanaye and Hajabdollahi [127], Najafi et al. [128], Hajabdollahi et al. [129], etc.

The second type of studies combined CFD simulation with generic algorithm to conduct the optimization. A typical work was reported by Hajabdollahi et al. [130] who optimized a compact heat exchanger with triangle fin geometry. The Fanning friction factor f and Colburn factor j for triangle fin geometry were evaluated using CFD. The optimization was then conducted using the ε-NTU method and genetic algorithm (NSGA-II). Mousavi, Hooman, and Mousavi [131] used GA to optimize the structure of a finned channel, for a fixed flow rate, in terms of the location and size of the fins. The fluid flow

17

and temperature fields were obtained using CFD code, assuming two-dimensional, laminar, steady state flow with constant properties [132]. In this study, the conjugate problem was not solved since the fins were considered perfectly conductive and of negligible thickness. Foli et al. [133] used a multi-objective GA to optimize the performance of a micro heat exchanger by considering the shape of its channels. They simultaneously maximized the heat transfer and minimized the pressure drop by searching for the optimal shape of the separator between the fluids. The flow and heat transfer were simulated using commercial CFD software and conjugate heat transfer effects between the solid and fluid were taken into account. It was reported that a month of calculations were necessary to do so. Some other work using CFD-GA combined method could be found from Hilbert et al. [134], Hooman and Gurgenci [135], etc. It is apparent that using CFD-GA combined method, the cost of the CFD simulations prevented the possibility of a more thorough search of the domain or more design variables at the same time.

The VAT based modeling method, however, addresses many of the undesirable characteristics of the methods discussed above. In the present study, a fin-and-tube heat exchanger is modeled using VAT and the closure is obtained using CFD evaluation as an application case.

2.2.2. Heat Sinks

The challenge posed by high heat fluxes in electronic chips makes thermal management an essential element in the development of these systems, which are driving conflicting needs for high performance as well as reduced power consumption, size and weight. Although many new cooling technologies such as cooling by heat pipes, cold water, and even by liquid nitrogen have been proposed and adopted, air cooling by heat sink, see Figure 2.2,

18

is still a commonly used solution for thermal management in electronic packaging due to its low cost, availability and reliability factors. In the electronic thermal management, heat sinks are usually attached on the tops of the electronic packages to enhance heat dissipation and control junction temperatures of these packages. With the trend towards increasing levels of electronic device integration density, it has become increasingly challenging to meet the thermal management requirements of the resulting elevated power dissipation. Therefore, the overall objective of the heat sink design is significant enhancement of convective heat transfer with minimal increases in the streamwise pressure drop penalties.
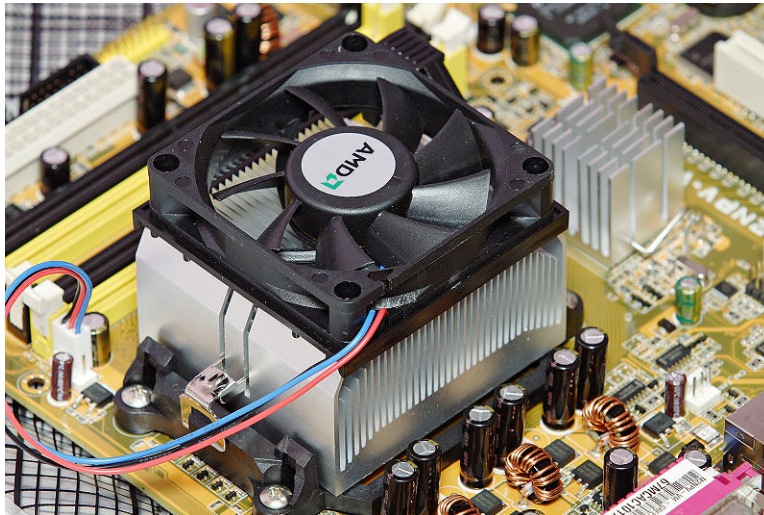
Figure 2.2: A commonly used heat sink-fan system for air cooling borrowed from Wikipedia.

Among the varieties of heat sinks, plate fin heat sinks (PFHSs) are the most widely used due to their simple structure and easy manufacturing. Many publications investigate the modelling and optimization of the PFHS to determine the optimum fin height, fin pitch, and fin thickness to obtain maximum heat dissipation.

Knight et al. [136, 137] presented a scheme to determine the dimensions of a microchannel heat sink that will minimize the thermal resistance using conservation equations presented in a generalized, dimensionless form along with applicable geometrical relationships. They [138] then used the optimization scheme to design, build and test several air cooled aluminium finned arrays. Teertstra et al. [139] presented an analytical model to predict the average heat transfer rate for forced convection, air cooled, plate fin heat sinks for electronics applications. Copeland [140] calculated the optimum dimensions of fin thickness and pitch for a variety of realistic operating conditions, using an analytical model. Culham and Muzychka [141] presented a procedure that allows the simultaneous optimization of heat sink design parameters based on a minimization of the entropy generation associated with heat transfer and fluid friction. Iyengar and Bar-Cohen [142] provided a viable technique for combining least-material optimization with the entropy minimization methodology by a coefficient of performance (COP_T) analysis for plate fin heat sinks in forced convection. Chiang [143] presented an effective method for predicting and optimizing the cooling performance of a plate fin heat sink module based on the Taguchi method. All the above investigations are focused on the optimization of plate fin heat sinks and show that the performance of PFHSs can be increased to a certain extent by adopting optimum geometries. However the optimization procedures cannot overcome the intrinsic shortcoming in the structure of a PFHS, i.e. air flows smoothly

through the heat sink channels due to the parallel plate fin arrangement, which leaves much room for further study on enhancing heat transfer performance of PFHSs.

Pin fin heat sinks are another efficient heat transfer device used in many electronic cooling applications. There are many publications on heat transfer in electronic cooling using pin fin heat sinks. Sparrow et al. [144] performed heat transfer and pressure drop experiments for in-line pin fin arrays to obtain basic data to complement available information for staggered arrays. Sparrow and Kang [145] performed heat transfer and pressure drop experiments for cross-flow tube banks in which the individual tubes were equipped with longitudinal fins. Sparrow and Grannis [146] performed a broad-ranging investigation encompassing complementary experimentation and numerical simulation to determine the pressure drop characteristics of diamond-shaped pin fins. Chapman et al. [147] designed elliptical pin fin heat sinks to minimize the pressure loss and enhance the thermal performance. Li et al. [148] carried out experiments to investigate heat transfer and flow resistance characteristics in rectangular ducts with staggered arrays of short elliptic pin fins in a crossflow of air. Yang et al [149] performed an experimental study of pin fin heat sinks having circular, elliptic, and square cross-sections. Horvat and Catton [150, 151] developed a fast running computational algorithm based on volume averaging theory (VAT) to simulate conjugate heat transfer process in a pin fin heat sink, which offers possibilities for geometry improvements and optimization, to achieve higher thermal effectiveness. Park et al. [152] performed the design optimization of a 7×7 pin fin heat sink numerically to achieve higher thermal performance of the heat sink, using the weighting method for predicting the multi-objective problem. Chen et al. [153] developed an effective method for performing the thermal optimization of fully confined pin fin heat sinks under

21

constraints of pressure drop, mass, and space limitations. Khan et al. [154, 155] studied the thermodynamic losses caused by heat transfer and pressure drop in cylindrical pin fin heat sinks by applying an entropy generation minimization, EGM, technique, which allows all relevant design parameters for pin-fin heat sinks, including geometric parameters, material properties and flow conditions to be simultaneously optimized. Chiang et al. [156, 157] explored the optimal values of designing parameters of a pin fin type heat sink under constrains of mass and space limitation to achieve the high thermal performance (or cooling efficiency) by experiment. There are also some publications on comparisons of fluid flow and thermal characteristics of plate fin and pin fin heat sinks. Jonsson and Moshfegh [158] conducted tests in a wind tunnel with seven types of heat sinks including plate fin, strip fin, and pin fin heat sinks. An empirical bypass correlation has been developed for the different fin designs. Soodphakdee et al. [159] compared the heat transfer performance of various commonly used fin geometries, which include plate fins (parallel plates and staggered plates) and pin fins (round, elliptical and square). It was concluded that the staggered plate fin geometry showed the highest heat transfer for a given combination of pressure gradient and flow rate. Kin et al. [160] compared the thermal performances of plate fin and pin fin heat sinks and proposed correlations for the friction factor and Nusselt number for each type of heat sink. Compared with plate fin heat sinks which have the advantages of simple structure and easy manufacturing, pin fin heat sinks have an advantage of hindering the development of a thermal boundary layer at the expense of an increased pressure drop.

Besides the commonly used plain fin and pin fin heat sinks, a variety of techniques [161] for surface heat transfer enhancement have been developed, including ribs [162-166], dimpled surfaces [167-170], surfaces with arrays of protrusions [171], and surface

roughness, which could be applied to a plain fin heat sink to augment the heat dissipation capability. All of these devices not only act to increase secondary flows and turbulence levels to enhance bulk flow mixing and to form coherent fluid motions in the form of streamwise oriented vortices, but also provide some heat transfer augmentation by increasing surface areas for convective heat transfer [161]. Recently, a new heat transfer enhancement surface geometry was developed by Chang et al. [2, 172-175] using deepened circular scale roughness with $P_t = P_l = D$, see Figure 2.3. The surface scales are arranged in a staggered manner in-line on opposing walls. The authors compared $\overline{Nu}/Nu_\infty$ and $\overline{f}/f_\infty$ of the scale-roughened surface with the flow and heat transfer results reported by different research groups for rib-roughened channels [162-166] and dimpled surfaces [167]. The heat transfer enhancement of the scale-roughened surface was surprisingly good compared with rib-roughened and dimpled surfaces and the channel with forward flow performs better than that with backward flow. It should be noted that the scale pitches is not necessarily equal to each other, which means the scale shape could be elliptic instead of circular.

Considering the impressive heat transfer enhancement capability of the scale-shaped surface roughness, it could be applied to a plate fin heat sink for electronics cooling. A schematic diagram of a plate fin heat sink with scale roughened surface is shown in Figure 2.4. Generally, the air could be forced to flow through the channels between the fins by a fan or impinging jet. A plate fin heat sink with elliptic scale-shaped roughness is modeled using VAT and closure is obtained as another application case.

23
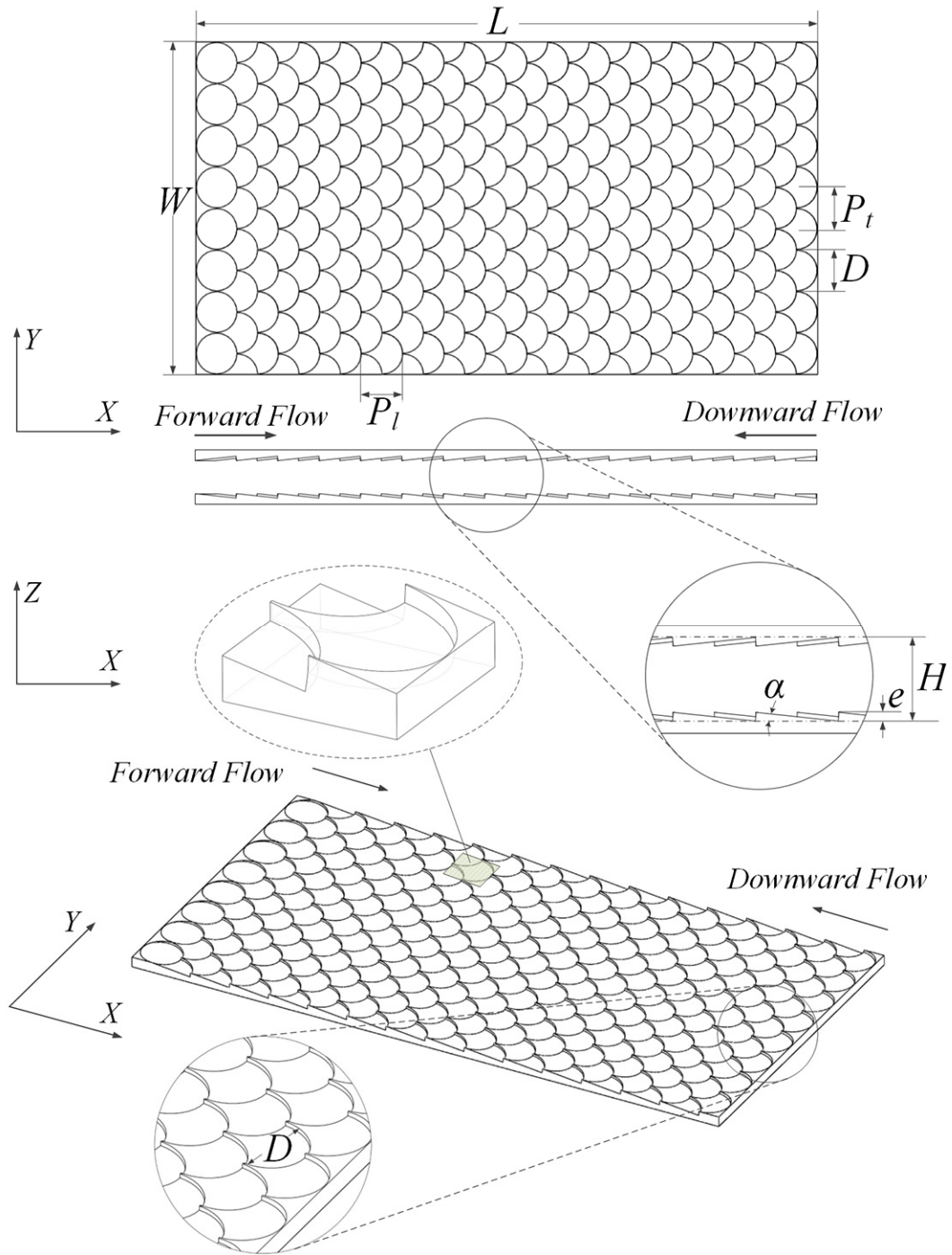
Figure 2.3: Geometrical details of circular scale-roughened surface.
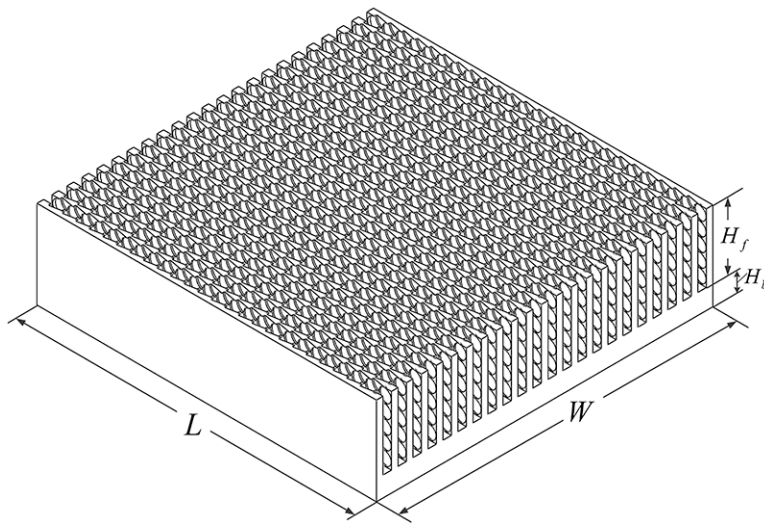
Figure 2.4: A plane fin heat sink with scale roughened surfaces.

2.3. Conclusions

Generally, there are three main different methods to design and optimize a heat exchanger, analytical method, experiment and CFD simulation. Analytical method usually works well for simple geometries, but for complicated especially hierarchical and heterogeneous structures, analytical analysis often comes with too many simplifications and assumptions. Experimental methods are expensive and time consuming, as many different models must be fabricated and tested. Numerical methods are more efficient, but many are specific to the type of geometry that is being tested and direct numerical simulation of the full 3D structure on system or device level is often not feasible.

If one wants to find the optimum configurations for these kinds of heterogeneous hierarchical heat transfer devices, which require many parameters to describe their geometries, analytical analysis, experiment or CFD simulation by itself is extremely difficult. In the case of a fin-and-tube heat exchanger, 15 parameters are required for its description: overall length, width and height, fin thickness, fin pitch, tube diameter, tube wall thickness, tube pitch in x and y directions, flow rates of fluid 1 and 2, initial temperatures of fluid 1, 2, material of construction and heat source. A heat sink with surface roughness also has up to 10 parameters to define its structure.

Using Volume Averaging Theory to model these heat exchangers, simplified upper-level governing equations could be obtained and easily solved discretely. Then the difficulty is reduced to how to obtain the closure correctly, which is the most challenging part of the whole process. The closure terms could be evaluated using CFD over a selected representative elementary volume, as introduced in section 1.2.2, instead of the whole geometry, which considerably lower the computational cost.

3. Volume Averaging Theory Based Modeling

The method of volume averaging begins by associating an averaging volume $\Delta\Omega$ with every point in space. The averaging volume, the representative elementary volume (REV), is illustrated in Figure 3.1 and is represented in terms of the volumes of the individual phases by

$$\Delta\Omega = \Delta\Omega_f\left(t,\vec{x}\right) + \Delta\Omega_s(\vec{x}) \tag{3.1}$$

The volumes of the fluid and solid phases can depend on position and, in addition, the volume of the fluid phase can depend on time. Average values are defined in terms of these volumes and these averaged values are associated with the centroid of $\Delta\Omega$. The general idea is to derive the upper-level governing equations by averaging the Navier-Stokes and thermal energy equations over a specified Representative Elementary Volume (REV).
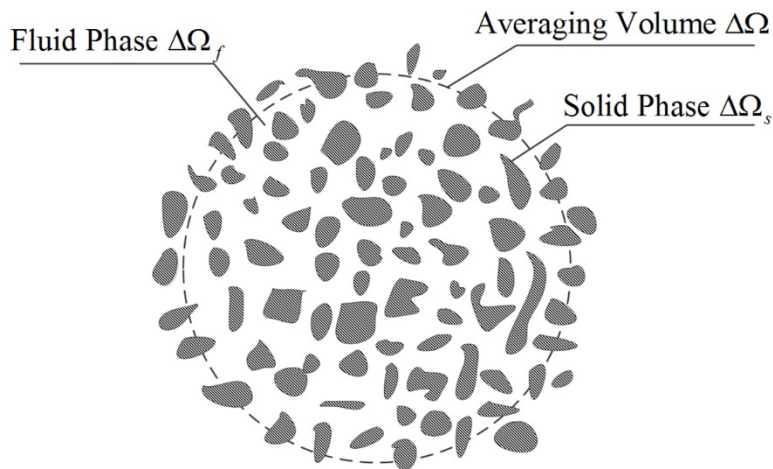
Figure 3.1: Representative elementary volume (REV).

3.1. Fundamentals of Volume Averaging Theory (VAT)

3.1.1. Averaging operators

In the development of volume averaged transport equations, a superficial average and an intrinsic average are defined in this section.

The superficial average of fluid temperature, T_f, is expressed as

$$\left\langle T_f \right\rangle = \frac{1}{\Delta\Omega} \int_{\Delta\Omega_f} T_f\left(\bar{x},t\right) d\omega \qquad (3.2)$$

in which $\Delta\Omega_f$ is the volume of the fluid phase contained within the volume of the REV, $\Delta\Omega$. Here it is understood that $\Delta\Omega_f$ depends on position.

The intrinsic average of fluid temperature is defined as

$$\tilde{T}_f = \frac{1}{\Delta\Omega_f} \int_{\Delta\Omega_f} T_f\left(\bar{x},t\right) d\omega \qquad (3.3)$$

The superficial average of a certain quantity is not a good meaningful representation of a particular phase quantity. Consider a following illustrative example when one has a constant quantity f_0 and then the superficial average is not a constant, since the fluid volume is not a constant. Thus, the intrinsic average appears to be a better representation of a fluid phase quantity.

The porosity, $<m>$, is the volume fraction of the fluid volume in the averaging volume $\Delta\Omega$, which is defined as

$$\left\langle m \right\rangle = \frac{\Delta\Omega_f}{\Delta\Omega} \qquad (3.4)$$

Since the porosity in a highly porous media is often anisotropic and randomly non-homogeneous, let us expand the random porosity function into additive components: the average value of $\langle m(\bar{x})\rangle$ in the REV and its fluctuation $\hat{m}(\bar{x})$ in various directions,

$$m(\bar{x}) = \langle m(\bar{x})\rangle + \hat{m}(\bar{x})$$

(3.5)

The averaged equations of turbulent filtration for a highly porous medium model are similar to those in an anisotropic porous medium. Five types of averaging operators are defined as follows:

The average of function f over the whole REV can be expressed as

$$
\begin{aligned}
\langle f \rangle &= \frac{1}{\Delta\Omega} \int_{\Delta\Omega} f(\bar{x},t)\,d\omega \\
&= \frac{\Delta\Omega_f}{\Delta\Omega} \frac{1}{\Delta\Omega_f} \int_{\Delta\Omega_f} f(\bar{x},t)\,d\omega + \frac{\Delta\Omega_s}{\Delta\Omega} \frac{1}{\Delta\Omega_s} \int_{\Delta\Omega_s} f(\bar{x},t)\,d\omega \\
&= \langle m \rangle \tilde{f} + (1-\langle m \rangle)\hat{f} \\
&= \langle f \rangle_f + \langle f \rangle_s
\end{aligned}
$$

(3.6)

The phase average of the function f in each component of the media is

$$\langle f \rangle_f = \frac{\Delta\Omega_f}{\Delta\Omega} \frac{1}{\Delta\Omega_f} \int_{\Delta\Omega_f} f(\bar{x},t)\,d\omega = \langle m \rangle \tilde{f}$$

(3.7)

$$\langle f \rangle_s = \frac{\Delta\Omega_s}{\Delta\Omega} \frac{1}{\Delta\Omega_s} \int_{\Delta\Omega_s} f(\bar{x},t)\,d\omega = (1-\langle m \rangle)\hat{f}$$

(3.8)

The interphase average of each component is

$$\tilde{f} = \{f\}_f = \frac{1}{\Delta\Omega_f} \int_{\Delta\Omega_f} f(\bar{x},t)\,d\omega$$

(3.9)

$$\hat{f} = \{f\}_s = \frac{1}{\Delta\Omega_s} \int_{\Delta\Omega_s} f(\bar{x},t)\,d\omega$$

(3.10)

where $\tilde{f}$ is an average over the fluid phase volume $\Delta\Omega_f$, $\hat{f}$ is an average over the solid phase volume $\Delta\Omega_s$, and $<f>$ is an average over the whole REV. When the interface is fixed in space, averaged functions for the fluid and solid phase within the REV and over the entire REV fulfill all four of the Reynolds conditions as well as the following four consequences, namely

1) The average of the sum is the sum of the averages:

$$\{f+g\}_f = \tilde{f} + \tilde{g} \qquad (3.11)$$

2) Constants do not affect and are not affected by averaging:

$$\{af\} = a\{f\}, \{a\} = a \qquad (3.12)$$

3) The average of the time or space derivative of a quantity is equal to the corresponding derivative of the average:

$$\left\{\frac{\partial f}{\partial t}\right\}_f = \frac{\partial \tilde{f}}{\partial t} \qquad (3.13)$$

4) The average of the product of an average and a function is equal to the product of the averages:

$$\{\tilde{f}g\}_f = \tilde{f}\tilde{g} \qquad (3.14)$$

The above equations of "Reynolds Conditions" have not been and cannot be derived; they are requirements that we impose on the averaging operator. What we are striving for here is nothing more or less than practical simplicity; averaging operators that do not satisfy the Reynolds conditions are just too unruly to be of much use [176].

From above equations we can derive the following four consequences:

$$\left\{\tilde{f}\right\} = \tilde{f}, \left\{f - \tilde{f}\right\} = 0, \left\{\tilde{f}\tilde{g}\right\} = \tilde{f}\tilde{g}, \left\{\tilde{f}\hat{g}\right\} = \tilde{f}\tilde{\hat{g}} = 0 \qquad (3.15)$$

It should be noted that $\langle f \rangle_f$ and $\langle f \rangle_s$ do fulfill neither the Reynolds conditions,

$$\langle a \rangle_f \neq a, \quad \langle a \rangle_f = \langle m \rangle a \qquad (3.16)$$

nor all the consequences of the Reynolds conditions.

The differentiation condition is,

$$\left\{\nabla f\right\}_f = \frac{1}{\Delta\Omega_f}\int_{\Delta\Omega_f}\nabla f\, d\omega = \frac{1}{\Delta\Omega_f}\int_{\Delta\Omega_f}\left(\nabla\tilde{f} + \nabla\hat{f}\right)d\omega$$
$$= \left\{\nabla\tilde{f} + \nabla\hat{f}\right\}_f = \nabla\tilde{f} + \frac{1}{\Delta\Omega_f}\int_{\partial S_w}\hat{f}\, d\bar{s} \qquad (3.17)$$

in which $\hat{f} = f - \tilde{f}, \quad f\forall\Delta\Omega_f$.

$$\langle\nabla f\rangle_f = \frac{1}{\Delta\Omega}\int_{\Delta\Omega_f}\nabla f\, d\omega = \nabla\langle f\rangle_f + \frac{1}{\Delta\Omega}\int_{\partial S_w}f\, d\bar{s} \qquad (3.18)$$

where ∂S_w is the inner surface in the REV, $d\bar{s}$ is the solid-phase, inward-directed differential area in the REV ($d\bar{s} = \bar{n}ds$). The fourth condition implies an unchanging porous medium morphology. All the above are well known from earlier work by Slattery [177], Whitaker [13], and Gray et al [15].

3.1.2. Application of Averaging Operators to Non-linear Terms

Most of the following analysis is based on averaging techniques developed by Whitaker [178-180] who focus on solving the linear diffusion problems and by Travkin and Catton [19] who focus on solving nonlinear turbulent diffusion problems.

Convection Term

The divergent and non-divergent forms of the averaged convective term are

$$
\langle \nabla (Tu_i) \rangle_f
$$

$$
= \nabla \langle Tu_i \rangle_f + \frac{1}{\Delta\Omega} \int_{\partial S_w} Tu_i \, d\bar{s}
$$

$$
= \nabla \left[\langle m \rangle \tilde{T}\tilde{u}_i + \langle m \rangle \{\hat{T}\hat{u}_i\}_f \right] + \frac{1}{\Delta\Omega} \int_{\partial S_w} Tu_i \, d\bar{s}
$$

$$
= \langle m \rangle \tilde{u}_i \frac{\partial}{\partial x_i} \tilde{T} - \tilde{T} \frac{1}{\Delta\Omega} \int_{\partial S_w} u_i \, d\bar{s} + \nabla \langle \hat{T}\hat{u}_i \rangle_f + \frac{1}{\Delta\Omega} \int_{\partial S_w} Tu_i \, d\bar{s}
$$

(3.19)

where,

$$
\langle Tu_i \rangle_f = \left\langle \left(\tilde{T} + \hat{T} \right)\left(\tilde{u}_i + \hat{u}_i \right) \right\rangle_f
$$

$$
= \left\langle \tilde{T}\tilde{u}_i + \hat{T}\tilde{u}_i + \hat{T}\tilde{u}_i + \hat{T}\hat{u}_i \right\rangle_f
$$

$$
= \langle \tilde{T}\tilde{u}_i \rangle_f + \tilde{T}\langle \hat{u}_i \rangle_f + \tilde{u}_i \langle \hat{T} \rangle_f + \langle \hat{T}\hat{u}_i \rangle_f
$$

$$
= \langle \tilde{T}\tilde{u}_i \rangle_f + \langle \hat{T}\hat{u}_i \rangle_f = \langle m \rangle \tilde{T}\tilde{u}_i + \langle m \rangle \{\hat{T}\hat{u}_i\}_f
$$

(3.20)

Similarly, the averaged momentum convection term in divergence form becomes,

$$
\left\langle \frac{\partial}{\partial x_j} (u_j u_i) \right\rangle_f = \left\langle \nabla (u_j u_i) \right\rangle_f
$$

$$
= \nabla \langle u_j u_i \rangle_f + \frac{1}{\Delta\Omega} \int_{\partial S_w} u_j u_i \, d\bar{s}
$$

$$
= \nabla \left[\langle m \rangle \tilde{u}_j \tilde{u}_i + \langle m \rangle \{\hat{u}_j \hat{u}_i\}_f \right] + \frac{1}{\Delta\Omega} \int_{\partial S_w} u_j u_i \, d\bar{s}
$$

(3.21)

Decomposition of the term $\nabla \langle Tu_i \rangle_f$ in Eq. (3.19) and $\nabla \langle u_j u_i \rangle_f$ term in Eq. (3.21) yields

fluctuation terms, $\langle m \rangle \{\hat{T}\hat{u}_i\}_f$ and $\langle m \rangle \{\hat{u}_j \hat{u}_i\}_f$ respectively, that need to be treated in some

way.

32

Gradient Term with Constant Coefficient

$$\left\langle k_f \nabla T \right\rangle_f = k_f \nabla \left\langle T \right\rangle_f + \frac{k_f}{\Delta\Omega} \int_{\partial S_w} T d\bar{s} = k_f \nabla \left\langle \tilde{T} + \hat{T} \right\rangle_f + \frac{k_f}{\Delta\Omega} \int_{\partial S_w} \left(\tilde{T} + \hat{T} \right) d\bar{s}$$

$$= k_f \nabla \cdot \left(\left\langle m \right\rangle \tilde{T} \right) + \tilde{T} \frac{k_f}{\Delta\Omega} \int_{\partial S_w} d\bar{s} + \frac{k_f}{\Delta\Omega} \int_{\partial S_w} \hat{T} d\bar{s}$$

$$= k_f \nabla \cdot \left(\left\langle m \right\rangle \tilde{T} \right) + k_f \tilde{T} \left(-\nabla \left\langle m \right\rangle \right) + \frac{k_f}{\Delta\Omega} \int_{\partial S_w} \hat{T} d\bar{s} \qquad (3.22)$$

$$= k_f \left\langle m \right\rangle \nabla \tilde{T} + \frac{k_f}{\Delta\Omega} \int_{\partial S_w} \hat{T} d\bar{s}$$

in which

$$\frac{1}{\Delta\Omega} \int_{\partial S_w} d\bar{s} = -\nabla \left\langle m \right\rangle \qquad (3.23)$$

was shown by Whitaker [178].

Thus two averaging form of the gradient term with constant coefficient are allowed,

$$\left\langle k_f \nabla T \right\rangle_f = k_f \nabla \cdot \left(\left\langle m \right\rangle \tilde{T} \right) + \frac{k_f}{\Delta\Omega} \int_{\partial S_w} T d\bar{s} \qquad (3.24)$$

or

$$\left\langle k_f \nabla T \right\rangle_f = k_f \left\langle m \right\rangle \nabla \tilde{T} + \frac{k_f}{\Delta\Omega} \int_{\partial S_w} \hat{T} d\bar{s} \qquad (3.25)$$

Similarly,

$$\left\langle \mu \nabla \bar{u} \right\rangle_f = \mu \nabla \cdot \left(\left\langle m \right\rangle \tilde{\bar{u}} \right) + \frac{\mu}{\Delta\Omega} \int_{\partial S_w} \bar{u} d\bar{s} \qquad (3.26)$$

or

$$\left\langle \mu \nabla \tilde{u} \right\rangle_f = \mu \left\langle m \right\rangle \nabla \tilde{u} + \frac{\mu}{\Delta \Omega} \int\limits_{\partial S_w} \hat{\tilde{u}} d\bar{s} \tag{3.27}$$

Diffusion Term with Constant Coefficient

The following averaged diffusion terms can be used in the transport equation (with constant coefficient of conductivity or diffusion).

$$\left\langle \nabla \left(k_f \nabla T \right) \right\rangle_f = k_f \left\langle \nabla \left(\nabla T \right) \right\rangle_f = k_f \nabla \left\langle \nabla T \right\rangle_f + \frac{k_f}{\Delta \Omega} \int\limits_{\partial S_w} \nabla T \cdot d\bar{s} \tag{3.28}$$

Substituting Eq. (3.24) into Eq. (3.28) yields,

$$\begin{aligned}
\left\langle \nabla \left(k_f \nabla T \right) \right\rangle_f &= k_f \nabla \left[\nabla \cdot \left(\left\langle m \right\rangle \tilde{T} \right) + \frac{1}{\Delta \Omega} \int\limits_{\partial S_w} T d\bar{s} \right] + \frac{k_f}{\Delta \Omega} \int\limits_{\partial S_w} \nabla T \cdot d\bar{s} \\
&= k_f \nabla^2 \left(\left\langle m \right\rangle \tilde{T} \right) + \nabla \cdot \left(\frac{k_f}{\Delta \Omega} \int\limits_{\partial S_w} T d\bar{s} \right) + \frac{1}{\Delta \Omega} \int\limits_{\partial S_w} k_f \nabla T \cdot d\bar{s}
\end{aligned} \tag{3.29}$$

Substituting Eq. (3.25) into Eq. (3.28) yields,

$$\begin{aligned}
\left\langle \nabla \left(k_f \nabla T \right) \right\rangle_f &= k_f \nabla \left[\left\langle m \right\rangle \nabla \tilde{T} + \frac{1}{\Delta \Omega} \int\limits_{\partial S_w} \hat{T} d\bar{s} \right] + \frac{k_f}{\Delta \Omega} \int\limits_{\partial S_w} \nabla T \cdot d\bar{s} \\
&= k_f \nabla \cdot \left(\left\langle m \right\rangle \nabla \tilde{T} \right) + \nabla \cdot \left[\frac{k_f}{\Delta \Omega} \int\limits_{\partial S_w} \hat{T} d\bar{s} \right] + \frac{1}{\Delta \Omega} \int\limits_{\partial S_w} k_f \nabla T \cdot d\bar{s}
\end{aligned} \tag{3.30}$$

Similarly,

$$\left\langle \mu \nabla \left(\nabla \bar{u} \right) \right\rangle_f = \mu \left\langle \nabla \left(\nabla \bar{u} \right) \right\rangle_f = \mu \nabla \left\langle \nabla \bar{u} \right\rangle_f + \frac{\mu}{\Delta \Omega} \int\limits_{\partial S_w} \nabla \bar{u} \cdot d\bar{s} \tag{3.31}$$

Substituting Eq. (3.26) into Eq. (3.31), leads to

$$\left\langle \mu \nabla \left(\nabla \bar{u} \right) \right\rangle_f = \mu \nabla^2 \left(\left\langle m \right\rangle \tilde{u} \right) + \nabla \cdot \left(\frac{\mu}{\Delta \Omega} \int_{\partial S_w} \bar{u} d\bar{s} \right) + \frac{1}{\Delta \Omega} \int_{\partial S_w} \mu \nabla \bar{u} \cdot d\bar{s} \qquad (3.32)$$

Substituting Eq. (3.27) into Eq. (3.31), leads to

$$\left\langle \mu \nabla \left(\nabla \bar{u} \right) \right\rangle_f = \mu \nabla \cdot \left(\left\langle m \right\rangle \nabla \tilde{u} \right) + \nabla \cdot \left[\frac{\mu}{\Delta \Omega} \int_{\partial S_w} \hat{\tilde{u}} d\bar{s} \right] + \frac{1}{\Delta \Omega} \int_{\partial S_w} \mu \nabla \bar{u} \cdot d\bar{s} \qquad (3.33)$$

Gradient Term with Nonconstant Coefficient

For some cases, such as turbulent flow in porous media, the fluid heat conductivity is not a constant, and then the averaging of the gradient term would be

$$
\begin{aligned}
\left\langle k_T \nabla T \right\rangle_f &= \left\langle \left(\tilde{k}_T + \hat{k}_f \right) \left(\nabla \tilde{T} + \nabla \hat{T} \right) \right\rangle_f \\
&= \left\langle \tilde{k}_T \nabla \tilde{T} + \tilde{k}_T \nabla \hat{T} + \hat{k}_T \nabla \tilde{T} + \hat{k}_T \nabla \hat{T} \right\rangle_f \\
&= \left\langle m \right\rangle \tilde{k}_T \nabla \tilde{T} + \left\langle \tilde{k}_T \nabla \hat{T} \right\rangle_f + \nabla \tilde{T} \left\langle \hat{k}_T \right\rangle_f + \left\langle \hat{k}_T \nabla \hat{T} \right\rangle_f \qquad (3.34) \\
&= \left\langle m \right\rangle \tilde{k}_T \nabla \tilde{T} + \tilde{k}_T \left(\nabla \left\langle \hat{T} \right\rangle_f + \frac{1}{\Delta \Omega} \int_{\partial S_w} \hat{T} d\bar{s} \right) + \left\langle \hat{k}_T \nabla \hat{T} \right\rangle_f \\
&= \left\langle m \right\rangle \tilde{k}_T \nabla \tilde{T} + \frac{\tilde{k}_T}{\Delta \Omega} \int_{\partial S_w} \hat{T} d\bar{s} + \left\langle \hat{k}_T \nabla \hat{T} \right\rangle_f
\end{aligned}
$$

where k_T is not a constant. The diffusion term of the fluid energy equation then becomes

$$
\begin{aligned}
\left\langle \nabla \cdot \left(k_T \nabla T \right) \right\rangle_f &= \nabla \cdot \left\langle k_T \nabla T \right\rangle_f + \frac{1}{\Delta \Omega} \int_{\partial S_w} k_T \nabla T \cdot d\bar{s} \\
&= \nabla \cdot \left[\left\langle m \right\rangle \tilde{k}_T \nabla \tilde{T} + \frac{\tilde{k}_T}{\Delta \Omega} \int_{\partial S_w} \hat{T} d\bar{s} + \left\langle \hat{k}_T \nabla \hat{T} \right\rangle_f \right] + \frac{1}{\Delta \Omega} \int_{\partial S_w} k_T \nabla T \cdot d\bar{s} \qquad (3.35) \\
&= \nabla \cdot \left(\left\langle m \right\rangle \tilde{k}_T \nabla \tilde{T} \right) + \nabla \cdot \left[\frac{\tilde{k}_T}{\Delta \Omega} \int_{\partial S_w} \hat{T} d\bar{s} \right] + \nabla \cdot \left(\left\langle \hat{k}_T \nabla \hat{T} \right\rangle_f \right) + \frac{1}{\Delta \Omega} \int_{\partial S_w} k_T \nabla T \cdot d\bar{s}
\end{aligned}
$$

Rearranging the first two terms on the right hand of Eq. (3.35) yields,

$$\langle \nabla \cdot (k_T \nabla T) \rangle_f = \nabla \cdot \left[\tilde{k}_T \nabla (\langle m \rangle \tilde{T}) - \tilde{k}_T \tilde{T} \nabla \langle m \rangle \right]$$

$$+ \nabla \cdot \left[\frac{\tilde{k}_T}{\Delta\Omega} \int_{\partial S_w} (T - \tilde{T}) d\bar{s} \right] + \nabla \cdot \left(\langle \hat{k}_T \nabla \hat{T} \rangle_f \right) + \frac{1}{\Delta\Omega} \int_{\partial S_w} k_T \nabla T \cdot d\bar{s}$$

$$= \nabla \cdot \left[\tilde{k}_T \nabla (\langle m \rangle \tilde{T}) \right] - \nabla \cdot \left(\tilde{k}_T \tilde{T} \nabla \langle m \rangle \right) + \nabla \cdot \left[\frac{\tilde{k}_T}{\Delta\Omega} \int_{\partial S_w} T d\bar{s} \right] - \nabla \cdot \left[\frac{\tilde{k}_T}{\Delta\Omega} \int_{\partial S_w} \tilde{T} d\bar{s} \right]$$

$$+ \nabla \cdot \left(\langle \hat{k}_T \nabla \hat{T} \rangle_f \right) + \frac{1}{\Delta\Omega} \int_{\partial S_w} k_T \nabla T \cdot d\bar{s}$$

$$= \nabla \cdot \left[\tilde{k}_T \nabla (\langle m \rangle \tilde{T}) \right] - \nabla \cdot \left(\tilde{k}_T \tilde{T} \nabla \langle m \rangle \right) + \nabla \cdot \left[\frac{\tilde{k}_T}{\Delta\Omega} \int_{\partial S_w} T d\bar{s} \right] + \nabla \cdot \left(\tilde{k}_T \tilde{T} \nabla \langle m \rangle \right)$$

$$+ \nabla \cdot \left(\langle \hat{k}_T \nabla \hat{T} \rangle_f \right) + \frac{1}{\Delta\Omega} \int_{\partial S_w} k_T \nabla T \cdot d\bar{s}$$

$$= \nabla \cdot \left[\tilde{k}_T \nabla (\langle m \rangle \tilde{T}) \right] + \nabla \cdot \left[\frac{\tilde{k}_T}{\Delta\Omega} \int_{\partial S_w} T d\bar{s} \right] + \nabla \cdot \left(\langle \hat{k}_T \nabla \hat{T} \rangle_f \right) + \frac{1}{\Delta\Omega} \int_{\partial S_w} k_T \nabla T \cdot d\bar{s} \quad (3.36)$$

Triple Function Averaging

There are several circumstances where triple function decomposition is needed. For example, the production term and diffusion transport term in turbulent kinetic energy equation are triple function terms. The triple function decomposition formulation is

$$\langle f_1 f_2 f_3 \rangle_1 = \langle \tilde{f}_1 \tilde{f}_2 \tilde{f}_3 \rangle_1 + \langle \hat{f}_1 \hat{f}_2 \tilde{f}_3 \rangle_1 + \langle \tilde{f}_1 \hat{f}_2 \hat{f}_3 \rangle_1 + \langle \hat{f}_1 \tilde{f}_2 \hat{f}_3 \rangle_1 + \langle \hat{f}_1 \hat{f}_2 \hat{f}_3 \rangle_1$$

$$= \langle m \rangle \left[\tilde{f}_1 \tilde{f}_2 \tilde{f}_3 + \tilde{f}_3 \{ \hat{f}_1 \hat{f}_2 \}_1 + \tilde{f}_1 \{ \hat{f}_2 \hat{f}_3 \}_1 + \tilde{f}_2 \{ \hat{f}_1 \hat{f}_3 \}_1 + \{ \hat{f}_1 \hat{f}_2 \hat{f}_3 \}_1 \right] \quad (3.37)$$

3.2. Laminar and Turbulent Transport in Porous Media

VAT based thermal physics and fluid mechanics governing equations in heterogeneous porous media will be developed from the Navier-Stokes momentum equation and the thermal energy equations as they are the starting point and the basis for studying flow and heat transfer in porous media. In this section, porous media governing

equation development for laminar and turbulent transport in porous media will be shown. The turbulent transport considered here is flow in a highly porous layer combined with a two energy equation model.

3.2.1. Continuity Equation

Now that the fundamentals of volume-averaged theory are established one can use the lower scale governing equations and scale transport phenomena mechanisms from lower (micro) to upper (macro) scale. For development of conservation laws on the upper scale, the starting point is the lower scale governing equations. For incompressible flow, the microscopic Reynolds, time averaged continuity equation of fluid phase in the porous media is

$$\frac{\partial \overline{u}_i}{\partial x_i} = 0 \tag{3.38}$$

By using spatial averaging theorem, Eq. (3.18), the averaged continuity equation in the fluid phase for flow in a porous media is written

$$\frac{\partial}{\partial x_i}\left(\langle m \rangle \tilde{\overline{u}}_i\right) + \frac{1}{\Delta \Omega} \int_{\partial S_w} \left(\tilde{\overline{u}}_i + \hat{\overline{u}}_i\right) d\vec{s} = 0 \tag{3.39}$$

3.2.2. Momentum Equation

The Reynolds averaged momentum equation for steady-state, incompressible, and turbulent Newtonian flow is expressed as

$$\overline{u}_j \frac{\partial \overline{u}_i}{\partial x_j} = -\frac{1}{\rho_f} \frac{\partial \overline{p}}{\partial x_i} + \frac{\partial}{\partial x_j}\left(\nu \frac{\partial \overline{u}_i}{\partial x_j} - \overline{u_i' u_j'}\right) \tag{3.40}$$

The volume averaged momentum equation of the porous medium is obtained by applying the volume averaging operators to Eq. (3.40), which, in general form, is

$$
\langle m \rangle \tilde{\bar{u}}_j \frac{\partial \tilde{\bar{u}}_i}{\partial x_j} - \tilde{\bar{u}}_i \frac{1}{\Delta\Omega} \int\limits_{\partial S_w} \left(\tilde{\bar{u}}_j + \hat{\bar{u}}_j \right) d\bar{s} + \frac{\partial}{\partial x_j} \left\langle \hat{\bar{u}}_i \hat{\bar{u}}_j \right\rangle_f + \frac{1}{\Delta\Omega} \int\limits_{\partial S_w} \bar{u}_j \bar{u}_i d\bar{s}
$$

$$
= -\frac{1}{\rho_f} \frac{\partial}{\partial x_i} \left(\langle m \rangle \tilde{\bar{p}} \right) - \frac{1}{\rho_f} \frac{1}{\Delta\Omega} \int\limits_{\partial S_w} \bar{p} d\bar{s} + \frac{\partial}{\partial x_j} \left(\langle m \rangle \nu \frac{\partial \tilde{\bar{u}}_i}{\partial x_j} \right) + \frac{1}{\Delta\Omega} \int\limits_{\partial S_{wL}} \nu \frac{\partial \bar{u}_i}{\partial x_j} d\bar{s} \quad (3.41)
$$

$$
+ \frac{\partial}{\partial x_j} \left\langle -\overline{u_i' u_j'} \right\rangle_f - \frac{1}{\Delta\Omega} \int\limits_{\partial S_w} \overline{u_i' u_j'} d\bar{s}
$$

In the general case, the convective flux integrals on the right-hand side of volume averaged momentum equation, Eq. (3.41), are not equal to zero, since there could be some penetration through the phase transition boundary changing the boundary conditions in the microelement to allow for heat and mass exchange through the interface surface as the values of velocity, concentrations and temperature at ∂S_w are not zero [181]. The third term on the left hand side of Eq. (3.41) is the divergence of the REV averaged product of velocity fluctuations caused by random morphological properties of the medium being penetrated and is responsible for convectional dispersion due to morphology in a particular porous medium. The fourth term on the right-hand side of the equation can be associated with the notion of diffusive dispersion of momentum in non-homogeneous medium. All of these integral and average terms appearing in the equation need proper closure and will be addressed later.

In analogy to the viscous stresses in laminar flows, the turbulent stresses can be assumed to be proportional to the mean-velocity gradients. For general flow situations the Reynolds stress can be expressed as

$$-\overline{u_i' u_j'} = \nu_T \left(\frac{\partial \overline{u}_i}{\partial x_j} + \frac{\partial \overline{u}_j}{\partial x_i} \right) \tag{3.42}$$

With this the momentum equation becomes

$$\langle m \rangle \tilde{\overline{u}}_j \frac{\partial \tilde{\overline{u}}_i}{\partial x_j} - \tilde{\overline{u}}_i \frac{1}{\Delta\Omega} \int\limits_{\partial S_w} \left(\tilde{\overline{u}}_j + \hat{\overline{u}}_j \right) d\overline{s} + \frac{\partial}{\partial x_j} \langle \hat{\overline{u}}_i \hat{\overline{u}}_j \rangle_f + \frac{1}{\Delta\Omega} \int\limits_{\partial S_w} \overline{u}_j \overline{u}_i d\overline{s}$$

$$= -\frac{1}{\rho_f} \frac{\partial}{\partial x_i} \left(\langle m \rangle \tilde{\overline{p}} \right) + \frac{\partial}{\partial x_j} \left(\langle m \rangle (\nu + \tilde{\nu}_T) \frac{\partial \tilde{\overline{u}}_i}{\partial x_j} \right) - \frac{1}{\rho_f} \frac{1}{\Delta\Omega} \int\limits_{\partial S_w} \overline{p} d\overline{s} \tag{3.43}$$

$$+ \frac{1}{\Delta\Omega} \int\limits_{\partial S_{wL}} (\nu + \nu_T) \frac{\partial \overline{u}_i}{\partial x_j} d\overline{s} + \frac{\partial}{\partial x_j} \left(\left\langle \hat{\nu}_T \frac{\partial \hat{\overline{u}}_i}{\partial x_j} \right\rangle_f \right)$$

For flow through porous media with impermeable interface, all the terms in Eq. (3.43) with

integration of velocity over the interface ∂S_w are zero, reducing it to

$$\langle m \rangle \tilde{\overline{u}}_j \frac{\partial \tilde{\overline{u}}_i}{\partial x_j} + \frac{\partial}{\partial x_j} \langle \hat{\overline{u}}_i \hat{\overline{u}}_j \rangle_f$$

$$= -\frac{1}{\rho_f} \frac{\partial}{\partial x_i} \left(\langle m \rangle \tilde{\overline{p}} \right) + \frac{\partial}{\partial x_j} \left(\langle m \rangle (\nu + \tilde{\nu}_T) \frac{\partial \tilde{\overline{u}}_i}{\partial x_j} \right) - \frac{1}{\rho_f} \frac{1}{\Delta\Omega} \int\limits_{\partial S_w} \overline{p} d\overline{s} \tag{3.44}$$

$$+ \frac{1}{\Delta\Omega} \int\limits_{\partial S_{wL}} (\nu + \nu_T) \frac{\partial \overline{u}_i}{\partial x_j} d\overline{s} + \frac{\partial}{\partial x_j} \left(\left\langle \hat{\nu}_T \frac{\partial \hat{\overline{u}}_i}{\partial x_j} \right\rangle_f \right)$$

Rearranging Eq. (3.44) yields,

$$\langle m \rangle \tilde{\overline{u}}_j \frac{\partial \tilde{\overline{u}}_i}{\partial x_j} = -\frac{1}{\rho_f} \frac{\partial}{\partial x_i} \left(\langle m \rangle \tilde{\overline{p}} \right) + \frac{\partial}{\partial x_j} \left(\langle m \rangle (\nu + \tilde{\nu}_T) \frac{\partial \tilde{\overline{u}}_i}{\partial x_j} \right)$$

$$-\frac{1}{\rho_f} \frac{1}{\Delta\Omega} \int\limits_{\partial S_w} \overline{p} d\overline{s} + \frac{1}{\Delta\Omega} \int\limits_{\partial S_{wL}} (\nu + \nu_T) \frac{\partial \overline{u}_i}{\partial x_j} d\overline{s} - \frac{\partial}{\partial x_j} \langle \hat{\overline{u}}_i \hat{\overline{u}}_j \rangle_f + \frac{\partial}{\partial x_j} \left(\left\langle \hat{\nu}_T \frac{\partial \hat{\overline{u}}_i}{\partial x_j} \right\rangle_f \right) \tag{3.45}$$

3.2.3. Energy Equations

The turbulent thermal energy transport equation in the fluid phase is written as

$$\rho_f c_{pf} \bar{u}_j \frac{\partial \bar{T}_f}{\partial x_j} = \frac{\partial}{\partial x_j}\left(k_f \frac{\partial \bar{T}_f}{\partial x_j} - \overline{T'_f u'_j} \right) \tag{3.46}$$

The volume averaged energy equation of fluid phase is obtained by applying the volume averaging operators to Eq. (3.46), which, in general form, is

$$
\begin{aligned}
&\rho_f c_{pf} \left[\langle m \rangle \tilde{u}_j \frac{\partial \tilde{\bar{T}}_f}{\partial x_j} - \tilde{\bar{T}}_f \frac{1}{\Delta\Omega} \int_{\partial S_w} \left(\tilde{\bar{u}}_j + \hat{\bar{u}}_j \right) d\bar{s} \right] \\
&+ \rho_f c_{pf} \left(\frac{\partial}{\partial x_j} \left\langle \hat{\bar{T}}_f \hat{\bar{u}}_j \right\rangle_f + \frac{1}{\Delta\Omega} \int_{\partial S_w} \bar{u}_j \bar{T}_f d\bar{s} \right) \\
&= \frac{\partial}{\partial x_j} \left(\langle m \rangle k_f \frac{\partial \tilde{\bar{T}}_f}{\partial x_j} \right) + \frac{1}{\Delta\Omega} \int_{\partial S_{wL}} k_f \frac{\partial \bar{T}_f}{\partial x_j} d\bar{s} + \frac{\partial}{\partial x_j} \left(\frac{k_f}{\Delta\Omega} \int_{\partial S_w} \hat{\bar{T}}_f d\bar{s} \right) \\
&+ \frac{\partial}{\partial x_j} \left\langle -\overline{T'_f u'_j} \right\rangle_f - \frac{1}{\Delta\Omega} \int_{\partial S_w} \overline{T'_f u'_j} d\bar{s}
\end{aligned}
\tag{3.47}
$$

In analogy to the concept of eddy viscosity, the turbulent fluctuation terms are proportional to the mean temperature gradients, yielding

$$
\begin{aligned}
&\rho_f c_{pf} \left[\langle m \rangle \tilde{u}_j \frac{\partial \tilde{\bar{T}}_f}{\partial x_j} - \tilde{\bar{T}}_f \frac{1}{\Delta\Omega} \int_{\partial S_w} \left(\tilde{\bar{u}}_j + \hat{\bar{u}}_j \right) d\bar{s} \right] \\
&+ \rho_f c_{pf} \left(\frac{\partial}{\partial x_j} \left\langle \hat{\bar{T}}_f \hat{\bar{u}}_j \right\rangle_f + \frac{1}{\Delta\Omega} \int_{\partial S_w} \bar{u}_j \bar{T}_f d\bar{s} \right) \\
&= \frac{\partial}{\partial x_j} \left(\langle m \rangle \left(k_f + \tilde{k}_T \right) \frac{\partial \tilde{\bar{T}}_f}{\partial x_j} \right) + \frac{1}{\Delta\Omega} \int_{\partial S_w} \left(k_f + k_T \right) \frac{\partial \bar{T}_f}{\partial x_j} d\bar{s} + \frac{\partial}{\partial x_j} \left(\frac{k_f}{\Delta\Omega} \int_{\partial S_w} \hat{\bar{T}}_f d\bar{s} \right)
\end{aligned}
\tag{3.48}
$$

For porous media with impermeable solid surface, Eq. (3.48) could be simplified and rearranged to

$$\rho_f c_{pf} \langle m \rangle \tilde{\bar{u}}_j \frac{\partial \tilde{\bar{T}}_f}{\partial x_j} = \langle m \rangle \frac{\partial}{\partial x_j} \left(\left(k_f + \tilde{k}_T \right) \frac{\partial \tilde{\bar{T}}_f}{\partial x_j} \right)$$

$$+ \frac{1}{\Delta \Omega} \int_{\partial S_w} \left(k_f + k_T \right) \frac{\partial \bar{T}_f}{\partial x_j} d\bar{s} - \rho_f c_{pf} \frac{\partial}{\partial x_j} \left\langle \hat{\bar{T}}_f \hat{\bar{u}}_j \right\rangle_f + \frac{\partial}{\partial x_j} \left(\frac{k_f}{\Delta \Omega} \int_{\partial S_w} \hat{\bar{T}}_f d\bar{s} \right)$$

(3.49)

The thermal energy transport equation in the solid phase is written as

$$\frac{\partial}{\partial x_i} \left[k_s \frac{\partial T_s}{\partial x_i} \right] = 0$$

(3.50)

where k_s is the effective thermal conductivity in the solid phase for turbulent flow in porous media. The volume averaged energy equation of solid phase is obtained by applying the volume averaging operators to Eq. (3.50), which, in general form, is

$$\frac{\partial}{\partial x_i} \left[\left(1 - \langle m \rangle \right) k_s \frac{\partial T_s}{\partial x_i} \right] + \frac{\partial}{\partial x_i} \left[\frac{k_s}{\Delta \Omega} \int_{\partial S_w} \hat{T}_s d\bar{s}_1 \right] + \frac{1}{\Delta \Omega} \int_{\partial S_w} k_s \frac{\partial T_s}{\partial x_i} d\bar{s}_1 = 0$$

(3.51)

where $d\bar{s}_1 = -d\bar{s}$.

To solve the above equations, the closure must be developed and evaluated, which will be addressed in the following chapter.

4. Closure Evaluation of VAT Equations

A rigorous VAT method was applied to the governing equations and the momentum and energy transport properties were scaled from lower micro to larger macro scale. This approach yields the large scale governing equations that are left open and still need the closure, therefore a general procedure of obtaining closure for VAT equations is addressed here.

4.1. Closure Problem

4.1.1. Closure for Momentum Equation

The reduced VAT based momentum equation, Eq. (3.45), derived above is repeated here,

$$\langle m \rangle \tilde{\bar{u}}_j \frac{\partial \tilde{\bar{u}}_i}{\partial x_j} = -\frac{1}{\rho_f} \frac{\partial}{\partial x_i} \left(\langle m \rangle \tilde{\bar{p}} \right) + \frac{\partial}{\partial x_j} \left(\langle m \rangle (\nu + \tilde{\nu}_T) \frac{\partial \tilde{\bar{u}}_i}{\partial x_j} \right)$$

$$-\frac{1}{\rho_f} \frac{1}{\Delta\Omega} \int_{\partial S_w} \bar{p} d\bar{s} + \frac{1}{\Delta\Omega} \int_{\partial S_{wL}} (\nu + \nu_T) \frac{\partial \bar{u}_i}{\partial x_j} d\bar{s} - \frac{\partial}{\partial x_j} \langle \hat{\bar{u}}_i \hat{\bar{u}}_j \rangle_f + \frac{\partial}{\partial x_j} \left(\left\langle \hat{\nu}_T \frac{\partial \hat{\bar{u}}_i}{\partial x_j} \right\rangle_f \right)$$

(3.45)

There are three integral terms that need to be evaluated,

$$-\frac{1}{\rho_f \Delta\Omega} \int_{\partial S_w} \bar{p} d\bar{s} + \frac{1}{\Delta\Omega} \int_{\partial S_{wL}} \nu \frac{\partial \bar{u}_i}{\partial x_j} d\bar{s} + \frac{1}{\Delta\Omega} \int_{\partial S_{wT}} \nu_T \frac{\partial \bar{u}_i}{\partial x_j} d\bar{s}$$

(4.1)

A natural way to close the integral terms in transport equations is to integrate over the interphase surface, or of some other outlined areas of this surface. From a physical point of view, these integration terms represent momentum loss due to the friction resistance and pressure (form) drag over all inter-phase surfaces. In particular, the first term of the integral

formula, (4.1), represents the pressure (form) drag. The second and third terms represent the laminar and turbulent flow contributions to skin friction, respectively.

The form drag coefficient c_{dp} for flow over an obstacle is defined as

$$c_{dp} = \frac{-\int_{\partial S_w} \bar{p}\, d\bar{s}}{\frac{1}{2}\rho_f A_{wp}\tilde{\bar{u}}_i^2} \tag{4.2}$$

where A_{wp} is the cross flow projected area. Using this definition, the pressure drag resistance integral term becomes

$$-\frac{1}{\rho_f \Delta\Omega}\int_{\partial S_w} \bar{p}\, d\bar{s} = \frac{1}{2}c_{dp}S_{wp}\tilde{\bar{u}}_i^2 \tag{4.3}$$

From the definition of the skin friction coefficient,

$$c_f = \frac{\int_{\partial S_w} \tau_w \cdot d\bar{s}}{\frac{1}{2}\rho_f A_w \tilde{\bar{u}}_i^2} \tag{4.4}$$

where τ_w is the wall shear stress and A_w is the solid surface area. The wall shear stress can be decomposed into two components, one for laminar regions τ_{wL}, defined as

$$\tau_{wL} = \rho_f \nu \frac{\partial \bar{u}_i}{\partial x_j} \tag{4.5}$$

and the other for turbulent regions τ_{wT}, defined as

$$\tau_{wT} = \rho_f \nu_T \frac{\partial \bar{u}_i}{\partial x_j} \tag{4.6}$$

With τ_w decomposed we can define two different skin friction coefficients, one for the laminar region c_{fL}, and another for the turbulent region c_{fT}, respectively, as

$$c_{fL} = \frac{\int_{\partial S_w} \tau_{wL} \cdot d\bar{s}}{\frac{1}{2}\rho_f A_w \tilde{\bar{u}}_i^2} = \frac{\int_{\partial S_w} \nu \frac{\partial \bar{u}_i}{\partial x_j} d\bar{s}}{\frac{1}{2} A_w \tilde{\bar{u}}_i^2} = \frac{\frac{1}{\Delta\Omega}\int_{\partial S_w} \nu \frac{\partial \bar{u}_i}{\partial x_j} d\bar{s}}{\frac{1}{2} S_w \tilde{\bar{u}}_i^2} \tag{4.7}$$

$$c_{fT} = \frac{\int_{\partial S_w} \tau_{wT} \cdot d\bar{s}}{\frac{1}{2}\rho_f A_w \tilde{\bar{u}}_i^2} = \frac{\int_{\partial S_w} \nu_T \frac{\partial \bar{u}_i}{\partial x_j} d\bar{s}}{\frac{1}{2} A_w \tilde{\bar{u}}_i^2} = \frac{\frac{1}{\Delta\Omega}\int_{\partial S_w} \nu_T \frac{\partial \bar{u}_i}{\partial x_j} d\bar{s}}{\frac{1}{2} S_w \tilde{\bar{u}}_i^2} \tag{4.8}$$

Using the definitions in Eq. (4.7) and (4.8), the skin friction integral terms become

$$\frac{1}{\Delta\Omega}\int_{\partial S_w} \nu \frac{\partial \bar{u}_i}{\partial x_j} d\bar{s} = \frac{1}{2} c_{fL} S_w \tilde{\bar{u}}_i^2 \tag{4.9}$$

$$\frac{1}{\Delta\Omega}\int_{\partial S_w} \nu_T \frac{\partial \bar{u}_i}{\partial x_j} d\bar{s} = \frac{1}{2} c_{fT} S_w \tilde{\bar{u}}_i^2 \tag{4.10}$$

Combining Eq. (4.3), Eq. (4.9) and Eq. (4.10), the three integral terms become

$$-\frac{1}{\rho_f \Delta\Omega}\int_{\partial S_w} \bar{p}\, d\bar{s} + \frac{1}{\Delta\Omega}\int_{\partial S_{wL}} \nu \frac{\partial \bar{u}_i}{\partial x_j} d\bar{s} + \frac{1}{\Delta\Omega}\int_{\partial S_{wT}} \nu_T \frac{\partial \bar{u}_i}{\partial x_j} d\bar{s}$$
$$= \frac{1}{2} c_{dp} S_{wp} \tilde{\bar{u}}_i^2 + \frac{1}{2} c_{fL} S_w \tilde{\bar{u}}_i^2 + \frac{1}{2} c_{fT} S_w \tilde{\bar{u}}_i^2 \tag{4.11}$$
$$= \left(c_{dp} \frac{S_{wp}}{S_w} + c_{fL} + c_{fT} \right) \frac{1}{2} S_w \tilde{\bar{u}}_i^2$$

Besides the three integral terms, there are still two fluctuation terms on the right hand side of Eq. (3.45), which also contribute to the flow resistance,

$$-\frac{\partial}{\partial x_j}\left\langle \hat{\tilde{u}}_i\hat{\tilde{u}}_j\right\rangle_f + \frac{\partial}{\partial x_j}\left(\left\langle \hat{v}_T\frac{\partial \hat{\tilde{u}}_i}{\partial x_j}\right\rangle_f\right)$$

$$= \left[\frac{-\dfrac{\partial}{\partial x_j}\left\langle \hat{\tilde{u}}_i\hat{\tilde{u}}_j\right\rangle_f}{\dfrac{1}{2}S_w\tilde{\tilde{u}}_i^2} + \frac{\dfrac{\partial}{\partial x_j}\left(\left\langle \hat{v}_T\dfrac{\partial \hat{\tilde{u}}_i}{\partial x_j}\right\rangle_f\right)}{\dfrac{1}{2}S_w\tilde{\tilde{u}}_i^2} \right]\frac{1}{2}S_w\tilde{\tilde{u}}_i^2 \qquad (4.12)$$

It will prove convenient to group these five resistance coefficients for turbulent flow into an overall drag coefficient defined as,

$$c_d = c_{dp}\frac{S_{wp}}{S_w} + c_{fL} + c_{fT} - \frac{\dfrac{\partial}{\partial x_j}\left\langle \hat{\tilde{u}}_i\hat{\tilde{u}}_j\right\rangle_f}{\dfrac{1}{2}S_w\tilde{\tilde{u}}_i^2} + \frac{\dfrac{\partial}{\partial x_j}\left(\left\langle \hat{v}_T\dfrac{\partial \hat{\tilde{u}}_i}{\partial x_j}\right\rangle_f\right)}{\dfrac{1}{2}S_w\tilde{\tilde{u}}_i^2} \qquad (4.13)$$

The fundamental distinction between the present resistance model and those exploited before is that all additive terms of closure for both the laminar and turbulent regimes are multiplied by the second power of velocity. The closure model is simple and presents a clear physical problem statement. The first three terms are form drag, laminar and turbulent contributions to skin friction, respectively. The fourth term represents the spatial flow oscillations, which are a function of porous media morphology and tells one how flow deviates from some mean value over the REV. The fifth term represents flow oscillations that are due to Reynolds stresses and are a function of porous media morphology and its time averaged flow oscillations. With this notation the VAT based momentum equation, Eq. (3.45), can now be simply written as

$$\langle m\rangle\tilde{\tilde{u}}_j\frac{\partial \tilde{\tilde{u}}_i}{\partial x_j} = -\frac{1}{\rho_f}\frac{\partial}{\partial x_i}\left(\langle m\rangle\tilde{\tilde{p}}\right) + \frac{\partial}{\partial x_j}\left(\langle m\rangle(v+\tilde{v}_T)\frac{\partial \tilde{\tilde{u}}_i}{\partial x_j}\right) + \frac{1}{2}c_d S_w\tilde{\tilde{u}}_i^2 \qquad (4.14)$$

For one-dimensional fully developed turbulent flow, Eq. (4.14) can be simplified to

$$\frac{\partial}{\partial z}\left(\langle m\rangle(v+\tilde{v}_T)\frac{\partial \tilde{\bar{u}}}{\partial z}\right)+\frac{1}{2}c_d S_w \tilde{\bar{u}}^2 = \frac{1}{\rho_f}\frac{\partial}{\partial z}\left(\langle m\rangle \tilde{\bar{p}}\right) \qquad (4.15)$$

The mean eddy viscosity $\tilde{v}_T$ is determined using Prandtl's mixing length theory. If choosing $\sqrt{b}$ as the velocity scale, $\tilde{v}_T$ can be expressed as

$$\tilde{v}_T = C_\mu \sqrt{b}\, l(z) \qquad (4.16)$$

where $C\mu$ is a constant, l is the mixing length scale function defined by the assumed porous medium structure, b is turbulent kinetic energy defined as

$$b = \frac{1}{2}\left(\overline{u'^2}+\overline{v'^2}+\overline{w'^2}\right) \qquad (4.17)$$

In order to determine $\tilde{v}_T$, an equation for the turbulent kinetic energy b must be introduced and solved. According to Rodi [182], the equation for the mean turbulent fluctuation energy b can be written as

$$\tilde{v}_T(z)\left(\frac{\partial \tilde{\bar{u}}}{\partial z}\right)^2 + \frac{d}{dz}\left[\left(\frac{\tilde{v}_T}{\sigma_b}+v\right)\frac{db(z)}{dz}\right] + \overline{X_i' u_i'} + 2v\left(\frac{db^{1/2}(z)}{dz}\right)^2 - \frac{g}{T\sigma_b}\left(\tilde{v}_T \frac{d\tilde{\bar{T}}}{dz}\right)$$
$$= C_D C_\mu \frac{b^2(z)}{\tilde{v}_T} \qquad (4.18)$$

where C_D, C_μ, and σ_b are empirical coefficients. $C_D C_\mu \approx 0.08$ and $\sigma_b = 1$ appear to be reasonable values of the empirical constants [4, 183, 184]. It can be concluded that [4, 183, 184]

$$\overline{X_i' u_i'} = c_d S_w \tilde{\bar{u}}^3 \qquad (4.19)$$

46

It follows that the equation for $b(z)$ can be written as

$$\tilde{v}_T \left(\frac{\partial \tilde{\tilde{u}}}{\partial z} \right)^2 + \frac{d}{dz} \left[\left(\frac{\tilde{v}_T}{\sigma_b} + v \right) \frac{db}{dz} \right] + c_d S_w \tilde{\tilde{u}}^3 + 2v \left(\frac{db^{1/2}}{dz} \right)^2 - \frac{g}{T\sigma_b} \left(\tilde{v}_T \frac{d\tilde{\tilde{T}}}{dz} \right)$$

$$= C_D C_\mu \frac{b^2}{\tilde{v}_T} \tag{4.20}$$

4.1.2. Closure for Energy Equations

General macro length scale energy equations for fluid and solid phase were developed where both equations are still open and in a need of closure. First closure will be shown for the fluid and later for the solid energy equation. The fluid energy equation has the following form

$$\rho_f c_{pf} \langle m \rangle \tilde{\tilde{u}}_j \frac{\partial \tilde{\tilde{T}}_f}{\partial x_j} = \langle m \rangle \frac{\partial}{\partial x_j} \left(\left(k_f + \tilde{k}_T \right) \frac{\partial \tilde{\tilde{T}}_f}{\partial x_j} \right)$$

$$+ \frac{1}{\Delta\Omega} \int_{\partial S_w} \left(k_f + k_T \right) \frac{\partial \overline{T}_f}{\partial x_j} d\vec{s} - \rho_f c_{pf} \frac{\partial}{\partial x_j} \left\langle \hat{\tilde{T}}_f \hat{\tilde{u}}_j \right\rangle_f + \frac{\partial}{\partial x_j} \left(\frac{k_f}{\Delta\Omega} \int_{\partial S_w} \hat{\tilde{T}}_f d\vec{s} \right) \tag{3.49}$$

where the integrals and fluctuations represent micro scale flow information and need to be closed. The solid energy equation has the following form

$$\frac{\partial}{\partial x_i} \left[\left(1 - \langle m \rangle \right) k_s \frac{\partial T_s}{\partial x_i} \right] + \frac{\partial}{\partial x_i} \left[\frac{k_s}{\Delta\Omega} \int_{\partial S_w} \hat{T}_s d\vec{s}_1 \right] + \frac{1}{\Delta\Omega} \int_{\partial S_w} k_s \frac{\partial T_s}{\partial x_i} d\vec{s}_1 = 0 \tag{3.51}$$

There are also two integral terms that need to be closed.

The VAT based fluid phase thermal energy equation can be closed in various ways and in general will depend on how many of the integral terms one uses and lumps into a single transport coefficient, see Travkin and Catton [4]. It can be seen from Eq. (3.49) that,

47

there are three extra terms on the right hand side of the equation. Two of them are integral terms over the interface ∂S_w, the third one is a product of two variable fluctuations.

The nature of the equation shows that the energy transferred from the surface is integrated over an area and then divided by an REV volume. Therefore, the heat transfer coefficient is defined in terms of the porous medium's morphology, usually described by the specific surface area and the porosity. The number and the nature of the closure terms in the macro scale governing equations were rigorously derived from the micro scale governing equations and they are clearly defined. The way one defines a heat transfer coefficient can vary but the complete form that uses all of the fluid phase energy equation integral terms is written as

$$
h = \frac{\dfrac{1}{\Delta\Omega}\displaystyle\int_{\partial S_w}\left(k_f+k_T\right)\nabla\overline{T}_f\cdot d\bar{s}-\rho_f c_{pf}\nabla\cdot\left(\langle m\rangle\widehat{\hat{\tilde{u}}_f\hat{\tilde{T}}_f}\right)+\nabla\cdot\left(\dfrac{k_f}{\Delta\Omega}\displaystyle\int_{\partial S_w}\hat{\tilde{T}}_f\,d\bar{s}\right)}{S_w\left(\tilde{T}_s-\tilde{\bar{T}}_f\right)}
\tag{4.21}
$$

The first term represents small scale inter-phase heat transfer, the second term represents spatial velocity and temperature fluctuations, and the third term represents large scale heat transfer.

The VAT based fluid phase energy equation can now be closed as

$$
\rho_f c_{pf}\langle m\rangle\tilde{\bar{u}}_j\frac{\partial\tilde{\bar{T}}_f}{\partial x_j}=\langle m\rangle\frac{\partial}{\partial x_j}\left(\left(k_f+\tilde{k}_T\right)\frac{\partial\tilde{\bar{T}}_f}{\partial x_j}\right)+hS_w\left(\tilde{T}_s-\tilde{\bar{T}}_f\right)
\tag{4.22}
$$

By performing an energy balance at the interface between the solid and fluid one can see that heat exchange from solid phase to fluid phase is of equal magnitude, but with opposite sign to the heat exchange from fluid phase to solid phase and it is obvious that the

heat transfer coefficient is the connection between the two phases at the macro scale level. Therefore, on the solid side, the heat transfer to the surface by conduction is expressed as

$$\frac{\partial}{\partial x_i}\left[\frac{k_s}{\Delta\Omega}\int_{\partial S_w}\hat{T}_s d\bar{s}_1\right]+\frac{1}{\Delta\Omega}\int_{\partial S_w}k_s\frac{\partial T_s}{\partial x_i}d\bar{s}_1=-hS_w\left(\tilde{T}_s-\tilde{\tilde{T}}_f\right) \tag{4.23}$$

The VAT based solid phase energy equation can now be closed as

$$\frac{\partial}{\partial x_i}\left[\left(1-\langle m\rangle\right)k_s\frac{\partial\tilde{T}_s}{\partial x_i}\right]-hS_w\left(\tilde{T}_s-\tilde{\tilde{T}}_f\right)=0 \tag{4.24}$$

For two-dimensional heat transfer in the fluid and solid phase (with one-dimensional turbulent flow, see Eq. (4.15)), the general fluid-phase thermal energy equation can be simplified to

$$\begin{aligned}\rho_f c_{pf}\langle m\rangle\tilde{\bar{u}}(z)&\frac{\partial\tilde{\tilde{T}}_f(x,z)}{\partial x}\\&=\langle m\rangle\frac{\partial}{\partial x}\left[\left(k_f+\tilde{k}_T\right)\frac{\partial\tilde{\tilde{T}}_f(x,z)}{\partial x}\right]+\langle m\rangle\frac{\partial}{\partial z}\left[\left(k_f+\tilde{k}_T\right)\frac{\partial\tilde{\tilde{T}}_f(x,z)}{\partial z}\right]\\&+hS_w\left(\tilde{T}_s-\tilde{\tilde{T}}_f\right)\end{aligned} \tag{4.25}$$

And the solid-phase thermal energy equation can be simplified to

$$\frac{\partial}{\partial x}\left[\left(1-\langle m\rangle\right)k_s(x,z)\frac{\partial\tilde{T}_s(x,z)}{\partial x}\right]+\frac{\partial}{\partial z}\left[\left(1-\langle m\rangle\right)k_s(x,z)\frac{\partial\tilde{T}_s(x,z)}{\partial z}\right]=hS_w\left(\tilde{T}_s-\tilde{\tilde{T}}_f\right)$$

$$\tag{4.26}$$

The local drag coefficient in the VAT momentum equations c_d, defined by Eq. (4.13), and the local heat transfer coefficient in the VAT energy equations, h, defined by Eq. (4.21),

were rigorously derived from lower scale governing equations. To properly evaluate these terms, namely closure problem, is the essential step to apply VAT successfully.

4.2. Selection of Representative Elementary Volume

By examining the closed form of the VAT based momentum equation, Eq. (4.14) and energy equations for fluid phase, Eq. (4.22), and solid phase, Eq. (4.24), we can see that there are two extra terms need to be evaluated besides the closure terms, the averaged porosity $<m>$ and the specific surface area S_w. $<m>$ and S_w are determined by the geometry of the porous media and it is quite easy to define them if one selects the REV correctly.

4.2.1. REV of A Fin-and-Tube Heat Exchanger

The selection for a fin-and-tube heat exchanger, see Figure 4.1, is seen to repeat in both the cross-stream and flow directions.
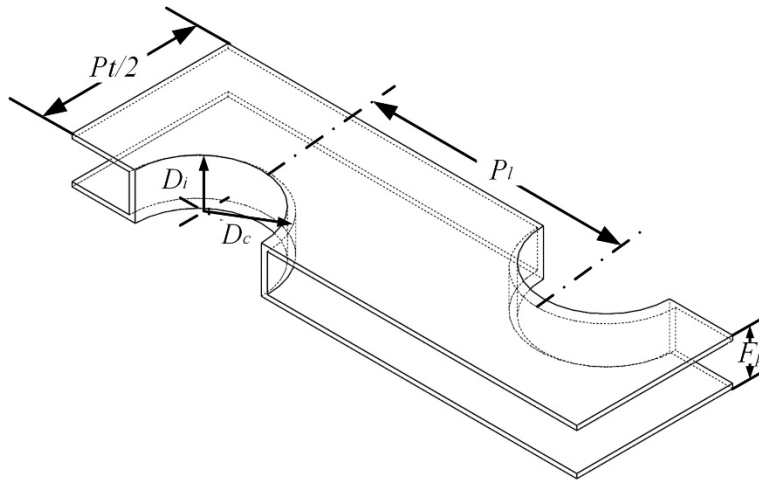
Figure 4.1: Representative Elementary Volume (REV) for a fin-and-tube heat exchanger [185].

The porosity for the air side of the fin-and-tube heat exchanger is

$$\langle m_1 \rangle = 1 - \frac{\delta_f}{F_p} - \frac{\pi D_c^2 \left(F_p - \delta_f \right)}{4 P_l P_t F_p} \tag{4.27}$$

and for the water side is

$$\langle m_2 \rangle = \frac{\pi D_i^2}{4 P_l P_t} \tag{4.28}$$

The specific surface area for the air side is given by

$$S_{w_1} = \frac{2 P_l P_t - 2\pi \left(\dfrac{D_c}{2} \right)^2 + \pi D_c \left(F_p - \delta_f \right)}{P_l P_t F_p} \tag{4.29}$$

and for the water side is

$$S_{w_2} = \frac{\pi D_i}{P_l P_t} \tag{4.30}$$

4.2.2. REV of A Plate Fin Heat Sink with Scale-Roughed Surface

The representative elementary volume of a plate fin heat sink with scale-roughed surface is shown in Figure 4.2. Therefore, the porosity is

$$\langle m \rangle = 1 - \frac{\Delta \Omega_s}{\Delta \Omega} = \frac{H - 2\kappa e}{F_p} \tag{4.31}$$

in which, $\Delta \Omega$ is the volume of the REV defined as

$$\Delta \Omega = P_t P_l F_p \tag{4.32}$$

$\Delta \Omega_s$ is the volume of the solid part of the REV defined by

51

$$\Delta\Omega_s = P_t P_l \left(F_p - H \right) + 2\kappa e P_t P_l \tag{4.33}$$

in which κ is the ratio of the solid volume of the scale to the total volume of the $e \times P_t \times P_l$

slab, see the shaded part in Figure 4.2. It can easily be shown that κ is a constant and $\kappa =$

3/4 - π/8.

The specific surface area, S_w, is defined as

$$S_w = \frac{A_w}{\Delta\Omega} = \frac{2P_t P_l + \pi \left[\frac{3}{4}(P_t + P_l) - \frac{1}{2}\sqrt{P_t P_l} \right] e}{P_t P_l F_p} \tag{4.34}$$
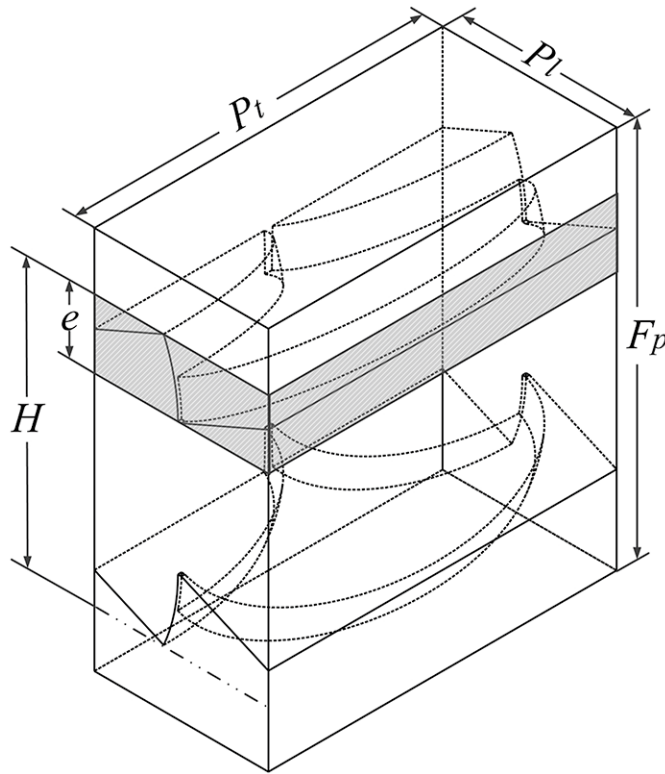
Figure 4.2: Representative Elementary Volume (REV) for a PFHS with elliptic scale-roughened surfaces [186].

4.3. A Universal VAT Based Length Scale

Before the closure evaluation is conducted, a proper length scale should be defined. In this section, a VAT based length scale is introduced and demonstrated to be very beneficial when scaling heat transfer and friction factor results [185, 187].

4.3.1. Derivation of the Length Scale

It was shown by Travkin and Catton [4] that globular media morphologies can be described in terms of S_w, $<m>$ and d_p and can generally be considered to be spherical particles with

$$S_w = \frac{6\left(1-\langle m \rangle\right)}{d_p} \tag{4.35}$$

$$D_h = \frac{2}{3} \frac{\langle m \rangle}{\left(1-\langle m \rangle\right)} d_p \tag{4.36}$$

This expression has the same dependency on equivalent pore diameter as found for a one diameter capillary morphology leading naturally to

$$S_w = \frac{6\left(1-\langle m \rangle\right)}{d_p} = \frac{6\left(1-\langle m \rangle\right)}{\dfrac{3}{2}\dfrac{\left(1-\langle m \rangle\right)}{\langle m \rangle}D_h} = \frac{4\langle m \rangle}{D_h} \tag{4.37}$$

This observation leads to defining a simple "universal" porous media length scale

$$D_h = \frac{4\langle m \rangle}{S_w} \tag{4.38}$$

that meets the needs of both morphologies: capillary and globular. This was also recognized by Whitaker [188] when he collected the experimental data and illustrated that a proper choice of the characteristic length (differing from Eq. (4.38) by a constant) and

velocity for packed beds and tube bundles could lead to a single correlation which satisfactorily predicts heat transfer rates in randomly packed beds and staggered tube bundles. Travkin and Catton [19, 56] showed that choosing the correct length scale, defined by Eq. (4.38), allows one to collapse true capillary flow and flow in a bed of spheres. This is a significant accomplishment, since it spans the physical description from globular to capillary geometry with a single length scale.

Therefore the hydraulic diameter for air side and water side of a fin-and-tube heat exchanger, D_{h1} and D_{h2}, are defined as,

$$D_{h_1} = \frac{4\langle m_1 \rangle}{S_{w_1}} = \frac{\left(4P_l P_t - \pi D_c^2\right)\left(F_p - \delta_f\right)}{2P_l P_t - 2\pi\left(\frac{D_c}{2}\right)^2 + \pi D_c\left(F_p - \delta_f\right)} \tag{4.39}$$

$$D_{h_2} = \frac{4 \cdot \langle m_2 \rangle}{S_{w_2}} = \frac{4 \cdot \dfrac{\pi D_i^2}{4P_l P_t}}{\dfrac{\pi D_i}{P_l P_t}} = D_i \tag{4.40}$$

The hydraulic diameter for elliptic scale roughed channel, D_h is defined as

$$D_h = \frac{4\langle m \rangle}{S_w} = \frac{4P_t P_l\left(H - 2\kappa e\right)}{2P_t P_l + \pi\left[\dfrac{3}{4}\left(P_t + P_l\right) - \dfrac{1}{2}\sqrt{P_t P_l}\right]e} \tag{4.41}$$

It can be seen that D_h is a function of e, P_t, P_l and H.

4.3.2. Friction Factor Data Collapses

This section will demonstrate how the universal length scale derived helps collapse data. From a literature review in section 2.2.1, it can be concluded that Wang et al. [63] proposed the most precise correlations of friction factor and Colburn j factor for the air side

54

performance of plain fin-and-tube heat exchangers. They were scaled with the fin collar

outside diameter, D_c, and the maximum velocity, u_{max}. The friction factor correlation is

$$f = 0.0267 \operatorname{Re}_{D_c}^{F_1} \left(\frac{P_t}{P_l} \right)^{F_2} \left(\frac{F_p}{D_c} \right)^{F_3} \tag{4.42}$$

$$F_1 = -0.764 + 0.739 \frac{P_t}{P_l} + 0.177 \frac{F_p}{D_c} - \frac{0.00758}{N}$$

$$F_2 = -15.689 + \frac{64.021}{\log_e \left(\operatorname{Re}_{D_c} \right)}$$

$$F_3 = 1.696 - \frac{15.695}{\log_e \left(\operatorname{Re}_{D_c} \right)}$$

The definition of Reynolds number in the above correlation is

$$\operatorname{Re}_{D_c} = \frac{u_{max} D_c}{\nu} \tag{4.43}$$

while to obtain closure for the VAT based model, the VAT based length scale and the

averaged velocity over the selected REV, $\tilde{\bar{u}}$, should be used. The Reynolds number using

the VAT length scale is defined as

$$\operatorname{Re}_{D_h} = \frac{\tilde{\bar{u}} D_h}{\nu} \tag{4.44}$$

For fin-and-tube heat exchanger morphology, it is not difficult to get the relationship

between Re_{Dc} and Re_{Dh}, which is

$$\operatorname{Re}_{D_h} = \frac{\tilde{\bar{u}} D_h}{u_{max} D_c} \operatorname{Re}_{D_c} = \frac{1}{\langle m \rangle} \frac{A_{min}}{A_{fr}} \frac{D_h}{D_c} \operatorname{Re}_{D_c} = \frac{4 \left(1 - \dfrac{D_c}{P_t} \right) \cdot \left(1 - \dfrac{\delta_f}{F_p} \right)}{S_w D_c} \operatorname{Re}_{D_c} \tag{4.45}$$

55

in which

$$\alpha = \frac{4\left(1 - \frac{D_c}{P_t}\right) \cdot \left(1 - \frac{\delta_f}{F_p}\right)}{S_w D_c}$$

(4.46)

is defined as the scaling factor for Reynolds number.

The friction factor defined by Wang et al. [63] is

$$f = \frac{A_{min}}{A_o} \frac{2\Delta p \rho}{G_{min}^2}$$

(4.47)

must be rescaled using the VAT length scale. According to Eq (4.47), the pressure drop can be written in the following form

$$\Delta p = \frac{A_o}{A_{min}} \frac{1}{2} \rho u_{max}^2 f$$

(4.48)

The friction factor using VAT length scale is defined as

$$f' = \frac{\Delta p}{\frac{1}{2}\rho \tilde{u}^2} \cdot \frac{D_h}{L}$$

(4.49)

Substitute Eq. (4.48) into Eq. (4.49) leads to

$$f' = \left[\frac{A_o}{A_{min}} \frac{D_h}{L} \left(\frac{u_{max}}{\tilde{u}}\right)^2\right] f = \left[\frac{A_o A_{fr}^2 \langle m \rangle^2}{A_{min}^3} \frac{D_h}{L}\right] f$$

(4.50)

allowing the scaling factor for friction factor to be defined as

$$\beta = \frac{A_o A_{fr}^2 \langle m \rangle^2}{A_{min}^3} \frac{D_h}{L}$$

(4.51)

In Figure 4.3, the friction factor results using Wang's length scale, followed by the rescaled results (Figure 4.4), are shown for comparison.

Just as Figure 4.3 shows, for fin-and-tube heat exchangers with different dimensions, see Table 4.1, friction factor results given by Wang's correlation [63] are scattered, leading to six different f - Re_{Dc} curves. However, if the data were rescaled with the "universal" porous media scale and velocity averaged over the selected REV, the six curves collapse to a single curve, shown in Figure 4.4, clearly demonstrating the value of the VAT based length scale.

With the data being collapsed onto a single curve, a correct form needs to be chosen to correlate the rescaled data. Travkin and Catton [56] showed that using the VAT based length scale enables one to write the friction factor of porous media in the following form

$$f_f = \frac{A}{Re_{D_h}} + B \tag{4.52}$$

The constants A and B correspond to different types of morphologies of porous media, with $A = 100/3$ and $B = 7/12$ for the Ergun equation [189] for packed bed porous media, $A = 50$ and $B = 0.145$ for the pin fin array [190].

Furthermore, Travkin and Catton [56] stated that the friction factor is related to the closure of the VAT momentum equations and they showed that

$$c_d \cong f_f \tag{4.53}$$

Note that the closure equation is an exact definition of friction factor and for fully developed flow Eq. (4.53) is more strictly defined as

$$c_d = f_f = \frac{A}{\text{Re}_{D_h}} + B \qquad\qquad (4.54)$$

Table 4.1: Geometric dimensions of the fin-and-tube heat exchangers shown in Figure 4.3 and Figure 4.4.

Legend	Case	N	D_c (mm)	F_p (mm)	P_t (mm)	P_l (mm)	δ_f (mm)
——————	Case 1	6	10.23	3.16	25.4	22	0.13
– – – –	Case 2	4	10.23	1.23	25.4	22	0.115
········	Case 3	5	10.55	2.2	30	28	0.2
—·—·—·	Case 4	4	10.23	1.55	25.4	22	0.115
—··—··—·	Case 5	6	8.51	3.16	25.4	22	0.13
- - - - - - - -	Case 6	6	7.53	3.16	25.4	22	0.13
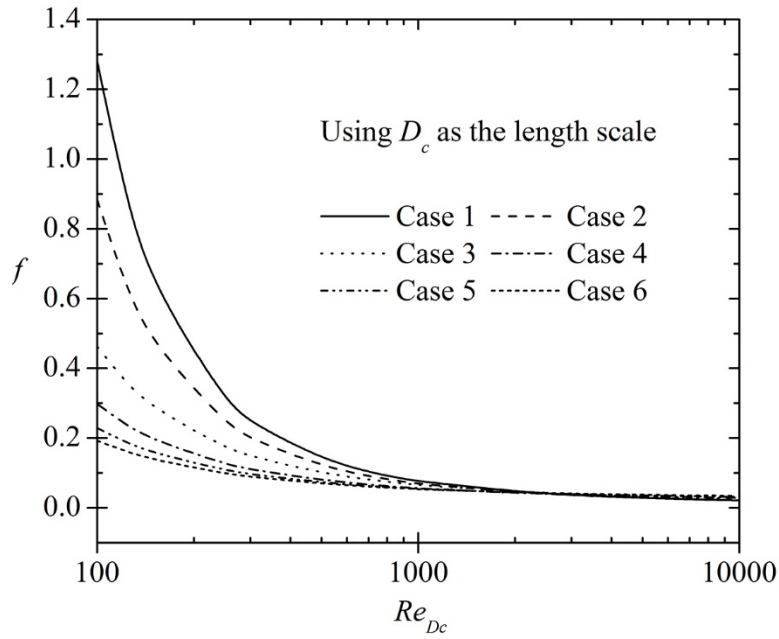
Figure 4.3: Overlay plot of friction factor using D_c as the length scale.

$$f' = \frac{112.4}{Re_{Dh}} + 0.252$$
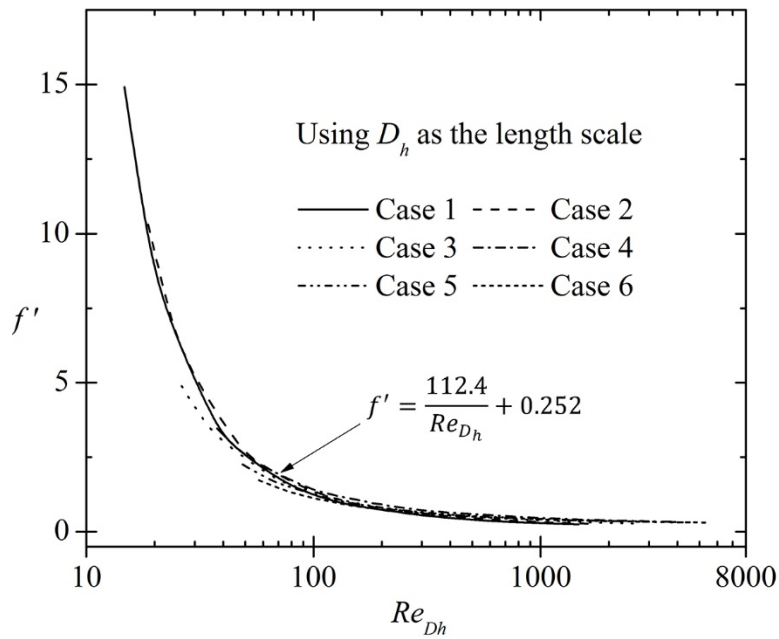
Figure 4.4: Overlay plot of friction factor using D_h as the length scale.

With the help of JMP 8 [191], an available statistical analysis tool, the collapsed data enabled us to develop a simple correlation of friction factor for the air side,

$$f' = \frac{112.4}{\text{Re}_{D_h}} + 0.252 \qquad (4.55)$$

4.3.3. Nusselt Number Data Collapses

It should be noted that the number of tube rows has different effects on the pressure drop and the heat transfer characteristics of fin-and-tube heat exchangers. Figure 4.5, which was plotted according to the correlations by Wang et al. [63], illustrates the difference.
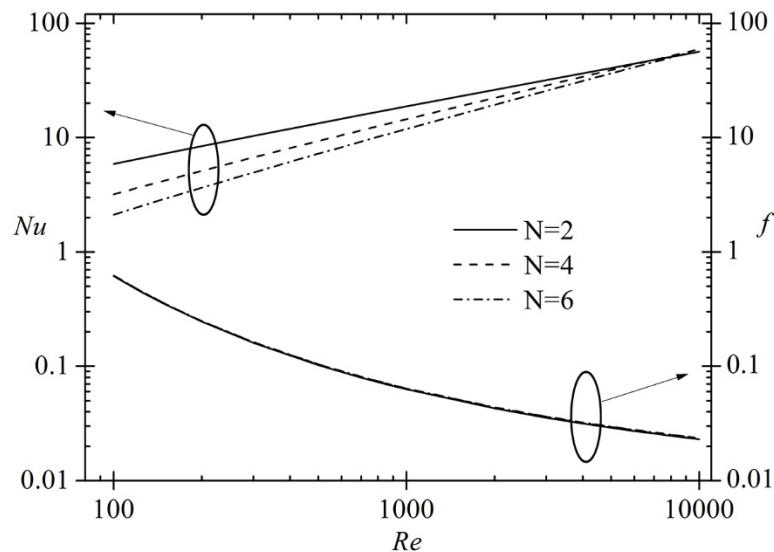
Figure 4.5: Effect of tube row number on f and Nu according to Wang correlations [63].

As can be seen, for fin-and-tube heat exchangers with multiple-row tubes, the friction factors are almost independent of the number of tube rows. This is why we could rescale Wang's [63] correlation of friction factor and collapse the data to a single curve, although

60

it is only suitable for small tube row number (from 1 to 6). Figure 4.5 also indicates that the Nusselt number decreases with the increasing of tube row number, which means that the entrance effect plays an important role in the air side heat transfer coefficient of fin-and-tube heat exchangers, while experimental data for fully developed flow is required to use the VAT based length scale.

It was reported by earlier work [3, 64, 65] that the heat transfer characteristic of fin-and-tube heat exchangers is independent of the number of tube rows when $N > 6$. So it is taken for granted that there is no need to do any research on fin-and-tube heat exchangers with tube row number larger than six, which causes the scarcity of available experimental data for fully developed flow. As far as the authors know, the only available experimental data for $N > 6$ was reported by Tang et al. [3, 65]. Fin-and-tube heat exchangers with tube row number of 6, 9 and 12 were tested experimentally. Unfortunately, all the tested samples have the same dimensions of D_c, F_p, P_t and P_l, so we cannot use Tang's data to show how the rescaled data could be collapsed. Xie et al. [64] tested fin-and-tube heat exchangers with tube row number varying from 1 to 7 numerically, but the 7-row cores, which also had the same geometrical parameters, were simulated only when the authors tried to present the effect of fin material. While when the effects of geometrical parameters were studied, the tube row number was kept to be three.

It was demonstrated by Tang et al. [3] that the difference between Nu-Re curves for $N = 6$, 9 and 12 is negligible, which means when $N = 6$ the flow could be considered as fully developed. Thus, hopefully we could still use Wang's correlation of the Colburn j factor [63] to show whether the rescaled data collapse or not by keeping the tube row

number to be six while changing the other dimensions. Wang's Colburn j factor correlation $(2 \le N \le 6)$ is:

$$j = 0.086 \operatorname{Re}_{D_c}^{P1} N^{P2} \left(\frac{F_p}{D_c}\right)^{P3} \left(\frac{F_p}{D_h}\right)^{P4} \left(\frac{F_p}{P_t}\right)^{-0.93} \tag{4.56}$$

$$P1 = -0.361 - \frac{0.042N}{\log_e\left(\operatorname{Re}_{D_c}\right)} + 0.158 \log_e\left(N\left(\frac{F_p}{D_c}\right)^{0.41}\right)$$

$$P2 = -1.224 - \frac{0.076\left(\dfrac{P_l}{D_h^*}\right)^{1.42}}{\log_e\left(\operatorname{Re}_{D_c}\right)}$$

$$P3 = -0.083 + \frac{0.058N}{\log_e\left(\operatorname{Re}_{D_c}\right)}$$

$$P4 = -5.735 + 1.21 \log_e\left(\frac{\operatorname{Re}_{D_c}}{N}\right)$$

$$D_h^* = \frac{4A_{min}L}{A_o}$$

and Wang's definition of Colburn j factor [1] is

$$j = \frac{h}{\rho u_{max} c_p} \operatorname{Pr}^{2/3} \tag{4.57}$$

which leads to

$$h = \frac{j \rho u_{max} c_p}{\operatorname{Pr}^{2/3}} = \left(\frac{\operatorname{Re}_{D_c} k}{D_c} \operatorname{Pr}^{1/3}\right) j \tag{4.58}$$

Using D_c as the length scale, we find the Nusselt number to be

$$Nu = \frac{hD_c}{k} = \left(\frac{\mathrm{Re}_{D_c} k}{D_c} \mathrm{Pr}^{1/3} \right) j \cdot \frac{D_c}{k} = \left(\mathrm{Re}_{D_c} \mathrm{Pr}^{1/3} \right) j \tag{4.59}$$

Using D_h as the length scale, the rescaled Nusselt number is

$$Nu' = \frac{hD_h}{k} = \left(\frac{\mathrm{Re}_{D_c} k}{D_c} \mathrm{Pr}^{1/3} \right) j \cdot \frac{D_h}{k} = \left(\mathrm{Re}_{D_c} \frac{D_h}{D_c} \mathrm{Pr}^{1/3} \right) j \tag{4.60}$$

Figure 4.6 and Figure 4.7 compare the variations of Nusselt number as a function of Reynolds number, using two different length scales. Obviously, the original data are scattered on Figure 4.6 while the rescaled data collapses to one single curve. The dimensions of fin-and-tube heat exchangers used to show this are tabulated in Table 4.2. Using JMP 8, a correlation of the rescaled Nusselt number data was found and is

$$Nu' = 0.24 \, \mathrm{Re}_{D_h}^{0.6} \, \mathrm{Pr}^{1/3} \tag{4.61}$$

It is argued by some researchers [3, 64-66] that Wang's correlations [63] have certain application ranges, like $1 \leq N \leq 6$, 6.35 mm $\leq D_o \leq 12.7$ mm, which are usually used in the HVAC&R engineering, and are not applicable to some applications of large industry, such as the inter-cooler of multistage compressor, in which the number of tube rows might be much larger and the outside diameter of tubes might be larger than 13 mm. As a result, investigations on the heat transfer and friction characteristics of fin-and-tube heat exchangers with large number of tube rows and large tube diameter were carried out either numerically [64, 192] or experimentally [3, 65, 66].

To verify the applicability of the correlations given by Eq. (4.55) and Eq. (4.61) to large tube diameters, and at the same time to show that it is the right way to use Wang's j factor correlation for $N = 6$ as fully developed flow, the experimental data by Tang et al.

[3] for fin-and-tube heat exchangers with 12 rows of tubes, which is also the only available data in published literature to the best of the authors' knowledge, is rescaled and compared with the correlations. It should be noted that the definition of friction factor given by Tang et al. [3] is different from that used by Wang et al. [63]. This requires a different scaling factor be used,

$$\gamma = \left(\frac{\langle m \rangle A_{fr}}{A_{\min}} \right)^2 \cdot \frac{D_h}{D_c} \tag{4.62}$$

It is shown in Figure 4.8 that the rescaled experimental data by Tang et al. [3] and the rescaled correlations agree well, demonstrating the power of the universal VAT based length scale.

It is worth noting that most of the data wouldn't collapse so well onto a single curve and it is hard to obtain a wide range of experiment data from different research groups. The difficulty is reflected in the following few aspects. First, different experimental methods, assumptions or data reduction procedures are adopted by different researchers, and sometimes this information was not presented in the papers due to the space limitation or some other reasons. Second, only part of the experimental data was presented in these papers, which was enough to explain the phenomenon for the authors. However, VAT based length scale does help make the data points get closer which helps develop simpler correlations. Thus, this universal length scale are adopted in the following study.
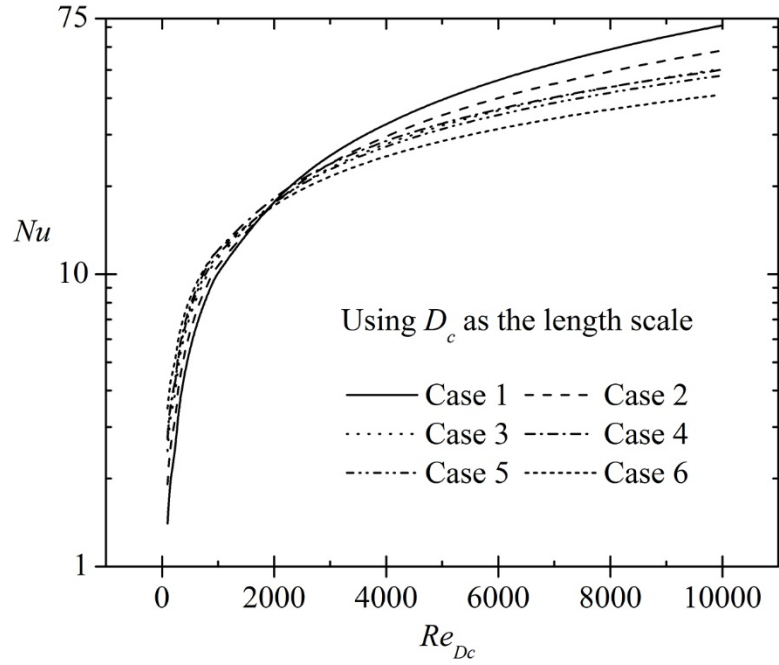
Figure 4.6: Overlay plot of Nu number using D_c as the length scale.
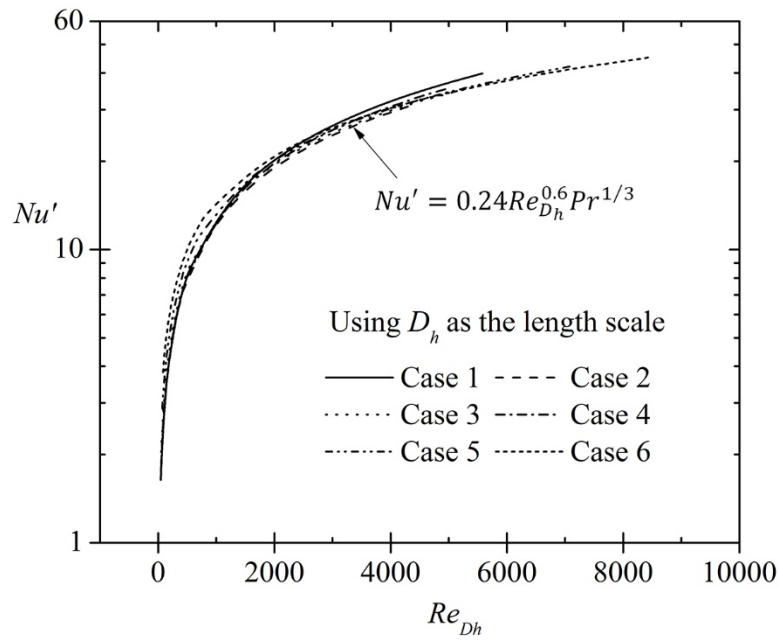
Figure 4.7: Overlay plot of Nu number using D_h as the length scale.

Table 4.2: Geometric dimensions of the fin-and-tube heat exchangers shown in Figure 4.6 and Figure 4.7.

Legend	Case	N	D_c (mm)	F_p (mm)	P_t (mm)	P_l (mm)	δ_f (mm)
——	Case 1	6	10.23	4.5	25.4	22	0.13
– – –	Case 2	6	10.23	3.5	25.4	22	0.115
· · · · ·	Case 3	6	10.55	4.5	30	28	0.2
—·—·—	Case 4	6	10.23	4	25.4	22	0.115
—··—··—	Case 5	6	8.51	4.5	25.4	22	0.13
– – – –	Case 6	6	7.53	4.5	25.4	22	0.13
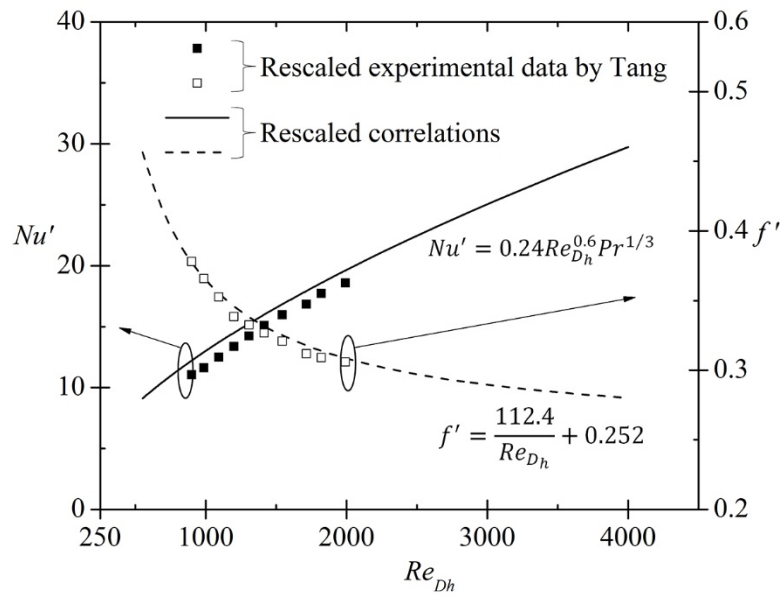
Figure 4.8: Comparison between rescaled correlations and data by Tang et al. [3].

4.4. Numerical Method and Domain Discretization

When CFD is used to obtain the closure, the friction factor and heat transfer are calculated rigorously by integrating the complete closure formula over the REV, which is a general way to obtain closures for the VAT based model [150, 151, 190, 193, 194], though closure evaluation by experiment is an alternative [195, 196]. To evaluate the closure terms properly, the discretization of the computational domain and numerical method adopted to conduct the CFD simulation play an important role in the whole procedure.

4.4.1. Numerical Method

In present CFD simulation, the air flow is assumed to be three-dimensional, incompressible, steady state and turbulent. Buoyancy and radiation heat transfer effects are not taken into consideration.

The three-dimensional governing equations for continuity, momentum and energy are as follows:

(1) Continuity equation

$$\frac{\partial \rho u_i}{\partial x_i} = 0 \tag{4.63}$$

(2) Momentum equation

$$\rho u_j \frac{\partial u_i}{\partial x_j} = \frac{\partial}{\partial x_j}\left[(\mu + \mu_T)\frac{\partial u_i}{\partial x_j}\right] - \frac{\partial p}{\partial x_i} \tag{4.64}$$

(3) Energy equation

$$\rho u_j \frac{\partial T}{\partial x_j} = \frac{\partial}{\partial x_j}\left[\left(\frac{\mu}{\text{Pr}} + \frac{\mu_T}{\text{Pr}_T}\right)\frac{\partial T}{\partial x_j}\right] \tag{4.65}$$

The *k-ω* based Shear-Stress-Transport (SST) model with automatic wall function treatment is used to predict the turbulent flow and heat transfer through the channel. The SST model blends the robust and accurate formulation of the *k-ω* model in the near-wall region with the free-stream independence of the *k-ε* model in the far field. The SST model gives a highly accurate prediction of the onset and the amount of flow separation under adverse pressure gradients by the inclusion of transport effects into the formulation of the eddy-viscosity. This results in a major improvement in terms of flow separation predictions. The superior performance of the SST model has been demonstrated for high accuracy boundary layer simulations in a large number of validation studies.

Menter [197-199] proposed the equations for the SST model as

$$\frac{D(\rho k)}{Dt} = \tilde{P}_k - \beta^* \rho k \omega + \frac{\partial}{\partial x_j}\left[\left(\mu + \sigma_k \mu_T\right)\frac{\partial k}{\partial x_i}\right] \tag{4.66}$$

$$\frac{D(\rho \omega)}{Dt} = \alpha \rho S^2 - \beta \rho \omega^2 + \frac{\partial}{\partial x_i}\left[\left(\mu + \sigma_\omega \mu_T\right)\frac{\partial \omega}{\partial x_i}\right] + 2(1-F_1)\rho\sigma_{\omega_2}\frac{1}{\omega}\frac{\partial k}{\partial x_i}\frac{\partial \omega}{\partial x_i} \tag{4.67}$$

where the blending function F_1 is defined by:

$$F_1 = \tanh\left\{\left\{\min\left[\max\left(\frac{\sqrt{k}}{\beta^*\omega y}, \frac{500\nu}{y^2\omega}\right), \frac{4\rho\sigma_{\omega_2}k}{CD_{k\omega}y^2}\right]\right\}^4\right\} \tag{4.68}$$

in which

$$CD_{k\omega} = \max\left(2\rho\sigma_{\omega_2}\frac{1}{\omega}\frac{\partial k}{\partial x_j}\frac{\partial \omega}{\partial x_j}, 10^{-10}\right) \tag{4.69}$$

The turbulent eddy viscosity is computed from:

$$v_T = \frac{a_1 k}{\max\left(a_1 \omega, SF_2\right)} \tag{4.70}$$

where S is the invariant measure of the strain rate and F_2 is a second blending function defined by

$$F_2 = \tanh\left\{\left[\max\left(2\frac{\sqrt{k}}{\beta^* \omega y}, \frac{500\nu}{y^2 \omega}\right)\right]^2\right\} \tag{4.71}$$

To prevent the build-up of turbulence in stagnation regions, a production limiter is used in the SST model:

$$P_k = \mu_t \frac{\partial u_i}{\partial x_j}\left(\frac{\partial u_i}{\partial x_j} + \frac{\partial u_j}{\partial x_i}\right) \rightarrow \tilde{P}_k = \min\left(P_k, 10 \cdot \beta^* \rho k \omega\right) \tag{4.72}$$

Each of the constants is a blend of the corresponding constants of the k-ε and the k-ω model:

$$\varphi = F_1 \varphi_1 + \left(1 - F_1\right)\varphi_2 \tag{4.73}$$

The constants for this model take the following values

$$\begin{aligned}
&\beta^* = 0.09, \\
&\alpha_1 = 5/9, \beta_1 = 3/40, \sigma_{k1} = 0.85, \sigma_{\omega 1} = 0.5, \\
&\alpha_2 = 0.44, \beta_2 = 0.0828, \sigma_{k2} = 1, \sigma_{\omega 2} = 0.856.
\end{aligned} \tag{4.74}$$

Two different commercial CFD codes, SC/Tetra from Cradle and CFX from Ansys, are adopted to conduct the numerical simulations. The numerical techniques and discretization schemes used in the SC/Tetra HPC Solver are a 2nd order Monotone Upstream-centred Schemes for Conservation Laws (MUSCL) for convective terms in the energy and momentum equations while for the momentum and energy diffusion terms, an

accuracy weighted scheme is used. A corrected version of the Semi-Implicit Method of the Pressure Linked Equations (SIMPLEC) is used for the pressure correction.

The Ansys CFX solver solves the discrete system of linearized equations using a multi-grid accelerated Incomplete Lower Upper (ILU) factorization technique and rapidly removes local errors in the solution. The algebraic multi-grid scheme is used to accelerate the convergence of the solver by computing the corrections on a series of coarse grid levels. The CFD code solves the Reynolds-averaged Navier–Stokes equations with a high resolution scheme for the advection terms as well as turbulence numerics. The fully coupled momentum and energy equations are solved simultaneously. The second-order upwind scheme is used for the discretization of the momentum and energy equations.

The RMS type residual for solution convergence criteria is set to be 10^{-5} for the momentum balance and 10^{-6} for the energy equation in all the simulations carried out in the present work.

4.4.2. Discretization of the Computational Domain

The computational domain consists of one or more REVs arranged in a row, see Figure 4.9 for fin-and-tube heat exchanger and Figure 4.10 for plate fin heat sink with scale-roughed surface. The number of REVs included in the computational domain is determined by the development of the boundary layers, referring to section 4.5 for more details.

Because of the thickness of the fin, the air velocity profile at the entrance is not uniform. The computational domain is extended upstream to a certain distance so that a uniform velocity distribution can be ensured at the domain inlet. The computational domain

is extended downstream a few times the streamwise fin length, so that at the outer flow boundary no flow recirculation exits.

A velocity boundary condition and a constant temperature is set at the domain inlet. The turbulence intensity of the flow entering through the inlet boundary is set to 5%. At the outlet of the computational domain, a pressure boundary condition is employed. The interface between the solid and the fluid is a no-slip wall with no thermal resistance. Due to the relatively large heat transfer coefficient on the tube side, the tube inner wall temperature was set equal to the fluid temperature. An iso-heat-flux thermal boundary condition is employed on the bottom surface of the scale-roughed channel. Slip and adiabatic wall conditions are provided on all the other confined walls. The boundary conditions applied to the computational domain are tabulated in Table 4.3.
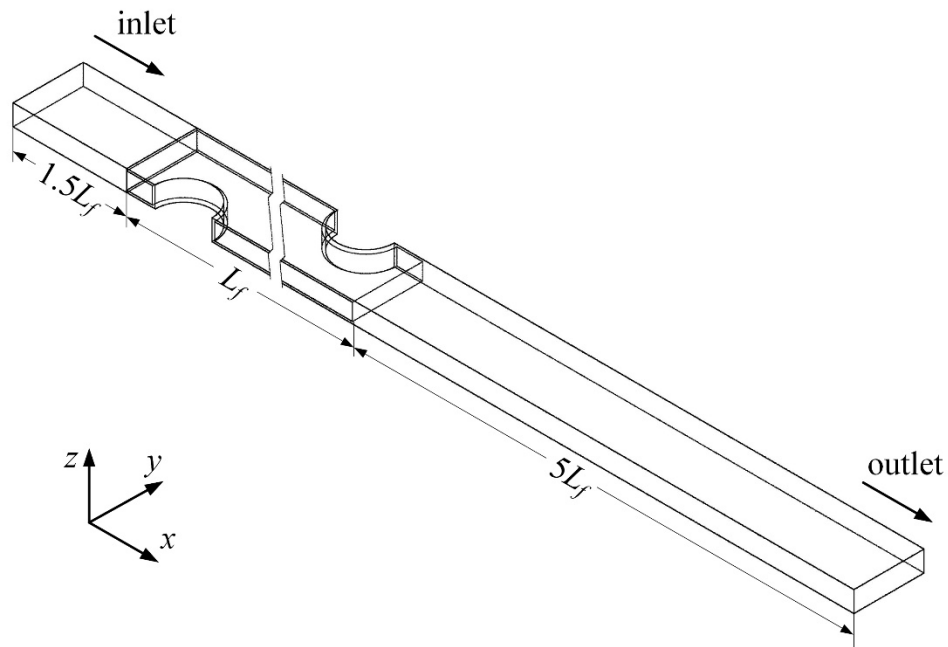
Figure 4.9: Computational domain for a fin-and-tube heat exchanger. The length of the extended region was not drawn in scale [200].

71
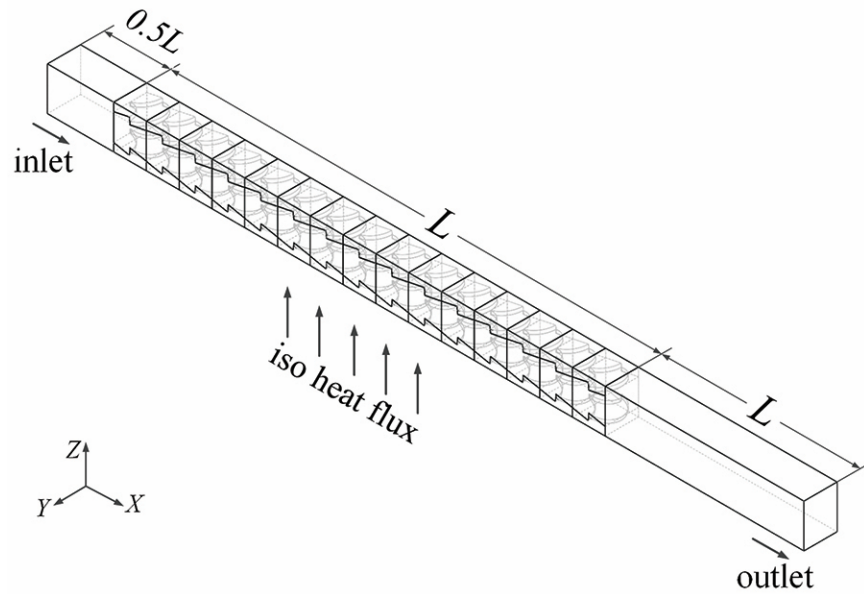
Figure 4.10: Computational domain for 15 REVs of scale roughed channel of a heat sink. The length of the extended region was not drawn in scale [201].

Table 4.3: Boundary conditions.

Inlet	$u = \text{const}, v = w = 0, T = \text{const}$
Outlet	$\dfrac{\partial u_i}{\partial x} = \dfrac{\partial T}{\partial x} = 0$
Interface between air and solid	no-slip, no thermal resistance
Tube inside wall	$u = v = w = 0, T_w = \text{const}$
The bottom of the scale-roughed wall	$u = v = w = 0, q'' = \text{const}$
The other surfaces	slip and adiabatic wall

The computational domain could be discretized using either unstructured mesh, see Figure 4.11, or structured mesh, Figure 4.12, depending on the complexity of the geometry. The unstructured mesh shown in Figure 4.11 was built by a commercial CFD code SC/Tetra Pre V8. This code utilizes a vertex based scheme for which the discrete equations are written in a relatively simple form and the number of control volumes is reduced compared to cell centered formulation. SC/Tetra controls the size of the mesh three dimensionally by creating an octree. When creating an octree, octants are refined automatically to prevent them from differing by two or more levels from the next octant. Mesh adaptive analysis was used to build the grid system. Fine elements are arranged where the change of pressure, velocity or temperature is large. As can be seen in Figure 4.11, fine elements were successfully arranged where the flow shows important phenomena, such as the region behind the tubes, boundaries that cause large temperature and/or flow changes, etc. Coarse elements were assigned where little change occurs, especially in the extended region. It can also be observed that the grid system has gradual variation from fine elements to coarse elements, which is quite important to maintain the calculation accuracy.

The other type of mesh, shown in Figure 4.12, which was built by Ansys Meshing. It is known that for flow-aligned geometries, hex mesh can provide higher-quality solutions with fewer cells than a comparable tet-mesh. Therefore, a structured hex-mesh is carefully created, aligning the mesh with the flow to reduce false diffusion. In the fin and tube region, fine grid is built with prism layers being inserted in the near wall region, while in the extended parts, a coarser grid is adopted to conserve computational resources. A gradual

73

variation in and after the fin region is also used to avoid the undesirable effect of an abrupt

grid width change in the computing region.

Extended Region   **Fin and Tube Region**   **Extended Region**

Gradual Variation   **Gradual Variation**
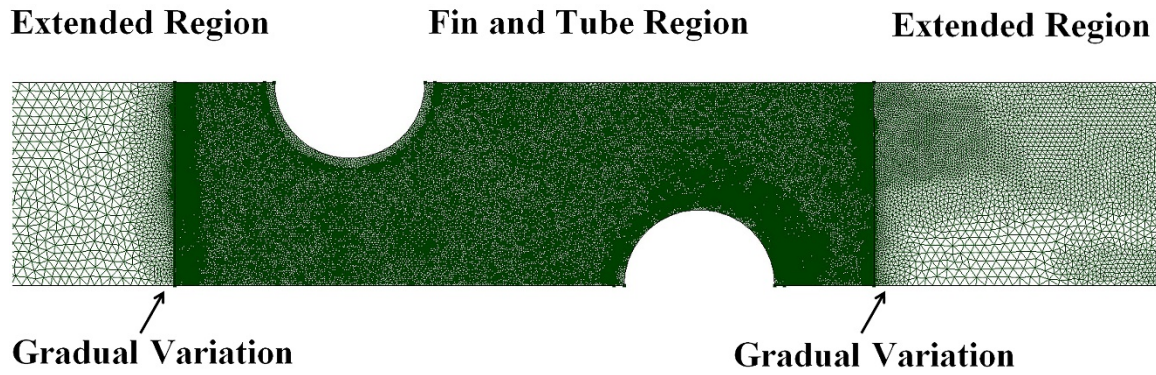
Figure 4.11: Grid system of one fin-and-tube heat exchanger model [200].
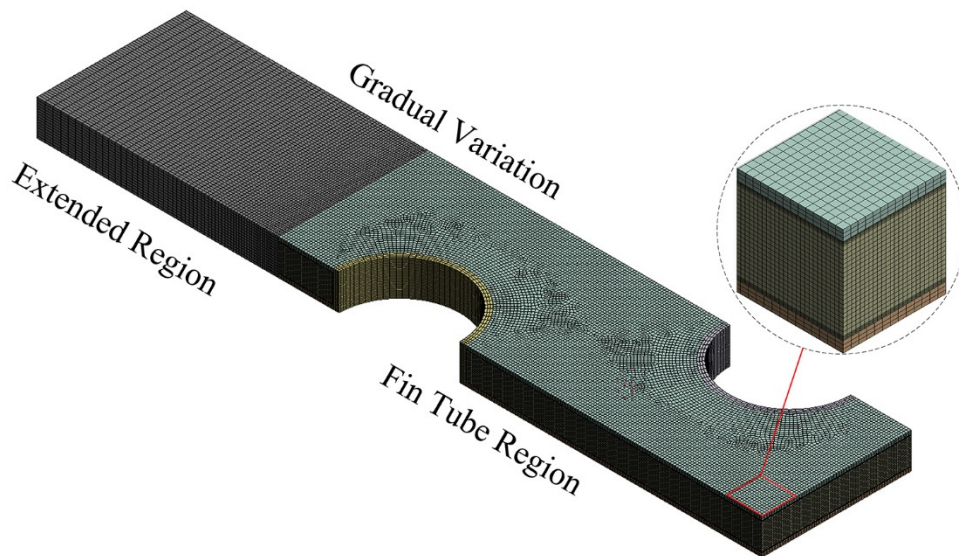
Figure 4.12: Grid system of one fin-and-tube heat exchanger model [202].

74

Compared to unstructured mesh, structured mesh needs much smaller number of grids to obtain the same accuracy and usually takes less time than an unstructured mesh calculation. However, it is more difficult to build structured mesh, especially for complicated geometry. Also unstructured mesh generation is usually much faster than structured mesh generation. It should be noted that for simpler problem, structured meshes are generally more accurate than unstructured. However, for more complex flows, the adaptivity facilitated by an unstructured grid may allow more accurate solutions. In the present study, for fin-and-tube heat exchanger, both adaptive unstructured mesh (Figure 4.11) and structured mesh (Figure 4.12) were built and tested. The accuracy of the two different types of mesh are comparable due to the relatively simple geometry.
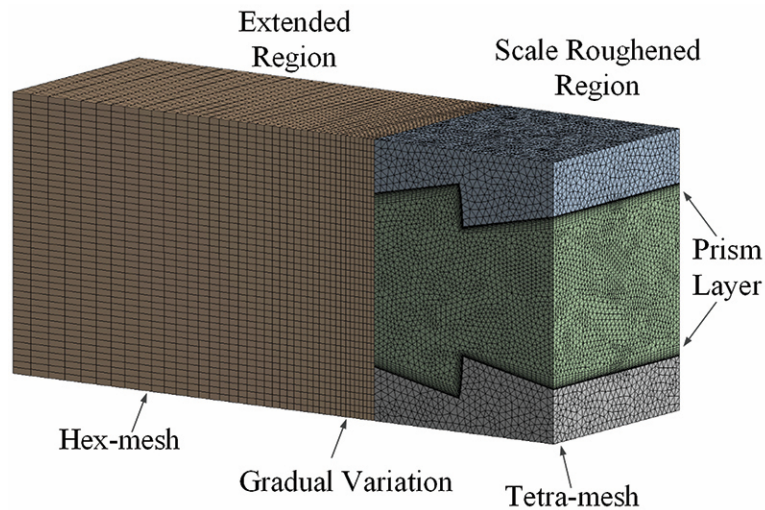
Figure 4.13: Example of the grid system. Only part of the whole model is shown [203].

As to the scale-roughed channel, a hybrid mesh, which consists of partially structured mesh and partially unstructured mesh, was adopted, see Figure 4.13. Due to the roughness of the wall that has many wedges and thin walls, it is very difficult to generate structured mesh for the scale roughed walls. An unstructured tetra-mesh is created for it, with prism layers being inserted in the near wall region. In the extended regions, a coarser and structured hex-mesh is adopted to conserve computational resources. It should be noted that in the scale-roughed region, the gird size should be small enough, i.e. at least 10 grids in the direction of the scale height, otherwise, the characteristics of the surface roughness cannot be captured correctly. For example, if only one grid was created along the scale height, then the difference between the scale-roughed surface and smooth surface cannot be recognized by the CFD code. This is especially important when the scale height is small, which usually requires finer mesh than the channel with large scale height.

To check whether the mesh is fine enough to minimize the computing error due to the grid, grid independence tests were made carefully by recursive refinement and comparison between the numerical simulation results. The above process was repeated until the variation of Nusselt number and friction factor was less than 0.5%, so that the numerical predictions can be regarded as grid-independent. With the turbulence predictions employed, the meshes near the fluid solid interface are fine enough to resolve the flow behavior close to the no-slip wall. For all the simulation cases, y^+ values in the near-wall region are less than 1.

However, the grid-independent solution still cannot be adopted until validation was done by comparing the predicted results with experimental data. Preliminary computations were conducted for a three-row plate fin-and-tube heat exchanger. The dimensions used in

the simulation are the same as those of the heat exchanger measured by Kang et al. [62] for his experiments. The Nusselt number and friction factor obtained from simulation solutions were compared with the correlations and experimental data by Kang et al. [62] and the correlations by Wang et al. [63] and are shown in Figure 4.14. From Figure 4.14 we can see that the maximum deviation of the friction factor and the Nusselt number from experiment are 10.4% and 11.9% with the average deviation being around 6% and 5.5% respectively.
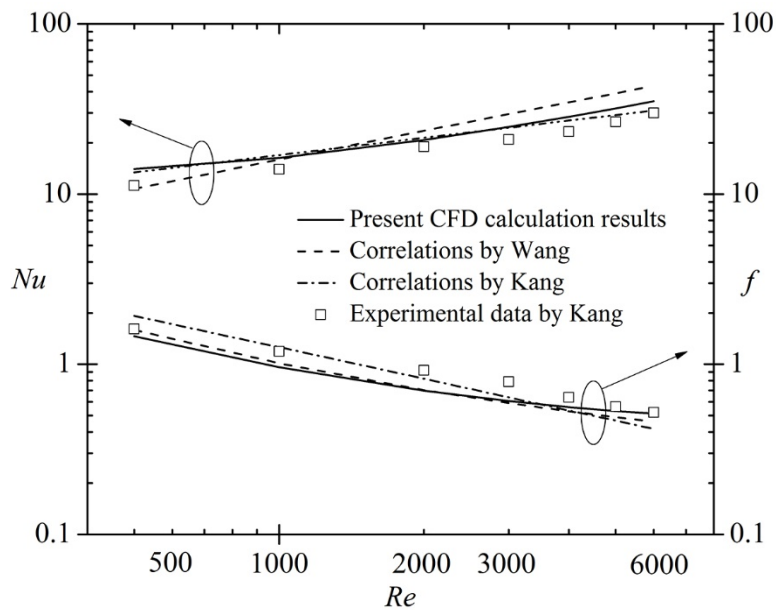
Figure 4.14: Comparison between the present CFD results and well-known correlations.

Definitions for the characteristic quantities which is used in the validation of the numerical results are presented the following:

$$Nu = \frac{hD_c}{k_f}$$ (4.75)

$$h = \frac{\dot{m}c_p \left(T_{in} - T_{out}\right)}{A_o \Delta T \eta_o}$$ (4.76)

$$\Delta T = \frac{\max\left(T_{in} - T_w, T_{out} - T_w\right) - \min\left(T_{in} - T_w, T_{out} - T_w\right)}{\log\left[\max\left(T_{in} - T_w, T_{out} - T_w\right) / \min\left(T_{in} - T_w, T_{out} - T_w\right)\right]}$$ (4.77)

$$f = \frac{\Delta p}{\frac{1}{2}\rho u_{max}^2} \cdot \frac{D_c}{L}$$ (4.78)

As has been discussed above, the computation is of a conjugated type where the fin efficiency is determined during the computations and cannot be obtained in advance. According to heat transfer theory [204, 205], the fin efficiency is defined as the actual heat transfer rate from the fin and tube divided by the heat transfer rate from the fin and tube when the fin is at the same temperature as the tube. In our numerical simulations, the fin efficiency η_f is computed by the approximation method described by Schmidt [206] and is as follows:

$$\eta_o = 1 - \frac{A_f}{A_o}\left(1 - \eta_f\right)$$ (4.79)

$$\eta_f = \frac{\tanh\left(mr\phi\right)}{mr\phi}$$ (4.80)

where

$$m = \sqrt{\frac{2h}{k_f \delta_f}} \qquad (4.81)$$

$$\phi = \left(\frac{R_{eq}}{r} - 1\right)\left[1 + 0.35\ln\left(\frac{R_{eq}}{r}\right)\right] \qquad (4.82)$$

$$\frac{R_{eq}}{r} = 1.27\frac{X_M}{r}\left(\frac{X_L}{X_M} - 0.3\right)^{1/2} \qquad (4.83)$$

$$X_L = \frac{\sqrt{(P_t/2)^2 + P_l^2}}{2} \qquad (4.84)$$

$$X_M = P_t/2 \qquad (4.85)$$

Numerical simulations were also conducted for a circular scale-roughened channel which had the same dimensions as the one experimentally tested by Chang et al. [2]. A quarter of the full test section is selected to be the computational domain, see Figure 4.15. The readers could refer to [2] for details as to how the measurements of f and Nu were performed.

From the figure we can see that the maximum deviation of the Nusselt number and the friction factor from experiment are 6.3% and 12.1% with the average deviation being around 3.5% and 5.8% respectively. Our predicted results and the experimental data agree very well, thereby showing the reliability of the physical model and the adopted numerical method.
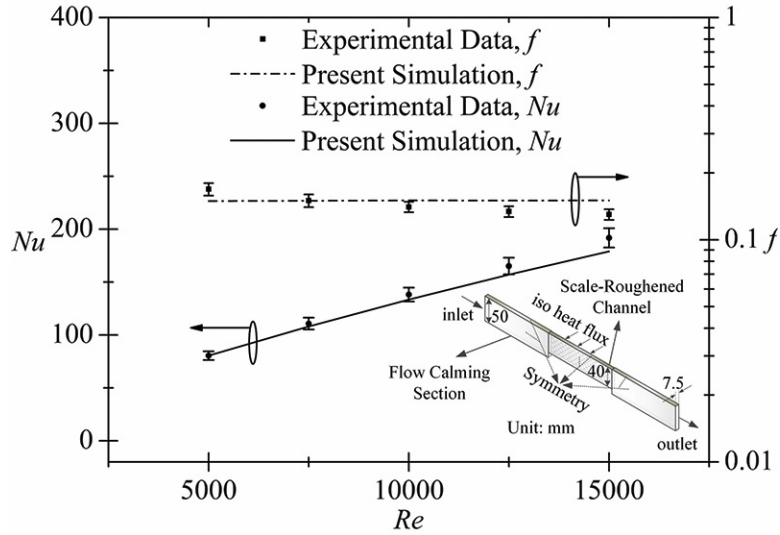
Figure 4.15: Validation of the present CFD simulation by comparing with experimental data by Chang et al. [2].

4.5. Number of REVs for Closure Evaluation

To treat a heat exchanger as porous media, entrance effects are important for both momentum and energy transport. When flow enters porous media, temperature and velocity profiles are uniform across the entrance area and as the flow progresses further downstream from the inlet, both thermal and momentum boundary layer are getting thicker until they merge with its counterpart at some particular location. Also, local values differ from the overall averaged as expected, therefore special attention should be paid when one uses the drag coefficient and heat transfer coefficient with the VAT governing equations to solve large scale problem. Local values are the only values that have a physical meaning when describing transport phenomena with VAT macro scale equations. Therefore, before evaluating the friction factor c_d and heat transfer coefficient h from the output of a CFD

code, the number of REVs one needs to simulate to obtain reasonable lower scale solutions

must be determined [185, 207].

4.5.1. Field Synergy Principle

Field Synergy Principle (FSP), a novel concept proposed and verified by Guo and

some other subsequent researchers [208-227], is adopted to help with the analysis. The

basic mechanism of FSP is that the convective heat transfer could be enhanced by

decreasing the intersection angle between the velocity and the temperature gradient. The

changing tendency of this intersection angle, in turn, provides a helpful means to explain

the variation in trends of the heat transfer coefficient and could help to verify the number

of REVs one should simulate to get reasonable lower scale solutions for VAT based

modeling. To analyze the numerical results using the Field Synergy Principle, the concept

of FSP is briefly reviewed as follows.
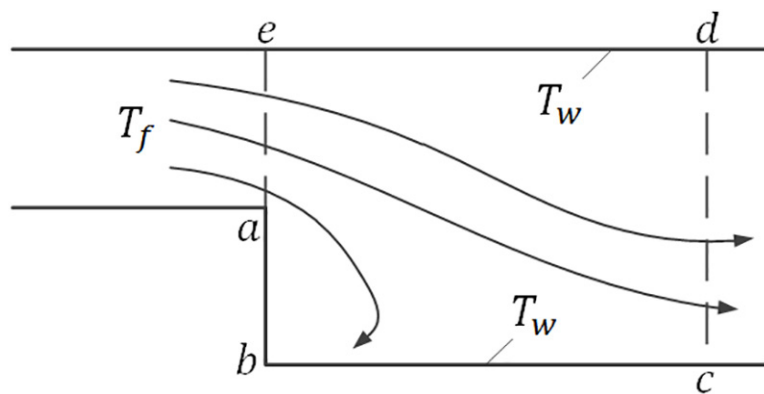
Figure 4.16: Fluid flow and heat transfer over a backward step.

For a steady-state elliptic flow of constant properties within an computational domain (taking the fluid flow and heat transfer over a backward step [214] as an example, as shown in Figure 4.16), its energy conservation equation can be described as:

$$\rho c_p \left(u \frac{\partial T}{\partial x} + v \frac{\partial T}{\partial y} + w \frac{\partial T}{\partial z} \right) = k_f \left(\frac{\partial^2 T}{\partial x^2} + \frac{\partial^2 T}{\partial y^2} + \frac{\partial^2 T}{\partial z^2} \right) \tag{4.86}$$

Integrate Eq. (4.86) over the entire domain Ω_{abcde} leading to:

$$\int_{\Omega_{abcde}} \rho c_p \left(\vec{U} \cdot \nabla T \right) dA = \int_{\Omega_{abcde}} k_f \nabla^2 T dA \tag{4.87}$$

Incorporating the Gauss law for reduction of the integral dimension, the right side of Eq. (4.87) can be written as:

$$\int_{\Omega_{abcde}} k_f \nabla^2 T dA = \int_{abc} k_f \vec{n} \cdot \nabla T ds + \int_{de} k_f \vec{n} \cdot \nabla T ds + \int_{cd} k_f \vec{n} \cdot \nabla T ds + \int_{ea} k_f \vec{n} \cdot \nabla T ds \tag{4.88}$$

The last two terms on the right-hand side of Eq. (4.88) represent the axial heat conduction within the fluid while the first two terms stand for the convective heat transfer between the fluid and solid. For flow with Peclet number greater than 100, the axial conduction terms can be neglected [228], leading to

$$\int_{\Omega_{abcde}} \rho c_p \left(\vec{U} \cdot \nabla T \right) dA = \int_{abc} k_f \vec{n} \cdot \nabla T ds + \int_{de} k_f \vec{n} \cdot \nabla T ds \tag{4.89}$$

For conventional working fluids adopted in engineering, the Peclet numbers are usually greater than 100, and hence, the integration $\int_{\Omega_{abcde}} \rho c_p \left(\vec{U} \cdot \nabla T \right) dA$ actually represents the energy transferred by convection [214]. The inner production $\vec{U} \cdot \nabla T = |\vec{U}||\nabla T|\cos\theta$, in which θ is the local intersection angle between the local velocity vector and the

82

temperature gradient. Therefore, it is obvious that besides increasing the velocity and temperature gradient, decreasing their intersection angle θ will also make the integration $\int_{\Omega_{abcde}} \rho c_p \left(\vec{U} \cdot \nabla T \right) dA$ larger, enhancing the heat transfer. On the other hand, for a given flow rate and temperature gradient, the changing tendency of this intersection angle helps explain the variation in trends of the convective heat transfer coefficient.

According to the concept of Field Synergy Principle, the following quantity is introduced:

$$M = \frac{\sum \left(\left| \vec{U} \right| \left| \nabla T \right| \right)}{n} \tag{4.90}$$

The local intersection angle between the velocity and temperature gradient is

$$\theta = \cos^{-1} \frac{u \dfrac{\partial T}{\partial x} + v \dfrac{\delta T}{\delta y} + w \dfrac{\partial T}{\partial z}}{\left| \vec{U} \right| \left| \nabla T \right|} \tag{4.91}$$

The average intersection angle of the computation domain is defined by

$$\theta_m = \frac{\sum \theta_{i,j,k} dv_{i,j,k}}{\sum dv_{i,j,k}} \tag{4.92}$$

where $dv_{i,j,k}$ is the volume element of the control volume (i, j, k).

4.5.2. Validation of FSP Application

Taking the plate fin-and-tube heat exchangers as a demonstration, 3D numerical simulations were performed with the tube row number varying from 1 to 9. A clear perspective of the variations of both overall and local fiction factor and Nusselt number as

83

the tube row number increases was presented. These variation trends were also explained from the view point of Field Synergy Principle.

To verify that the FSP is suitable to our problem, computation was conducted for the three-row case and the effect of Reynolds number on heat transfer characteristic of plate fin-and-tube heat exchangers was analyzed by FSP. The Reynolds number based on the fin collar outside diameter varied from 500 to 6000 and the corresponding air frontal velocity was ranged from 0.38m/s to 4.6m/s.

Figure 4.17 (a) shows the variation of M/M_0 as a function of Reynolds number, where M_0 is the value of M when Re = 500. In the Reynolds number range of our computation, the increase in air flow velocity is the main reason why the heat transfer rate increased. Therefore, it is not surprising that the value of M has a nearly linear-increasing relationship with Reynolds number, which should lead the Nusselt number to be proportional to Re. However, the increasing trend of the average Nusselt number with Re was weakened as the Reynolds number increases, just as Figure 4.17 (b) shows. The reason why this happened is that the intersection angle between velocity and temperature gradient increased with Re, shown in Figure 4.17 (b), which leads to the worsening of the synergy. Consequently, the increasing trend of the intersection angle is similar to that of the Nusselt number.
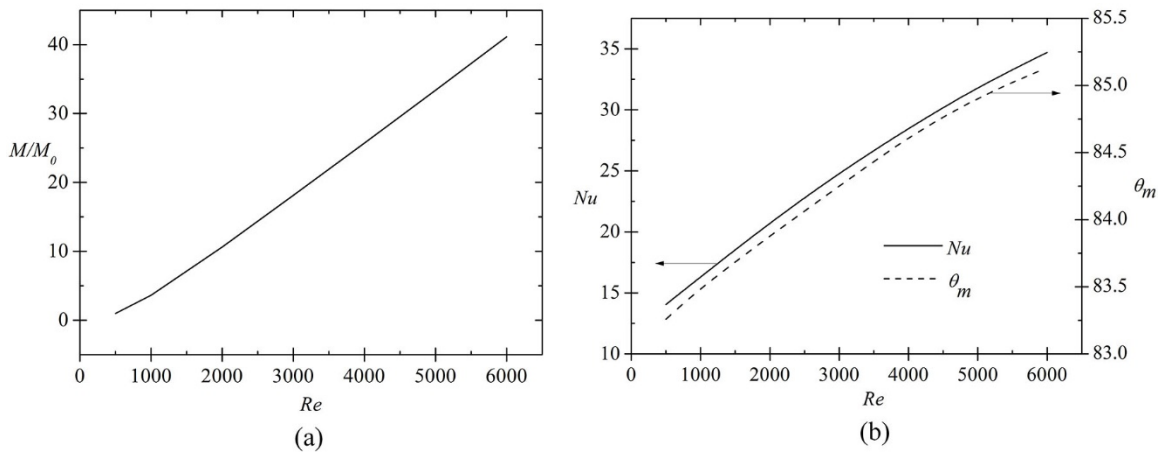
Figure 4.17: (a) Variation curve of M/M_0 with Re; (b) Comparison between the variation trend of Nu and θ_m with Re.

(a) 0m/s 1.22m/s

(b) 20℃ 120℃

(c) 0° 90°
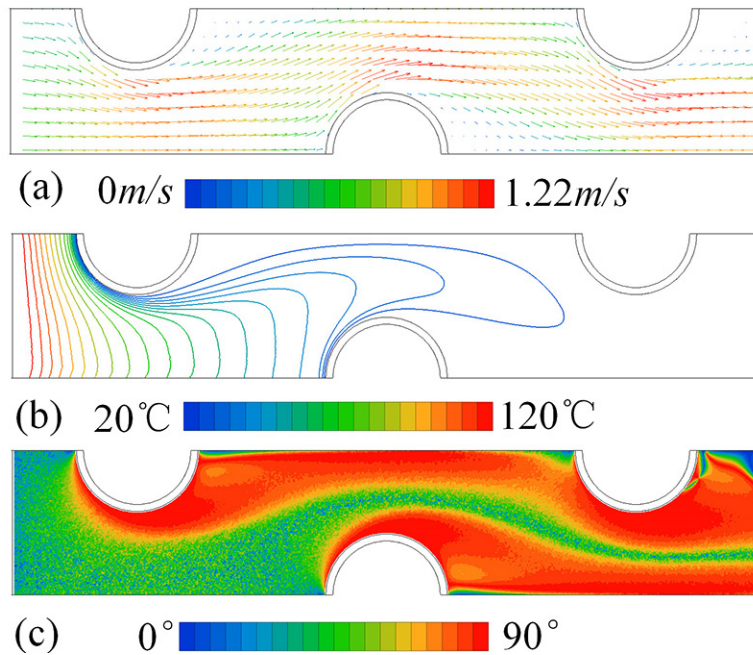
Figure 4.18: Re = 500, N = 3, (a) velocity, (b) temperature, and (c) intersection angle.
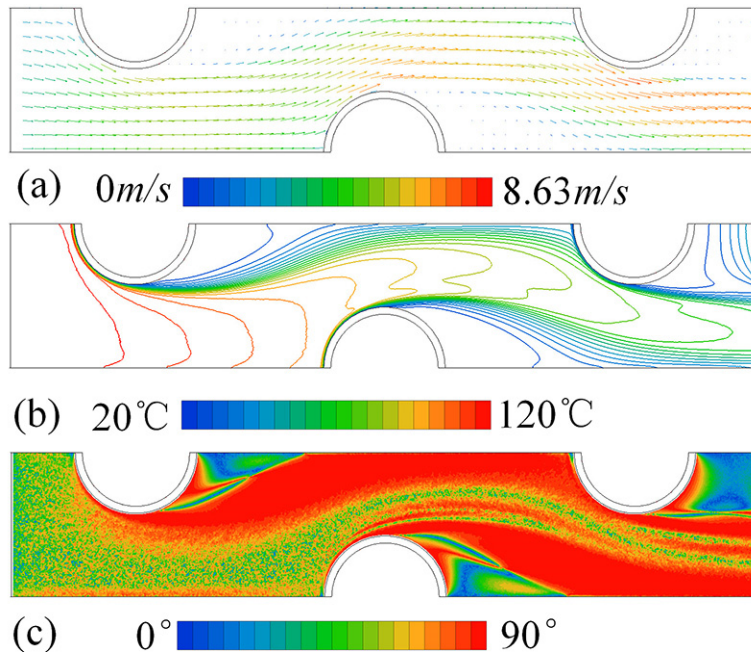
Figure 4.19: Re = 3000, N = 3, (a) velocity, (b) temperature, and (c) intersection angle.
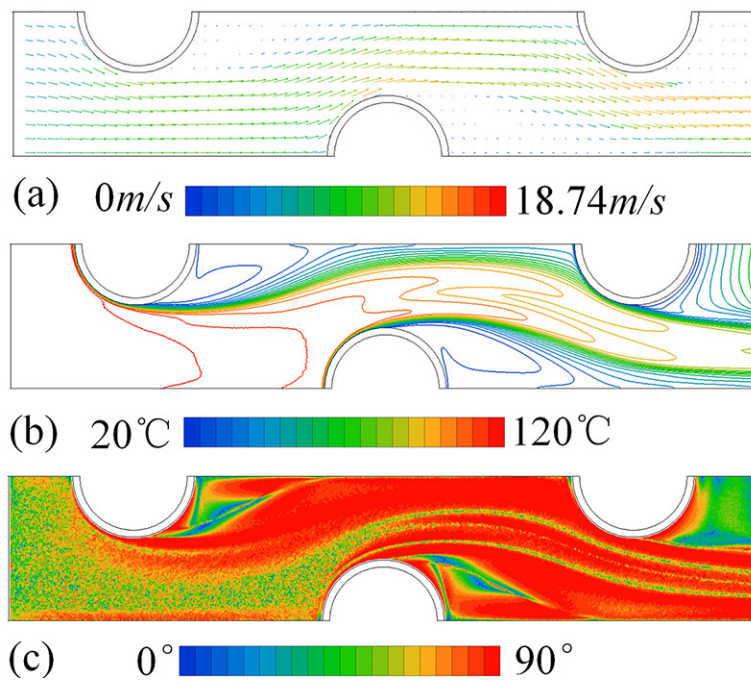
Figure 4.20: Re = 6000, N = 3, (a) velocity, (b) temperature, and (c) intersection angle.

Figure 4.18, Figure 4.19 and Figure 4.20 present the local distributions of velocity (a), temperature (b) and intersection angle (c) on the *x-y* plane at $z = 0.0011$m for Re = 500, 3000 and 6000 respectively. Basically, these pictures reveal two main pieces of information:

1) The synergy becomes worse in the direction of air flow stream. At the inlet region, the isothermals are almost perpendicular to the velocity vector, which leads to a quite small intersection angle at the inlet part. After the flow passes through the first tube, the velocity vector almost parallels the isothermals, which results in a worse synergy.

2) That synergy becomes worse with increasing Reynolds number can be observed qualitatively by noting region of red color in the paint graphs of intersection angle distribution. Comparing Figure 4.20 with Figure 4.18, we find that for large Reynolds number, even at the inlet, the synergy is not good, let alone the remaining part of the simulation region. Therefore, the increase of heat transfer rate brought by the increase of air flow velocity is counteracted partly by the deteriorated synergy.

Based on the above analysis, the increasing trend of Nusselt number with Reynolds number was explained well by the FSP. Thus it is meaningful to use FSP to analyze the heat transfer characteristic of heat exchangers and help to determine the number of required REVs for our purpose without any simplifying assumption, such as ideal fin and ideal temperature difference, which was adopted by studies [19-22] while verifying the FSP.

4.5.3. Determination of Number of REVs Using FSP

As can be seen in Figure 4.5, for fin-and-tube heat exchangers with multiple-row tubes, the friction factors are almost independent of the number of tube rows, while the Nusselt

number decreases with the increasing of tube row number. Our simulation results, conducted with the tube row number varying from 1 to 9, came to the same conclusion, shown by Figure 4.21. It can be seen that the variation of friction factor with N is quite small, and when the row number is larger than 3, f could be considered independent of N. Wang et al. [1, 229] also arrived at the same conclusion by means of experiments. It is also shown that the Nusselt number decreases with the increasing of tube row number N, and when $N > 4$, the decreasing trend slows down. When $N > 6$, the variations of friction factor and Nusselt number are quite subtle, making it reasonable to conclude that the effect of tube row on the heat transfer and fluid flow could be neglected when the number of tube rows is greater than six.
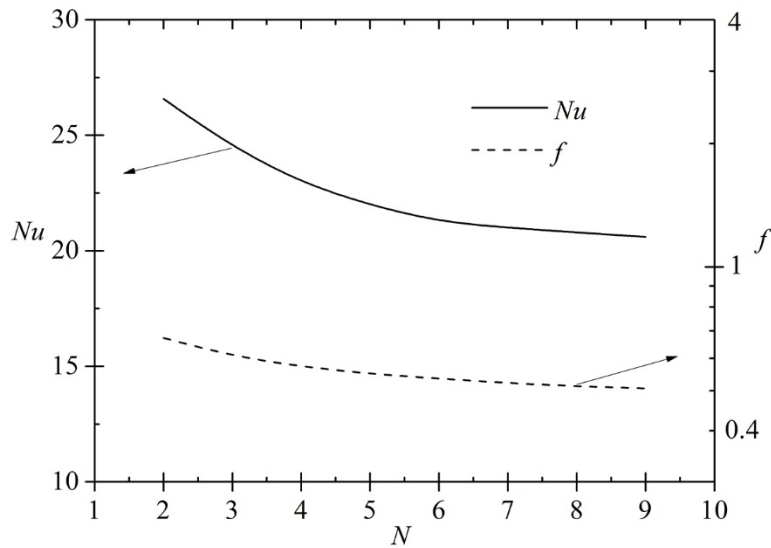
Figure 4.21: Variation of Nu and f with tube row number by CFD simulation.
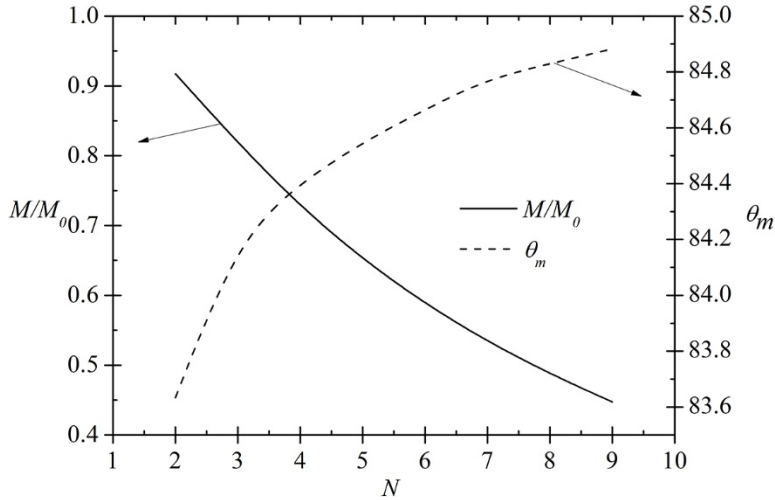
Figure 4.22: Variation of M/M_0 and θ_m with tube row number N.

Figure 4.22 shows the variation of M/M_0 and θ_m with the increasing tube row number, where M_0 is the M value for one-row case. As can be seen, the average product of $\left|\vec{U}\right|$ and $\left|\nabla T\right|$ decreases with the increasing of N. It also can be found that the intersection angle between air flow velocity and temperature gradient increases with the increasing of tube row number and the increasing trend slows down when $N > 4$. This explains well the change in trend of Nusselt with the increasing of N.

To get a more vivid impression, two more figures, Figure 4.23 and Figure 4.24, together with Figure 4.19, comparisons of local distributions of velocity vector, isothermals and intersection angle on the x-y plane for 3-row case, 6-row case and 9-row case are presented. It is obvious that as the number of tube rows increases, the percentage of the area which has deteriorated synergy (red area) increases. It is also found that when $N > 6$, the flow field, temperature field and the distribution of intersection angle are marked with obvious periodicity, shown by the dashed frame in Figure 4.24.

(a) 0m/s ▭ 7.98m/s

(b) 20℃ ▭ 120℃

(c) 0° ▭ 90°
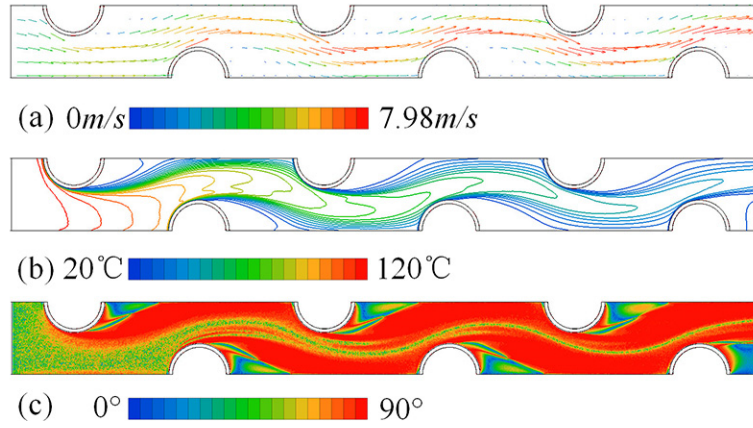
Figure 4.23: Re = 3000, N = 6, (a) velocity, (b) temperature, and (c) intersection angle.

(a) 0m/s ▭ 8.25m/s

(b) 20℃ ▭ 120℃

(c) 0° ▭ 90°
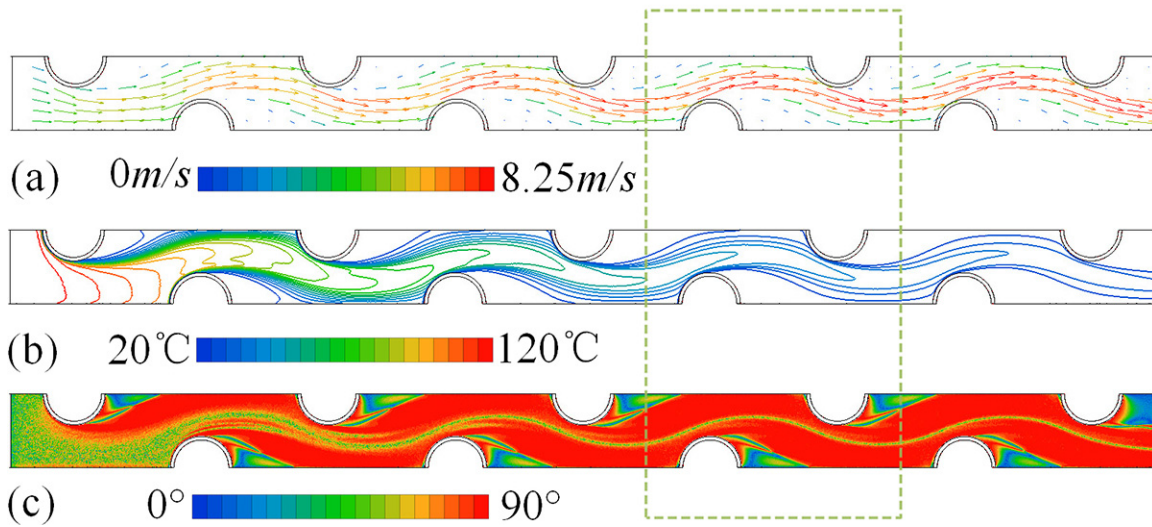
Figure 4.24: Re = 3000, N = 9, (a) velocity, (b) temperature, and (c) intersection angle.

It should be noted that the above discussion is based on values averaged over the whole simulation domain, while to use volume average theory to optimize the heat exchangers, we are more concerned about values averaged over a selected REV (local values). As a result, although we arrived at the conclusion that when the number of tube rows is larger than six, the flow field and thermal field could be considered as periodic in the streamwise direction, we cannot say that the computational domain including six tube rows is long enough to get a reasonable lower scale solution.
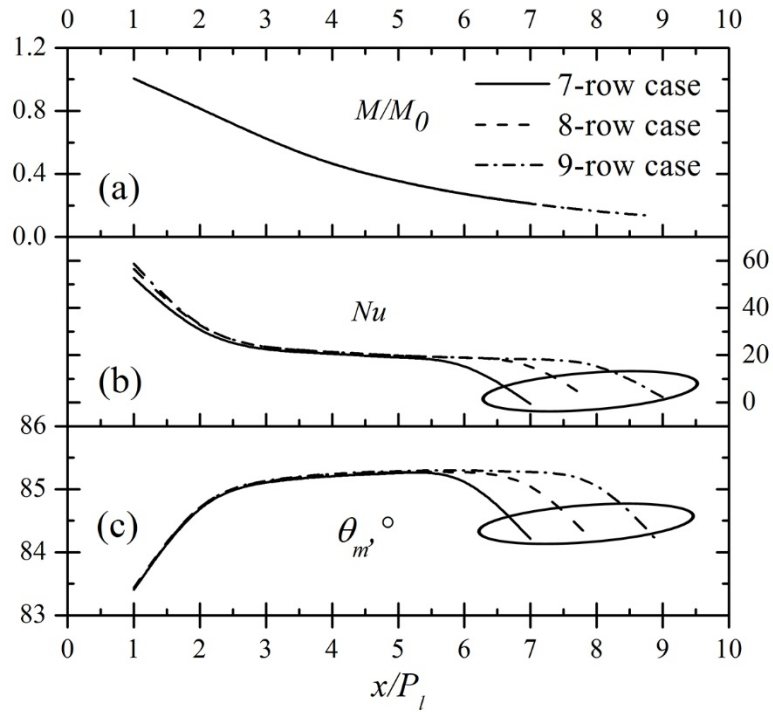
Figure 4.25: Variation of local values in the streamwise direction.

91

In-depth observations should be carried out on the variation of concerned parameters for every single REV along the air flow direction. Thus, we divided the computational domain of the 7, 8 and 9-row cases into 7, 8, and 9 REVs and then calculated the Nusselt numbers, M values and intersection angles for the total 24 elementary volumes, and plotted the variation curves in Figure 4.25. Some conclusions that can be drawn from the graphs are the following:

(1) The averaged local M value over every single elementary volume decreases along with the direction of air flow. This is why the magnitude of M averaged over the whole domain decreases as the number of tube rows increase.

(2) Since the curves of M for the three cases collapse to a single curve, it is reasonable to say that the number of tube rows has no effect on the trend of local M from the domain inlet all the way to the outlet.

(3) Excluding the last data point, the curves of Nu and θ_m also collapse to two single curves. However, the Nu number and intersection angle for the last elementary volume is unusual due to the reason that the air-flow recirculation happens when it flows from the trailing edge of the fin to the extended domain. For this reason, the solution of the last volume shouldn't be used to calculate the closure for VAT based model.

(4) The averaged local Nusselt number decreases along with the direction of air flow and almost keeps constant when $x/P_l > 4$, while the averaged local intersection angle increases along with the direction of air flow and reaches a plateau when $x/P_l > 4$. Both the local averaged Nusselt number and intersection angle for elementary

volume five, six and seven have subtle differences. The variation trends of local averaged Nu and θ_m agree pretty well.

Therefore, in conclusion, $N > 4$ is needed to get a believable local value, which means that the tube row number should not be less than 4+2+2 rows (2+1+1 REVs). The first 2 REVs is to develop the velocity and temperature field, and 3rd REV is where to calculate the closure. The solution of the 4th REV is not for use considering the invalidity of the last data point. We recommend that 6+2+2 rows (3+2+1 REVs) be simulated and that the closure be obtained by averaging the local value over the 4th and 5th REV. Similar study was done for the channel with scale-roughed surface before the evaluation of the closure was conducted.

4.6. The Closure Evaluation Procedure

In this section, the closure terms rigorously derived in section 4.1 are evaluated over the selected REVs by numerical simulation on the pore-scale. The closure terms for momentum equation and energy equations are repeated here for convenience. The momentum closure is

$$c_d = c_{dp}\frac{S_{wp}}{S_w} + c_{fL} + c_{fT} - \frac{\dfrac{\partial}{\partial x_j}\left\langle \hat{\bar{u}}_i\hat{\bar{u}}_j\right\rangle_f}{\frac{1}{2}S_w\tilde{\bar{u}}_i^2} + \frac{\dfrac{\partial}{\partial x_j}\left(\left\langle \hat{v}_T\dfrac{\partial \hat{\bar{u}}_i}{\partial x_j}\right\rangle_f\right)}{\frac{1}{2}S_w\tilde{\bar{u}}_i^2} \tag{4.13}$$

in which c_{dp}, c_{fL} and c_{fT} are defined by Eq. (4.2), Eq. (4.7) and Eq. (4.8) respectively. With the definitions of c_{dp}, c_{fL} and c_{fT}, Eq. (4.13) becomes,

$$c_d = \frac{-\int_{\partial S_w} \overline{p}\, d\overline{s}}{\frac{1}{2}\rho_f A_{wp}\tilde{\overline{u}}_i^2}\frac{S_{wp}}{S_w} + \frac{\int_{\partial S_w} \tau_{wL}\cdot d\overline{s}}{\frac{1}{2}\rho_f A_w\tilde{\overline{u}}_i^2} + \frac{\int_{\partial S_w} \tau_{wT}\cdot d\overline{s}}{\frac{1}{2}\rho_f A_w\tilde{\overline{u}}_i^2} - \frac{\frac{\partial}{\partial x_j}\left\langle \hat{\overline{u}}_i\hat{\overline{u}}_j\right\rangle_f}{\frac{1}{2}S_w\tilde{\overline{u}}_i^2} + \frac{\frac{\partial}{\partial x_j}\left(\left\langle \hat{v}_T\frac{\partial \hat{\overline{u}}_i}{\partial x_j}\right\rangle_f\right)}{\frac{1}{2}S_w\tilde{\overline{u}}_i^2}$$

$$\text{(4.93)}$$

The energy closure is

$$h = \frac{\frac{1}{\Delta\Omega}\int_{\partial S_w}\left(k_f + k_T\right)\nabla\overline{T}_f\cdot d\overline{s} - \rho_f c_{pf}\nabla\cdot\left(\langle m\rangle\widetilde{\hat{\overline{u}}_f\hat{\overline{T}}_f}\right) + \nabla\cdot\left(\frac{k_f}{\Delta\Omega}\int_{\partial S_w}\hat{\overline{T}}_f\, d\overline{s}\right)}{S_w\left(\tilde{T}_s - \tilde{\overline{T}}_f\right)} \qquad \text{(4.21)}$$

To obtain closure for momentum equation and energy equations, numerical simulations are performed on the lower pore scale. As described in section 4.4.1, the flow is assumed to be three-dimensional, steady state, incompressible and with constant property. Therefore, the momentum and energy equations are decoupled, allowing them to be solved sequentially and the energy equation is solved after the flow field is obtained, which is beneficial in reducing computational cost.

After the numerical solutions are completed, Eq. (4.93)and Eq. (4.21) are evaluated to obtain the momentum closure as represented by drag resistant coefficient and energy equation closure as represented by the heat transfer coefficient. The numerical procedure is presented as the following four steps:

Step 1: Use CFD code to solve the momentum equation and energy equations, together with the turbulence model, with appropriate boundary conditions.

Fluid phase:

$$\rho u_j \frac{\partial u_i}{\partial x_j} = \frac{\partial}{\partial x_j} \left[(\mu + \mu_T) \frac{\partial u_i}{\partial x_j} \right] - \frac{\partial p}{\partial x_i} \tag{4.94}$$

$$\rho u_j \frac{\partial T_f}{\partial x_j} = \frac{\partial}{\partial x_j} \left[\left(\frac{\mu}{\mathrm{Pr}} + \frac{\mu_T}{\mathrm{Pr}_T} \right) \frac{\partial T_f}{\partial x_j} \right] \tag{4.95}$$

In which the turbulent viscosity μ_T and turbulent Prandtl number Pr_T are computed using SST model proposed by Menter [197, 198], referring to section 4.4.1 for details about SST.

Solid phase:

$$\frac{\partial}{\partial x_j} \left(\frac{\partial T_s}{\partial x_j} \right) = 0 \tag{4.96}$$

Step 2: Calculate the volume averaged variables by averaging the local pointwise variables over the selected REV, which includes velocity $\boldsymbol{u}$, pressure p, fluid temperature T_f and solid temperature T_s.

Fluid phase:

$$\tilde{\bar{u}}_i = \frac{1}{\Delta \Omega_f} \int_{\Delta \Omega_f} \bar{u}_i dV \tag{4.97}$$

$$\tilde{\bar{T}}_f = \frac{1}{\Delta \Omega_f} \int_{\Delta \Omega_f} \bar{T}_f dV \tag{4.98}$$

Solid phase:

$$\tilde{T}_s = \frac{1}{\Delta \Omega_s} \int_{\Delta \Omega_s} T_s dV \tag{4.99}$$

Step 3: Calculate the spatial fluctuations of flow variables,

$$\hat{\bar{u}}_i = \bar{u}_i - \tilde{\bar{u}}_i \tag{4.100}$$

$$\hat{\bar{T}}_f = \bar{T}_f - \tilde{\bar{T}}_f \tag{4.101}$$

Step 4: Evaluate Eq. (4.13) and Eq. (4.21) over the selected REV to compute the drag resistance coefficient and heat transfer coefficient.

4.7. Closure for Fin-and-Tube Heat Exchangers

As discussed in Section 4.5, the computational domain should be long enough, so that closure can be evaluated over an REV that is not affected by entrance or re-circulation effects near the outlet. Therefore, a computational domain with six REVs (twelve rows of tubes) was selected as the computational domain, see Figure 4.26. The only experimental data for large number of tube rows can be found in open literature was reported by Tang et al. [65] who tested a fin-and-tube heat exchanger with 12 rows of tubes. Therefore, after grid independency test, preliminary computations were conducted for a FTHX which had the same dimensions as the one experimentally tested by Tang et al. [65] to further validate and verify the applicability of the adopted model to large number of tube rows. Figure 4.27 shows a maximum deviation of Nusselt number and friction factor from experiment of 4.8% and 2%, respectively, which validates our numerical model and method.
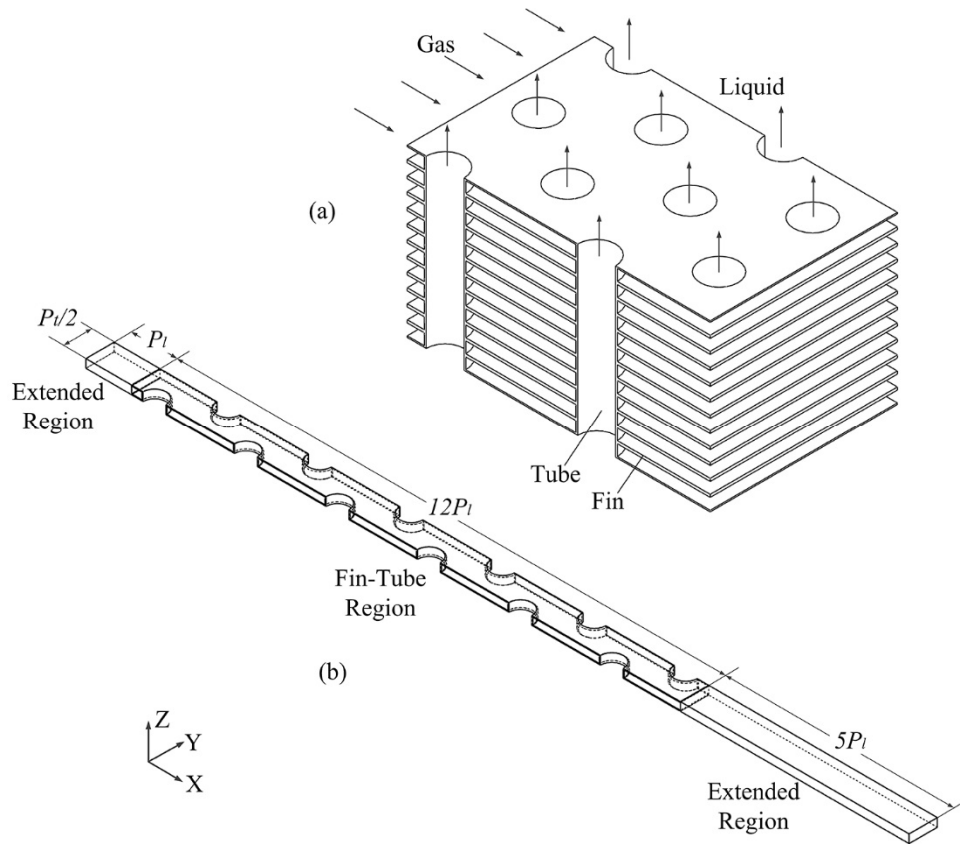
Figure 4.26: Computational domain for 12-row case [202].
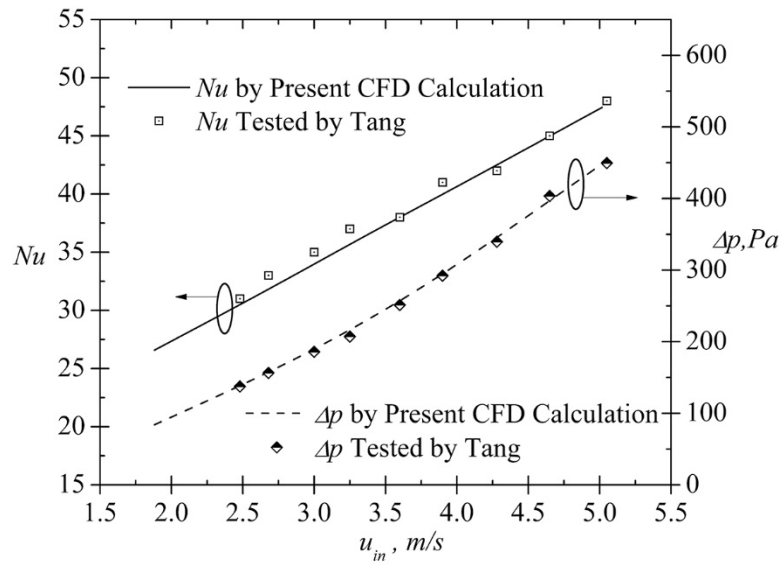
Figure 4.27: Comparison between the present CFD results and experimental data by Tang et al. [65].

4.7.1. Air-side Closures

To develop correlations for local friction factor and heat transfer coefficient, 6 more different sets of design dimensions besides the one which is the same as what Tang et al. [65] experimentally tested, see Table 4.4, were simulated at different Re_{Dc}, ranging from 2000 to 12000.

The friction factor and Nusselt number evaluated using the length scale D_c as a function of Re_{Dc} for fin-and-tube heat exchangers with different dimensions are shown in Figure 4.28 and Figure 4.29 respectively. The numerically predicted results are scattered, leading to seven different Nu_{Dc} - Re_{Dc} and $f_{Dc} - Re_{Dc}$ curves. However, the friction factor and Nusselt number obtained by evaluating the rigorously derived closure terms collapse to two single curves, shown in Figure 4.30 and Figure 4.31, respectively.

Table 4.4: Geometric dimensions of the numerically tested fin-and-tube heat exchangers.

	P_t/D_c	P_l/D_c	F_p/D_c
Base Case	2.26	1.83	0.167
Case 1	2.53	2.05	0.187
Case 2	2.04	1.65	0.150
Case 3	2.26	1.72	0.167
Case 4	2.26	1.94	0.167
Case 5	2.04	1.83	0.167
Case 6	2.47	1.83	0.167

With the help of JMP 9, an available statistical analysis tool, the collapsed data enabled us to develop a simple correlation of friction factor for the air side,

$$f_{D_h} = \frac{A}{\mathrm{Re}_{D_h}} + B = \frac{128.2}{\mathrm{Re}_{D_h}} + 0.149 \tag{4.102}$$

A comparison of values of A and B with other morphologies is shown in Table 4.5 [230].

Similarly, the collapsed Nusselt number was correlated as

$$Nu_{D_h} = 0.171 \mathrm{Re}_{D_h}^{0.559} \mathrm{Pr}^{1/3} \tag{4.103}$$

Table 4.5: Closure coefficients of friction factor for different morphologies.

Morphology	A	B	Porosity range
Packed bed	100/3	7/12	0.3-0.72
Pin fins-inline	50	0.145	0.65-0.91
Pin fins-staggered	50	0.145	0.65-0.91
Staggered plain fin-and-tube HX (Average)	112.4	0.252	0.65-0.9
Staggered plain fin-and-tube HX (Local)	128.2	0.149	0.65-0.9
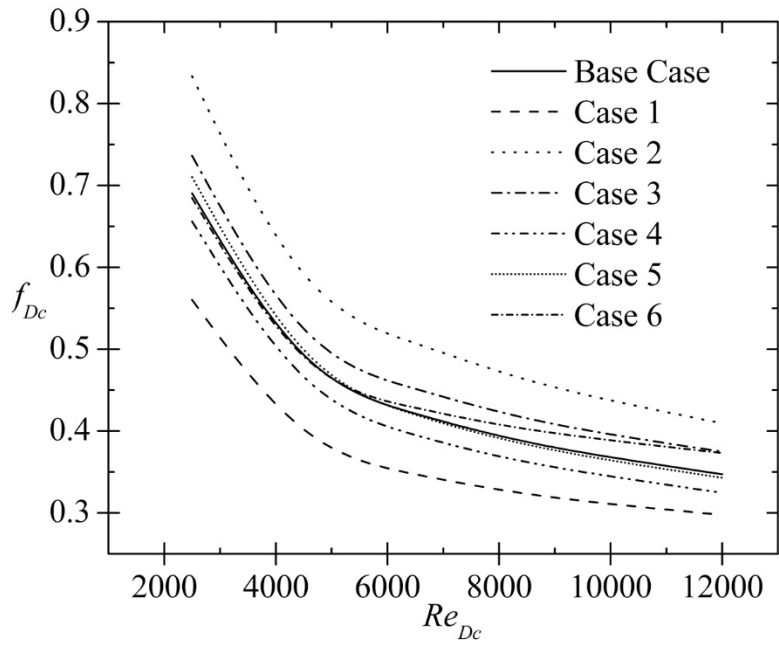
Figure 4.28: Friction factor as a function of Re_{Dc} using D_c as the length scale.
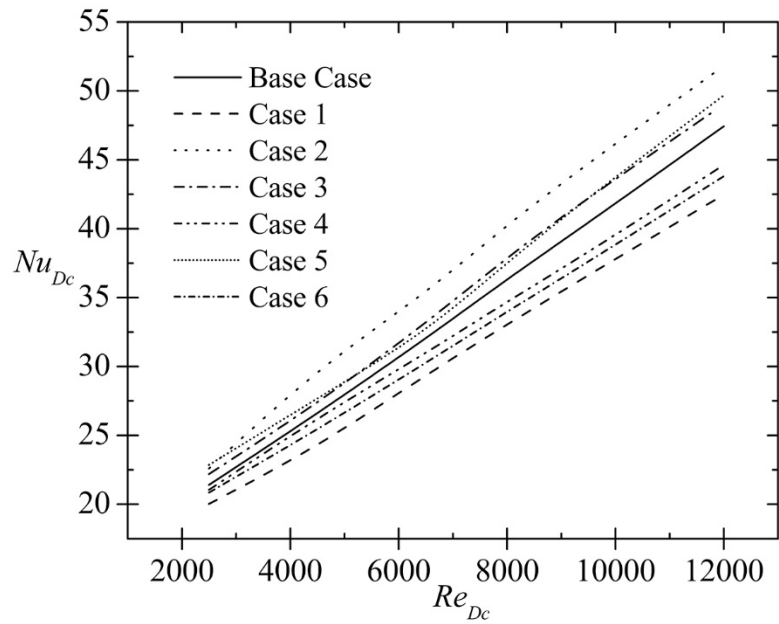
Figure 4.29: Nusselt number as a function of Re_{Dc} using D_c as the length scale.
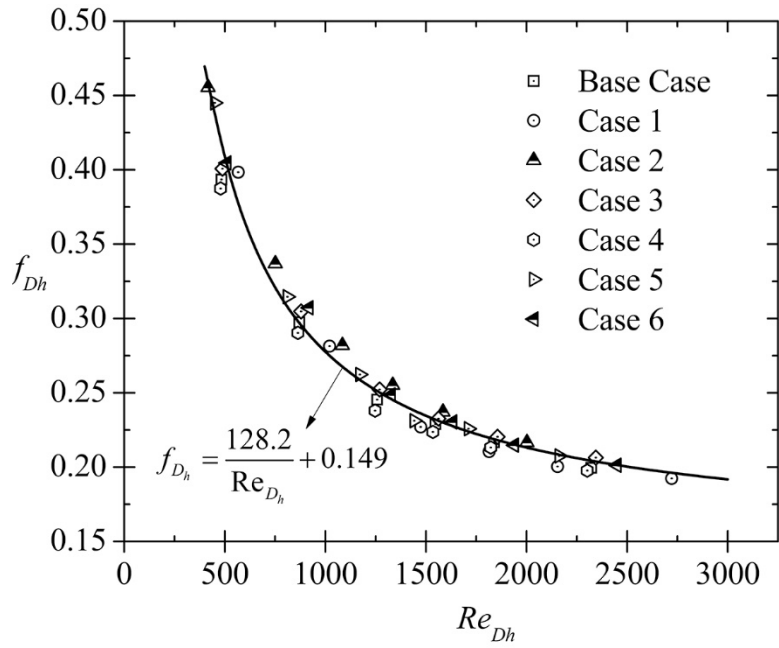
Figure 4.30: Friction factor as a function of Re$_{Dh}$ using D_h as the length scale.
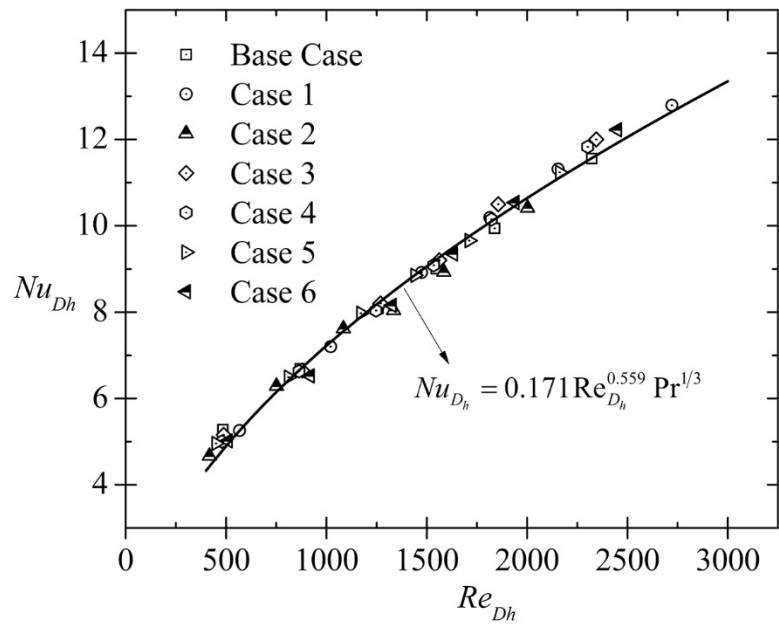
Figure 4.31: Nusselt number as a function of Re$_{Dh}$ using D_h as the length scale.
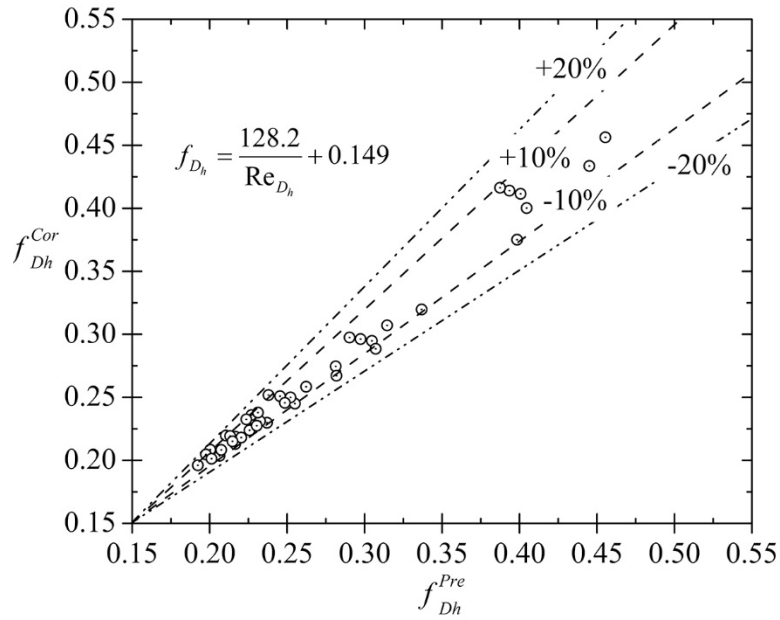
Figure 4.32: Deviation of the proposed friction factor correlation.

The friction factor correlation shown in the figure:

$$f_{D_h} = \frac{128.2}{Re_{D_h}} + 0.149$$
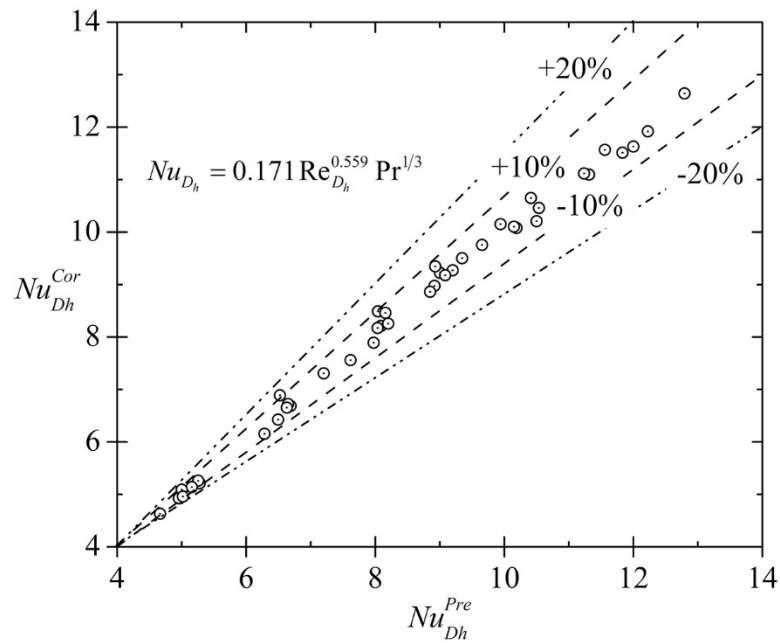
Figure 4.33: Deviation of the proposed Nusselt number correlation.

The Nusselt number correlation shown in the figure:

$$Nu_{D_h} = 0.171 Re_{D_h}^{0.559} Pr^{1/3}$$

Figure 4.32 and Figure 4.33 show the comparison between the numerical simulation results and the results predicted by the proposed correlations. The proposed friction factor correlation, Eq. (4.102), can predict 83.3% of data within a deviation of 10% and an average deviation of 2.6%. The correlation of Nusselt number, Eq. (4.103), can describe all the simulation results within a deviation of 10% and an average deviation of 1.6%.

It should be noted that the correlations proposed by rescaling experimental data available in public literature were average values, while the correlations proposed in the present section were obtained by evaluating the rigorously derived closure terms over a selected REV which were local values. They are fundamentally different by definition, but describing the same heat transfer phenomena essentially. Local heat transfer coefficient is the heat transfer driven by the local REV average temperature gradients, while the average coefficient represents the total heat transfer, ranging from the inlet all the way to the exit [190]. When designing a heat exchanger device, this type of control volume analysis would be adequate, but for more detailed differential analysis, a local heat transfer that is based purely on theoretical arguments would be a more adequate choice [190, 231]. The comparison of the two different sets of correlations is shown in Figure 4.34.

Local values averaged over REV in fully developed regions are the only values that have a physical meaning when describing transport phenomena with VAT upper-level equations. Thus to be consistent with the VAT theory, only the local values of heat transfer closure can be used in calculations to accurately predict total heat transfer in porous media, although average values are more important for comparison with experimental data. Therefore, the closure for the air side momentum equations is,

104

$$c_{d_1} = f_{D_h} = \frac{128.2}{\mathrm{Re}_{D_h}} + 0.149 \qquad (4.104)$$

And the closure for the air side energy equation is,

$$h_1 = \frac{Nu_{D_h} k_1}{D_{h_1}} = 0.171 \mathrm{Re}_{D_h}^{0.559} \mathrm{Pr}^{1/3} \left(\frac{k_1}{D_{h_1}} \right) \qquad (4.105)$$
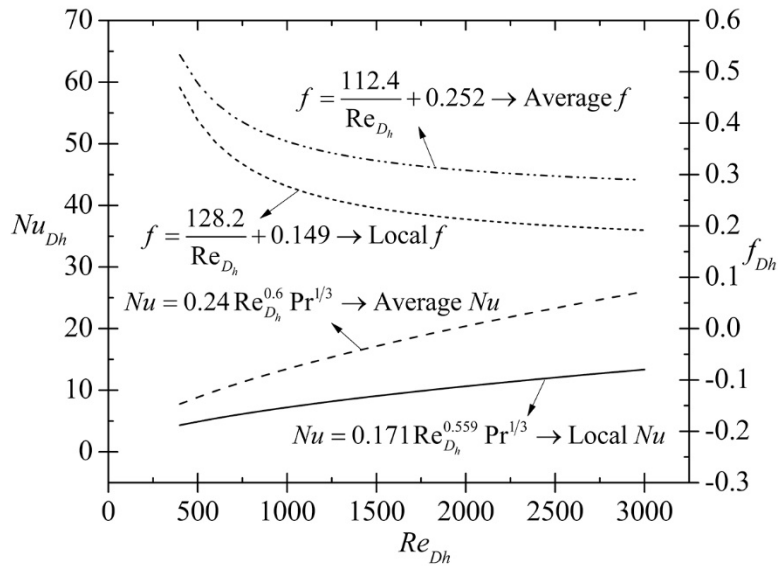
Figure 4.34: Local and average closure.

4.7.2. Distributions of Local Closures

Another interesting thing that is worth paying attention to is how the VAT based local drag resistance defined by Eq. (4.93) and the VAT based local heat transfer coefficient defined by Eq. (4.21) vary from the first REV to the last one as the flow is developing from its initial uniform entrance condition to its more fully developed state.

When the determination of the number of REVs to obtain a fully developed flow is presented in section 4.5, the local f and Nu have large values at the first REV and decrease along the direction of the flow. Also the values of the last REV are not reasonable due to the flow recirculation as it flows from the trailing edge of the fin to the extended region.

To show what the VAT based local values look like, the pointwise solution of the 6 REVs from flow entrance and all the way to its exit are selected to conduct the evaluation [232]. The local drag resistance as a function of computational domain length, x/L, is shown in Figure 4.35. It can be seen that at different Reynolds number, the drag resistance is almost constant from the second REV to the last REV but one. For conditions of flow through a periodic and symmetric geometry, the spatial flow oscillation term (fourth and fifth term in Eq. (4.93)) within a REV is calculated to be a very small number close to zero (usually a few orders of magnitude smaller than the other terms). Therefore, Eq. (4.93) can be simplified to

$$c_d = c_{dp} \frac{S_{wp}}{S_w} + c_{fL} + c_{fT} = \frac{-\int_{\partial S_w} \overline{p} d\overline{s}}{\frac{1}{2} \rho_f A_{wp} \widetilde{\overline{u}}_i^2} \frac{S_{wp}}{S_w} + \frac{\int_{\partial S_w} \tau_{wL} \cdot d\overline{s}}{\frac{1}{2} \rho_f A_w \widetilde{\overline{u}}_i^2} + \frac{\int_{\partial S_w} \tau_{wT} \cdot d\overline{s}}{\frac{1}{2} \rho_f A_w \widetilde{\overline{u}}_i^2} \qquad (4.106)$$

The high drag resistance at the first REV is because of two reasons. The first is that the flow is still developing in the first REV, which leads to a thinner boundary layer and

thus higher wall shear stress. The other reason is that before the first REV, there is a extended region which has a larger channel height than the fin region. The channel height of the extended region is F_p, while the channel height of the fin region is $F_p - \delta_f$. The channel contraction leads to some pressure drop. The drag resistance of the last REV is also relatively higher than the REVs in between due to the flow recirculation at the trailing edge of the fin.

It is shown by Eq. (4.106) that the drag resistance has two distinctive contributions: one is due to pressure and the other is due to viscous forces. The relative contributions to the total drag resistance coefficient are shown in Figure 4.36 for fin-and-tube heat exchanger. It can be seen that as Re_{Dh} increases, the drag resistance due to pressure increases. For the whole Re_{Dh} range, more than 96% of drag resistance comes from form drag and when Re_{Dh} is higer than 1000, form drag contributes 98% of the total drag resistance. Similar results were reported by Aleksander Vadnjal for flow through packed bed [190], as shown in Figure 4.37. In the present study, which focuses on turbulent flow with Reynolds number higher than 500, it is safe to say that form drag is the most dominant contributor to the total drag resistance. Considering that in the flow direction, all the REVs have the same geometric dimensions, the form drag of each REV except the first and last one should have close values. This explains why the local drag resistance coefficient remains almost constant from the second REV to the fifth REV, as shown in Figure 4.35.

The average temperatures for fluid and solid phase within different REVs are computed for a flow at Re_{Dh} =1845 and the results are shown on Figure 4.38. As expected, the average temperatures of fluid and solid are increasing from the inlet to the exit. The biggest temperature difference is at the inlet while the smallest is at the exit.
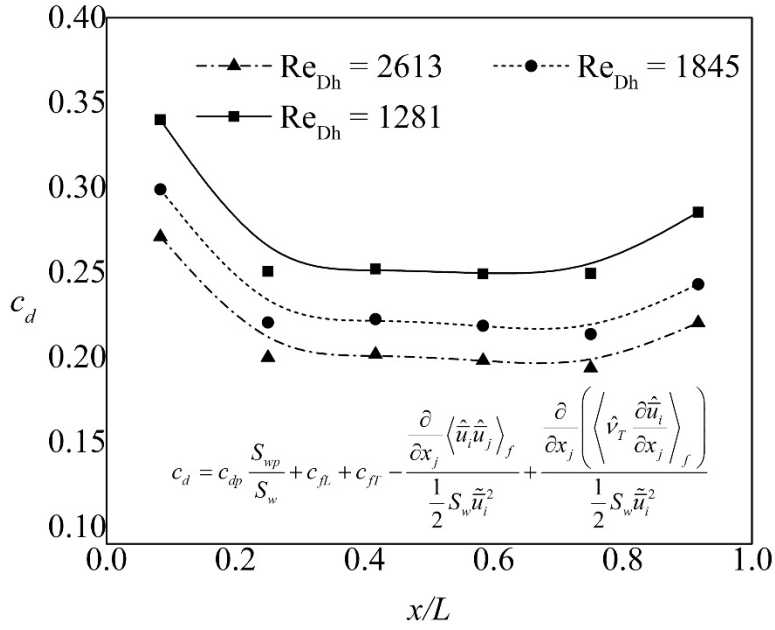
Figure 4.35: Local drag resistance at Re_{Dh} = 1281, Re_{Dh} = 1845 and Re_{Dh} = 2613.
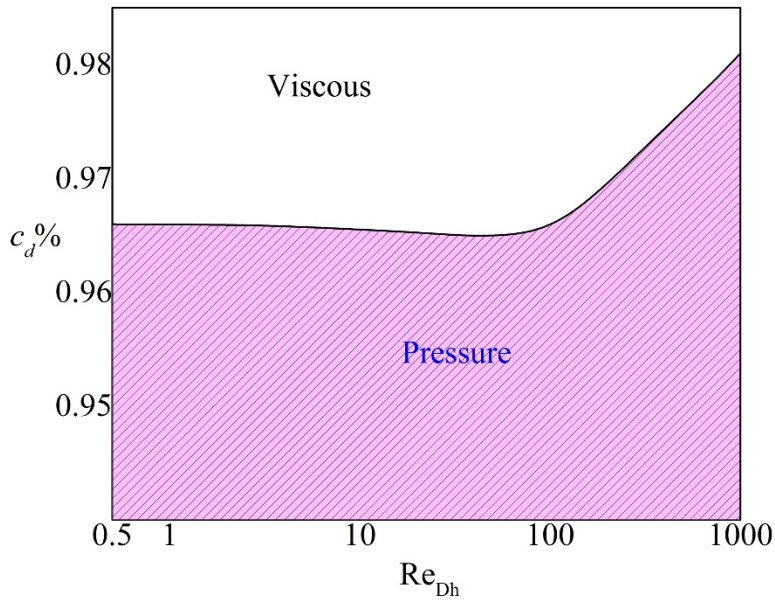
Figure 4.36: Contribution of skin friction and pressure drag to the total drag resistance for flow through fin side of a fin-and-tube heat exchanger.
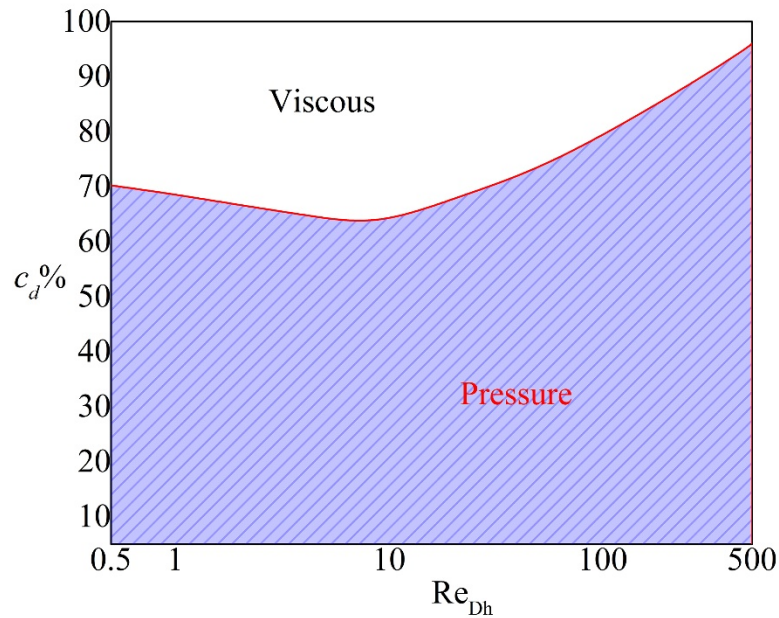
Figure 4.37: Contribution of skin friction and pressure drag to the total drag resistance for flow through packed bed. Replotted from Figure 23 in [190].

As to the local heat transfer coefficient, it would be intuitive to think that it is the largest at the entrance and that it would gradually asymptote to some value until thermally fully developed flow is reached, just as shown in Figure 4.25 in section 4.5. By computing the heat transfer coefficient over each REV at $Re_{Dh} = 1281$, $Re_{Dh} = 1845$ and $Re_{Dh} = 2613$, see Figure 4.39, it is surprising to see that the local coefficient is almost constant throughout the domain. Although h is still relatively large at the inlet where the temperature difference between solid and fluid is the largest, the difference is not as remarkable as shown in Figure 4.25 in section 4.5 and could be neglected.
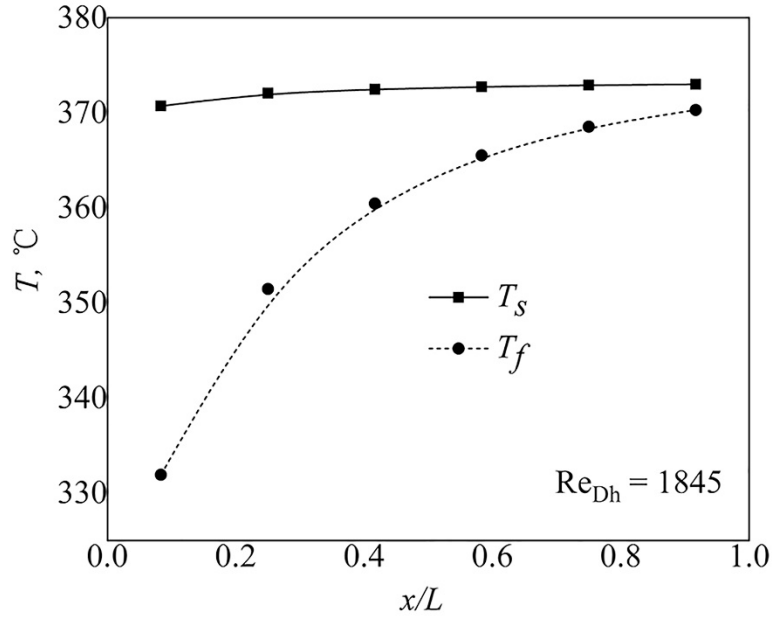
Figure 4.38: Development of averaged temperatures of fluid and solid at Re$_{Dh}$ = 1845.
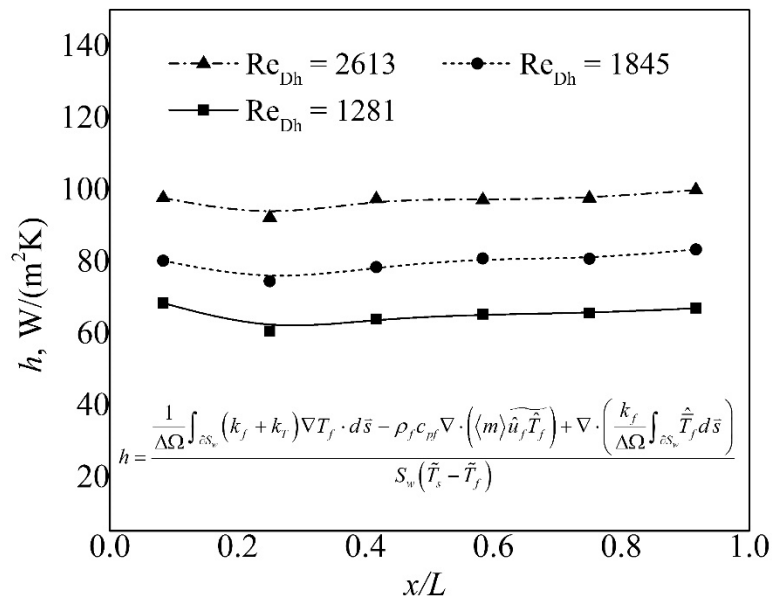
Figure 4.39: Local heat transfer coefficient, Re$_{Dh}$ = 1281, Re$_{Dh}$ = 1845 and Re$_{Dh}$ = 2613.

The reason why this is the case can be explained by analyzing the definition of the VAT based heat transfer coefficient. One can use scaling arguments to compare the magnitude of the first and third terms [190]. Assuming that the length scale within the REV is l and that the length scale over the whole REV is L, see , allows one to estimate the order of magnitude of the first term as

$$\frac{k_f}{\Delta\Omega} \int_{\partial S_w} \nabla \overline{T}_f d\overline{s} = O\left(\frac{k_f \Delta \overline{T}_f}{Ll}\right) \tag{4.107}$$

and the order of magnitude of the third term as

$$\nabla \cdot \left(\frac{k_f}{\Delta\Omega} \int_{\partial S_w} \hat{\overline{T}}_f d\overline{s}\right) = O\left(\frac{k_f \Delta \overline{T}_f}{L^2}\right) \tag{4.108}$$
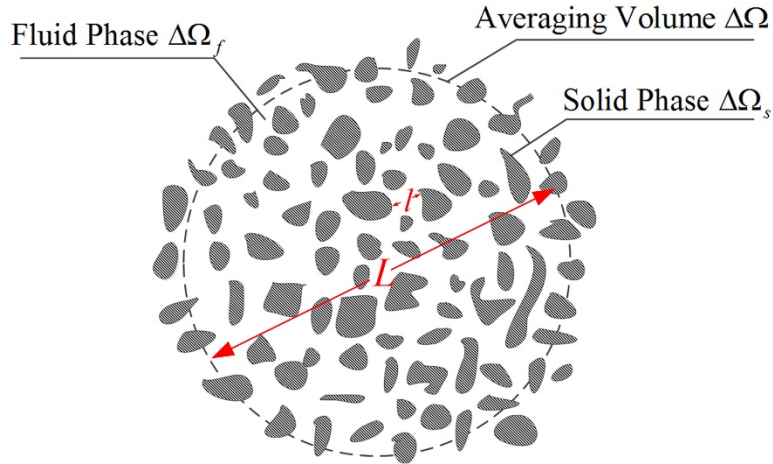
Figure 4.40: Different length scales in porous media.

Since the macro-level length scale is much larger than the micro-level length scale, $l \ll L$, it is concluded that the third term is much smaller than the first term and can therefore be ignored, yielding

$$h \approx \frac{\dfrac{1}{\Delta\Omega}\int_{\partial S_w}\left(k_f + k_T\right)\nabla\overline{T}_f \cdot d\vec{s} - \rho_f c_{pf}\nabla \cdot \left(\langle m\rangle\widetilde{\hat{\vec{u}}_f\hat{\overline{T}}_f}\right)}{S_w\left(\tilde{T}_s - \tilde{\overline{T}}_f\right)} \tag{4.109}$$

Similar to the drag resistance coefficient, for conditions of flow through a periodic and symmetric geometry, the spatial flow oscillation term in Eq. (4.109) within a REV is also calculated to be close to zero. Thus, the heat transfer coefficient is reduced to

$$h \approx \frac{\dfrac{1}{\Delta\Omega S_w}\int_{\partial S_w}\left(k_f + k_T\right)\nabla\overline{T}_f \cdot d\vec{s}}{\left(\tilde{T}_s - \tilde{\overline{T}}_f\right)} \tag{4.110}$$

greatly simplifying the scope of the problem, and indicating that the main mechanism of inter-phase heat transfer takes place on the small scale.

Inspecting Eq. (4.110), it can be seen that the reduced heat transfer coefficient has two parts, the numerator,

$$q'' = \frac{\int_{\partial S_w}\left(k_f + k_T\right)\nabla\overline{T}_f \cdot d\vec{s}}{S_w\Delta\Omega} \tag{4.111}$$

and the denominator,

$$\Delta T = \tilde{T}_s - \tilde{\overline{T}}_f \tag{4.112}$$

each representing the physics of interfacial heat transfer. The integral term represents the heat transfer across the interface. S_w is specific surface which is defined as the wetting

surface per unit volume, thus $S_w\Delta\Omega$ represents the total wetting surface per REV. Therefore the numerator actually represents the averaged surface heat flux within the REV, while the temperature difference represents its potential. Figure 4.41 shows their values and their development from the inlet to the exit with $Re_{Dh} = 1281$ and it is interesting to see that their slope is almost identical.
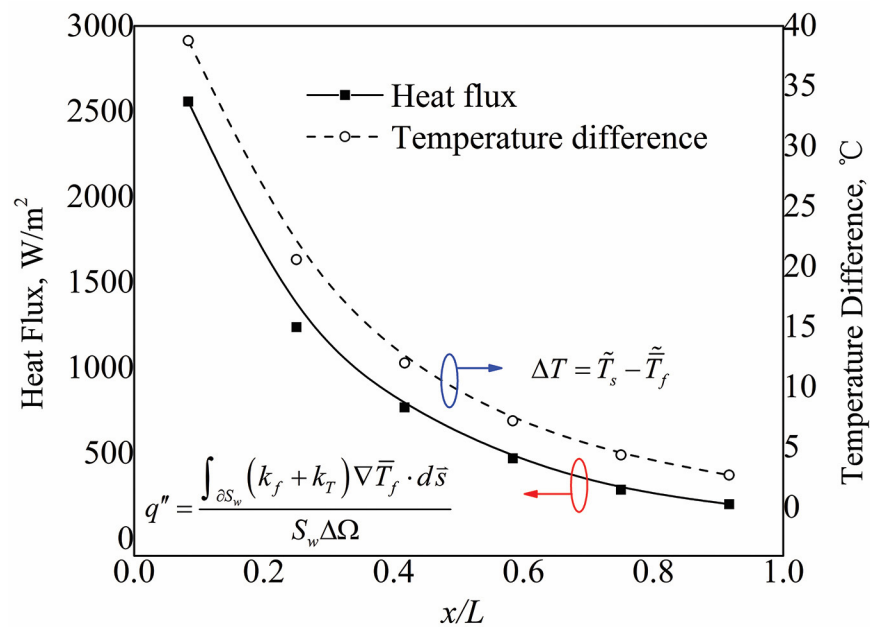
Figure 4.41: Development of the interface heat flux and temperature difference, $Re_{Dh} = 1281$.

This phenomenon was also found by Aleksander Vadnjal [190] when flow through pack of spheres at low Reynolds number ($Re_{Dh} < 500$). Therefore, in general, at the entrance the point local and average heat transfer coefficient will both be some large number and they both asymptote to corresponding numbers. For the micro scale solution obtained for the whole domain, a local point value heat transfer coefficient on a solid-fluid interface

was found to be largest at the entrance and gradually decreases as flow progresses further downstream. However, the local VAT average heat transfer coefficient is essentially independent of entrance region. This surprising result is very helpful when developing a simple model based on VAT.

4.7.3. Water-Side Closures

For closure of the water side, all the scaling factors are equal to one and the friction factor and Nusselt number correlations for fully developed flow in a pipe are applicable to close the water side VAT equations, due to the reason that the hydraulic diameter of the water side could be simplified to:

$$D_{h_2} = \frac{4 \cdot \langle m_2 \rangle}{S_{w_2}} = \frac{4 \cdot \dfrac{\pi D_i^2}{4 P_l P_t}}{\dfrac{\pi D_i}{P_l P_t}} = D_i \tag{4.40}$$

Techo et al. [233] correlated the friction factor for turbulent pipe flow as follows

$$\frac{1}{\sqrt{f}} = 1.7372 \ln \left[\frac{\mathrm{Re}_{D_h}}{1.964 \ln\left(\mathrm{Re}_{D_h}\right) - 3.8215} \right] \tag{4.113}$$

which leads to

$$c_{d_2} = \frac{1}{\left\{ 1.7372 \ln \left[\dfrac{\mathrm{Re}_{D_h}}{1.964 \ln\left(\mathrm{Re}_{D_h}\right) - 3.8215} \right] \right\}^2} \tag{4.114}$$

As for the heat transfer coefficient, h_2, Whitaker [188] showed that the experimental data of Nusselt number from a number of investigators for turbulent pipe flow is quite nicely re-correlated by the expression

114

$$Nu_2 = 0.015\,\mathrm{Re}_{D_h}^{0.83}\,\mathrm{Pr}^{0.42}(\frac{\mu_b}{\mu_0})^{0.14} = \frac{h_2 D_{h_2}}{k_2} \qquad (4.115)$$

in which, the ratio μ_b/μ_0 represents the ratio of the viscosity evaluated at the mean bulk temperature to the viscosity evaluated at the mean wall temperature. For air, the variation in the viscosity is negligible. At this point, the VAT based model of FTHXs is fully closed.

4.8. Closure for Plate Fin Heat Sink with Scales

4.8.1. Development of Elliptic Scale Roughed Surface

Before evaluating the closure terms for the channel with circular scale roughed surface developed by Chang [2], whether the heat transfer would be enhanced or decreased if the scales are elongated or squeezed is studied. Six new types of elliptic scale-roughened surfaces, which include elliptic scales with the long axis aligned parallel to the flow direction (P_t/P_l = 0.3, 0.5, 0.7) and elliptic scales with the long axis aligned perpendicularly to the flow direction (P_t/P_l = 1.43, 2, 3.33) are proposed and numerically simulated to compare with the original circular scale-roughened surface. The scale arrangement and the print shapes of the seven types of scales including the circular scale are shown in Figure 4.42 and Figure 4.43 respectively.

To get a more vivid picture of the different scales, 3D models and dimensions of them are tabulated in Table 4.6. The elliptic scale case 2, 3, 4 and 5, and the circular scale case, with four different scale depths are also simulated to show the effects of the scale depth. The objective of this work is to determine whether or not the elliptic scales can further enhance the heat transfer performance, to show how the scale depth and orientation play a

role and to unveil the mystery of heat transfer augmentation by scales, which should be helpful to the readers who are interested in heat transfer enhancement techniques.

To validate the CFD simulation results, the Reynolds number, hydraulic diameter, Nusselt number and friction factor are defined the same as that used by Chang et al.[2], see Figure 4.15. However, in the following performance evaluation, the universal VAT based length scale defined was adopted.
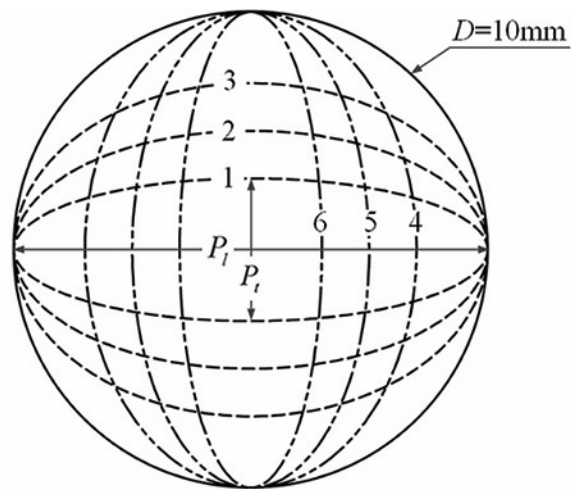
Figure 4.42: Print shapes of the elliptic scales.
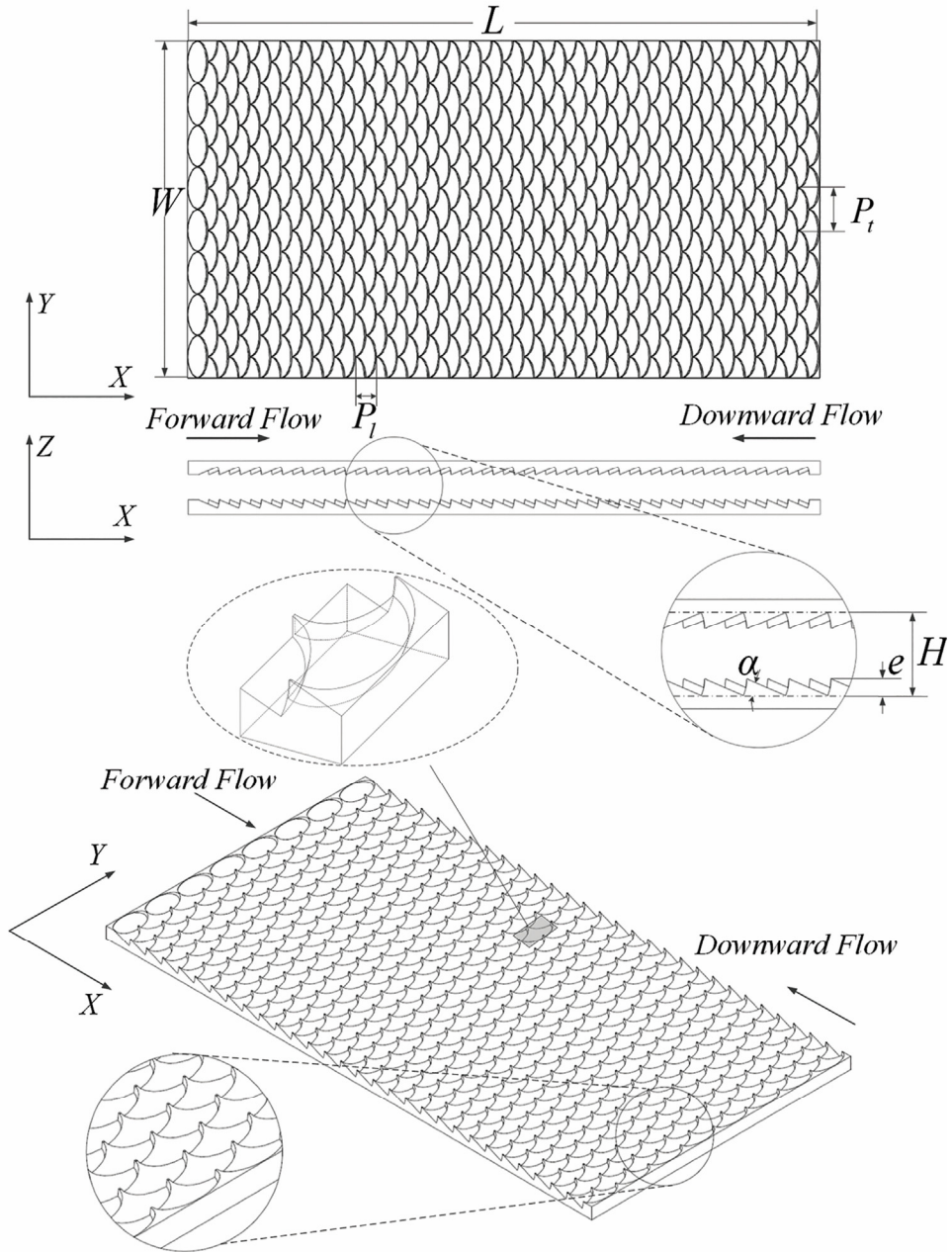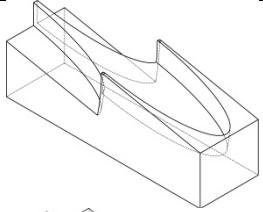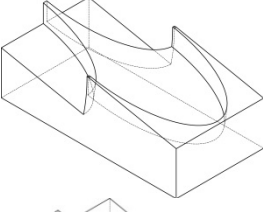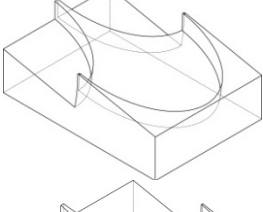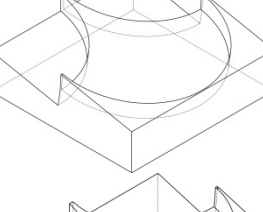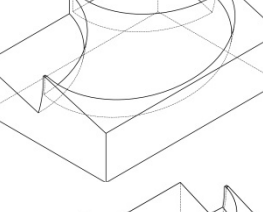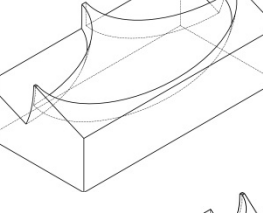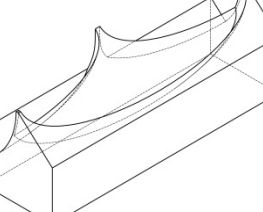
Figure 4.43: Geometrical details of one of the elliptic scale-roughened surfaces [234].

Table 4.6: The different scale shapes for the present numerical studied.

Tested Cases	3D Models	P_t, mm	P_l, mm	P_t/P_l	e, mm	α, °	H, mm
	Flow Direction						
Elliptic Scale 1		3	10	0.3	2	11.54	10
Elliptic Scale 2		5	10	0.5	1, 1.5, 2, 2.5	5.74, 8.63, 11.54, 14.48	10
Elliptic Scale 3		7	10	0.7	2	11.54	10
Circular Scale		10	10	1	1, 1.5, 2, 2.5	5.74, 8.63, 11.54, 14.48	10
Elliptic Scale 4		10	7	1.43	2	16.60	10
Elliptic Scale 5		10	5	2	1, 1.5, 2, 2.5	11.54, 17.46, 23.58, 30	10
Elliptic Scale 6		10	3	3.33	2	41.81	10

Besides the heat transfer coefficient and drag resistance coefficient defined in section 4.1, we still need a third parameter to evaluate the overall effectiveness of the heat transfer devices, which not only takes the conjugate effect into consideration and describe the physical phenomena involved in the cooling processes but also has a wide application, allowing one to compare different geometries with different fluid properties [203].

The pumping power per unit volume is

$$P_p''' = \frac{P_p}{\Omega} = \frac{\Delta p \dot{m}}{\rho \Omega} = 2 f_{D_h} \operatorname{Re}_{D_h}^3 \frac{\mu^3}{\rho^2} \frac{\langle m \rangle}{D_h^4} \tag{4.116}$$

For constant pumping power per unit volume,

$$\left(P_p''' \right)_E = \left(P_p''' \right)_\infty \tag{4.117}$$

and the relationship between friction and Reynolds number can be expressed as:

$$\left(2 f_{D_h} \operatorname{Re}_{D_h}^3 \frac{\mu^3}{\rho^2} \frac{\langle m \rangle}{D_h^4} \right)_E = \left(2 f_{D_h} \operatorname{Re}_{D_h}^3 \frac{\mu^3}{\rho^2} \frac{\langle m \rangle}{D_h^4} \right)_\infty \tag{4.118}$$

It should be noted that, for smooth channel, $D_h = 2H$, which is the same as traditional length scale used for parallel channel. Therefore, in the following presentation, the subscript D_h will be omitted for reference parameters. From Eq.(4.118), we get

$$\operatorname{Re}_\infty = \operatorname{Re}_{D_h} \left(\frac{f_{D_h}}{f_\infty} \right)^{1/3} \left(\frac{\langle m \rangle}{\langle m \rangle_\infty} \right)^{1/3} \left(\frac{D_{h\infty}}{D_h} \right)^{4/3} \frac{\mu}{\mu_\infty} \left(\frac{\rho_\infty}{\rho} \right)^{2/3} \tag{4.119}$$

The thermal enhancement factor, η_{eff}, is defined as the ratio of the heat transfer coefficient, h of an augmented surface to that of a smooth surface, h_∞, at a constant pumping power;

$$\eta_{eff} = \frac{q/\Delta T}{\left(q/\Delta T\right)_{\infty}}\bigg|_{P_p} = \frac{h}{h_{\infty}}\bigg|_{P_p} = \frac{Nu_{D_h} D_{h\infty} k}{Nu_{\infty} D_h k_{\infty}}\bigg|_{P_p}$$

$$= \frac{Nu_{D_h} D_{h\infty}}{Nu_{\infty} D_h}\left(\frac{f_{D_h}}{f_{\infty}}\right)^{-1/3}\left(\frac{\langle m\rangle}{\langle m\rangle_{\infty}}\right)^{-1/3}\left(\frac{D_{h\infty}}{D_h}\right)^{-4/3}\left(\frac{k}{k_{\infty}}\right)\left(\frac{\mu_{\infty}}{\mu}\right)\left(\frac{\rho_{\infty}}{\rho}\right)^{-2/3} \tag{4.120}$$

Simplify Eq.(4.120), we get

$$\eta_{eff} = \frac{Nu_{D_h}}{Nu_{\infty}}\left(\frac{f_{D_h}}{f_{\infty}}\right)^{-1/3}\left(\frac{\langle m\rangle}{\langle m\rangle_{\infty}}\right)^{-1/3}\left(\frac{D_{h\infty}}{D_h}\right)^{-1/3}\left(\frac{k}{k_{\infty}}\right)\left(\frac{\mu_{\infty}}{\mu}\right)\left(\frac{\rho_{\infty}}{\rho}\right)^{-2/3} \tag{4.121}$$

The effectiveness factor defined by Eq. (4.121) gives more information about the characteristics of the heat transfer devices and is not limited to the same fluid when reporting data. The last 3 terms in Eq. (4.121) could be eliminated when the fluids for the comparative reference case and the enhanced channels are the same and have equivalent properties. For the present study, Eq. (4.121) could be further simplified to

$$\eta_{eff} = \frac{Nu_{D_h}}{Nu_{\infty}}\left(\frac{f_{D_h}}{f_{\infty}}\right)^{-1/3}\left(\frac{\langle m\rangle}{\langle m\rangle_{\infty}}\right)^{-1/3}\left(\frac{D_{h\infty}}{D_h}\right)^{-1/3} \tag{4.122}$$

In which Nu_{∞} and f_{∞} are Dittus–Boelter correlation and Blasius equation for turbulent flow,

$$Nu_{\infty} = 0.023\,\mathrm{Re}^{0.8}\,\mathrm{Pr}^{0.4} \tag{4.123}$$

$$f_{\infty} = 0.079\,\mathrm{Re}^{-0.25} \tag{4.124}$$

The comparisons of flow and heat transfer characteristics of the different scale roughened channels, in terms of Nusselt number and pressure drop, are plotted in Figure 4.44 and Figure 4.45.

From Figure 4.44, it is clear that the elliptic scales with the long axis aligned perpendicularly to the flow direction offer a surprisingly high Nusselt number. The channel with the scale pitch ratio of $P_t/P_l = 1.43$ provides more than a 22% increase in the Nusselt number compared with the circular scale-roughened channel, and if further increase the ratio of scale pitches P_t/P_l to 2, another 17% increment is seen (about 40% over circular scale case in total). It should be noted that since a different length scale is used in the present work, the Nusselt number ratio between the elliptic scale-roughened and smooth channel flows (Nu_{Dh}/Nu_∞) is around 3.1. However, if the same length scale was used as Chang et al. [2], the ratio, Nu/Nu_∞, would be around 6.5 for this case, compared with $Nu/Nu_\infty \approx 4.5$ reported by Chang [2] for circular scale-roughened surface. If we increase the scales to a pitch ratio of 3.33, no significant difference is seen. As to the elliptic scales with the long axis aligned parallel to the flow direction, all the three numerically tested cases with P_t/P_l from 0.3 to 0.7 showed worse performance than circular scale case. The $P_t/P_l = 0.7$ case shows a 21% decrement while a 40% decrease is seen when P_t/P_l decreases to 0.5. If we further elongate the scales in the flow direction, no sharp deterioration is seen, which is similar to the increasing trend when we squeeze the scales. Based on the above analysis, it seems that the range of scale pitch ratio that has a prominent effect on the heat transfer augmentation is $0.5 \leq P_t/P_l \leq 2$.
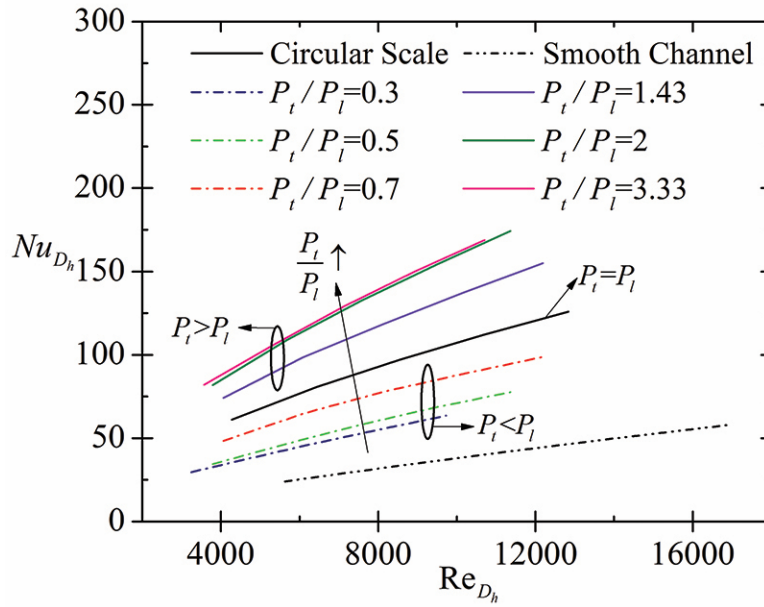
Figure 4.44: Nusselt number VS. Reynolds number.
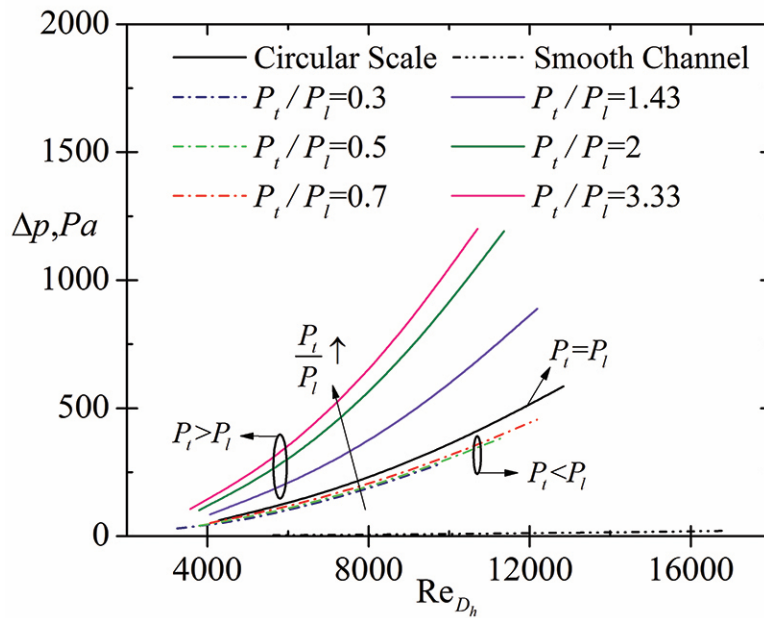
Figure 4.45: Δp VS. Reynolds number.

Comparisons of pressure drop are presented in Figure 4.45. Since heat transfer enhancement is usually accompanied by a high pressure penalty, it is not surprising that the pressure drop increases as the scale pitch ratio, P_t/P_l, increases. The elliptic scales with $P_t/P_l = 2$ and 1.43 have around 70% and 40% higher pressure drop than the circular scales respectively at lower Reynolds number. As Reynolds number increases, the percentage of pressure drop increment further increases, comparing with an almost linear increasing trend of Nusselt number with Reynolds number. Therefore, the overall efficiency of the scale roughened channel is expected to decrease as the Reynolds number increases. For the elliptic scales with $P_t/P_l < 1$ the pressure drop could be as much as 75% lower than the circular scales, which is not unexpected considering their poorer heat transfer performance. Similar to the Nusselt number, the effect of the scale pitch ratio on pressure drop concentrates mainly in the range of $0.5 \leq P_t/P_l \leq 2$. This provides a rough idea for engineers who are interested in using elliptic scale-roughened surfaces for heat transfer enhancement purposes.
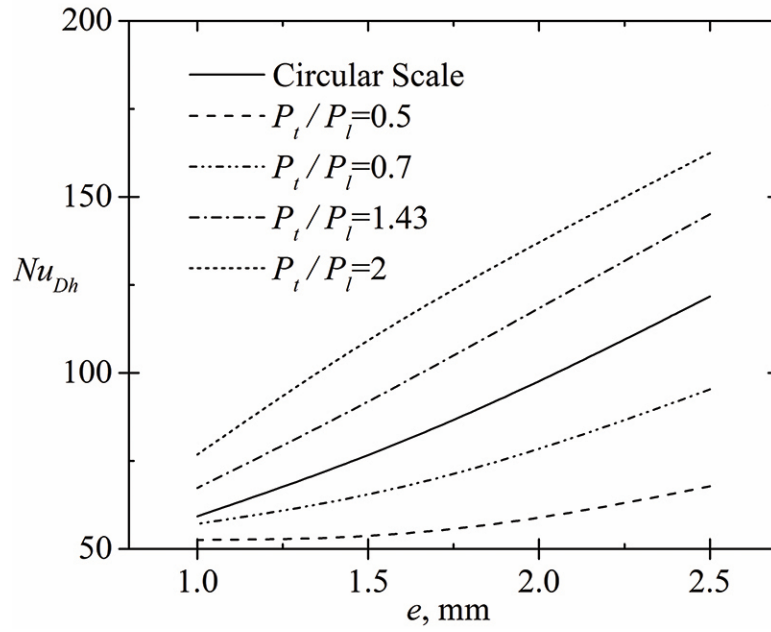
Figure 4.46: Nusselt number VS. scale height, $Re_{Dh} = 10000$.
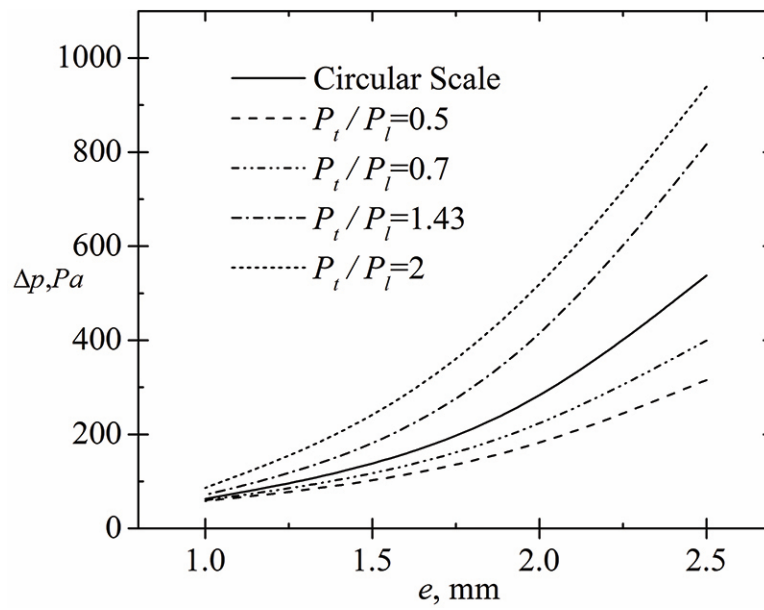
Figure 4.47: Pressure drop VS. scale height, $Re_{Dh} = 10000$.

The effects of scale height on the heat transfer enhancement and pressure penalty of scale-roughened surfaces with Reynolds number being at 10,000 are shown in Figure 4.46 and Figure 4.47, taking the circular scale case and elliptic scale cases with P_t/P_l = 0.5, 0.7, 1.43 and 2 as an example. As the scale height increases, more solid roughness penetrates into the near wall flow, forcing the fluid to divert and mix with the bulk channel flow. Therefore, higher Nusselt number and form drag are expected. It should be noted that the depth of the scale cannot be increased unboundedly since it is limited by the longitudinal pitch of the scale which is the theoretical maximum of the depth (with attack angle α = $\pi/2$). Also, for a specific scale longitudinal pitch, a large scale depth means a large scale attack angle which would be more difficult to fabricate. Besides, the scale depth cannot be larger than half the thickness of the fins, supposing one would like to apply this technique to heat transfer devices with fins.

Figure 4.44 ~ Figure 4.47 compare the channels with different scale pitch ratios and scale heights regarding heat transfer enhancement and pressure drop increment separately. However, increasing Nusselt number is accompanied by increasing pressure drop which is undesirable. Thus, based only on Figure 4.44 ~ Figure 4.47, it is almost impossible to come to a final conclusion as to which type of channels performs better than the others if both the heat transfer enhancement and power consumption are considered simultaneously. Therefore, a comprehensive performance comparison should be made to evaluate the effectiveness of different types of channels, see Figure 4.48.

It is found that all the elliptic scale-roughened channels with $P_t > P_l$ as well as circular scale case have higher effectiveness factor than 1 in the present Reynolds number region. Compared with the circular scale-roughened channel, the elliptic scale cases with P_t/P_l =

2 and $P_t/P_l = 1.43$ shows 11% and 7% enhancements respectively. Further increasing the pitch ratio P_t/P_l to 3.33 decreases the effectiveness factor to almost the same as circular scale case. On the other hand, the elliptic scale cases with $P_t/P_l < 1$ have no advantage compared with the circular scale-roughened channel. The two cases with P_t/P_l smaller than 0.5 even have a η_{eff} lower than 1. Therefore, it is obvious that the elliptic scale-roughened surface with the long axis aligned perpendicularly to the flow direction shows a considerable potential to further enhance the heat transfer performance while the channels with the long axis aligned parallel to the flow direction don't outperform the circular scale-roughened channels.
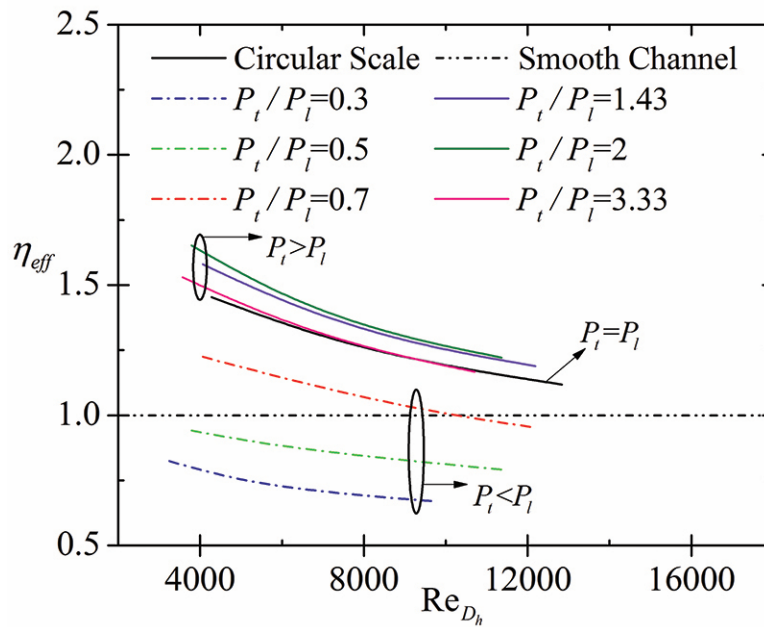
Figure 4.48: Effectiveness factor vs. Reynolds number.

Another thing that should be noted is that the effectiveness factors of all types of scale-roughened surfaces decrease with increasing Reynolds number, as expected from observations obtained when the Nusselt number and pressure drop were analyzed separately.

To have a qualitative view into the flow behavior, Figure 4.49 provides insight into the local distributions of the streamlines on three cross-sections in the y-z planes normal to the flow direction at Re=10000 for elongated scale-roughened (P_t/P_l =0.5) and squeezed scale-roughened (P_t/P_l = 2) channels, respectively. The three planes are located at the inlet, the center plane and outlet of the 11th and 21st REV for elongated scale and squeezed scale respectively, showing how the streamlines develop when the fluid flows through one cycle of the elliptic scale-roughened channels. For elongated scale case, it is found that when the flow starts entering the REV, some cone-shaped streamlines are formed above the scales. After that the flow starts spinning in the spanwise direction. As the fluid flows farther downward, the spinning becomes stronger. Different from the elongated scale case, no cone-shaped streamlines are seen for the squeezed scale-roughened channel. Instead, more intense rotation is found all the way from the leading edge to the trailing edge of the scale. The strong spinning of the flow breaks the near wall boundary layers continuously and enhances the bulk flow mixing. It is easy for one to turn the plane streamlines into 3D footage in mind and imagine how the flow is marching in a spiral pattern. This explains why the heat transfer is augmented by the elliptic scale-roughened surface and why squeezed scale-roughened channels have better heat transfer performance than elongated scale-roughened channels.
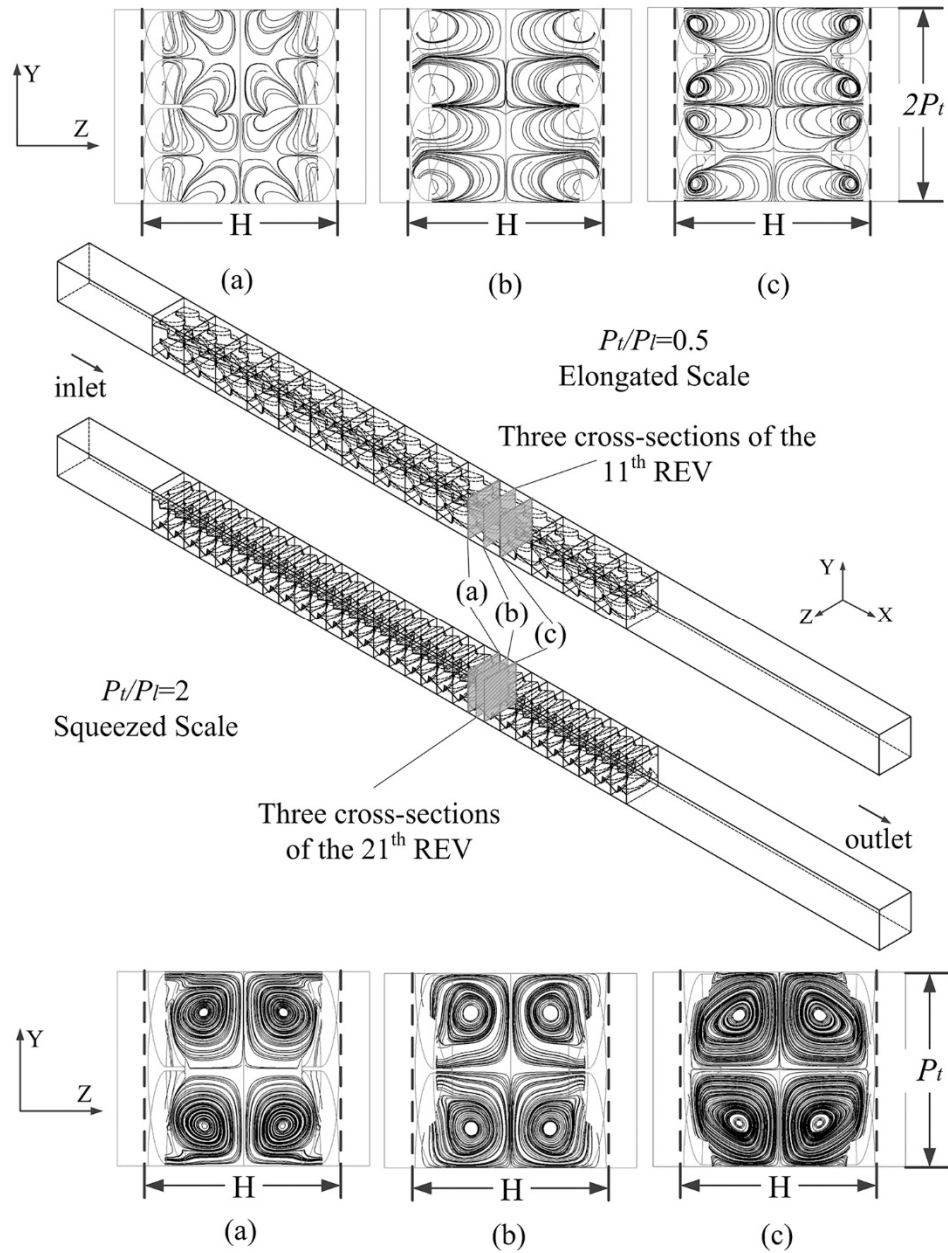
Figure 4.49: Streamlines on the planes normal to flow direction, Re=10000.

Based on the results of the present study, the following conclusions can be drawn.

1. The pitch ratio, depth and orientation of scales affect the flow and heat transfer characteristics of the channels significantly.

2. Generally, the elliptic scales with $P_t > P_l$ enhance the heat transfer performance, while the elongated scales with $P_t < P_l$ have lower Nusselt numbers and pressure drops compared to the circular scale-roughened channels.

3. The range of scale pitch ratio that has a prominent effect on the heat transfer augmentation and pressure drop is $0.5 \leq P_t/P_l \leq 2$.

4. Both the Nusselt number and pressure drop penalty are enhanced as the scale depth increases.

5. Flow through the scale-roughened channels is strongly rotated in the spanwise direction by the scale-shaped roughness. Bulk flow mixing is enhanced by the spirally marching flow.

6. Nusselt number ratios between the squeezed scale-roughened and smooth channel flows (Nu/Nu_∞) could be enhanced to around 6.5, which is a 40% improvement compared to the circular scale-roughened channels.

4.8.2. Closure for Elliptic Scale Roughed Channels

Considering the potential heat transfer enhancement by varying the axis ratio of the scales, two more parameters, namely scale longitudinal pitch P_l and transverse pitch P_t, are taken into consideration when the closure is obtained. To make the closure correlations applicable to relatively wide range of dimensions of scale roughened channels, 112 different sets of design dimensions, see Table 4.7, were simulated at different Reynolds numbers, ranging from 3×10^2 to 8×10^4. The scale pitch ratio, P_t/P_l, and the ratio of the

129

scale height to the scale longitudinal pitch, e/P_l, or the angle of attack, $\alpha = \arcsin\left(e/P_l\right)$, define the shape of the scales. The ratio of the channel height to the scale longitudinal pitch, H/P_l, specifies the shape of the channel. Therefore, P_t/P_l, e/P_l and H/P_l could specify the shape of the REV. The REVs, which have the same P_t/P_l, e/P_l and H/P_l but different scale longitudinal pitch, are dynamically similar, and they are governed by the same physical laws and associated equations, which produce exactly the same solution in terms of dimensionless variables, such as Nu and f, at the same Re. Therefore, P_t/P_l, e/P_l and H/P_l are selected to be the design parameters. However, since D_h is a function of e, P_t, P_l and H, and D_h is the chosen length scale, the heat transfer and friction closure relationships were correlated in terms of e/D_h, H/D_h, etc., using a multiple regression technique [186].

The resulting Nusselt number correlation is

$$Nu_{D_h} = \frac{hD_h}{k_f} = \left\{ 0.144\,\mathrm{Re}_{D_h}^{0.765} \left[\left(\frac{e}{D_h}\right)^{0.695} + 0.457 \right] \left(\frac{H}{D_h}\right)^{1.018} + 8.235 \right\} \left(\frac{P_t}{P_l}\right)^{S_1}$$

$$S_1 = \left(\frac{e}{D_h}\right)^{0.539}$$

(4.125)

The resulting friction factor is in the form

$$f_{D_h} = \left[\frac{94.53}{\mathrm{Re}_{D_h}} + 0.0019\,\mathrm{Re}_{D_h}^{0.217} + 3.544 \left(\frac{e}{D_h}\right)^{1.465} \left(\frac{H}{D_h}\right)^{0.0232} \right] \left(\frac{P_t}{P_l}\right)^{S_2}$$

$$S_2 = \left(-\frac{129.28}{\mathrm{Re}_{D_h}} + 2.74 \right) \left(\frac{e}{D_h}\right)^{0.771}$$

(4.126)

Therefore the left two closures for the energy and momentum equations are

$$h = \frac{Nu_{D_h} k_f}{D_h}, \; c_d = f_{D_h}$$

(4.127)

Table 4.7: Dimensions of the numerically tested models.
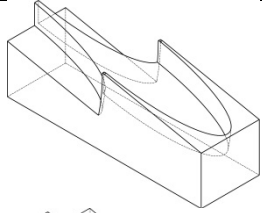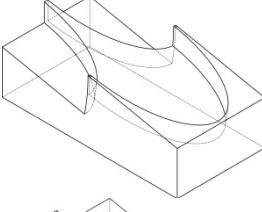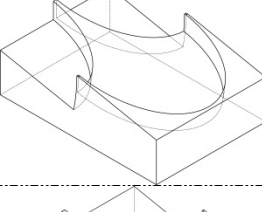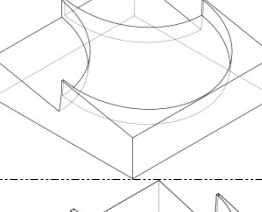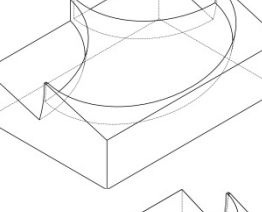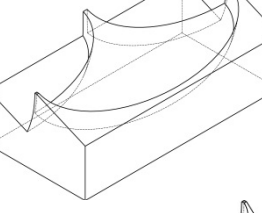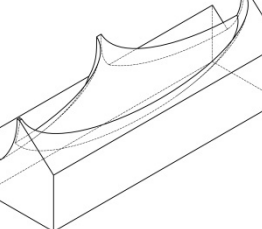
Tested Models	Scale Shape ↘ Flow Direction	P_t / P_l	e / P_l	H / P_l
Elongated Scale Type 1 Model 1~16		0.3	0.1, 0.15, 0.2, 0.25	0.75, 1.25, 1.75, 2.25
Elongated Scale Type 2 Model 17~32		0.5	0.1, 0.15, 0.2, 0.25	0.75, 1.25, 1.75, 2.25
Elongated Scale Type 3 Model 33~48		0.7	0.1, 0.15, 0.2, 0.25	0.75, 1.25, 1.75, 2.25
Circular Scale Model 49~64		1	0.1, 0.15, 0.2, 0.25	0.75, 1.25, 1.75, 2.25
Squeezed Scale Type 1 Model 65~80		1.43	0.14, 0.21, 0.29, 0.36	1.1, 1.8, 2.5, 3.2
Squeezed Scale Type 2 Model 81~96		2	0.2, 0.3, 0.4, 0.5	1.5, 2.5, 3.5, 4.5
Squeezed Scale Type 3 Model 97~112		3.33	0.33, 0.5, 0.67, 0.83	2.5, 4.2, 5.8, 7.5

Figure 4.50 and Figure 4.51 show the comparison between the numerical simulation results and the results predicted by the proposed correlations. The proposed heat transfer correlation, Eq.(4.125), can describe all the simulation results within a deviation of 20% and 91% of them within 15%. The correlation of friction factor, Eqs.(4.126), also can predict all of them within a deviation of 20%. The correlations of Nusselt number and friction factor have an average deviation of 7.5% and 10%, respectively.

It should be noted that the present correlations are not only applicable to elliptic scale-roughened channels but also converge to those for smooth channels when $e = 0$. From the definition of D_h, Eq. (4.41), it is known that $D_h = 2H$ as e becomes zero and the proposed correlations converge to

$$Nu_{D_h} = 0.0325 \, Re_{D_h}^{0.765} + 8.235 \tag{4.128}$$

and

$$f_{D_h} = \frac{94.53}{Re_{D_h}} + 0.0019 \, Re_{D_h}^{0.217} \tag{4.129}$$

Besides, Eqs. (4.125) and (4.126) are reduced to the correlations for circular scale-roughened channels if $P_t = P_l$. To validate the predictive capability of the present correlations, the results predicted by Eqs. (4.125) and (4.126) for different P_t/P_l with scale height of 2mm are compared with the rescaled experimental data by Chang et al. [2] as shown in Figure 4.52 and Figure 4.53, see section 4.3 on how to rescale available experimental data using the VAT suggested length scale. Both Figure 4.52 and Figure 4.53 show that the rescaled experimental data by Chang et al. [2] and the proposed correlations agree very well.

132

$$S_1 = \left(\frac{e}{D_h}\right)^{0.539}$$

$$Nu_{D_h} = \left\{0.144\,\mathrm{Re}_{D_h}^{0.765}\left[\left(\frac{e}{D_h}\right)^{0.695} + 0.457\right]\left(\frac{H}{D_h}\right)^{1.018} + 8.235\right\}\left(\frac{P_t}{P_l}\right)^{S_1}$$
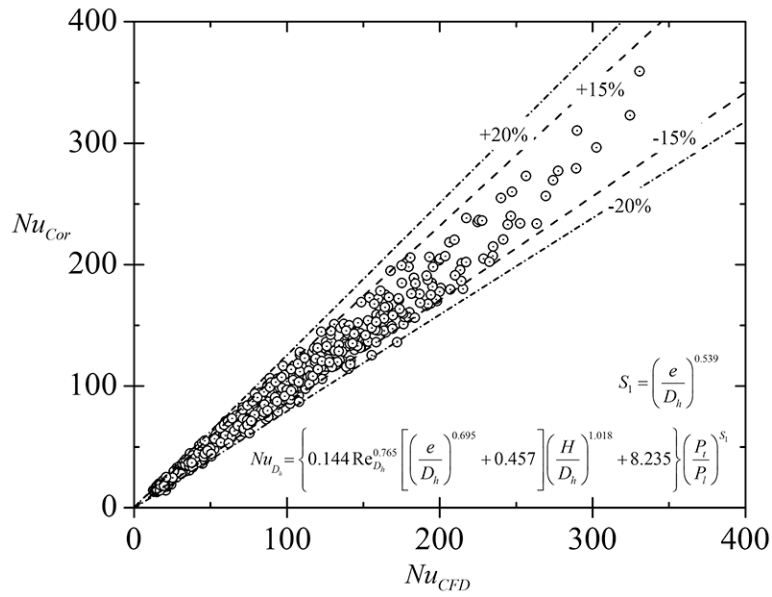
Figure 4.50: Deviation of the proposed Nusselt number correlation.

$$S_2 = \left(-\frac{129.28}{\mathrm{Re}_{D_h}} + 2.74\right)\left(\frac{e}{D_h}\right)^{0.771}$$

$$f_{D_h} = \left[\frac{94.53}{\mathrm{Re}_{D_h}} + 0.0019\,\mathrm{Re}_{D_h}^{0.217} + 3.544\left(\frac{e}{D_h}\right)^{1.465}\left(\frac{H}{D_h}\right)^{0.0232}\right]\left(\frac{P_t}{P_l}\right)^{S_2}$$
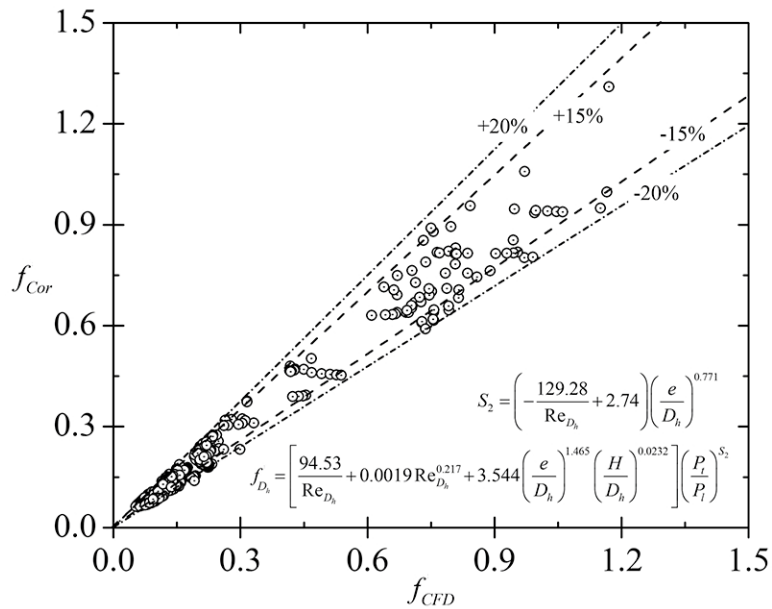
Figure 4.51: Deviation of the proposed friction factor correlation.

133

$$Nu_{Dh} = \left\{ 0.144\,Re_{D_h}^{0.765} \left[\left(\frac{e}{D_h} \right)^{0.695} + 0.457 \right] \left(\frac{H}{D_h} \right)^{1.018} + 8.235 \right\} \left(\frac{P_t}{P_l} \right)^{S_1}$$

$$S_1 = \left(\frac{e}{D_h} \right)^{0.539}$$

$P_t/P_l \uparrow$

▼ Rescaled Experimental Data by Chang
----- $P_t/P_l = 0.5$ ——— $P_t/P_l = 1$
-·-·- $P_t/P_l = 1.43$ ——— $P_t/P_l = 2$
——— $e = 0$ ——— $Nu = 8.235$
········ Dittus-Boelter Equation
----- Sieder-Tate Equation
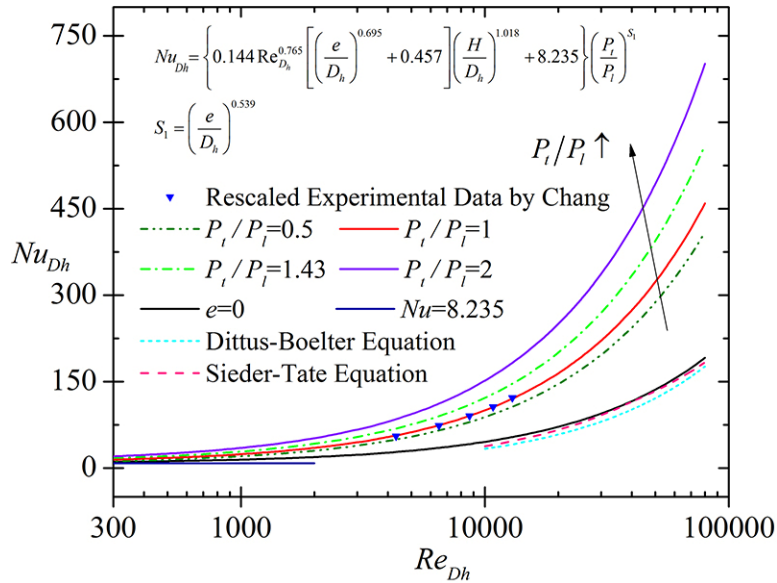
Figure 4.52: Comparison of the present Nusselt number correlation and rescaled experimental data, and some well-known correlations for smooth channel.

▼ Rescaled Experimental Data by Chang
-·-·- $P_t/P_l = 0.5$ ——— $P_t/P_l = 1$ -·-·- $P_t/P_l = 1.43$
——— $P_t/P_l = 2$ ——— $e = 0$ ----- $f = 96/Re_{Dh}$
-··-··- Beaver Equation

$P_t/P_l \uparrow$

$$f_{D_h} = \left[\frac{94.53}{Re_{D_h}} + 0.0019\,Re_{D_h}^{0.217} + 3.544 \left(\frac{e}{D_h} \right)^{1.465} \left(\frac{H}{D_h} \right)^{0.0232} \right] \left(\frac{P_t}{P_l} \right)^{S_2}$$

$$S_2 = \left(-\frac{129.28}{Re_{D_h}} + 2.74 \right) \left(\frac{e}{D_h} \right)^{0.771}$$
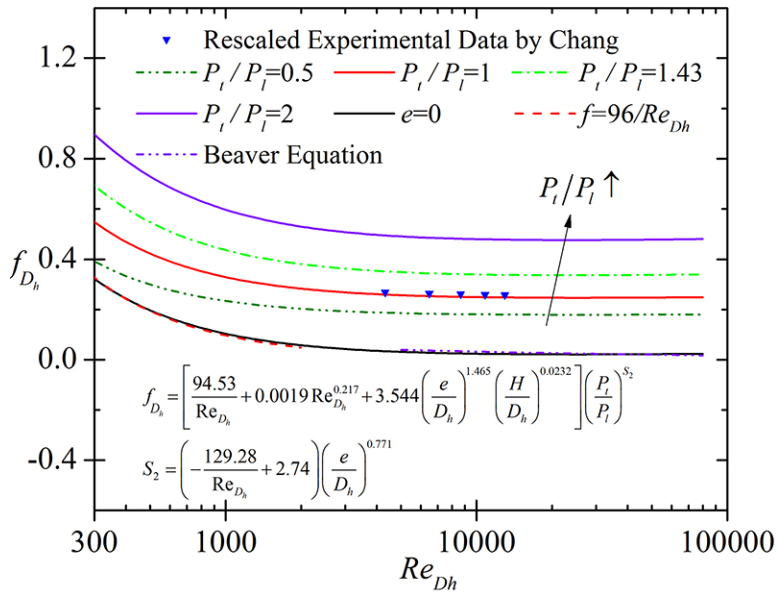
Figure 4.53: Comparison of the present friction factor correlation and rescaled experimental data, and some well-known correlations for smooth channel.

To further check whether our correlations converged to smooth channel when $e = 0$, a few well known correlations for smooth channels are brought into the comparison. It is shown in Figure 4.52 that the converged Nu correlation, Eq. (4.125), for smooth parallel plate channel can predict the Nusselt number with an average deviation of 4.0% from the correlation proposed by Sieder and Tate [235] and around 12% above Dittus-Boelter equation [236] for turbulent flow. Also, when Reynolds is decreased, the Nusselt number converges to the analytical solution for laminar flow through parallel plate ducts with uniform heat flux at two walls, which is $Nu = 8.235$. From Figure 4.53, it is seen that the converged friction factor correlation, Eq.(4.126), almost coincides with the analytical solution for laminar flow through parallel plate ducts, which is $f = 96/Re_{Dh}$, and the correlation by Beavers et al. [237] for turbulent flow. At this point, the VAT based governing equations for plate fin heat sinks with elliptic scales are closed.

4.9. Conclusions and Guidelines to Obtain Closures Using CFD

Volume Averaging Theory is little more than a judicious application of Green's and Stokes' theorems to carry out the integration needed to average the point-wise conservation equations in a rigorous way. By treating the closure part of the problem carefully, the result remains rigorous in spite of its simplicity. Many everyday engineered devices are hierarchical and heterogeneous and can be effectively treated by application of VAT. It is an approach that can be applied to many different types of transport phenomena, see Travkin and Catton [4], only with the closure terms need to be looked into for the specific morphologies.

The present chapter describes an effort to obtain the closure for VAT based governing equations by CFD evaluation, which could be summarized into the following guidelines.

Step 1: Select the representative elementary volume correctly. In the case of periodic media, one can simply choose a periodic unit cell (which, however, may be non-unique), but in random media, the situation is much more complicated. Refer to Whitaker [16] for more details about the criterion of the selection of an REV for random media.

Step 2: Define the length scale. In the present study, the length scale defined by Travkin and Catton [4] is adopted, however, this length scale is not unique, i.e. Whitaker [188] developed a proper characteristic length (differing from our choice by a constant) to collapse experimental data into a single correlation which satisfactorily predicts heat transfer rates in randomly packed beds and staggered tube bundles.

Step 3: Select a proper numerical method according to the flow condition, i.e. laminar or turbulent. If the flow is laminar, then the closures would be simplified since some terms related to turbulence flow would disappear.

Step 4: Discretize the computational domain carefully. Grid independency test should be done by recursive refinement. Predicted results should be validated by comparing with experimental data.

Step 5: Determine the number of REVs needed to obtain a reasonable fully developed local values. Increase the number of REVs gradually until fully developed flow and heat transfer are reached.

Step 6: Conduct CFD simulations. Select the parameters which define the geometry of the REV and determine the range of these parameters. Conduct CFD simulations for different combination of these selected design variables.

Step 7: Extract the macroscopic hydrodynamic and thermal characteristics from the microscopic results by evaluating the closures over the REV. Refer to Section 4.6 for the closure evaluation procedure.

Step 8: Collect the evaluated results for friction factor and heat transfer coefficient and develop the corresponding correlations.

The closures can be obtained by following the above eight steps. It should be pointed out that these correlations are not necessarily the most accurate available, however, they have wide application, are easy to use, and are quite satisfactory for most design calculations [188]. Also, for optimization, extreme accuracy is not vital because variation in the parameter being optimized can be as much as an order of magnitude.

With closure in terms of the friction factor and the heat transfer coefficient, the problem is closed and the porous media governing equations derived from VAT are functions only of porous media morphology, represented by porosity and specific surface area, and its closure. With the closure correlations, the governing equation set is relatively simple and can be solved discretely in seconds. With the help of a statistical tool for Design of Experiments (DOE) or Genetic Algorithm (GA), a heat exchanger could be designed and optimized in an hour, instead of days of CFD or experimental work.

5. Application of VAT to Heat Exchangers

In this chapter, the VAT based modelling method is applied to fin-and-tube heat exchangers and plate fin heat sinks with elliptic scale roughed surfaces. Together with the closures developed in Chapter 4, the upper level VAT governing equations are closed and finite difference method is adopted to discretize and solve the equations, leading to a fast-running solver. The VAT based solver is then combined with some optimization subroutine to pursue the optimum.

In Chapter 3, the thermal physics and fluid mechanics governing equations in heterogeneous porous media were developed from the Navier-Stokes equation and the thermal energy equations based on rigorous averaging techniques developed by Whitaker [16] who focused on solving linear diffusion problems and by Travkin and Catton [4, 19] who focused on solving nonlinear turbulent diffusion problems. This is the starting point for studying flow and heat transfer in porous media and also the basis of the present work.

5.1. Application to Fin-and-Tube Heat Exchangers

5.1.1. VAT Based Modeling

In this section, a model based on Volume Averaging Theory is developed to describe transport phenomena in fin-and-tube heat exchangers. The air flow and water flow are considered as 'porous flow', in which the term 'porous' is used in a broad sense.

The momentum equation for the air side is

$$-\frac{1}{\rho_1}\frac{\partial \langle \bar{p}_1 \rangle_f}{\partial x} + \frac{\partial}{\partial z}\left(\langle m_1 \rangle \left(\tilde{v}_{T_1} + v_1 \right) \frac{\partial \tilde{\bar{u}}_1}{\partial z} \right) + c_{d_1} S_{w_1} \frac{\tilde{\bar{u}}_1^2}{2} = 0 \qquad (5.1)$$

and for the water side is

$$-\frac{1}{\rho_2}\frac{\partial\langle\overline{P}_2\rangle_f}{\partial z}+\frac{\partial}{\partial x}\left(\langle m_2\rangle\left(\tilde{v}_{T_2}+v_2\right)\frac{\partial\tilde{\overline{w}}_2}{\partial x}\right)+c_{d_2}S_{w_2}\frac{\tilde{\overline{w}}_2^2}{2}=0 \qquad (5.2)$$

Because we are dealing with a conjugate type of problem, the thermal energy equations for both the solid and fluid states are required. For the air side, the VAT based energy equation is

$$\langle m_1\rangle\rho_1\tilde{\overline{u}}_1 c_{p_1}\frac{\partial\tilde{\overline{T}}_1}{\partial x}=h_1 S_{w_1}\left(\tilde{T}_s-\tilde{\overline{T}}_1\right) \qquad (5.3)$$

and for the water side is

$$\langle m_2\rangle\rho_2\tilde{\overline{w}}_2 c_{p_2}\frac{\partial\tilde{\overline{T}}_2}{\partial z}=h_2 S_{w_2}\left(\tilde{T}_s-\tilde{\overline{T}}_2\right) \qquad (5.4)$$

For the solid phase, the VAT based energy equation is

$$\frac{\partial}{\partial x}\left[\left(1-\langle m_1\rangle-\langle m_2\rangle\right)k_s\frac{\partial\tilde{T}_s}{\partial x}\right]+\frac{\partial}{\partial z}\left[\left(1-\langle m_1\rangle-\langle m_2\rangle\right)k_s\frac{\partial\tilde{T}_s}{\partial z}\right]$$
$$=h_1 S_{w_1}\left(\tilde{T}_s-\tilde{\overline{T}}_1\right)+h_2 S_{w_2}\left(\tilde{T}_s-\tilde{\overline{T}}_2\right) \qquad (5.5)$$

here, $\left(1-\langle m_1\rangle-\langle m_2\rangle\right)$ can be considered as the averaged "blockage".

The porosity and specific surface are defined in Section 4.2.1 and repeated here for convenience. The porosity for the air side of the fin-and-tube heat exchanger is

$$\langle m_1\rangle=1-\frac{\delta_f}{F_p}-\frac{\pi D_c^2\left(F_p-\delta_f\right)}{4P_l P_t F_p} \qquad (4.27)$$

and for the water side is

$$\left\langle m_2 \right\rangle = \frac{\pi D_i^2}{4 P_l P_t} \tag{4.28}$$

The specific surface area for the air side is given by

$$S_{w_1} = \frac{2 P_l P_t - 2\pi \left(\dfrac{D_c}{2}\right)^2 + \pi D_c \left(F_p - \delta_f\right)}{P_l P_t F_p} \tag{4.29}$$

and for the water side is

$$S_{w_2} = \frac{\pi D_i}{P_l P_t} \tag{4.30}$$

The closures are developed in Section 4.7 and repeated here for convenience. The closure for the air side momentum equations is,

$$c_{d_1} = \frac{128.2}{\mathrm{Re}_{D_h}} + 0.149 \tag{4.104}$$

And the closure for the air side energy equation is,

$$h_1 = 0.171 \mathrm{Re}_{D_h}^{0.559} \, \mathrm{Pr}^{1/3} \left(\frac{k_1}{D_{h_1}}\right) \tag{4.105}$$

The closure for the water side momentum equations is,

$$c_{d_2} = \frac{1}{\left\{1.7372 \ln\left[\dfrac{\mathrm{Re}_{D_h}}{1.964 \ln\left(\mathrm{Re}_{D_h}\right) - 3.8215}\right]\right\}^2} \tag{4.114}$$

And the closure for the water side energy equation is,

$$h_2 = 0.015 \, \text{Re}_{D_h}^{0.83} \, \text{Pr}^{0.42} (\frac{\mu_b}{\mu_0})^{0.14} \left(\frac{k_2}{D_{h_2}} \right) \tag{4.115}$$

5.1.2. VAT Based Solver
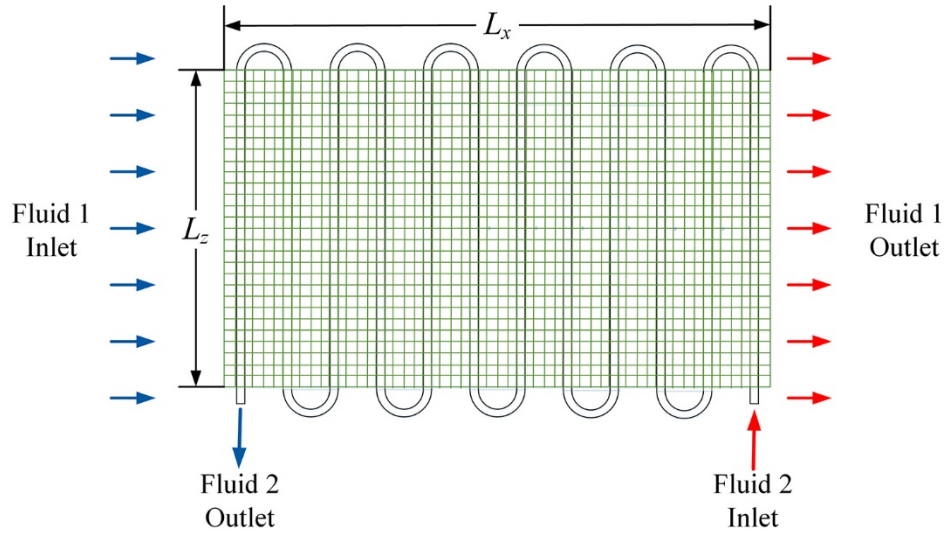
Figure 5.1: Schematic of computational grid on a physical model.

Now we have the fin-and-tube heat excha1nger being described by the closed VAT governing equations, a numerical solution method is needed to solve these equations. Finite difference method was adopted considering the simplicity of these VAT based governing equations, so that a fast solution is possible. A schematic diagram of the fin-and-tube heat exchanger coil circuitry is shown in Figure 5.1. Fluid 1 (usually is air) flows straight through the outside of the heat exchanger in the positive x - direction, and fluid 2 (usually is water) follows inside of the oscillatory tubes. Both the flow outside of the tubes and inside the tubes are modeled as porous flow. The porous flow through the tubes alternates its direction periodically and pressure drop through the tube bends is neglected for simplicity.

The grid system is shown on top of the heat exchanger in Figure 5.1. A uniform grid is adopted and the grid independency test was conducted by recursively refine the mesh until a stable solution was obtained. Moreover, only one row of tubes in the y - direction was considered for this case as symmetry allows the heat exchanger capability to be increased by increasing the number of rows in the y - direction.

5.1.3. Optimization

In the present study, a basic Genetic Algorithm (GA) is employed to conduct the optimization of a fin-and-tube heat exchanger as a simple demonstration of application. Refer to [238-240] for more details about optimization of heat exchangers using genetic algorithm, which is based on the VAT model and closure developed in the present study. The general idea of this optimization method is outlined in Appendix B.
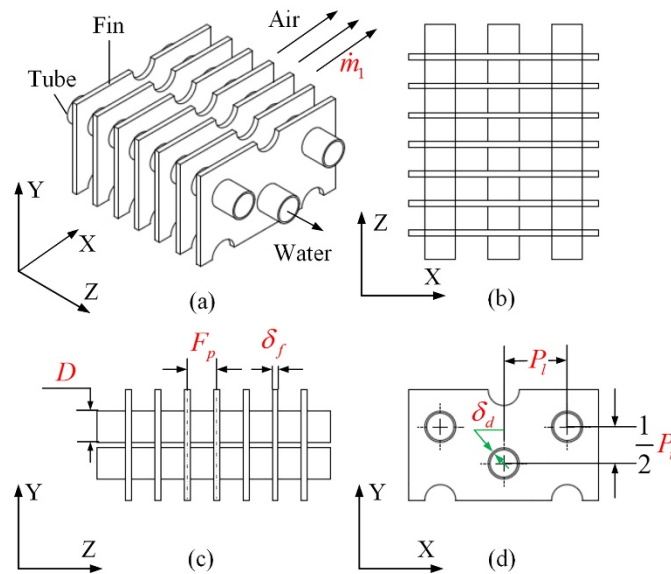
Figure 5.2: Design variables of the fin-and-tube heat exchanger.

Before initiating the optimization procedure, what is to be optimized must be determined and the constraints must be set from physical and specified limitations. There are a lot of different ways to define a fitness function, such as annual operation cost, the total weight of the heat exchanger, etc. and in the present study, the heat exchanger effectiveness is chosen to be the fitness function

$$F\left(\underline{x}\right) = \varepsilon = \dot{Q}_1 / \dot{Q}_{max} \tag{5.6}$$

in which F is the fitness function, $\underline{x}$ defines the design variables, $\dot{Q}_1$ is the total heat transfer rate on the fin side and $\dot{Q}_{max}$ is the maximum heat transfer rate defined as

$$\dot{Q}_{max} = \dot{m}_2 c_{p2} \left(T_{2,in} - T_{1,in}\right) \tag{5.7}$$

The geometric parameters which strongly influence the performance of the heat exchanger include the diameter of the tube D, the tube thickness δ_d, non-dimensionalized tube pitches S_t and S_l ($S_t = P_t/D$, $S_l = P_l/D$), fin pitch F_p and fin thickness δ_f, which are marked in red in Figure 5.2. These design variables are bounded between minimum and maximum values and are considered as continuous variables, not being restricted to a particular set of possible values, see Table 5.1. The overall dimensions of the heat exchanger, L_x, L_y, L_z, the mass flow rate through the tube $\dot{m}_2$, the inlet temperatures of fluid 1 $T_{1,in}$ and fluid 2 $T_{2,in}$ are fixed at constant values. It should be noted that the present method is also applicable if one wants to use a discrete set of possible values found from handbooks or production catalogs.

143

Table 5.1: Search range of selected design variables of FTHX.

Design Variables	Ranges	
	Minimum	Maximum
Tube diameter, D, mm	5	20
Tube thickness, δ_d, mm	1	5
Tube transverse pitch over tube diameter, S_t	1	5
Tube longitudinal pitch over tube diameter, S_l	1	5
Fin pitch, F_p, mm	1	10
Fin thickness, δ_f, mm	0.5	10
Air flow rate, $\dot{m}_1$, kg/s	1	40

In addition to the search ranges of the design variables, several optimization constraints are implemented, such as the tube inner diameter, $D_{in} = D - 2\delta_d$, shouldn't be zero, the tubes should touch each other, the spacing between fins shouldn't be zero. In the present study, we set the lower limits of these distance mentioned above to be 1mm. Besides, the total pumping power which includes the pumping power in the air side and water side shouldn't be higher than 60kW and the total mass of the heat exchanger should be less than 300kg.

Constraints:

$$D - 2\delta_d \geq 1\text{mm} \tag{5.8}$$

$$\sqrt{P_t^2/4 + P_l^2} - D \geq 1\text{mm} \tag{5.9}$$

$$P_t - D \geq 1\text{mm} \tag{5.10}$$

$$2P_l - D \geq 1\text{mm} \tag{5.11}$$

$$F_p - \delta_f \geq 1\text{mm} \tag{5.12}$$

$$PP_T \leq 60 \text{ kW} \tag{5.13}$$

$$W \leq 300 \text{ kg} \tag{5.14}$$

The overall dimensions of the heat exchanger, L_x, L_y, L_z, the mass flow rate through the tube $\dot{m}_2$, the inlet temperatures of fluid 1 $T_{1,in}$ and fluid 2 $T_{2,in}$ are fixed at constant values,

$$
\begin{aligned}
&L_x = 0.2m,\ L_y = 0.3m,\ L_z = 1.5m \\
&\dot{m}_2 = 1.0\,kg/s,\ T_{1,in} = 30°C,\ T_{2,in} = 60°C
\end{aligned}
\tag{5.15}
$$
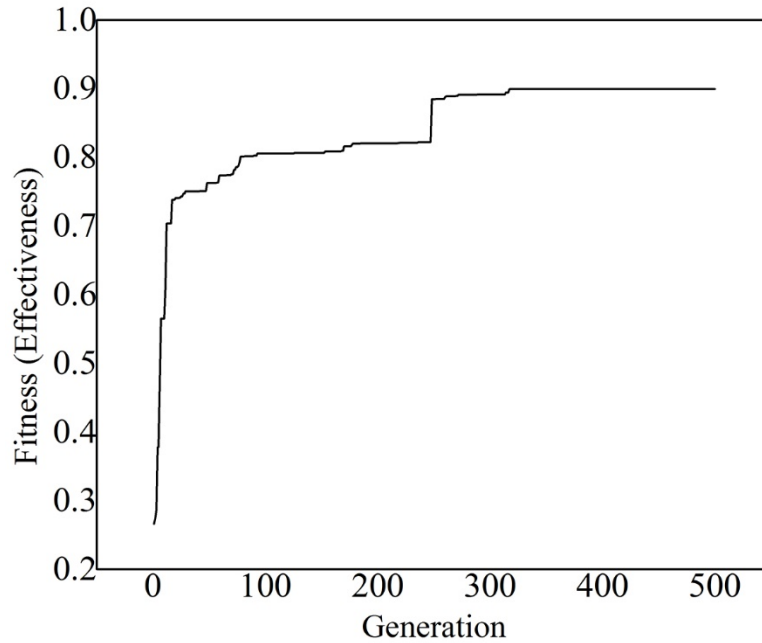
Figure 5.3: Evolution of the best individual in each generation.

145

The fitness evolution of the best individual in each generation is shown in Figure 5.3. It can be seen that the solution starts converging from 350 generations and the effectiveness of the fin-and-tube heat exchanger converges at 0.9. The final design of the FTHX is summarized in Figure 5.2.

Table 5.2: Optimized geometry of the fin-and-tube heat exchanger.

Design Parameters	Optimum
Tube diameter, D, mm	7.7
Tube thickness, δ_d, mm	1.36
Tube transverse picth, P_t, mm	10.7
Tube rows in transverse direction, N_t	28
Tube longitudinal picth, P_l, mm	25
Tube rows in longitudinal direction, N_l	8
Fin pitch, F_p, mm	2.13
Fin thickness, δ_f, mm	0.5
Air flow rate, $\dot{m}_1$, kg/s	5.27

5.2. Application to Plate Fin Heat Sinks with Elliptic Scales

5.2.1. VAT Based Modeling

In this section, the VAT based modeling method is used to describe transport phenomena in plate fin heat sinks with elliptic scale roughed surfaces and shielded top, at which a boundary condition of slip wall is applied.

146

The modeling procedure is similar to what is done for fin-and-tube heat exchanger in section 5.1 except two main differences. The first is that, for fin-and-tube heat exchanger, there are two fluids and one solid, while for heat sink, there are only one fluid and one solid. The second difference is that, a fin-and-tube heat exchanger becomes a complete homogeneous media as the VAT applied to it, but for heat sink, only the fin region becomes homogeneous media and the interface between the fin region and solid base needs to be dealt with specifically when the VAT equations are solved numerically.

The VAT based one-dimensional momentum equation is written as

$$0 = -\frac{1}{\rho_f}\frac{d\langle\overline{p}\rangle_f}{dx} + c_d\frac{S_w}{\langle m(z)\rangle}\frac{\tilde{u}^2}{2} + \frac{\partial}{\partial z}\left(\langle m(z)\rangle(v+\tilde{v}_t)\frac{\partial\tilde{u}}{\partial z}\right) \tag{5.16}$$

The two dimensional energy equation for fluid phase is

$$\rho_f c_{pf}\langle m\rangle\tilde{u}\frac{\partial\tilde{\overline{T}}_f}{\partial x} = \frac{\partial}{\partial z}\left(\langle m\rangle(k_f+\tilde{k}_t)\frac{\partial\tilde{\overline{T}}_f}{\partial z}\right) + hS_w\left(\tilde{\overline{T}}_s - \tilde{\overline{T}}_f\right) \tag{5.17}$$

The two dimensional energy equation for solid phase is

$$\frac{\partial}{\partial x}\left[(1-\langle m\rangle)k_s\frac{\partial\tilde{T}_s}{\partial x}\right] + \frac{\partial}{\partial z}\left[(1-\langle m\rangle)k_s\frac{\partial\tilde{T}_s}{\partial z}\right] = hS_w\left(\tilde{T}_s - \tilde{\overline{T}}_f\right) \tag{5.18}$$

The porosity and specific surface are defined in Section 4.2.2 and repeated here for convenience. The porosity is

$$\langle m\rangle = \frac{H - 2\kappa e}{F_p} \tag{4.31}$$

The specific surface area, S_w, is defined as

$$S_w = \frac{2P_t P_l + \pi \left[\frac{3}{4}(P_t + P_l) - \frac{1}{2}\sqrt{P_t P_l} \right] e}{P_t P_l F_p}$$ (4.34)

The closures are developed in Section 4.8 and repeated here for convenience. The closure for the energy equations is,

$$h = \left\{ 0.144 \, \text{Re}_{D_h}^{0.765} \left[\left(\frac{e}{D_h} \right)^{0.695} + 0.457 \right] \left(\frac{H}{D_h} \right)^{1.018} + 8.235 \right\} \left(\frac{P_t}{P_l} \right)^{S_1} \left(\frac{k_f}{D_h} \right)$$

$$S_1 = \left(\frac{e}{D_h} \right)^{0.539}$$ (4.125)

The closure for the momentum equation is,

$$f_{D_h} = \left[\frac{94.53}{\text{Re}_{D_h}} + 0.0019 \, \text{Re}_{D_h}^{0.217} + 3.544 \left(\frac{e}{D_h} \right)^{1.465} \left(\frac{H}{D_h} \right)^{0.0232} \right] \left(\frac{P_t}{P_l} \right)^{S_2}$$

$$S_2 = \left(-\frac{129.28}{\text{Re}_{D_h}} + 2.74 \right) \left(\frac{e}{D_h} \right)^{0.771}$$ (4.126)

5.2.2. VAT Based Solver

The VAT-based momentum, turbulent kinetic energy, and thermal energy equations developed in previous section are solved numerically with the finite difference method over the two-dimensional x–z plane [184, 241, 242]. In particular, statements for one-dimensional fully developed turbulent flow and two-dimensional, two-temperature heat transfer in a porous layer and heat transfer in a base plate are used. Uniform grid is employed in the base plate and over most of the channel, however a higher density grid in the flow (x) direction is implemented near the channel inlet and outlet regions.
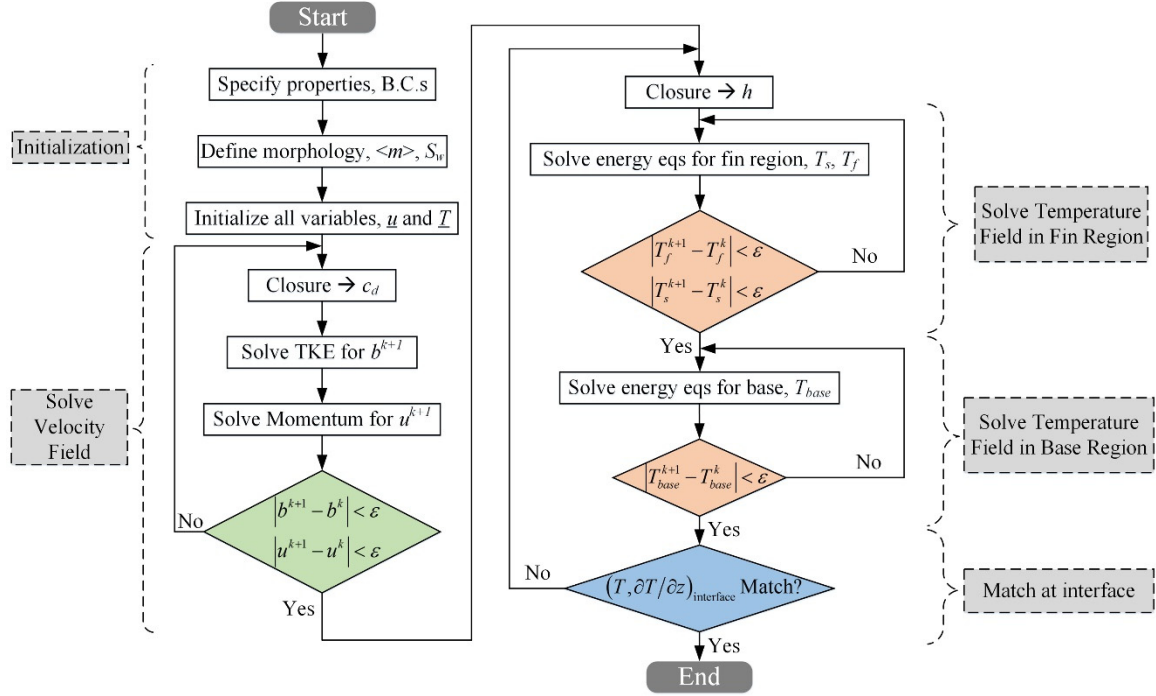
Figure 5.4: Solution procedure of the VAT based solver.

The flow chart of the solution method is illustrated in Figure 5.4. It is assumed that the flow is incompressible and all the properties are constant, so that the VAT solver could solve the velocity field and temperature field separately. After initialization, the solver evaluates the closure for momentum equation and then solve the turbulent kinetic energy equation and momentum equation until convergent solution is obtained. Then the solver evaluates the closure for energy equations and solve the temperature field in the fin region. After that temperature distribution in the base region is solved. The iteration continues until the temperature distributions match at the interface.

5.2.3. Optimization

In the present study, optimization based on DOE (referring to Appendix C for details about DOE) was conducted to optimize the configuration of a heat sink with elliptic scales

149

to meet the requirements of the MACE program goals, which is shown in Table 5.3. Basically, it is required that for a 4"×4"×1" heat sink heated by a 1kW heat source, the overall thermal resistance should be lower than 0.05°C/W while keeping the pumping power not higher than 33W and the total mass lower than 300g. The optimization was accomplished using commercial DOE optimization software, JMP 11, along with the VAT-based heat sink solver. All heat sinks were aluminum cooled by air at 25°C.

Table 5.3: The requirements of the MACE program goal specified by DARPA.

	Heat Source	Overall Dimensions	Mass	Pumping Power	Thermal Resistance
DARPA Goal	1kW	4"×4"×1"	300g	33W	0.05°C/W

The fin of the heat sink has a trapezoid shaped cross-section and the elliptic scales will be applied to the fin surfaces, see Figure 5.5. The overall heat sink dimensions are fixed to be 101.6mm × 101.6mm × 25.4mm (4"×4"×1") according to the requirements of the MACE program goals and the base thickness is maintained to be 1.5 mm. The geometric parameters which strongly influence the performance of the heat sink include the fin thickness at the base δ_b, fin thickness at the tip δ_t, fin pitch F_p, scale transverse and longitudinal pitch P_t and P_l, scale height e. The six variables are marked in red in Figure 5.5.
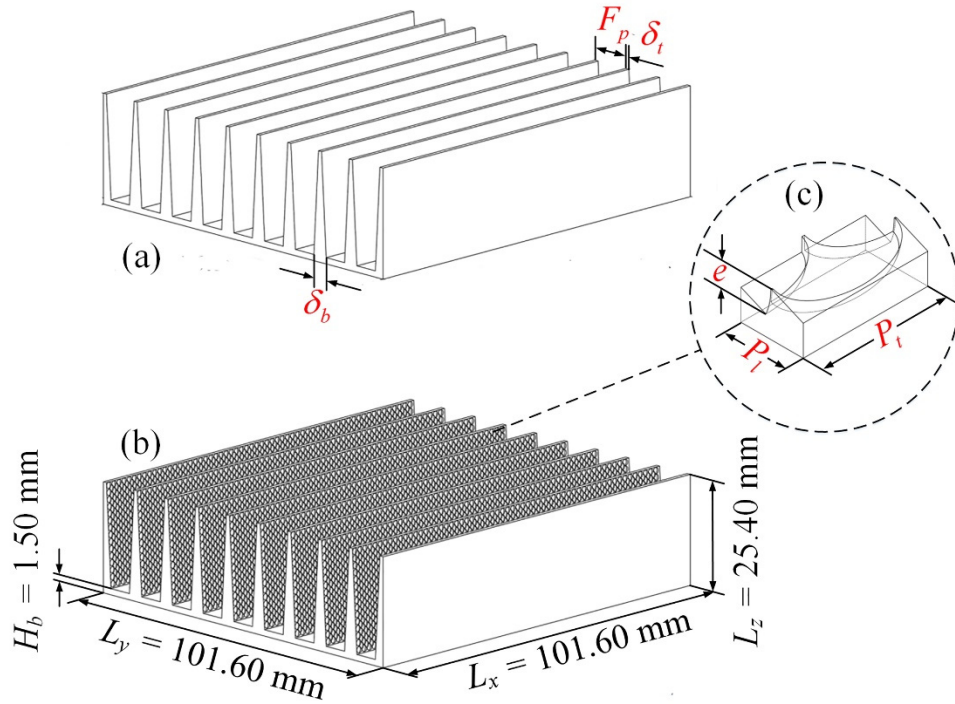
Figure 5.5: Schematic of the heat sinks with tapered fins. (a) Heat sink with smooth surface. (b) Heat sink with scale-shaped roughness. (c) An enlarged scale.

Table 5.4: Ranges of the selected design variables.

Design Variables	Ranges	
	Minimum	Maximum
Plate fin heat sink		
Fin thickness at the base, δ_b, mm	1	3
Fin thickness at the tip, δ_t, mm	0.5	2
Fin pitch, F_p, mm	1.5	10
Surface scale roughness		
Scale height, e, mm	0.1	0.5
Scale transverse pitch, P_t, mm	1	4
Scale longitudinal pitch, P_l, mm	1	4

The range of these variables are determined based on our previous studies [186, 203, 243] and are summarized in Table 5.4. There are also some constraints applied to the design, such as the fin thickness at the base should be thicker than that at the tip, the fin pitch should be wider than 1.5 time of the fin thickness at the base, the attack angle of the scale $\alpha = \text{atan}(e/P_l)$ should be smaller than 20°,

$$\delta_b \geq \delta_t \tag{5.19}$$

$$F_p / \delta_b \geq 1.5 \tag{5.20}$$

$$\alpha = \text{atan}\left(e/P_l\right) \leq 20° \tag{5.21}$$

The thermal resistance is selected to be the optimization objective function,

$$R_{th} = \frac{\Delta T}{\dot{Q}} \tag{5.22}$$

Therefore, the goal is to minimize the thermal resistance as much as possible with the pumping power being fixed at 33W.

The design points are determined by a standard Response Surface Methodology (RSM) design method. Since we have six independent design variables, to obtain an accurate response model, a total of 500 design points are generated. Without a fast-running solver, it is impossible to evaluate this large amount of design points within an acceptable time frame. Using the proposed VAT based solver, the average evaluation time for one design point is around 1.1 seconds.
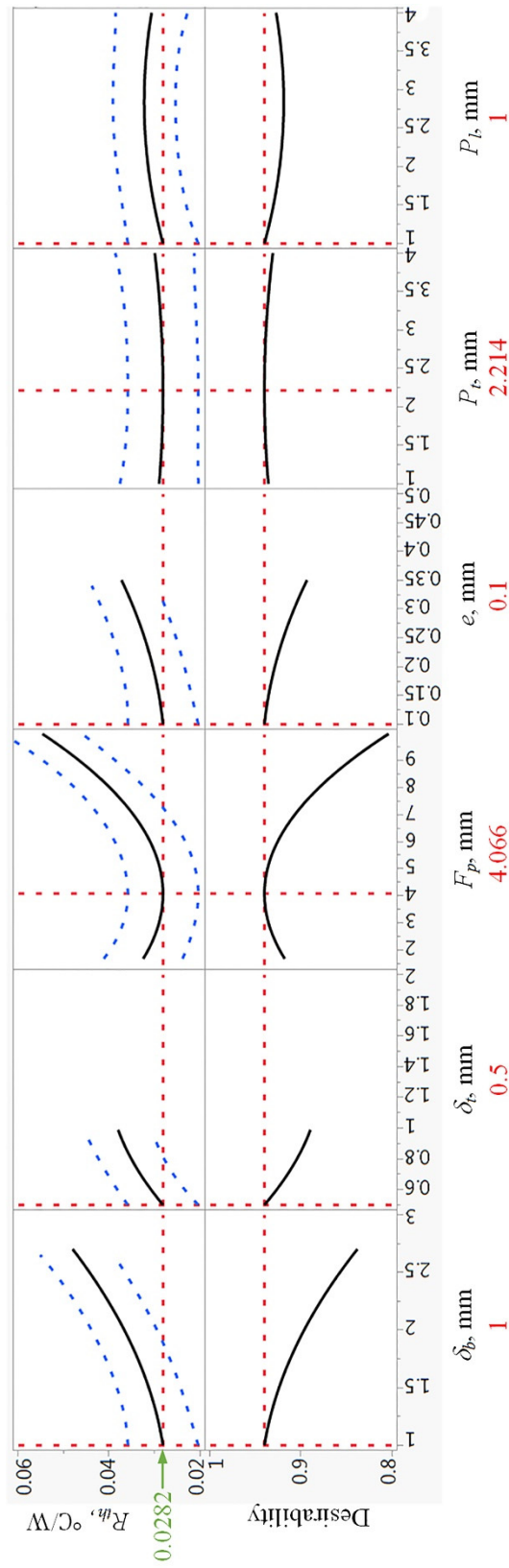
Figure 5.6: Prediction profiler with maximum desirability set.

153

Table 5.5: Optimized geometry of the plate fin heat sink with scale-shaped roughness.

Design Parameters	Optimum
Fin thickness at the base, δ_b, mm	1
Fin thickness at the tip, δ_t, mm	0.5
Fin pitch, F_p, mm	4.07
Scale height, e, mm	0.1
Scale transverse pitch, P_t, mm	2.21
Scale longitudinal pitch, P_l, mm	1

The VAT based solver took around 10 minutes to complete the 500 runs. The calculated thermal resistance of these 500 different designs were fed back to JMP and Figure 5.6 shows the results of the most desirable settings for the six variables. The final optimized design has a thermal resistance of 0.028°C/W with a mass of only 185g, which comfortably exceeds all MACE program goals. The optimized geometrical dimensions are summarized in Table 5.5. The VAT solver could also couple with other optimization method, i.e. particle swarm optimization [244, 245].

5.3. Potential Application to Plate-Pin Fin Heat Sinks

Besides the two applications presented in the previous sections, there are still a lot of potential applications of VAT. In this section, a new compound plate-pin fin heat sink (PFHSs) is introduced, which could be a potential application of volume averaging theory modelling [246-249].

To overcome the intrinsic shortcomings in structures of PFHSs mentioned above, which is undesirable for enhancing heat transfer performances of heat sinks, Yu et al. [250-

252] developed a new compound heat sink based on the plate fin heat sink, by placing circular pin fins into the flow channels to increase the turbulence. Yang and Peng [253] used numerical solutions to compare the thermal and hydraulic performances of both circular and square PPFHS with plate fin heat sink. It was found that the thermal resistance of compound heat sinks was lower than PFHS at the same flow velocity. However, the pressure drop of the compound heat sink is much higher than the PFHS. To overcome the shortcomings in structure of plate-pin fin heat sinks, mixed-height pins were used by Yang and Peng [254] in a subsequent work to improve the hydraulic performance. The synthetical performance of the PPFHS with mixed-height pins was better than the original circular plate-pin fin heat sink, but the improvement was quite limited.

However, there are still a large space of improvement of the synthetical performance of the new type of compound heat sink by employing different types of pin fins. In this section, the plate-pin fin heat sinks with various shapes of cross-section (square, circular, elliptic, NACA 0050 profile, and dropform) and different ratios of pin widths to plate fin spacing (0.3, 0.4, 0.5 and 0.6) are studied. The thermal and hydraulic performance of these PPFHSs was compared with plate fin and pin fin heat sinks in terms of Nusselt number, pressure drop and heat transfer effectiveness factor.

5.3.1. Physical Model

Schematic diagrams of the plate fin and pin fin heat sinks having the same fin spacing and fin thickness were experimentally compared by Jonsson and Moshfegh [158], shown in Figure 5.7 (a) and (b). These two commonly used heat sinks are adopted to calculate a baseline for the flow characteristics and heat transfer performance. The circular plate-pin fin heat sink tested by Yu [252] is shown in Figure 5.7 (c). All the heat sinks are fully-

shrouded and the top surface is insulated. The dimensions of the heat sinks are tabulated in Table 5.6.
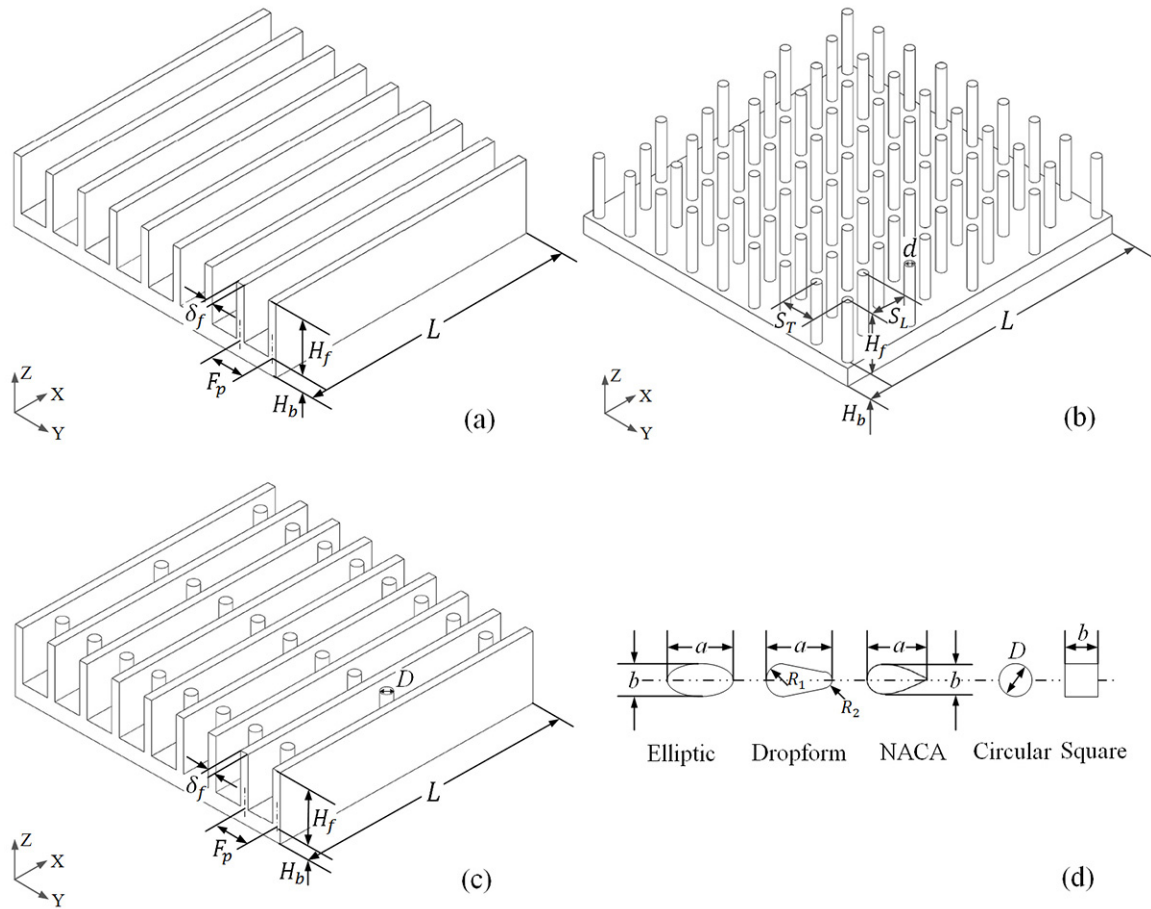
Figure 5.7: Some schematic diagrams: (a) Plate fin heat sink; (b) Pin fin heat sink; (c) Plate-pin fin heat sink; (d) Cross-sections of the five types of pins.

Besides circular pins, four other types of pins having elliptic, dropform, NACA 0050 profiles [255-257] and square cross-sections are adopted to build different kinds of plate-pin fin heat sinks, as shown in Figure 5.7 (d). In order to provide a fair and physically meaningful basis for the comparison, the areas projected in the flow direction or the flow

156

blockage areas are kept to the same, which means the width of all the pins, b, is set to be equal to the diameter of the circular pin, D. The pitch between adjacent pin fins and the pin length are also kept the same.

Table 5.6: Dimensions of the heat sinks.

	Parameters	mm		Parameters	mm
L	Length of the plate fin	51	H_f	Height of the fin	10
H_b	Height of the base	3	S_f	Plate fin spacing	5
δ_f	Plate fin thickness	1.5	F_p	Plate fin pitch	6.5
S_T	Transverse pitch of pin fins	6.5	S_L	Longitudinal pitch of pin fins	6.5
D	Pin diameter of PPFHS	1.5, 2, 2.5, 3	d	Pin diameter of pin fin HS	1.5

Table 5.7: Dimensions of the pins.

	Dimensions of pins			
b/S_f	a	b	R_1	R_2
0.3	3	1.5	0.75	0.225
0.4	4	2	1	0.3
0.5	5	2.5	1.25	0.375
0.6	6	3	1.5	0.45

To make the comparisons more generalized and to see how the dimensionless width of the pins, b/S_f, effects the performance of the PPFHSs, the widths of all five types of pins are 1.5mm, 2mm, 2.5mm and 3mm, with the corresponding values of b/S_f being 0.3, 0.4, 0.5 and 0.6. In total, 22 types of heat sink models, including the plate fin and pin fin heat sinks, are numerically tested and compared at four different velocities, ranging from 6.5m/s to 12.2m/s. The dimensions of the pins are tabulated in Table 5.7.

5.3.2. Computational Domain and Grid System
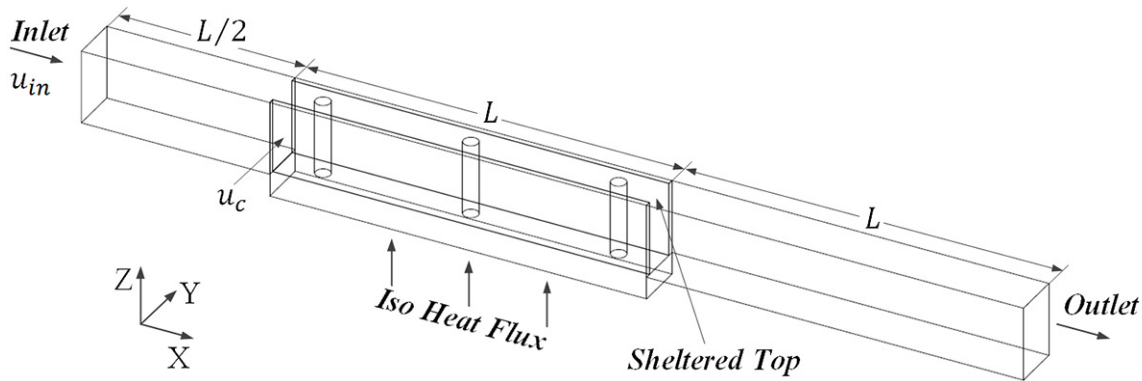
Figure 5.8: Computational domain.

Since the fin geometry is periodic in the spanwise direction, a single passage between the midlines of two proximate fins of the heat sink is selected to be the computational domain, see Figure 5.8. Because of the thickness of the fin, the air velocity profile at the entrance of the channel is not uniform. The computational domain is then extended upstream 0.5 times the stream-wise fin length, and the downstream boundary of the computational domain is located at the distance of a fin length from the trailing edge of the fin in the streamwise direction.

158

The velocity boundary condition and a constant temperature is set at the domain inlet. The turbulence intensity of the flow entering through the inlet boundary is set to 5%. The velocity at the inlet of extended region, u_{in}, changed from 5m/s to 9.4m/s so that the wind velocity passing through the smooth passages of the heat sinks, u_c, will be 6.5, 8.0, 10.0 and 12.2 m/s respectively. At the outlet of the computational domain, a pressure boundary condition is employed. The interface between the solid and the fluid is a no-slip wall with no thermal resistance. An iso-heat-flux thermal boundary condition is employed on the bottom surface of each type of heat sink, and the total heat load is 10W. Slip and adiabatic wall conditions are provided on all the other confined walls. The grid systems for all the heat sink models are built by Ansys Meshing. The grid system for one of the heat sinks is shown in Figure 5.9. Grid independence tests were made carefully by recursive refinement and comparison between the numerical simulation results. For all the simulation cases, y^+ values in the near-wall region are less than 1.
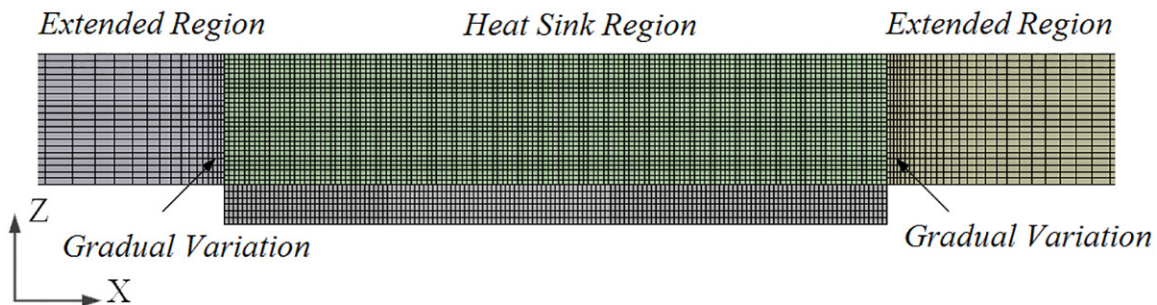
Figure 5.9: Mesh for the computational domain.

5.3.3. Parameter Definition and Data Reduction

Definitions are presented for the characteristic quantities which will be used in the presentations of numerical results.

The thermal resistance of the heat sinks R_{th} is defined by

$$R_{th} = \frac{\Delta T}{Q} \tag{5.23}$$

It should be noted that Jonsson and Moshfegh [158] and Yu [252] defined the temperature difference ΔT differently. Jonsson and Moshfegh [158] defined ΔT as the difference between the average temperature on the base and the inlet air temperature, while Yu [252] defined it as the difference between the highest temperature on the base and the inlet air temperature. Given the different definitions of ΔT, when the simulation results are validated by comparison with the experimental data, the corresponding definitions of ΔT are adopted for different heat sinks, while when quantitative comparisons are made for all types of heat sinks, ΔT is uniformly defined using Yu's [252] definition.

The average Nusselt number Nu is defined by

$$Nu = \frac{QD_h}{A_P \Delta T \lambda_f} \tag{5.24}$$

where D_h is the hydraulic diameter of the wind tunnel with no bypass suggested by Jonsson and Moshfegh [158], which is

$$D_h = 2 \cdot CH \cdot CB / (CH + CB) \tag{5.25}$$

The friction factor f is defined as

$$f = \frac{\Delta p}{0.5 \rho u_{in}^2} \cdot \frac{D_h}{4L} \tag{5.26}$$

The Reynolds number is defined as

$$\mathrm{Re} = \frac{\rho u_{in} D_h}{\mu} \tag{5.27}$$

To evaluate the comprehensive performance of all the heat sinks, the heat transfer effectiveness factor η_{eff} is defined as

$$\eta_{eff} = \frac{Nu / Nu_\infty}{\left(f / f_\infty\right)^{1/3}} \tag{5.28}$$

where the comparative references of heat transfer Nu_∞ and friction factor f_∞ are selected as the levels in smooth circular tube with fully developed flow, which is defined by Dittus-Boelter correlation for turbulent flow, Eq. (4.123), and Blasius equation for turbulent flow, Eq. (4.124), respectively.

5.3.4. Results and Discussion

The numerical analysis in this section consists of four parts. First, the computational model and the method adopted in current numerical simulations are verified and validated by comparing the CFD results with the experimental data. Then the streamlines and temperature contours of different types of PPFHSs in a plane normal to z-axis are compared. After having a qualitative view into the flow behavior and heat transfer phenomenon, the thermal and hydraulic performances of different types of PPFHSs are compared with plate fin and pin fin heat sinks quantitatively by means of Nusselt number and pressure drop respectively. Finally, a comprehensive comparison is made to evaluate the synthetical performance of all types of PPFHSs.

To verify the computational model and the method adopted in current numerical simulation, preliminary computations were first conducted for the plate fin, pin fin and circular plate-pin fin heat sinks, the dimensions of which are the same as the heat sinks tested by Jonsson and Moshfegh [158] and by Yu [252].

The comparisons of thermal resistance and pressure drop between the current simulation results and the experimental data are shown in Figure 5.10. We find that the maximum deviations in thermal resistance and pressure drop are less than 5% for all the three kinds of heat sinks. Our predicted results and the experimental data agree very well, demonstrating the accuracy of the physical model and the adopted numerical method.

For the present CFD simulation, the velocity streamlines and temperature fields are three-dimensional, so the presentation of these parameters are done for a plane normal to z-axis. Figure 5.11 provides insight into the local distributions of the streamlines for the section in the x-y plane through $z = 8$mm for $u_c = 10$m/s. It can be clearly seen from Figure 5.11 that there are some recirculation zones in the rear pin portion. It is known that a dead zone is characterized by the stationary recirculation region that forms when the flow separates at the rear portion of a pin and reattaches at the front of the following pin. The dead flow zone will decrease the convective heat transfer to the pin but enhance the heat transfer to the plate fin.
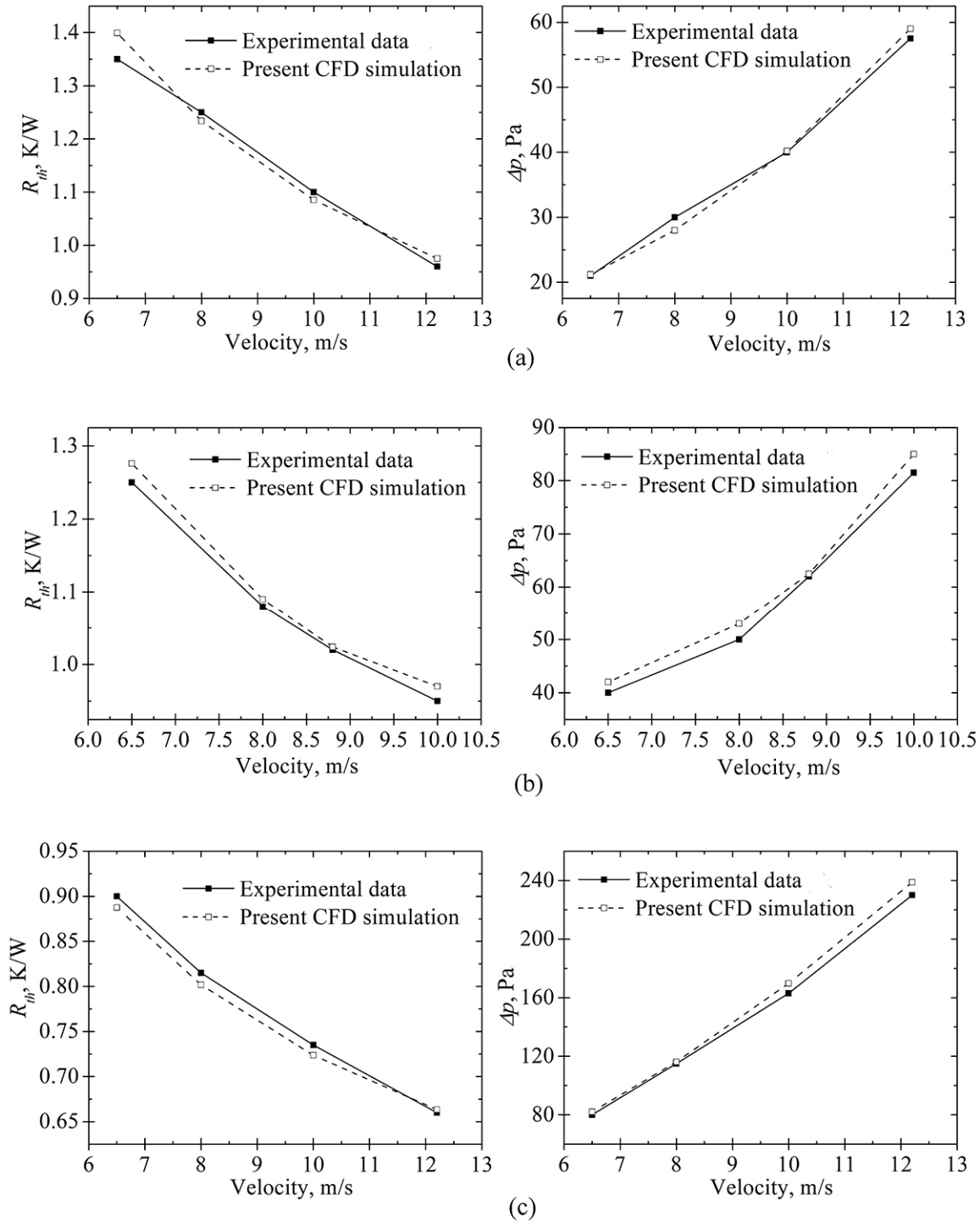
Figure 5.10: Comparison between the present CFD results and experimental data: (a) Plate fin heat sink [158]; (b) Pin fin heat sink [158]; (c) Plate-pin fin heat sink [252].

163
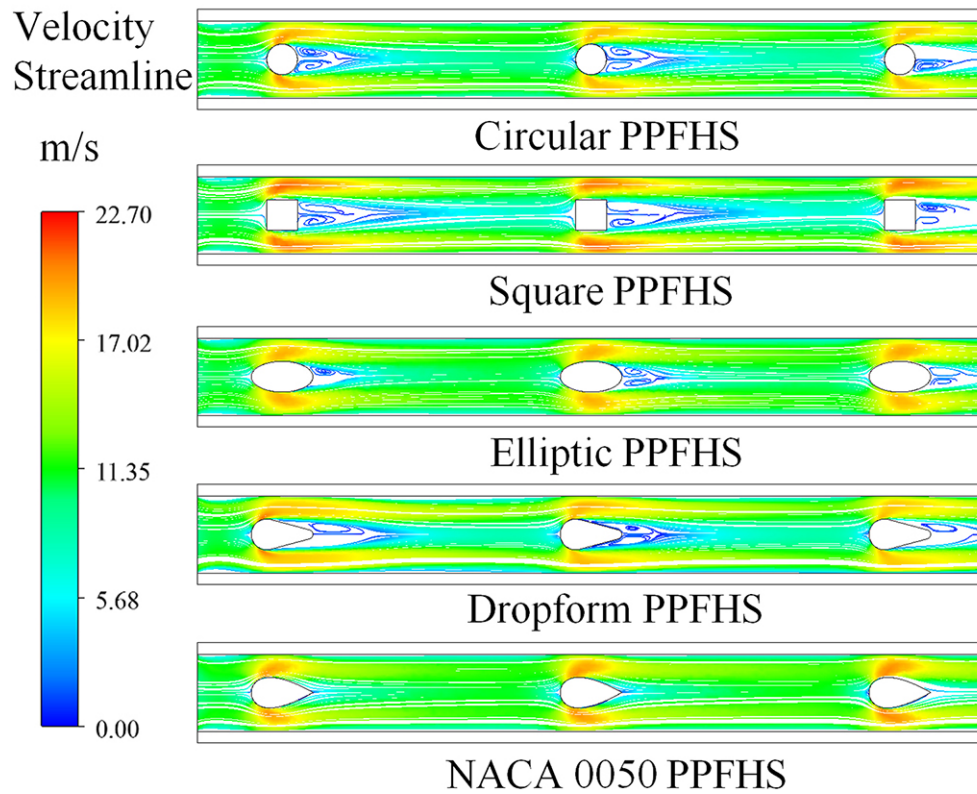
Figure 5.11: Streamline patterns in the plane z = 8mm, u_c = 10m/s.
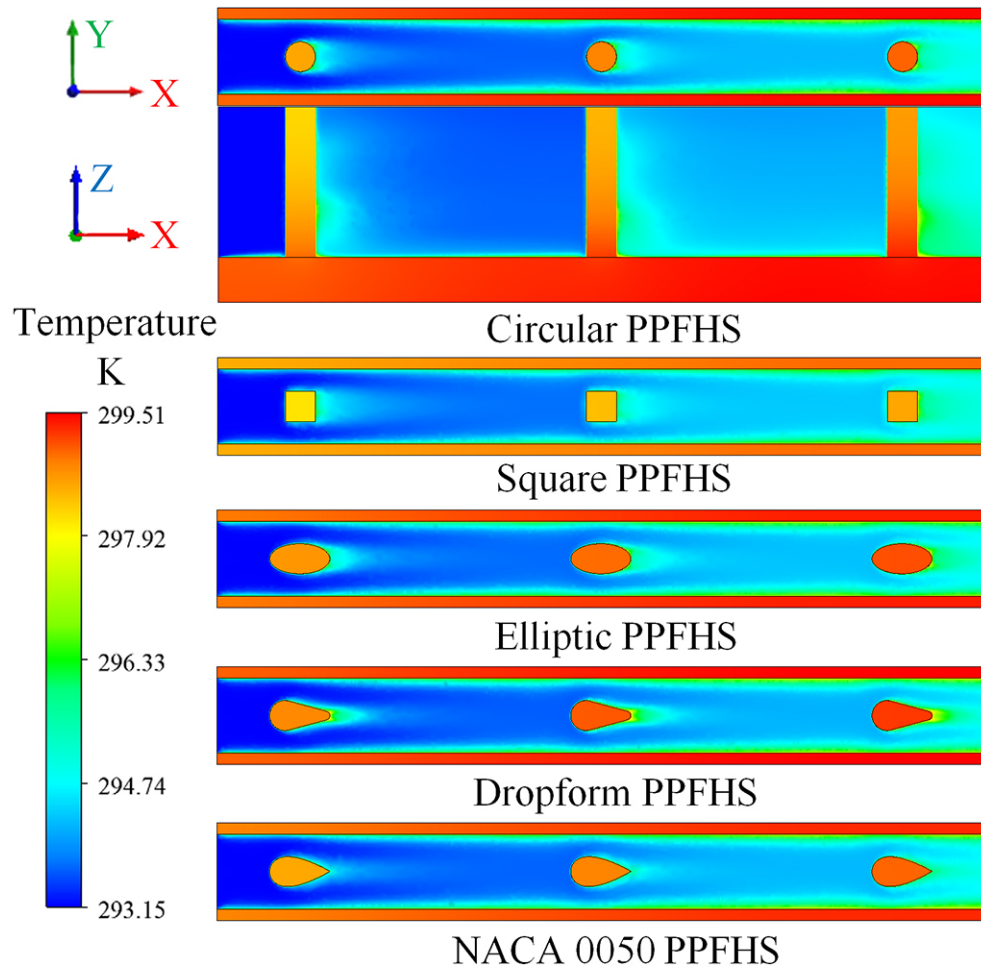
Figure 5.12: Temperature contours in the plane z = 8mm, u_c = 10m/s.

The flow seperates at different angles for different types of pins. The angle between the stagnation point and the separation point for circular and square pins is smaller than the streamline-shaped pins. The seperation from a square pin is the most prominent of all the five types. By comparing the streamline patterns of the five types of pins, it can be seen that there are larger scale vortices in the rear region of circular and square pins, especially for a square pin, due to the sharp corners.

The temperature contours in the flow channels around the pin fins are shown in Figure 5.12 for u_c = 10 m/s. Compared with the streamline figures, an extra image showing the temeperature distribution in the x-z plane through y = 3.25 is added to the figures of temperature countours. Since the temperature variation along the pins is qualitatively similar for all the types of PPFHS, only the x-z images for circular PPFHS are presented.

It can be seen that all fluid-solid interfaces, including the surface around the pins, the surface covered the base, and interfaces between fluid and the plate fins, are covered by a thermal boundary layer, the development of which is similar to the velocity boundary layer. Due to the existence of pins in the heat sink channels, the development of the thermal boundary layers which cover the plate fins is hindered periodically. Since the top wall is set to be free slip and adiabatic, no boundary layer develops there.

To get a more quantitative impression, the comparisons of flow and heat transfer characteristics of the PPFHSs with the plate fin and pin fin heat sinks, in terms of Nusselt number and pressure drop, are plotted in Figure 5.13-Figure 5.16. In Figure 5.13 and Figure 5.14, the dimensionless width of all the pins is set to be 0.4 and the wind velocity increases from 6.5m/s to 12.2 m/s. In Figure 5.15 and Figure 5.16, the wind velocity is set to be 6.5m/s and the dimensionless width of all the pins increases from 0.3 to 0.6.

From Figure 5.13, it is clear that the pin fin heat sink has higher Nusselt number (around 9%) than the plate fin heat sink, which agrees with the experimental data of Jonsson and Moshfegh [158]. By placing pin fins in the channels of plate fin heat sinks, the heat transfer capability increases greatly, with the Nusselt number being over 60% higher than the plate fin heat sinks. The square type PPFHS has the highest Nu compared with the other heat sinks. The augmentation of Nu is over 75% higher than PFHS and the maximum augmentation reaches 86%. The NACA type and the elliptic type of PPFHSs present similar heat transfer characteristics, yielding an average increment of 71%. The dropform type PPFHS has the lowest Nu, except for the circular type, with average augmentation of 68% and 63% for the former and latter, respectively.

Comparisons of pressure drop are presented in Figure 5.14. The pin fin heat sink has about 97% higher pressure drop than the plate fin heat sink. For the PPFHSs, it is not surprising that the square type PPFHS has the highest pressure drop compared to the other types of PPFHSs. The pressure drop of a square PPFHS is over 525% higher than that of PFHS at the same wind velocity. The pressure drop of the circular type PPFHS is much lower compared with the square type, but is still about 307% higher than the PFHS. The streamline-shaped pins (dropform, NACA 0050, elliptic) increase the pressure drop by a much smaller percentage, having an average increase of 214%, 201% and 186%, respectively. It should be noted that the NACA type of PPFHS doesn't show any advantage regarding the pressure drop compared with the other streamline-shaped types of PPFHSs. The elliptic type shows a little better hydraulic performance than the NACA type. The reason why this happened is that the maximum thickness as a fraction of the chord for the NACA profile chosen in the present work is far higher than the optimum ratio which is of

the order of 0.2. With the blockage area being the same and the pressure drop being primarily form drag, the lack of large differences for streamline-shaped types of PPFHSs is not unexpected.

Figure 5.15 and Figure 5.16 show the effect of the dimensionless width of the pins, b/S_f, on the Nusselt number and pressure drop for different plate-pin fin heat sinks. Just as expected, shown in Figure 5.15, the Nu numbers of all the five types of plate-pin fin heat sinks increase as b/S_f increases. With the increase of b/S_f, the square type PPFHS keeps showing the highest Nusselt number, followed by NACA type and elliptic type, which have a similar Nu. The dropform type and ciruclar type have lower Nu number, with the dropform type outweighing the circular type a little. On the other hand, as shown in Figure 5.16, the pressure drops also increase as b/S_f increases and still, the square type PPFHS has the highest pressure drop, followed by the circular type. The streamline-shaped types of PPFHSs have a similar pressure drop, much lower than the square and circular types. It's worth noting that the Nu numbers for all the PPFHSs have a similar increasing trend as b/S_f increases, while the pressure drops for the PPFHSs are diverging with the increase of b/S_f, which indicates the existence of an optimum width of pins, if both the heat transfer augmentation and the friction-loss increase are taken into consideration.
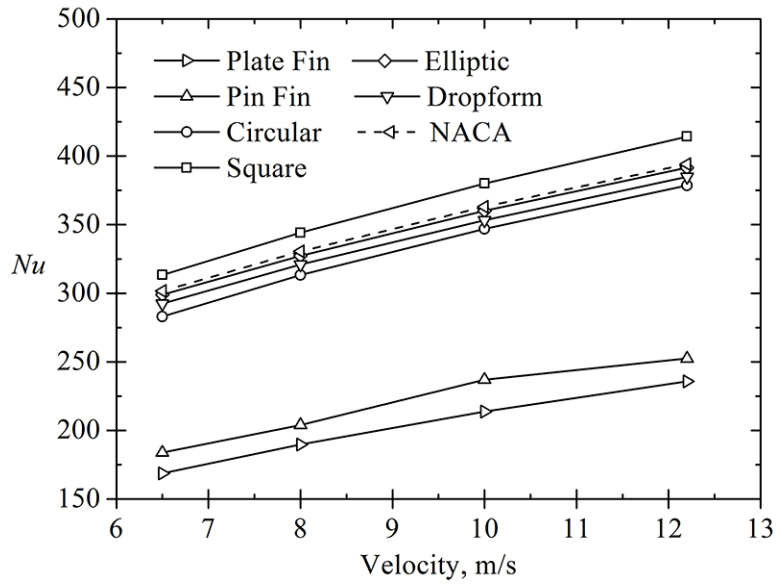
Figure 5.13: Nusselt numbers of heat sinks as a function of wind velocity, $b/S_f = 0.4$.
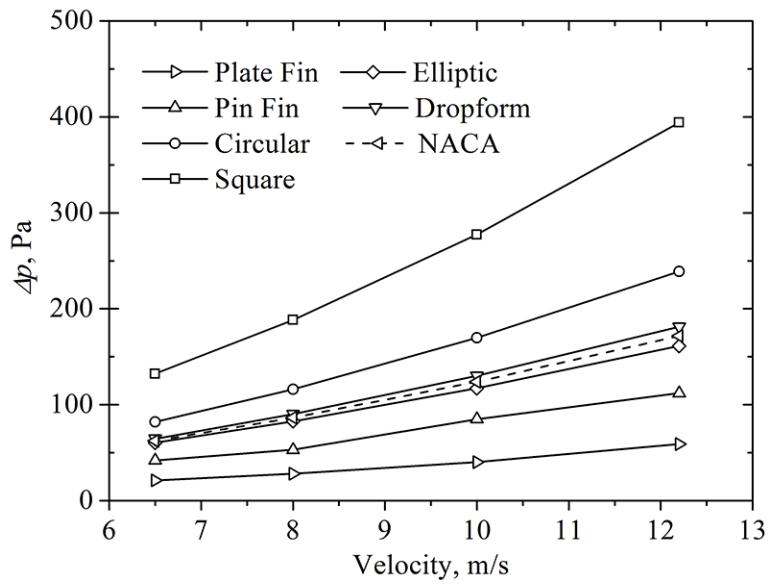
Figure 5.14: Pressure drops of heat sinks as a function of wind velocity, $b/S_f = 0.4$.
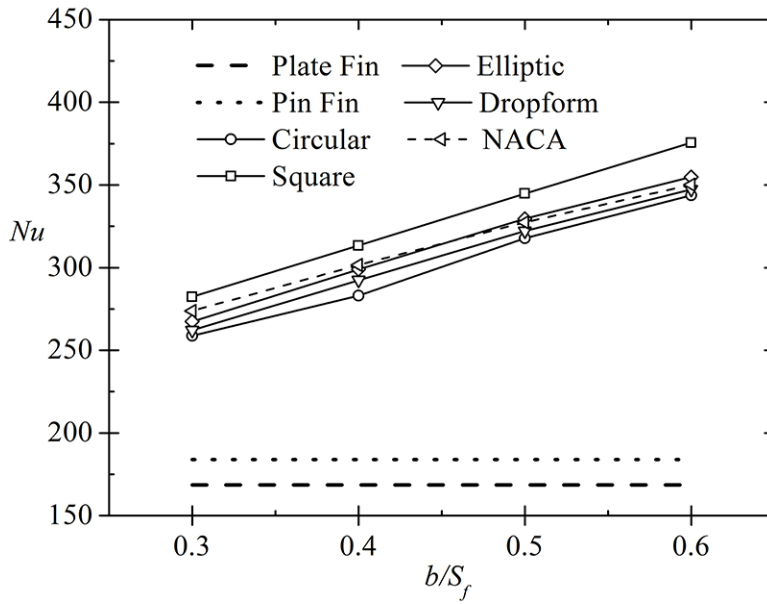
Figure 5.15: Nusselt numbers of heat sinks as a function of b/S_f, u_c = 6.5m/s.
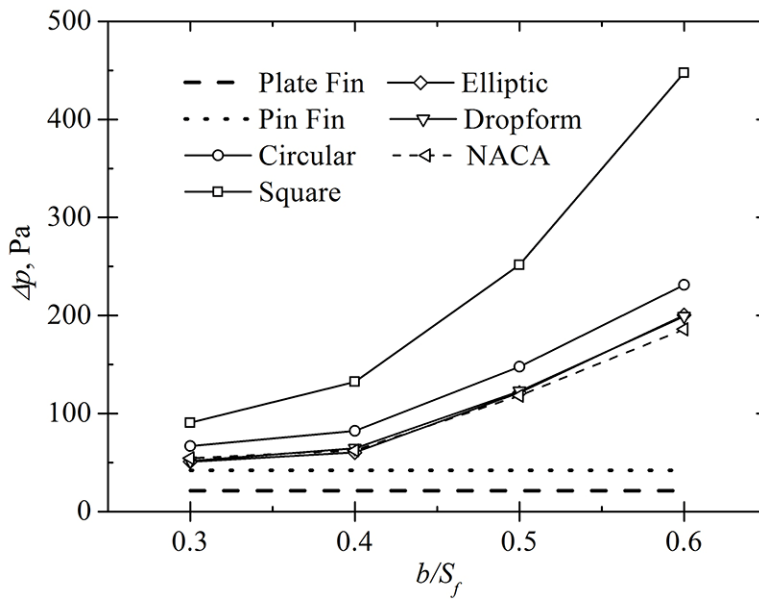
Figure 5.16: Pressure drops of heat sinks as a function of b/S_f, u_c = 6.5m/s.

Figure 5.13-Figure 5.16 compare the heat sinks with various shapes of pin cross-section and different dimensionless pin widths regarding heat transfer enhancement and pressure drop increment separately. However, increasing Nusselt number is accompanied by increasing pressure drop which is undesirable. Thus, based only on Figure 5.13-Figure 5.16, it is almost impossible to come to a final conclusion as to which type of heat sinks performs better than the others if both the heat transfer enhancement and power consumption are considered simultaneously. Therefore, a comprehensive performance comparison should be made to evaluate the effectiveness of different types of heat sinks.

A comprehensive comparison of heat transfer effectiveness factor is made and shown in Figure 5.17-Figure 5.19 using the definition given by Eq.(5.28). The geometric configuration that has the maximum η_{eff} can dissipate more heat while consuming the less power and keeping the temperature of the base at a lower value.
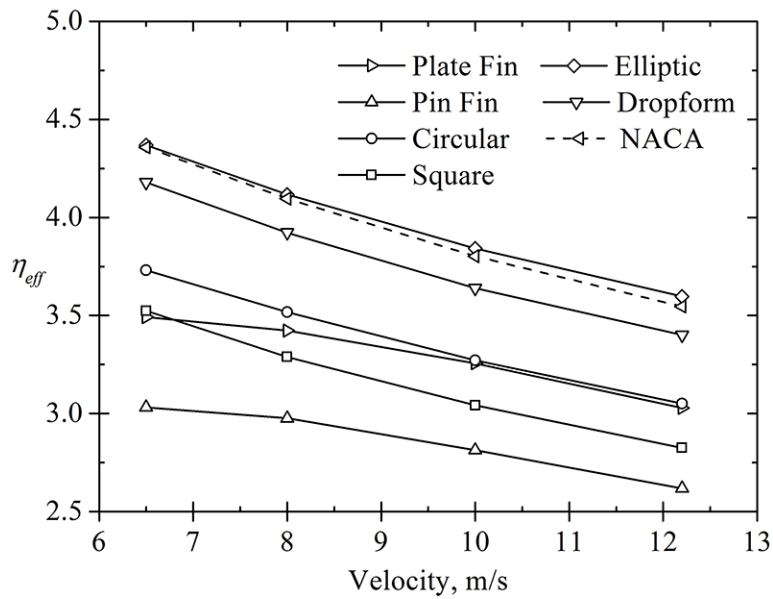
Figure 5.17: Heat sink performance η_{eff} as a function of wind velocity, $b/S_f = 0.4$.

From Figure 5.17, it is easy to see that the plate fin heat sink has a higher heat transfer effectiveness factor than the pin fin heat sink in the tested wind velocity region and that not all the five types of PPFHSs have higher comprehensive performance than the plate fin heat sink. The one which performs worse than the plate fin heat sink is the square type PPFHS, since planting the square pin fins in the channel of a plate fin heat sink leads to a considerably higher pressure drop which offsets its heat transfer enhancement potential. The efficiency of the circular type is much better than the square type. When the wind velocity is 6.5m/s, the effectiveness factor of the circular type is about 7% higher than the plate fin heat sink, while as the wind velocity increases, the advantage of the circular type PPFHS diminishes, but is still higher than the plate fin heat sink. Yu et al. [252] reached a similar conclusion based on their experimental data.

By employing streamline-shaped pins, the effectiveness of this new compound heat sink takes a step forward and is much higher than the original circular type. The elliptic type PPFHS has the best overall performance (around 20.5% over the plate fin heat sink), outweighing the NACA type a little, which has about 19.5% higher η_{eff} than PFHS. The elliptic pins minimize the pressure drop across the heat sink by reducing the vortex effects and enhance the thermal performance by maintaining large exposed surface area available for heat transfer. The dropform type PPFHS performs the worst among the three types of streamline-shaped PPFHSs, but still shows almost 15% higher η_{eff} than the plate fin heat sink.

Figure 5.18 and Figure 5.19 present a comparison of η_{eff} for different heat sinks as a function of the dimensionless width of pins. The wind velocity is set to 6.5m/s and 12.2m/s

in Figure 5.18 and Figure 5.19, respectively. These two pictures reveal three main pieces of information:

1) It is obvious that the effectiveness factor of all the PPFHSs peaks at $b/S_f = 0.4$ except the square type. For the square type PPFHS, it seems that the smaller the b/S_f is, the higher η_{eff} it has. As the b/S_f increases from 0.4 to 0.6, the effectiveness of all the PPFHSs decreases.

2) Figure 5.18 shows that when wind velocity is 6.5m/s, b/S_f shouldn't be larger than 0.6, since when $b/S_f = 0.6$, all the five types of PPFHSs have no advantage over the plate fin heat sink. As the wind velocity increases, the maximum allowable dimensionless width of pins decreases. From Figure 5.19, it can be seen that when the wind velocity is 12.2m/s, a b/S_f not higher than 0.5 is recommended.

3) With the increase of b/S_f, the elliptic type and NACA type of PPFHSs continue to perform the best, with the elliptic type having a little higher η_{eff} than the NACA type, followed by the dropform type. The square type PPFHS has the lowest η_{eff} among the five types of PPFHSs and the η_{eff} curve as a function of b/S_f for the circular type lies between those of the dropform type and square type.

All of the above analysis indicates that choosing a proper pin fin cross-section profile and dimensionless width of pins plays an important role in increasing the overall performance of this new compound plate-pin fin heat sink. The employment of the streamline-shaped pins with appropriate ratio of pin width to the plate fin spacing considerably increases the synthetical performance of PPFHS and makes them highly competitive heat dissipation solutions.
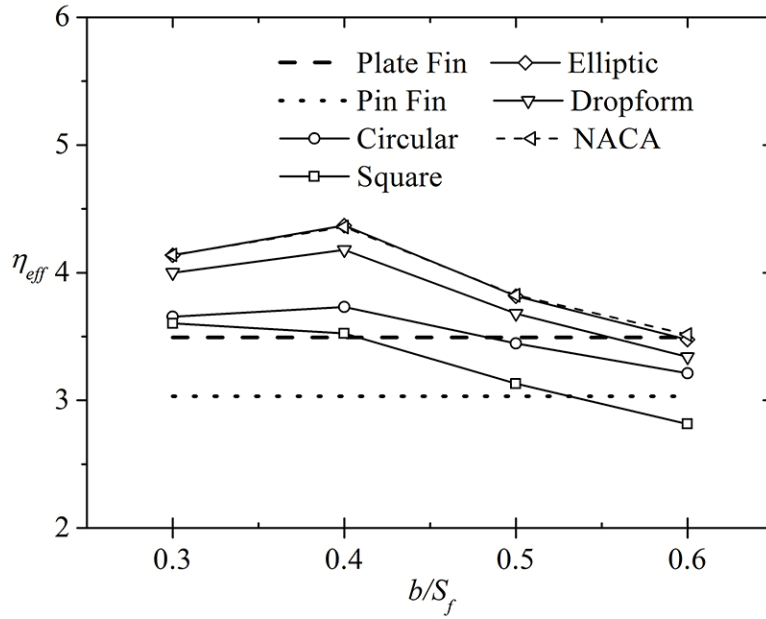
Figure 5.18: Heat sink performance η_{eff} as a function of b/S_f, $u_c = 6.5$m/s.
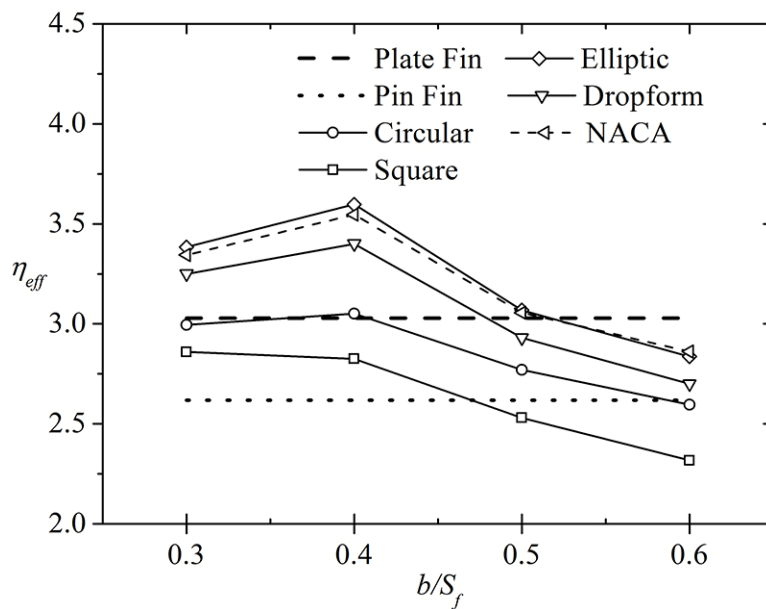
Figure 5.19: Heat sink performance η_{eff} as a function of b/S_f, $u_c = 12$ m/s.

5.3.5. Summary

By placing pin fins in the flow channel of a smooth plate fin heat sink, the thermal and fluid dynamic boundary layers are interrupted periodically and the fluid parts with different temperatures mix better. The present section describes an effort to numerically analyze the forced convective heat transfer through the channels of different types of plate-pin fin heat sinks. Twenty two types of heat sink models in total, including the commonly used plate fin and pin fin heat sinks, were simulated. Based on the results of the present study, the following conclusions can be drawn.

1. Placing pin fins in the flow channels is a good way to overcome the intrinsic shortcomings of smooth plate fin heat sinks. All the tested PPFHSs have higher Nusselt numbers as well as higher pressure drops than plate fin and pin fin heat sinks. However, considering the heat transfer enhancement and power consumption simultaneously, not all the PPFHSs have better overall performance than the plate fin heat sink.

2. The heat transfer enhancement of square type PPFHS, which is the highest of all the heat sinks considered, is offset by its high pressure drop, leading to lower heat transfer effectiveness than the plate fin heat sink. The effectiveness of the circular type is higher than the square type, however as the wind velocity increases, the advantage of the circular type PPFHS diminishes.

3. The streamline-shaped types of PPFHSs perform much better than the circular and square types, and among them the elliptic type and NACA 0050 type have similar overall performance, with the elliptic type outweighing the NACA type a little, followed by the dropform type.

175

4. The effectiveness factor of all the PPFHSs peaks at $b/S_f = 0.4$, except the square type, indicating the existence of an optimum width for pins. Further increasing b/S_f will decrease the effectiveness of PPFHSs.

5. Basically, in the tested velocity range, the performance of the five types of PPFHSs can be ordered as follows: elliptic $\approx$ NACA $>$ dropform $>$ circular $>$ plate fin heat sink $>$ square $>$ pin fin heat sink.

There are a number of other factors that need further evaluation before one can say more than that these results are promising but not definitive. The large number of parameters and consequent numbers of trials needed for optimization will require other than a full numerical approach. These new types of plate-pin fin heat sinks are some potential application objects of the methodology developed in the present study.

5.4. Conclusions

In this chapter, the VAT based hierarchical modeling method is applied to a fin-and-tube heat exchanger and a plate fin heat sink with elliptic scale-roughened surfaces. With closure in terms of the friction factor and the heat transfer coefficient obtained in Chapter 4, the problem is closed and the governing equation set is relatively simple. Finite difference method is adopted to solve these equations discretely, leading to a fast-running VAT based solver.

The VAT based solver could be coupled with some commonly used optimization methods, i.e. genetic algorithm and design of experiment, to obtain a fast optimum. The VAT based solver could be either run as a subroutine of other optimization code or run solo as a design evaluation tool. In this chapter, a two-stream fin-and-tube heat exchanger

was optimized using the VAT solver integrated with a genetic algorithm as a subroutine. A plate fin heat sink was optimized using the VAT solver as a complete evaluation tool to conduct the design points provided by a statistical tool JMP. It has been demonstrated that modeling transport phenomena in heterogeneous and hierarchical engineered devices with VAT is a very powerful tool, i.e. heat exchangers could be designed and optimized in an hour, instead of days of CFD or experimental work.

6. Conclusions and Future Work

This chapter summarizes the main contributions of the present study and makes recommendations for future work beyond the results reported in this thesis.

6.1. Main Contributions

The present study not only presented the application of volume averaging theory based modeling method to heterogeneous and hierarchical engineered devices but also proposed a new closure method, which utilizes a CFD code to evaluate the closure terms at a pore scale, to complete the upper level VAT based the model. The main contributions of this thesis can be summarized as follows.

6.1.1. Development of A General Closure Evaluation Method

A method to obtain the closure for VAT based governing equations using CFD simulation over selected REVs is developed, taking the fin-and-tube heat exchanger and heat sinks with elliptic scales as examples.

First, A universal length scale was introduced, which is very beneficial when scaling heat transfer and friction factor results. Reported correlations of friction factor and Colburn j factor for fin-and-tube heat exchangers were rescaled using the universal length scale, collapsing all the data onto a single curve for friction factor and Nusselt number, respectively.

After that, the field synergy principle (FSP) was adopted to determine the number of REVs that will be large enough to obtain good estimates of the closure parameters for the VAT-based modeling of heat exchangers.

Finally, the rigorously derived closure terms of heat transfer coefficient and friction factor were evaluated over the carefully selected REV. Two correlations of friction factor and Nusselt number were established based on the simulation results for fin-and-tube heat exchanger and heat sinks with elliptic scales, respectively.

In addition, a compound plate-pin fin heat sinks (PPFHS) with pin fins being placed in the channels of a plate fin heat sink was introduced. The pins have various shapes of cross-section (square, circular, elliptic, NACA 0050 profile, and dropform). The thermal and hydraulic performance of these PPFHSs was compared with plate fin and pin fin heat sinks in terms of Nusselt number, pressure drop and heat transfer effectiveness factor. The elliptic PPFHS performed the best, but not being optimized yet, which leave possibility for future application of the method introduced in the present work.

6.1.2. Application of VAT Model to Heat Exchangers

The present study properly applied the volume averaging theory based modeling technique to a two-stream fin-and-tube heat exchanger and a plate fin heat sink with scale-shaped surface roughness. The application of VAT yields many desirable features as a tool to characterize the physical processes taking place in heat exchangers:

1. VAT allows effects of interfaces and boundaries to be included in the modeling.
2. VAT incorporates the morphology description of the different phases (i.e. solid, liquid, and vapor) directly into the integrodifferential field equations.
3. VAT describes separate and combined fields and their interactions exactly through the integral terms appearing in the field equations (i.e. no assumptions about effective transport coefficients are required).

179

4. VAT provides for the consideration of lower-scale fluctuations of variables, cross-effects of different variable fluctuations, and interface variable fluctuation effects, and effective coefficients are rigorously derived.

5. The hierarchical physical description provided by the VAT governing equations connects properties and morphological characteristics to component features.

6. The non-local description of hierarchical, multi-scale processes makes it possible to conduct a search for the optimum over a wide range using population based optimization methods.

Combined with the developed closures, the VAT models are closed and solve discretely, leading to fast-running VAT based solvers. Optimization of heat exchangers was demonstrated briefly with the developed VAT solvers combined with some commonly used optimization methods. Final optimums were provided.

6.2. Future Work

This section presents several recommendations and suggestions for future modeling and optimization efforts to engineered devices.

6.2.1. Future VAT Based Solver for 2-D Equations

Volume averaging theory has been used extensively for applications with constant porosity, 1-D fully developed flow (i.e. the VAT based solver for 1-D fully developed flow and heat transfer in fluid part and 2-D heat transfer in solid part has been successfully developed). However, there is still a lot of space for development of the solver to extend its application area:

1. Revisit the governing equations solved by our VAT solver to include variable porosity and developing flow, which means a 2-D momentum equation for the fluid part needs to be solved.

2. Develop a high performance solution procedure for the 2-D flow.

3. Develop a technique for evaluating closure terms when a 2-D momentum equation needs to be solved.

Such 2-D VAT based solver could be applied to more complicated scenario, i.e. plate fin heat sink with widening fins, converging channel with packed bed of spheres, etc.

6.2.2. Future Optimization Subroutines

In the present study, the development of the optimization algorithms is not the focus of the present work, so the optimization methods adopted in the present study is very basic. More advanced optimization algorithm needs to be integrated into our optimization tool.

There have been quite a lot different genetic algorithms being developed. Deb et al. [258] developed a popular constraint-handling Multi-Objective Evolutionary Algorithm (MOEA) that they labeled as the Nondominated Sorting Genetic Algorithm II (NSGA-II). NSGA-II employs a computationally fast nondominated sorting procedure, an elitist strategy, a parameterless approach, and an effective constraint-handling method to obtain a diverse Pareto-optimal set in a single run. In the future development of optimization tool which combine VAT solver with GA, more advanced algorithm like NSGA-II would be implemented.

As to the design of experiment method, right now commercial DOE tool JMP is used together with our VAT solver. A subroutine could be developed to determine the design

points, generate the response model and provide the optimum. So that when optimization is conducted, the user could have two options, either using GA or DOE without referring to any commercial DOE tool.

6.2.3. Future Application Areas

Catalytic reactors have taken a central role in many industrial processes, including hydrogen production by Steam Methane Reforming (SMR) and reduction of emissions from automobiles and the combustion of natural gas. The growing demand for clean energy and environmental protection has made the design and optimization of these devices an intense area of research. Fixed bed reactors composed of porous substrates have been recognized as superior due to their high surface area and enhanced flow mixing. The performance of such reactors can be improved by optimizing the geometry of the porous medium and optimizing the operating conditions (inlet temperature, pressure, composition, etc.). The understanding of how these parameters affect the overall system performance can be extended by developing transport models based on Volume Averaging Theory (VAT).

Photonic integrated circuits (PICs) involving high optical, electrical and thermal power are starting to find application in many defense and civilian areas, such as Directed Energy Weapons (DEW), infrared illumination, electro-optical sensors, communications, industrial materials processing and medical equipment. The wide adoption of PICs for these applications is currently limited in great measure by the lack of suitable thermal management technology. These devices can generate heat fluxes of the order of 1 kW/cm^2 and larger and heat densities of the order of 1 kW/cm^3 and larger, creating hot spots that force a significant physical separation between active components in the chip and at the

same time severely limiting their performance. More and more researchers start exploring 'embedded' thermal management by bringing microfluidic cooling inside the substrate, chip or package and by including thermal management in the earliest stages of electronics design. Those on-chip cooling techniques usually involve hierarchical structures which could be modeled and optimized using volume averaging theory.

Exciting and promising new applications for VAT-based modeling of hierarchical transport phenomena in heterogeneous porous media extend beyond the examples discussed above. There are a wide range of different areas where VAT can be implemented, such as biology [259-263], solar energy [264], etc. A VAT-based hierarchical model can describe those multi-scale problems by a single set of equations and yield fast simulations, thus allowing the massive number of design variables to be optimized simultaneously.

Appendix

Multi-Parameter Optimization

The conflicting desire of improving heat transfer capability while minimizing pressure losses requires exploration of novel techniques for developing heat exchangers of progressively higher heat transfer performance. The traditional way of proceeding by continued tailoring of flow structures and heat transfer enhancement methods involves numerous separate trial and error experiments or simulations.

Optimization, by no means a new concept and being progressing strongly in recent years, can provide a path to the most suitable design, balancing the multiple objectives of the design. The need to optimize is very important in the design of systems, particularly thermal systems, and has become crucial in recent times due to growing global competition. It no longer is enough to obtain a workable or feasible thermal system that performs the desired tasks and meets the given constraints. At the very least, several workable designs should be generated and the final design, one that minimizes or maximizes an appropriately chosen quantity, be selected from these [265].

A proper choice of the optimization method is essential to the design of modern heat transfer equipment and processes. There have been a lot of different optimization algorithms developed by researchers, such as genetic algorithm (GA), design of experiment (DOE), topology optimization, etc. Generally, optimization methods could be divided into gradient and non-gradient methods, see Figure A 1.

The Gradient algorithm, also called steepest descent method [266, 267], is a minimization technique based on a line search in the negative direction of the first

derivative of the objective function, also called the gradient. Compared to non-gradient based optimization methods, gradient based methods have two disadvantages at least [268]. One disadvantage is that they require the derivatives of the objective function in order to calculate the optimum. Another disadvantage is that gradient method is more likely to find a local optimum other than a global optimum as non-gradient based method might do. Refer to [266, 267] for more details about gradient based optimization methods.
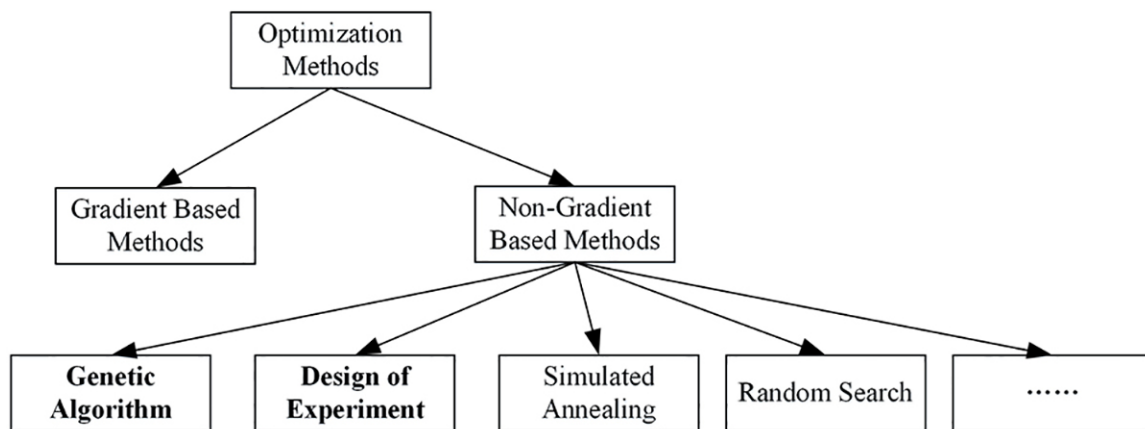
Figure A 1: Classifications of optimization methods.

In real word the engineering design and optimization problems are usually driven by many conflicting objectives, which is what usually called multi-objective optimization problem. Typically, the optimization procedure involves numerical simulations, analytical analysis, catalogue selections, etc. Usually, it is difficult to calculate the derivatives of the different objective functions. Therefore, in the present study, non-gradient based optimization methods are adopted to perform the optimization procedure.

Many of non-gradient optimization methods need a large population of different designs to be generated within the specified search ranges and design constraints, and these design points need to be evaluated and selected according to a certain objective function, so that an optimum could be found. However, the primary hurdle to use these optimization algorithm is that the commonly available evaluation methods, e.g. a system or device level CFD simulation or experiment, are time-consuming and expensive. This makes device-oriented optimization very costly and population-based optimization nearly impossible, which has resulted in most designs being based on ad hoc considerations, resulting in constrained performance, and thus accumulating financial losses for those manufacturing and operating the devices, and troubling environmental effects, i.e. excessive carbon emissions and thermal pollution, due to the accompanying energy losses [240].

With the VAT based solver being developed, the evaluation of each design points could be done in seconds and the non-gradient optimization methods can be exploited to guide the design to its optimal configuration. During the optimization process, when evaluation of the objective function is needed, the VAT based solver is called. The VAT based solver feeds back the evaluation results to the optimization tool as a response. The process continues until the optimum is found.

To demonstrate the advantages brought by VAT, the optimization by Design of Experiment is introduced as an example. Design of experiment theory (DOE) is a branch of statistics providing researchers with methods for selecting the independent variable values at which a limited number of experiments will be conducted [269, 270]. Prior to design an experiment, the allowable range of the n independent variables need to be defined by minimum and maximum values. According to the ranges of the variables specified by

186

the designer, these experiment design methods create various combinations of different experiments (design points). An objective function or multi objective functions are defined and evaluated for these design points. The sensitivity of these objective functions, identified as the response, to the independent variables are investigated using regression analysis or analysis of variance (ANOVA). The above procedure is termed as Response Surface Methodology (RSM).
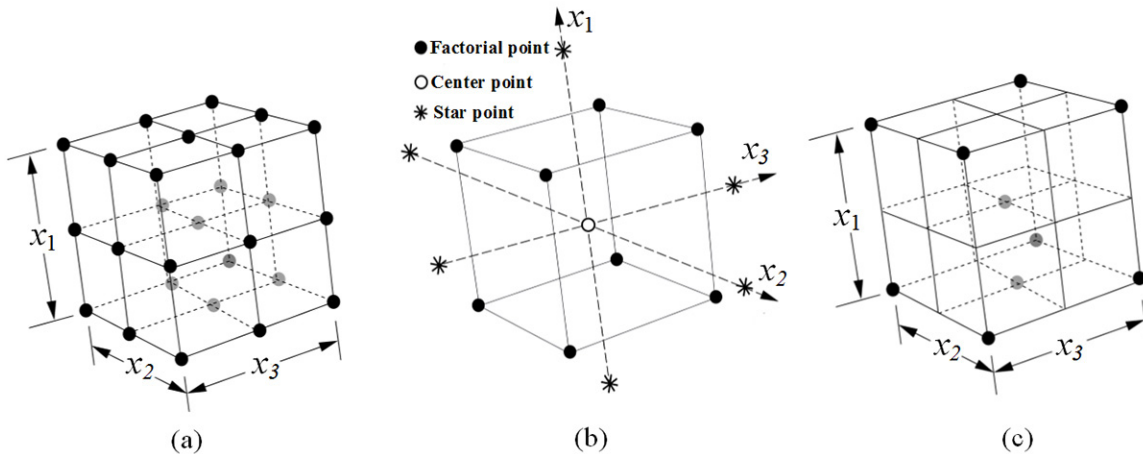
Figure A 2: Three different design of experiment methods. (a) A 3^3 full factorial experimental design. (b) A three variable central composite design (CCD). (c) A three variable D-optimal experimental design [269].

The number of generated designs points depends on the number of independent variables and the methods of the experimental design. If each variable is specified only at the minimum and maximum values (two levels), the experimental design is called 2^n full factorial design. If each variable is specified one more point, the midpoint, then a 3^n full factorial design is created, see Figure A 2 (a). To reduce the number of needed design points, a central composite design (CCD) was developed. In CCD a 2^n full factorial

experiment design is employed along with 2n star points and one or more center points, see Figure A 2 (b). The total design points created by CCD is $2^n + 2n + x$ ($x \geq 1$, number of center points). Both full factorial and CCD experimental design methods employ a full factorial design which are intended for use with rectangular design space. D-optimal experimental design was developed for irregularly shaped design space. The needed design points for D-optimal may be fewer than CCD's $2^n + 2n + 1$, see Figure A 2 (c).

There are some other experimental design methods available, which could be referred to Myers and Montgomery [270] for details. It could be found that, as the number of design variables n increases, the number of the needed design points increases exponentially. Although there have been work being done by many researchers using DOE to optimize a heat transfer device, e.g. heat sinks, they were limited to a few design variables, typically less than 4. And the number of total design points is usually less than 50, which may result in a response model that cannot provide the real optimum.

Some of these studies used experimental methods to evaluate the design points. Chou et al. [271] conducted experiment to find the optimal design parameters for a heat sink with parallel plain fin using the L_{16} (4^5) orthogonal arrays table, which is four levels and five factors type of factorial design, and a grey-based fuzzy algorithm. A total of 16 experimental cases were carried out, and the response graph and the analysis of variance (ANOVA) were used to find the optimal design. The parallel plain fin heat sink also optimized by the same group [143] using the standard L_{12} (2^{11}) orthogonal array to design experiments and Taguchi method to conduct the optimization.

Chiang [272] optimized the designing parameters for a parallel plain fin heat sink with confined impinging jet using DOE and experimental tests. The experimental plan was

generated using CCD (4 factors and 3 levels) and a total of 30 experiments were conducted to build the response surface.

Chiang, Chou and Liu [156, 273] adopted central composite design and response surface methodology to identify the effects of four design parameters on the thermal performance of the pin fin heat sink. The CCD adopted was a two level full factorial design with eight star points and six central points. A sum of 30 experiments were carried out and ANOVA analysis and RSM was used to seek the optimum. The authors [157] also conducted a similar study to optimize the pin fin heat sink but using the L_9 (3^4) orthogonal arrays to design the experiments and grey-fuzzy logic to find the optimum.

A Taguchi approach for determination of optimum design parameters for a pin fin heat sink was used by Sahin [274]. A total of 9 wind tunnel experiments, designed using L_9 (3^3) orthogonal array method, were carried out to analyze the effects of three variables, Reynolds number, the fin tip clearance and the interfin spacing. The data collected from the experiments were analyzed using the ANOVA-TM computer software package for evaluation of the effect of each parameter on the optimization criterion.

Sahin et al. [275] conducted wind-tunnel experiments and DOE optimization to study effects of the longitudinal and lateral separations of consecutively enlarged-contracted arranged fin pairs, width of the fins, angle of attack, heights of fins and flow velocity on the performance of rectangular fin heat sinks. The orthogonal array experimental design method, L_{18} (2^1*3^7), was chosen to determine the experimental plan. The Taguchi method was used to obtain the optimum with the help of the ANOVA-TM computer software package.

Owing to the relatively less expensive nature of CFD simulation compared to experimental work, a lot of past work employed design of experiment along with CFD simulation to obtain the optimized configuration of heat sinks. Kota, Burton and Joshi [276] employed Design of Experiment with response surface methodology and CFD simulation to seek an optimum configuration of an air-cooled heat sink with microscale dimples under transitional flow conditions. Three independent variables were selected as the response variables and the design points were generated using central composite design (CCD) with face centered structure. Owing to the expensive computational nature of CFD simulation, the total number of design points is limited to $2^n + 2^n + 1 = 15$ ($n = 3$, number of variables).

Devi, Manivannan and Rao [268] conducted a Taguchi based L_9 design of experiment optimization for a cylindrical pin fin heat sink. Four independent variables were considered and using standard Taguchi L_9 DOE method, 9 design points were generated. Also, a full factorial high lever DOE is not practical considering that a radiation simulation tool Ansoft HFSS and CFD-Flotherm were used to conduct the evaluation of objective functions. A similar work [277] was conducted by the same group using L_{27} (6 factors, 3 levels) Taguchi's design of experiments to optimize a flat plate heat sink. A total of 27 design points were evaluated using the same numerical simulation tools.

Jang, Yu and Lee [278] used Kriging model based DOE combined with a micro-genetic algorithm to optimize the cooling performance of a pin-fin radial heat sink. Three design variables were selected and 25 experimental cases were generated using the orthogonal array (OA) $L_{25}(5^3)$. A commercial CFD code Fluent was used to calculate the cooling performance of the 25 design points.

Abdullah et al. [279] used the central composite design (CCD) and response surface methodology (RSM) to exploit the optimum tip gap (variable 1) and orientation of multi-piezofan (variable 2) for heat transfer enhancement of finned heat sink in microelectronic cooling. A total of 13 runs were obtained from the CCD and three-dimensional simulation using CFD code Fluent was carried out to evaluate the design points.

Besides the above work, there are some other studies on optimization of heat sink using DOE and CFD [143, 280-284], which are not listed here. It can be found that when DOE is used to conduct optimization of heat sinks along with CFD simulations or physical experiments, the number of design variables are limited to 3 ~ 4 and the optimization is usually 2 level (sometimes 3 level is adopted) since the CFD simulation and physical experiments are time-consuming and expensive. This might result in a heat sink configuration which is actually not the final optimum. To conduct optimization by DOE with more variables being considered at the same time, the evaluation process of the design points needs to be sped up.

There are some previous work being done to speed up the design point evaluation process. Chen et al. [285] developed a semi-empirical analyzer to calculate the thermal and hydraulic performance of a plate fin heat sink. The analyzing process consists of three steps: (1) Evaluate the performance of fin extended surfaces using correlations from literature; (2) Perform heat sink base conduction analysis using the analytical solution for 3-D heat spreader; (3) Combine the above two analyses to perform an iterative thermal analysis procedure for the overall thermal and hydraulic performance of PPF heat sinks. Then a Response Surface Methodology is applied to establish analytical models for the thermal resistance and pressure drop in terms of the key design factors with a CCD experimental

design. The authors considered up to nine design variables and use 5 level DOE method to generate the design points. The same method was also applied to fin-fin heat sinks to obtain the optimum [286]. However, the method proposed by Chen et al. [285, 286] is limited to simple geometry, e.g. plate fin heat sink and circular pin fin heat sink, which has accurate correlations to be used for the fin region.

Therefore, we need a more general method to model and analyze the thermal and hydraulic performance of the heat sink, which theoretically can be applied to any type of heat sinks. The VAT based optimization method is one of the answers to this problem. It addresses many of the undesirable characteristics of the other methods discussed above. This VAT based optimization method has wide application, not limited to simple geometries. It speeds up the evaluation of objective functions, which makes the wide-range multi-parameter non-gradient optimization possible.

References

[1] Wang, C.-C., and Chi, K.-Y., 2000, "Heat transfer and friction characteristics of plain fin-and-tube heat exchangers, part I: new experimental data," International Journal of Heat and Mass Transfer, 43(15), pp. 2681-2691.

[2] Chang, S. W., Liou, T.-M., and Lu, M. H., 2005, "Heat transfer of rectangular narrow channel with two opposite scale-roughened walls," International Journal of Heat and Mass Transfer, 48(19-20), pp. 3921-3931.

[3] Tang, L.-H., Min, Z., Xie, G.-N., and Wang, Q.-W., 2009, "Fin pattern effects on air-side heat transfer and friction characteristics of fin-and-tube heat exchangers with large number of large-diameter tube rows," Heat Transfer Engineering, 30(3), pp. 171 - 180.

[4] Travkin, V. S., and Catton, I., 2001, "Transport phenomena in heterogeneous media based on volume averaging theory," Advances in Heat Transfer, 34, pp. 1-144.

[5] Travkin, V. S., Gratton, L., and Catton, I., "A Morphological Approach for 2-Phase Porous Medium Transport and Optimal Design Applications in Energy Engineering," Proc. the 12th Symposium on Energy Engineering Sciences, Conf. 9404137, pp. 48-55, pp. 48-55.

[6] Bejan, A., and Morega, A. M., 1993, "Optimal Arrays of Pin Fins and Plate Fins in Laminar Forced Convection," Journal of Heat Transfer, 115(1), pp. 75-81.

[7] Keil, F. J., and Rieckmann, C., 1994, "Optimization of three-dimensional catalyst pore structures," Chemical Engineering Science, 49(24, Part A), pp. 4811-4822.

[8] Anderson, T. B., and Jackson, R., 1967, "Fluid Mechanical Description of Fluidized Beds. Equations of Motion," Industrial & Engineering Chemistry Fundamentals, 6(4), pp. 527-539.

[9] Slattery, J. C., 1967, "Flow of viscoelastic fluids through porous media," AIChE Journal, 13(6), pp. 1066-1071.

[10] Whitaker, S., 1967, "Diffusion and dispersion in porous media," AIChE Journal, 13(3), pp. 420-427.

[11] Zolotarev, P. P., and Radushkevich, L. V., 1968, "An approximate analytical solution of the internal diffusion problem of dynamic absorption in the linear region of an isotherm," Russian Chemical Bulletin, 17(8), pp. 1818-1820.

[12] Slattery, J. C., 1972, Momentum, energy, and mass transfer in continua, McGraw-Hill Book Co., New York.

[13] Whitaker, S., 1977, "Simultaneous heat, mass and momentum transfer in porous media: a theory of drying," Advances in Heat Transfer, 13, pp. 119-203.

[14] Kaviany, M., 1995, Principles of Heat Transfer in Porous Media, Springer, New York

[15] Gray, W. G., Leijnse, A., Kolar, R. L., and Blain, C. A., 1993, Mathematical tools for changing spatial scales in the analysis of physical systems, CRC Press, Boca Raton.

[16] Whitaker, S., 1999, The Method of Volume Averaging, Kluwer Academic Publishers, Boston.

[17] Dullien, F. A. L., 1991, Porous Media: Fluid Transport and Pore Structure, Academic Press, New York.

[18] Adler, P. M., 1992, Porous media : geometry and transports, Butterworth-Heinemann, Boston.

[19] Travkin, V. S., and Catton, I., 1998, "Porous media transport descriptions -- non-local, linear and non-linear against effective thermal/fluid properties," Advances in Colloid and Interface Science, 76-77, pp. 389-443.

[20] Catton, I., 2006, "Transport phenomena in heterogeneous media based on volume averaging theory," Heat and Mass Transfer, 42(6), pp. 537-551.

[21] Travkin, V. S., Catton, I., and Gratton, L., "Single phase turbulent transport in prescribed non-isotropic and stochastic porous media," Proc. Heat Transfer in Porous Media.

[22] Gratton, L. J., Travkin, V. S., and Catton, I., 1995, "The influence of morphology upon two-temperature statements for convective transport in porous media," Journal of Enhanced Heat Transfer, 3(2), pp. 129-145.

[23] Travkin, V. S., and Catton, I., 1999, "Turbulent Flow and Heat Transfer Modeling in a Flat Channel with Regular Highly Rough Walls," International Journal of Fluid Mechanics Research, 26(2), pp. 159-199.

[24] Travkin, V. S., and Catton, I., "Models of turbulent thermal diffusivity and transfer coefficients for a regular packed bed of spheres," Proc. 28th National Heat Transfer Conference, ASME, pp. 15-23.

[25] Pedras, M. H. J., and de Lemos, M. J. S., 2000, "On the definition of turbulent kinetic energy for flow in porous media," International Communications in Heat and Mass Transfer, 27(2), pp. 211-220.

[26] Marcos H. J. Pedras, M. J. S. d. L., 2001, "Simulation of turbulent flow in porous media using a spatially periodic array and a low-Re two-equation closure," Numerical Heat Transfer, Part A: Applications, 39(1), pp. 35-59.

[27] Pedras, M. H. J., and de Lemos, M. J. S., 2001, "Macroscopic turbulence modeling for incompressible flow through undeformable porous media," International Journal of Heat and Mass Transfer, 44(6), pp. 1081-1093.

[28] Lemos, M. J. S. d., 2006, Turbulence in Porous Media: Modeling and Applications, Elsevier.

[29] Rocamora Jr, F. D., and de Lemos, M. J. S., 2000, "Analysis of convective heat transfer for turbulent flow in saturated porous media," International Communications in Heat and Mass Transfer, 27(6), pp. 825-834.

[30] de Lemos, M. J. S., and Braga, E. J., 2003, "Modeling of turburlent natural convection in porous media," International Communications in Heat and Mass Transfer, 30(5), pp. 615-624.

[31] Pedras, M. H. J., and de Lemos, M. J. S., 2003, "Computation of turbulent flow in porous media using a low-Reynolds k -ε model and an infinite array of transversally displaced elliptic rods," Numerical Heat Transfer, Part A: Applications, 43(6), pp. 585-602.

[32] Silva, R. A., and de Lemos, M. J. S., 2003, "Turbulent flow in a channel occupied by a porous layer considering the stress jump at the interface," International Journal of Heat and Mass Transfer, 46(26), pp. 5113-5121.

[33] Braga, E. J., and de Lemos, M. J. S., 2004, "Turbulent natural convection in a porous square cavity computed with a macroscopic κ–ε model," International Journal of Heat and Mass Transfer, 47(26), pp. 5639-5650.

[34] de Lemos, M. J. S., and Tofaneli, L. A., 2004, "Modeling of double-diffusive turbulent natural convection in porous media," International Journal of Heat and Mass Transfer, 47(19–20), pp. 4233-4241.

[35] de Lemos, M. J. S., 2005, "Turbulent kinetic energy distribution across the interface between a porous medium and a clear region," International Communications in Heat and Mass Transfer, 32(1–2), pp. 107-115.

[36] de Lemos, M. J. S., and Silva, R. A., 2006, "Turbulent flow over a layer of a highly permeable medium simulated with a diffusion-jump model for the interface," International Journal of Heat and Mass Transfer, 49(3–4), pp. 546-556.

[37] Nakayama, A., and Kuwahara, F., 1999, "A Macroscopic Turbulence Model for Flow in a Porous Medium," Journal of Fluids Engineering, 121(2), pp. 427-433.

[38] Nakayama, A., and Kuwahara, F., 2008, "A General Macroscopic Turbulence Model for Flows in Packed Beds, Channels, Pipes, and Rod Bundles," Journal of Fluids Engineering, 130(10), p. 101205.

[39] Brenner, H., 1980, "Dispersion Resulting from Flow through Spatially Periodic Porous Media," Philosophical Transactions of the Royal Society of London. Series A, Mathematical and Physical Sciences, 297(1430), pp. 81-133.

[40] Brenner, H., and Adler, P. M., 1982, "Dispersion Resulting from Flow through Spatially Periodic Porous Media II. Surface and Intraparticle Transport," Philosophical Transactions of the Royal Society of London. Series A, Mathematical and Physical Sciences, 307(1498), pp. 149-200.

[41] Mei, C. C., and Auriault, J.-L., 1991, "The effect of weak inertia on flow through a porous medium," Journal of Fluid Mechanics, 222, pp. 647-663.

[42] Giorgi, T., 1997, "Derivation of the Forchheimer Law Via Matched Asymptotic Expansions," Transport in Porous Media, 29(2), pp. 191-206.

[43] Chen, Z., Lyons, S. L., and Qin, G., 2001, "Derivation of the Forchheimer Law via Homogenization," Transport in Porous Media, 44(2), pp. 325-335.

[44] Carbonell, R. G., and Whitaker, S., 1983, "Dispersion in pulsed systems—II: Theoretical developments for passive dispersion in porous media," Chemical Engineering Science, 38(11), pp. 1795-1802.

[45] Sahraoui, M., and Kaviany, M., 1994, "Slip and no-slip temperature boundary conditions at the interface of porous, plain media: Convection," International Journal of Heat and Mass Transfer, 37(6), pp. 1029-1044.

[46] Hsiao, K.-T., and Advani, S. G., 1999, "A theory to describe heat transfer during laminar incompressible flow of a fluid in periodic porous media," Physics of Fluids, 11(7), pp. 1738-1748.

[47] Hsiao, K.-T., and Advani, S. G., 1999, "Modified effective thermal conductivity due to heat dispersion in fibrous porous media," International Journal of Heat and Mass Transfer, 42(7), pp. 1237-1254.

[48] Kuwahara, F., Kameyama, Y., Yamashita, S., and Nakayama, A., 1998, "Numerical modeling of turbulent flow in porous media using a spatially periodic array," Journal of Porous Media, 1(1), pp. 47-55.

[49] Nakayama, A., and Kuwahara, F., 2000, "Numerical Modeling of Convective Heat Transfer in Porous Media Using Microscopic Structures," Handbook of porous media, K. Vafai, ed., pp. 441-488.

[50] Kuwahara, F., and Nakayama, A., 1999, "Numerical Determination of Thermal Dispersion Coefficients Using a Periodic Porous Structure," Journal of Heat Transfer, 121(1), pp. 160-163.

[51] Nakayama, A., Kuwahara, F., Umemoto, T., and Hayashi, T., 2002, "Heat and Fluid Flow Within an Anisotropic Porous Medium," Journal of Heat Transfer, 124(4), pp. 746-753.

[52] Lemos, M. J. S. d., and Pedras, M. H. J., 2001, "Recent Mathematical Models for Turbulent Flow in Saturated Rigid Porous Media," Journal of Fluids Engineering, 123(4), pp. 935-940.

[53] Pedras, M. H. J., and de Lemos, M. J. S., 2001, "On the Mathematical Description and Simulation of Turbulent Flow in a Porous Medium Formed by an Array of Elliptic Rods," Journal of Fluids Engineering, 123(4), pp. 941-947.

[54] Vafai, K., 2000, "Handbook of Porous Media," Marcel Dekker, Inc., New York.

[55] Vafai, K., 2005, "Handbook of Porous Media," Taylor & Francis.

[56] Travkin, V., and Catton, I., 1995, "A two-temperature model for turbulent flow and heat transfer in a porous layer," Journal of Fluids Engineering, 117(1), pp. 181-188.

[57] Kakac, S., and Liu, H., 2002, Heat Exchangers: Selection, Rating, and Thermal Design, CRC.

[58] Rich, D. G., 1975, "The effect of the number of tubes rows on heat transfer performance of smooth plate fin-and-tube heat exchangers," ASHRAE Transactions, 81, pp. 307-317.

[59] McQuiston, F. C., 1978, "Correlations of heat mass and momentum transport coefficients for plate-fin-tube heat transfer surfaces with staggered tubes," ASHRAE Transactions, Part 1(84), pp. 294-308.

[60] Rich, D. G., 1973, "The effect of fin spacing on the heat transfer and friction performance of multirow, smooth plate fin-and-tube heat exchangers," ASHRAE Trans., 79(2), pp. 135-145.

[61] Gray, D. L., and Webb, R. L., 1986, "Heat transfer and friction correlations for plate fin-and-tube heat exchangers having plain fins.," Eighth International Heat Transfer Conference, San Francisco, California, pp. 2745-2750.

[62] Kang, H. J., Li, W., Li, H. Z., Xin, R. C., and Tao, W. Q., 1994, "Experimental study on heat transfer and pressure drop characteristics of four types of plate fin-and-tube heat exchanger surfaces," Journal of Thermal Science, 3(1), pp. 34-42.

[63] Wang, C.-C., Chi, K.-Y., and Chang, C.-J., 2000, "Heat transfer and friction characteristics of plain fin-and-tube heat exchangers, part II: Correlation," International Journal of Heat and Mass Transfer, 43(15), pp. 2693-2700.

[64] Xie, G., Wang, Q., and Sunden, B., 2009, "Parametric study and multiple correlations on air-side heat transfer and friction characteristics of fin-and-tube heat exchangers with large number of large-diameter tube rows," Applied Thermal Engineering, 29(1), pp. 1-16.

[65] Tang, L. H., Zeng, M., and Wang, Q. W., 2009, "Experimental and numerical investigation on air-side performance of fin-and-tube heat exchangers with various fin patterns," Experimental Thermal and Fluid Science, 33(5), pp. 818-827.

[66] Tang, L. H., Xie, G. N., Zeng, M., Wang, H. G., Yan, X. H., and Wang, Q. W., 2007, "Experimental investigation on heat transfer and flow friction characteristics in three types of plate fin-and-tube heat exchangers.," J. Xi'an Jiaotong Univ., 41(2007), pp. 521-525 (in Chinese).

[67] Torikoshi, K., Xi, G., Nakazama, Y., and Asano, H., 1994, "Flow and heat transfer performance of a plate fin-and-tube heat exchanger," Heat Transfer, 4, pp. 411-416.

[68] Jang, J.-Y., Wu, M.-C., and Chang, W.-J., 1996, "Numerical and experimental studies of three dimensional plate-fin and tube heat exchangers," International Journal of Heat and Mass Transfer, 39(14), pp. 3057-3066.

[69] Jang, J.-Y., and Chen, L.-K., 1997, "Numerical analysis of heat transfer and fluid flow in a three-dimensional wavy-fin and tube heat exchanger," International Journal of Heat and Mass Transfer, 40(16), pp. 3981-3990.

[70] Jang, J.-Y., and Yang, J.-Y., 1998, "Experimental and 3-D numerical analysis of the thermal-hydraulic characteristics of elliptic finned-tube heat exchangers," Heat Transfer Engineering, 19(4), pp. 55 - 67.

[71] McQuiston, F. C., and Tree, D. R., 1971, "Heat transfer and flow friction data for two fin-tube surfaces," ASME J. Heat Transfer, 93, pp. 249-250.

[72] Saboya, F. E. M., and Sparrow, E. M., 1976, "Transfer characteristics of two-row plate fin and tube heat exchanger configurations," International Journal of Heat and Mass Transfer, 19(1), pp. 41-49.

[73] McQuiston, F. C., 1978, "Heat mass and momentum transfer data for five plate-fin-tube heat transfer surfaces," ASHRAE Transactions, Part 1(84), pp. 266-293.

[74] Rosman, E. C., Carajilescov, P., and Saboya, F. E. M., 1984, "Performance of One- and Two-Row Tube and Plate Fin Heat Exchangers," Journal of Heat Transfer, 106(3), pp. 627-632.

[75] Chen, Z. Q., and Ren, J. X., 1988, "Effect of fin spacing on the heat transfer and pressure drop of a two-row plate fin and tube heat exchanger," International Journal of Refrigeration, 11(6), pp. 356-360.

[76] Fiebig, M., Chen, Y., Grosse-Gorgemann, A., and Mitra, N. K., 1995, "Conjugate heat transfer of a finned tube Part B: heat transfer augmentation and avoidance of heat transfer reversal by longitudinal vortex generators," Numerical Heat Transfer; Part A: Applications, 28(Compendex), pp. 147-155.

[77] Fiebig, M., Grosse-Gorgemann, A., Chen, Y., and Mitra, N. K., 1995, "Conjugate heat transfer of a finned tube Part A: heat transfer behavior and occurrence of heat transfer reversal," Numerical Heat Transfer; Part A: Applications, 28(Compendex), pp. 133-146.

[78] Kim, N. H., Yun, J. H., and Webb, R. L., 1997, "Heat transfer and friction correlations for wavy plate fin-and-tube heat exchangers," Journal of Heat Transfer, 119(Compendex), pp. 560-567.

[79] Rocha, L. A. O., Saboya, F. E. M., and Vargas, J. V. C., 1997, "A comparative study of elliptical and circular sections in one- and two-row tubes and plate fin heat exchangers," International Journal of Heat and Fluid Flow, 18(2), pp. 247-252.

[80] Wang, C. C., Fu, W. L., and Chang, C. T., 1997, "Heat transfer and friction characteristics of typical wavy fin-and-tube heat exchangers," Experimental Thermal and Fluid Science, 14(2), pp. 174-186.

[81] Wang, C. C., Lee, C. J., Chang, C. T., and Lin, S. P., 1998, "Heat transfer and friction correlation for compact louvered fin-and-tube heat exchangers," International Journal of Heat and Mass Transfer, 42(11), pp. 1945-1956.

[82] Wang, C.-C., Chi, K.-Y., Chang, Y.-J., and Chang, Y.-P., 1998, "An experimental study of heat transfer and friction characteristics of typical louver fin-and-tube heat exchangers," International Journal of Heat and Mass Transfer, 41(4-5), pp. 817-822.

[83] Kang, H. C., and Kim, M. H., 1999, "Effect of strip location on the air-side pressure drop and heat transfer in strip fin-and-tube heat exchanger," International Journal of Refrigeration, 22(4), pp. 302-312.

[84] Kim, N. H., Youn, B., and Webb, R. L., 1999, "Air-Side Heat Transfer and Friction Correlations for Plain Fin-and-Tube Heat Exchangers With Staggered Tube Arrangements," Journal of Heat Transfer, 121(3), pp. 662-667.

[85] Wang, C. C., Lee, C. J., Chang, C. T., and Chang, Y. J., 1999, "Some Aspects of Plate Fin-and-Tube Heat Exchangers: With and Without Louvers," Journal of Enhanced Heat Transfer, 6(5), pp. 357-368.

[86] Wang, C.-C., Tao, W.-H., and Chang, C.-J., 1999, "An investigation of the airside performance of the slit fin-and-tube heat exchangers," International Journal of Refrigeration, 22(8), pp. 595-603.

[87] Yun, J. Y., and Lee, K. S., 1999, "Investigation of heat transfer characteristics on various kinds of fin-and-tube heat exchangers with interrupted surfaces," International Journal of Heat and Mass Transfer, 42(13), pp. 2375-2385.

[88] Du, Y.-J., and Wang, C.-C., 2000, "An experimental study of the airside performance of the superslit fin-and-tube heat exchangers," International Journal of Heat and Mass Transfer, 43(24), pp. 4475-4482.

[89] Romero-Méndez, R., Sen, M., Yang, K. T., and McClain, R., 2000, "Effect of fin spacing on convection in a plate fin and tube heat exchanger," International Journal of Heat and Mass Transfer, 43(1), pp. 39-51.

[90] Wang, C.-C., Lin, Y.-T., and Lee, C.-J., 2000, "Heat and momentum transfer for compact louvered fin-and-tube heat exchangers in wet conditions," International Journal of Heat and Mass Transfer, 43(18), pp. 3443-3452.

[91] Wang, C.-C., Webb, R. L., and Chi, K.-Y., 2000, "Data reduction for air-side performance of fin-and-tube heat exchangers," Experimental Thermal and Fluid Science, 21(4), pp. 218-226.

[92] Yan, W.-M., and Sheen, P.-J., 2000, "Heat transfer and friction characteristics of fin-and-tube heat exchangers," International Journal of Heat and Mass Transfer, 43(9), pp. 1651-1659.

[93] Halici, F., Taymaz, I., and Gunduz, M., 2001, "The effect of the number of tube rows on heat, mass and momentum transfer in flat-plate finned tube heat exchangers," Energy, 26(11), pp. 963-972.

[94] Leu, J.-S., Liu, M.-S., Liaw, J.-S., and Wang, C.-C., 2001, "A numerical investigation of louvered fin-and-tube heat exchangers having circular and oval tube configurations," International Journal of Heat and Mass Transfer, 44(22), pp. 4235-4243.

[95] Saboya, S. M., and Saboya, F. E. M., 2001, "Experiments on elliptic sections in one- and two-row arrangements of plate fin and tube heat exchangers," Experimental Thermal and Fluid Science, 24(1-2), pp. 67-75.

[96] Wang, C.-C., Lee, W.-S., and Sheu, W.-J., 2001, "A comparative study of compact enhanced fin-and-tube heat exchangers," International Journal of Heat and Mass Transfer, 44(18), pp. 3565-3573.

[97] Kim, C. N., Jeong, J., and Youn, B., 2003, "Evaluation of thermal contact conductance using a new experimental-numerical method in fin-tube heat exchangers," International Journal of Refrigeration, 26(8), pp. 900-908.

[98] Leu, J.-S., Wu, Y.-H., and Jang, J.-Y., 2004, "Heat transfer and fluid flow analysis in plate-fin and tube heat exchangers with a pair of block shape vortex generators," International Journal of Heat and Mass Transfer, 47(19-20), pp. 4327-4338.

[99] Perrotin, T., and Clodic, D., 2004, "Thermal-hydraulic CFD study in louvered fin-and-flat-tube heat exchangers," International Journal of Refrigeration, 27(4), pp. 422-432.

[100] Taler, D., 2004, "Determination of heat transfer correlations for plate-fin-and-tube heat exchangers," Heat and Mass Transfer, 40(10), pp. 809-822.

[101] Taler, D., 2004, "Experimental determination of heat transfer and friction correlations for plate fin-and-tube heat exchangers," Journal of Enhanced Heat Transfer, 11(Compendex), pp. 183-204.

[102] Tutar, M., and Akkoca, A., 2004, "Numerical Analysis of Fluid Flow and Heat Transfer Characteristics in Three-Dimensional Plate Fin-And-Tube Heat Exchangers," Numerical Heat Transfer, Part A: Applications: An International Journal of Computation and Methodology, 46(3), pp. 301 - 321.

[103] Erek, A., Ozerdem, B., Bilir, L., and Ilken, Z., 2005, "Effect of geometrical parameters on heat transfer and pressure drop characteristics of plate fin and tube heat exchangers," Applied Thermal Engineering, 25(14-15), pp. 2421-2431.

[104] Kim, Y., and Kim, Y., 2005, "Heat transfer characteristics of flat plate finned-tube heat exchangers with large fin pitch," International Journal of Refrigeration, 28(6), pp. 851-858.

[105] Lin, C.-W., and Jang, J.-Y., 2005, "3D Numerical heat transfer and fluid flow analysis in plate-fin and tube heat exchangers with electrohydrodynamic enhancement," Heat and Mass Transfer, 41(7), pp. 583-593.

[106] Wongwises, S., and Chokeman, Y., 2005, "Effect of fin pitch and number of tube rows on the air side performance of herringbone wavy fin and tube heat exchangers," Energy Conversion and Management, 46(13-14), pp. 2216-2231.

[107] Zhou, J. J., and Tao, W. Q., 2005, "Three dimensional numerical simulation and analysis of the airside performance of slotted fin surfaces with radial strips," Engineering Computations, 22(8), p. 18.

[108] Halici, F., and Taymaz, I., 2006, "Experimental study of the airside performance of tube row spacing in finned tube heat exchangers," Heat and Mass Transfer, 42(9), pp. 817-822.

[109] Hsieh, C.-T., and Jang, J.-Y., 2006, "3-D thermal-hydraulic analysis for louver fin heat exchangers with variable louver angle," Applied Thermal Engineering, 26(14-15), pp. 1629-1639.

[110] Chen, H.-T., Chou, J.-C., and Wang, H.-C., 2007, "Estimation of heat transfer coefficient on the vertical plate fin of finned-tube heat exchangers for various air speeds and fin spacings," International Journal of Heat and Mass Transfer, 50(1-2), pp. 45-57.

[111] Sahin, H. M., Dal, A. R., and Baysal, E., 2007, "3-D Numerical study on the correlation between variable inclined fin angles and thermal behavior in plate fin-tube heat exchanger," Applied Thermal Engineering, 27(11-12), pp. 1806-1816.

[112] Tao, Y. B., He, Y. L., Huang, J., Wu, Z. G., and Tao, W. Q., 2007, "Numerical study of local heat transfer coefficient and fin efficiency of wavy fin-and-tube heat exchangers," International Journal of Thermal Sciences, 46(8), pp. 768-778.

[113] Huang, C.-H., Yuan, I. C., and Ay, H., 2009, "An experimental study in determining the local heat transfer coefficients for the plate finned-tube heat exchangers," International Journal of Heat and Mass Transfer, 52(21-22), pp. 4883-4893.

[114] Oliet, C., Perez-Segarra, C. D., Oliva, A., and Castro, J., 2009, "Multidimensional and Unsteady Simulation of Fin-and-Tube Heat Exchangers," Numerical Heat Transfer, Part A: Applications: An International Journal of Computation and Methodology, 56(3), pp. 193-210.

[115] Paeng, J., Kim, K., and Yoon, Y., 2009, "Experimental measurement and numerical computation of the air side convective heat transfer coefficients in a plate fin-tube heat exchanger," Journal of Mechanical Science and Technology, 23(2), pp. 536-543.

[116] Wen, M.-Y., and Ho, C.-Y., 2009, "Heat-transfer enhancement in fin-and-tube heat exchanger with improved fin design," Applied Thermal Engineering, 29(5-6), pp. 1050-1057.

[117] Borrajo-Peláez, R., Ortega-Casanova, J., and Cejudo-López, J. M., 2010, "A three-dimensional numerical study and comparison between the air side model and the air/water side model of a plain fin-and-tube heat exchanger," Applied Thermal Engineering, 30(13), pp. 1608-1615.

[118] Choi, J. M., Kim, Y., Lee, M., and Kim, Y., 2010, "Air side heat transfer coefficients of discrete plate finned-tube heat exchangers with large fin pitch," Applied Thermal Engineering, 30(2-3), pp. 174-180.

[119] Lu, C.-W., Huang, J.-M., Nien, W. C., and Wang, C.-C., 2011, "A numerical investigation of the geometric effects on the performance of plate finned-tube heat exchanger," Energy Conversion and Management, 52(3), pp. 1638-1643.

[120] Xie, G. N., Sunden, B., and Wang, Q. W., 2008, "Optimization of compact heat exchangers by a genetic algorithm," Applied Thermal Engineering, 28(8–9), pp. 895-906.

[121] Xie, G., Wang, Q., and Sunden, B., 2008, "Application of a Genetic Algorithm for Thermal Design of Fin-and-Tube Heat Exchangers," Heat Transfer Engineering, 29(7), pp. 597-607.

[122] Domanski, P. A., 1989, "EVSIM: An Evaporator Simulation Model Accounting for Refrigerant and One Dimensional Air Distribution," No. NISTIR 89-4133, D. o. E., NISTIR 89-4133, Washington, DC.

[123] Domanski, P. A., and Yashar, D., 2007, "Optimization of finned-tube condensers using an intelligent system," International Journal of Refrigeration, 30(3), pp. 482-488.

[124] Jiang, H., Aute, V., and Radermacher, R., 2006, "CoilDesigner: a general-purpose simulation and design tool for air-to-refrigerant heat exchangers," International Journal of Refrigeration, 29(4), pp. 601-610.

[125] Abdelaziz, O., Aute, V., Azarm, S., and Radermacher, R., 2010, "Approximation-Assisted Optimization for Novel Compact Heat Exchanger Designs," HVAC&R Research, 16(5), pp. 707-728.

[126] Ozkol, I., and Komurgoz, G., 2005, "Determination of the Optimum Geometry of the Heat Exchanger Body Via A Genetic Algorithm," Numerical Heat Transfer, Part A: Applications, 48(3), pp. 283-296.

[127] Sanaye, S., and Hajabdollahi, H., 2010, "Thermal-economic multi-objective optimization of plate fin heat exchanger using genetic algorithm," Applied Energy, 87(6), pp. 1893-1902.

[128] Najafi, H., Najafi, B., and Hoseinpoori, P., 2011, "Energy and cost optimization of a plate and fin heat exchanger using genetic algorithm," Applied Thermal Engineering, 31(10), pp. 1839-1847.

[129] Hajabdollahi, H., Ahmadi, P., and Dincer, I., 2011, "Multi-Objective Optimization of Plain Fin-and-Tube Heat Exchanger Using Evolutionary Algorithm," Journal of Thermophysics and Heat Transfer, 25(3), pp. 424-431.

[130] Hajabdollahi, H., Tahani, M., and Shojaee Fard, M. H., 2011, "CFD modeling and multi-objective optimization of compact heat exchanger using CAN method," Applied Thermal Engineering, 31(14–15), pp. 2597-2604.

[131] Mousavi, S. S., Hooman, K., and Mousavi, S. J., 2007, "Genetic algorithm optimization for finned channel performance," Appl. Math. Mech.-Engl. Ed., 28(12), pp. 1597-1604.

[132] Mousavi, S. S., and Hooman, K., 2006, "Heat and fluid flow in entrance region of a channel with staggered baffles," Energy Conversion and Management, 47(15–16), pp. 2011-2019.

[133] Foli, K., Okabe, T., Olhofer, M., Jin, Y., and Sendhoff, B., 2006, "Optimization of micro heat exchanger: CFD, analytical approach and multi-objective evolutionary algorithms," International Journal of Heat and Mass Transfer, 49(5–6), pp. 1090-1099.

[134] Hilbert, R., Janiga, G., Baron, R., and Thévenin, D., 2006, "Multi-objective shape optimization of a heat exchanger using parallel genetic algorithms," International Journal of Heat and Mass Transfer, 49(15–16), pp. 2567-2577.

[135] Hooman, K., and Gurgenci, H., 2010, "Porous Medium Modeling of Air-Cooled Condensers," Transport in Porous Media, 84(2), pp. 257-273.

[136] Knight, R. W., Goodling, J. S., and Hall, D. J., 1991, "Optimal Thermal Design of Forced Convection Heat Sinks-Analytical," Journal of Electronic Packaging, 113(3), pp. 313-321.

[137] Knight, R. W., Hall, D. J., Goodling, J. S., and Jaeger, R. C., 1992, "Heat sink optimization with application to microchannels," Components, Hybrids, and Manufacturing Technology, IEEE Transactions on, 15(5), pp. 832-842.

[138] Knight, R. W., Goodling, J. S., and Gross, B. E., 1992, "Optimal thermal design of air cooled forced convection finned heat sinks-experimental verification," Components, Hybrids, and Manufacturing Technology, IEEE Transactions on, 15(5), pp. 754-760.

[139] Teertstra, P., Yovanovich, M. M., and Culham, J. R., 2000, "Analytical forced convection modeling of plate fin heat sinks," Journal of Electronics Manufacturing, 10(Compendex), pp. 253-261.

[140] Copeland, D., "Optimization of parallel plate heatsinks for forced convection," Proc. Semiconductor Thermal Measurement and Management Symposium.

210

[141] Culham, J. R., and Muzychka, Y. S., 2001, "Optimization of plate fin heat sinks using entropy generation minimization," Components and Packaging Technologies, IEEE Transactions on, 24(2), pp. 159-165.

[142] Iyengar, M., and Bar-Cohen, A., 2003, "Least-energy optimization of forced convection plate-fin heat sinks," Components and Packaging Technologies, IEEE Transactions on, 26(1), pp. 62-70.

[143] Chiang, K.-T., 2005, "Optimization of the design parameters of Parallel-Plain Fin heat sink module cooling phenomenon based on the Taguchi method," International Communications in Heat and Mass Transfer, 32(9), pp. 1193-1201.

[144] Sparrow, E. M., Ramsey, J. W., and Altemani, C. A. C., 1980, "Experiments on In-line Pin Fin Arrays and Performance Comparisons with Staggered Arrays," Journal of Heat Transfer, 102(1), pp. 44-50.

[145] Sparrow, E. M., and Kang, S. S., 1985, "Longitudinally-finned cross-flow tube banks and their heat transfer and pressure drop characteristics," International Journal of Heat and Mass Transfer, 28(2), pp. 339-350.

[146] Sparrow, E. M., and Grannis, V. B., 1991, "Pressure drop characteristics of heat exchangers consisting of arrays of diamond-shaped pin fins," International Journal of Heat and Mass Transfer, 34(3), pp. 589-600.

[147] Chapman, C. L., Lee, S., and Schmidt, B. L., "Thermal performance of an elliptical pin fin heat sink," Proc. Semiconductor Thermal Measurement and Management Symposium, 1994. SEMI-THERM X., Proceedings of 1994 IEEE/CPMT 10th, pp. 24-31.

[148] Li, Q., Chen, Z., Flechtner, U., and Warnecke, H.-J., 1998, "Heat transfer and pressure drop characteristics in rectangular channels with elliptic pin fins," International Journal of Heat and Fluid Flow, 19(3), pp. 245-250.

[149] Yang, K.-S., Chu, W.-H., Chen, I.-Y., and Wang, C.-C., 2007, "A comparative study of the airside performance of heat sinks having pin fin configurations," International Journal of Heat and Mass Transfer, 50(23-24), pp. 4661-4667.

[150] Horvat, A., and Catton, I., 2003, "Numerical technique for modeling conjugate heat transfer in an electronic device heat sink," International Journal of Heat and Mass Transfer, 46(12), pp. 2155-2168.

[151] Horvat, A., and Mavko, B., 2005, "Hierarchic modeling of heat transfer processes in heat exchangers," International Journal of Heat and Mass Transfer, 48(2), pp. 361-371.

[152] Park, K., Choi, D.-H., and Lee, K.-S., 2004, "Numerical shape optimization for high performance of a heat sink with pin-fins," Numerical Heat Transfer, Part A: Applications: An International Journal of Computation and Methodology, 46(9), pp. 909 - 927.

[153] Chen, H.-T., Chen, P.-L., Horng, J.-T., and Hung, Y.-H., 2005, "Design Optimization for Pin-Fin Heat Sinks," Journal of Electronic Packaging, 127(4), pp. 397-406.

[154] Khan, W. A., Culham, J. R., and Yovanovich, M. M., 2005, "Optimization of pin-fin heat sinks using entropy generation minimization," Components and Packaging Technologies, IEEE Transactions on, 28(2), pp. 247-254.

[155] Khan, W. A., Culham, J. R., and Yovanovich, M. M., 2008, "Optimization of Pin-Fin Heat Sinks in Bypass Flow Using Entropy Generation Minimization Method," Journal of Electronic Packaging, 130(3), pp. 031010-031017.

[156] Chiang, K.-T., and Chang, F.-P., 2006, "Application of response surface methodology in the parametric optimization of a pin-fin type heat sink," International Communications in Heat and Mass Transfer, 33(7), pp. 836-845.

[157] Chiang, K.-T., Chang, F.-P., and Tsai, T.-C., 2006, "Optimum design parameters of Pin-Fin heat sink using the grey-fuzzy logic based on the orthogonal arrays," International Communications in Heat and Mass Transfer, 33(6), pp. 744-752.

[158] Jonsson, H., and Moshfegh, B., 2001, "Modeling of the thermal and hydraulic performance of plate fin, strip fin, and pin fin heat sinks-influence of flow bypass," Components and Packaging Technologies, IEEE Transactions on, 24(2), pp. 142-149.

[159] Soodphakdee, D., Behnia, M., and Copeland, D. W., 2001, "A Comparison of Fin Geometries for Heatsinks in Laminar Forced Convection: Part I- Round, Elliptical, and Plate Fins in Staggered and In-Line Configurations," The International Journal of Microcircuits and Electronic Packaging, 24(1).

[160] Kim, S. J., Kim, D.-K., and Oh, H. H., 2008, "Comparison of Fluid Flow and Thermal Characteristics of Plate-Fin and Pin-Fin Heat Sinks Subject to a Parallel Flow," Heat Transfer Engineering, 29(2), pp. 169 - 177.

[161] Ligrani, P. M., Oliveira, M. M., and Blaskovich, T., 2003, "Comparison of heat transfer augmentation techniques," AIAA Journal, 41(3), pp. 337-362.

[162] Taslim, M. E., Li, T., and Kercher, D. M., 1996, "Experimental heat transfer and friction in channels roughened with angled, V-shaped, and discrete ribs on two opposite walls," J. Turbomach.-Trans. ASME, 118(1), pp. 20-28.

[163] Han, J. C., Zhang, Y. M., and Lee, C. P., 1991, "Augmented Heat Transfer in Square Channels With Parallel, Crossed, and V-Shaped Angled Ribs," Journal of Heat Transfer, 113(3), pp. 590-596.

[164] Gao, X., and Sunden, B., 2001, "Heat transfer and pressure drop measurements in rib-roughened rectangular ducts," Experimental Thermal and Fluid Science, 24(1-2), pp. 25-34.

[165] Park, J. S., Han, J. C., Huang, Y., Ou, S., and Boyle, R. J., 1992, "Heat transfer performance comparisons of five different rectangular channels with parallel angled ribs," International Journal of Heat and Mass Transfer, 35(11), pp. 2891-2903.

[166] Cho, H. H., Wu, S. J., and Kwon, H. J., 2000, "Local Heat/Mass Transfer Measurements in a Rectangular Duct With Discrete Ribs," Journal of Turbomachinery, 122(3), pp. 579-586.

[167] Mahmood, G. I., Hill, M. L., Nelson, D. L., Ligrani, P. M., Moon, H. K., and Glezer, B., 2001, "Local Heat Transfer and Flow Structure on and Above a Dimpled Surface in a Channel," Journal of Turbomachinery, 123(1), pp. 115-123.

[168] Mahmood, G. I., and Ligrani, P. M., 2002, "Heat transfer in a dimpled channel: combined influences of aspect ratio, temperature ratio, Reynolds number, and flow structure," International Journal of Heat and Mass Transfer, 45(10), pp. 2011-2020.

[169] Burgess, N. K., and Ligrani, P. M., 2005, "Effects Of Dimple Depth on Channel Nusselt Numbers and Friction Factors," Journal of Heat Transfer, 127(8), pp. 839-847.

[170] Wee, H., Zhang, Q., Ligrani, P. M., and Narasimhan, S., 2008, "Numerical Predictions of Heat Transfer and Flow Characteristics of Heat Sinks with Ribbed and

Dimpled Surfaces in Laminar Flow," Numerical Heat Transfer, Part A: Applications: An International Journal of Computation and Methodology, 53(11), pp. 1156 - 1175.

[171] Mahmood, G. I., Sabbagh, M. Z., and Ligrani, P. M., 2001, "Heat Transfer in a Channel with Dimples and Protrusions on Opposite Walls," Journal of Thermophysics and Heat Transfer, 15(3), pp. 275-283.

[172] Chang, S. W., Liou, T. M., Chiang, K. F., and Hong, G. F., 2008, "Heat transfer and pressure drop in rectangular channel with compound roughness of V-shaped ribs and deepened scales," International Journal of Heat and Mass Transfer, 51(3-4), pp. 457-468.

[173] Chang, S. W., Yang, T. L., Liou, T.-M., and Fang, H. G., 2009, "Heat transfer in rotating scale-roughened trapezoidal duct at high rotation numbers," Applied Thermal Engineering, 29(8-9), pp. 1682-1693.

[174] Chang, S. W., Yang, T. L., Liou, T.-M., and Hong, G. F., 2009, "Heat transfer of rotating rectangular duct with compound scaled roughness and V-ribs at high rotation numbers," International Journal of Thermal Sciences, 48(1), pp. 174-187.

[175] Chang, S. W., and Lees, A. W., 2010, "Endwall heat transfer and pressure drop in scale-roughened pin-fin channels," International Journal of Thermal Sciences, 49(4), pp. 702-713.

[176] Randall, D. A., 2000, General Circulation Model Development: Past, Present, and Future, Academic Press.

[177] Slattery, J. C., 1981, Momentum, Energy, and Mass Transfer in Continua, Krieger Pub Co.

[178] Whitaker, S., 1986, "Flow in porous media I: A theoretical derivation of Darcy's law," Transport in Porous Media, 1(1), pp. 3-25.

[179] Whitaker, S., 1986, "Flow in porous media II: The governing equations for immiscible, two-phase flow," Transport in Porous Media, 1(2), pp. 105-125.

[180] Whitaker, S., 1986, "Flow in porous media III: Deformable media," Transport in Porous Media, 1(2), pp. 127-154.

[181] Crapiste, G. H., Rotstein, E., and Whitaker, S., 1986, "A general closure scheme for the method of volume averaging," Chemical Engineering Science, 41(2), pp. 227-235.

[182] Rodi, W., 1984, Turbulence models and their applications in hydraulics - A state of the art review, AIRH.

[183] Monin, A. S., and Yaglon, A. M., 1975, Statistical Fluid Mechanics, MIT Press, Cambridge, MA.

[184] Hu, K., 2002, "Flow and heat transfer over rough surfaces in porous media," Ph.D., University of California, Los Angeles.

[185] Zhou, F., Hansen, N., Geb, D., and Catton, I., 2011, "Obtaining Closure for Fin-and-Tube Heat Exchanger Modeling Based on Volume Averaging Theory (VAT)," Journal of Heat Transfer, 133(11), p. 111802.

[186] Zhou, F., and Catton, I., 2013, "Obtaining closure for a plane fin heat sink with elliptic scale-roughened surfaces for Volume Averaging Theory (VAT) based modeling," International Journal of Thermal Sciences, 71(0), pp. 264-273.

[187] Zhou, F., Hansen, N., and Catton, I., "Obtaining closure for heat exchanger modeling based on Volume Averaging Theory (VAT)," Proc. 2010 14th International Heat Transfer Conference, IHTC14, August 8, 2010 - August 13, 2010, American Society of Mechanical Engineers, pp. 693-701.

[188] Whitaker, S., 1972, "Forced convection heat transfer correlations for flow in pipes, past flat plates, single cylinders, single spheres, and for flow in packed beds and tube bundles," AIChE Journal, 18(2), pp. 361-371.

[189] Ergun, S., 1952, "Fluid flow through packed columns," Chemical Engineering Progress, 48(2), pp. 89-94.

[190] Vadnjal, A., 2009, "Modeling of a Heat Sink and High Heat Flux Vapor Chamber, PhD Thesis," PhD Thesis, University of California Los Angeles, Los Angeles.

[191] Inc., S. I., 2008, JMP® 8 statistics and graphics guide, Volumes 1 and 2. Cary, NC: SAS Institute Inc.

[192] Zhou, F., Geb, D., and Catton, I., "Numerical investigation on air side performance of fin-and-tube heat exchangers with large diameter tubes and large number of tube rows," Proc. ASME 2011 International Mechanical Engineering Congress and Exposition, IMECE 2011, November 11, 2011 - November 17, 2011, American Society of Mechanical Engineers, pp. 805-813.

[193] Horvat, A., and Catton, I., 2003, "Application of Galerkin Method to Conjugate Heat Transfer Calculation," Numerical Heat Transfer, Part B: Fundamentals: An International Journal of Computation and Methodology, 44(6), pp. 509 - 531.

[194] Horvat, A., and Mavko, B., 2005, "Calculation of conjugate heat transfer problem with volumetric heat generation using the Galerkin method," Applied Mathematical Modelling, 29(5), pp. 477-495.

[195] Geb, D., Zhou, F., and Catton, I., 2012, "Internal Heat Transfer Coefficient Determination in a Packed Bed From the Transient Response Due to Solid Phase Induction Heating," Journal of Heat Transfer, 134(4), p. 042604.

[196] Geb, D., Chu, J., Zhou, F., and Catton, I., "Obtaining experimental closure for the VAT-based energy equations modeling a heat sink as a porous medium," Proc. ASME 2011 International Mechanical Engineering Congress and Exposition, IMECE 2011, November 11, 2011 - November 17, 2011, American Society of Mechanical Engineers, pp. 119-128.

[197] Menter, F. R., 1994, "Two-equation eddy-viscosity turbulence models for engineering applications," AIAA Journal, 32(8), pp. 1598-1605.

[198] Menter, F. R., Kuntz, M., and Langtry, R., 2003, "Ten years of industrial experience with the SST turbulence model," Turbulence, Heat and mass transfer, 4, pp. 625-632.

[199] Menter, F. R., and Esch, T., 2001, "Elements of industrial heat transfer predictions," 16th Bazilian Congress of Mechanical Engineering (COBEM), Uberlandia, Brazil.

[200] Zhou, F., Hansen, N., Geb, D., and Catton, I., 2011, "Determination of the Number of Tube Rows to Obtain Closure for Volume Averaging Theory Based Model of Fin-and-Tube Heat Exchangers," Journal of Heat Transfer, 133(12), p. 121801.

[201] Zhou, F., Vasquez, D. A., DeMoulin, G. W., Geb, D. J., and Catton, I., "Volume Averaging Theory (VAT) based modeling and closure evaluation of scale-roughened plane fin heat sink," Proc. 28th Annual IEEE Semiconductor Thermal Measurement and Management Symposium, SEMI-THERM 2012, March 18, 2012 - March 22, 2012, Institute of Electrical and Electronics Engineers Inc., pp. 260-268.

[202] Zhou, F., and Catton, I., 2012, "Volume Averaging Theory (VAT) based modeling and closure evaluation for fin-and-tube heat exchangers," Heat and Mass Transfer, 48(10), pp. 1813-1823.

[203] Zhou, F., and Catton, I., 2013, "A Numerical Investigation of Turbulent Flow and Heat Transfer in Rectangular Channels With Elliptic Scale-Roughened Walls," Journal of Heat Transfer, 135(8), pp. 081901-081901.

[204] Kupprn, T., 2000, Heat Exchanger Design Handbook, Marcel Dekker, Inc., New York.

[205] Bejan, A., and Kraus, A., 2003, Heat Transfer Handbook, John Wiley & Sons

[206] Schmidt, T. E., 1949, "Heat transfer calculations for extended surfaces," Refrigerating Engineering, 57, pp. 351-357.

[207] Zhou, F., Hansen, N., and Catton, I., "Determining the computational domain length to obtain closure for VAT based modeling by 3D numerical simulation and field synergy analysis (IMECE 2010-37561)," Proc. ASME 2010 International Mechanical Engineering Congress & Exposition, IMECE 2010.

[208] Guo, Z. Y., Li, D. Y., and Wang, B. X., 1998, "A novel concept for convective heat transfer enhancement," International Journal of Heat and Mass Transfer, 41(14), pp. 2221-2225.

[209] Ma, L.-D., Li, Z.-Y., and Tao, W.-Q., 2007, "Experimental verification of the field synergy principle," International Communications in Heat and Mass Transfer, 34(3), pp. 269-276.

[210] Tao, W. Q., He, Y. L., Wang, Q. W., Qu, Z. G., and Song, F. Q., 2002, "A unified analysis on enhancing single phase convective heat transfer with field synergy principle," International Journal of Heat and Mass Transfer, 45(24), pp. 4871-4879.

[211] Guo, Z. Y., Tao, W. Q., and Shah, R. K., 2005, "The field synergy (coordination) principle and its applications in enhancing single phase convective heat transfer," International Journal of Heat and Mass Transfer, 48(9), pp. 1797-1807.

[212] He, Y. L., Tao, W. Q., Song, F. Q., and Zhang, W., 2005, "Three-dimensional numerical study of heat transfer characteristics of plain plate fin-and-tube heat exchangers from view point of field synergy principle," International Journal of Heat and Fluid Flow, 26(3), pp. 459-473.

[213] Guo, Z.-Y., Zhou, S.-Q., Li, Z.-X., and Chen, L.-G., 2002, "Theoretical analysis and experimental confirmation of the uniformity principle of temperature difference field in heat exchanger," International Journal of Heat and Mass Transfer, 45(10), pp. 2119-2127.

[214] Tao, W.-Q., Guo, Z.-Y., and Wang, B.-X., 2002, "Field synergy principle for enhancing convective heat transfer--its extension and numerical verifications," International Journal of Heat and Mass Transfer, 45(18), pp. 3849-3856.

[215] Cheng, Y. P., Qu, Z. G., Tao, W. Q., and He, Y. L., 2004, "Numerical design of efficient slotted fin surface based on the field synergy principle," Numerical Heat Transfer, Part A: Applications: An International Journal of Computation and Methodology, 45(6), pp. 517 - 538.

[216] Min Zeng, W.-Q. T., 2004, "Numerical verification of the field synergy principle for turbulent flow," J Enhanc Heat Transfer, 11, pp. 451-457.

[217] Qu, Z. G., Tao, W. Q., and He, Y. L., 2004, "Three-Dimensional Numerical Simulation on Laminar Heat Transfer and Fluid Flow Characteristics of Strip Fin Surface With X-Arrangement of Strips," Journal of Heat Transfer, 126(5), pp. 697-707.

[218] Cai, R., and Gou, C., 2007, "Discussion on the convective heat transfer and field synergy principle," International Journal of Heat and Mass Transfer, 50(25-26), pp. 5168-5176.

[219] Chen, Q., Ren, J., and Meng, J.-a., 2007, "Field synergy equation for turbulent heat transfer and its application," International Journal of Heat and Mass Transfer, 50(25-26), pp. 5334-5339.

[220] Tao, Y. B., He, Y. L., Huang, J., Wu, Z. G., and Tao, W. Q., 2007, "Three-dimensional numerical study of wavy fin-and-tube heat exchangers and field synergy principle analysis," International Journal of Heat and Mass Transfer, 50(5-6), pp. 1163-1175.

[221] Wu, J. M., and Tao, W. Q., 2007, "Investigation on laminar convection heat transfer in fin-and-tube heat exchanger in aligned arrangement with longitudinal vortex generator from the viewpoint of field synergy principle," Applied Thermal Engineering, 27(14-15), pp. 2609-2617.

[222] Chen, Q., Ren, J., and Guo, Z., 2008, "Field synergy analysis and optimization of decontamination ventilation designs," International Journal of Heat and Mass Transfer, 51(3-4), pp. 873-881.

[223] Chen, Q., Ren, J., and Guo, Z., 2008, "Fluid flow field synergy principle and its application to drag reduction," Chinese Science Bulletin, 53(11), pp. 1768-1772.

[224] Cheng, Y. P., Lee, T. S., and Low, H. T., 2008, "Numerical simulation of conjugate heat transfer in electronic cooling and analysis based on field synergy principle," Applied Thermal Engineering, 28(14-15), pp. 1826-1833.

[225] Liu, W., Liu, Z., and Guo, Z., 2009, "Physical quantity synergy in laminar flow field of convective heat transfer and analysis of heat transfer enhancement," Chinese Science Bulletin, 54(19), pp. 3579-3586.

[226] Wei, L., Zhichun, L., Tingzhen, M., and Zengyuan, G., 2009, "Physical quantity synergy in laminar flow field and its application in heat transfer enhancement," International Journal of Heat and Mass Transfer, 52(19-20), pp. 4669-4672.

[227] Wu, L., Li, Z., and Song, Y., 2009, "Field synergy principle of heat and mass transfer," Chinese Science Bulletin, 54(24), pp. 4604-4609.

[228] Kays, W. M., and Crawford, M. E., 1980, Convective Heat and Mass Transfer, McGraw-Hill Book Company, New York.

[229] Wang, C.-C., Chang, Y.-J., Hsieh, Y.-C., and Lin, Y.-T., 1996, "Sensible heat and friction characteristics of plate fin-and-tube heat exchangers having plane fins," International Journal of Refrigeration, 19(4), pp. 223-230.

[230] Zhou, F., Geb, D., DeMoulin, G., and Catton, I., "Hierarchical modeling and closure evaluation for fin-and-tube heat exchangers using 3-D numerical simulation," Proc. ASME 2012 Heat Transfer Summer Conference Collocated with the ASME 2012 Fluids Engineering Div. Summer Meeting and the ASME 2012 10th Int. Conf. on Nanochannels, Microchannels and Minichannels, HT 2012, July 8, 2012 - July 12, 2012, American Society of Mechanical Engineers, pp. 9-19.

[231] Catton, I., 2011, "Conjugate Heat Transfer Within a Heterogeneous Hierarchical Structure," Journal of Heat Transfer, 133(10), p. 103001.

[232] Zhou, F., Hansen, N., and Catton, I., "VAT based modeling of heat exchanger and obtaining closure from CFD solution," Proc. ASME 2010 International Mechanical

Engineering Congress & Exposition, IMECE 2010, November 12, 2010 - November 18, 2010.

[233] Techo, R., Tickner, R. R., and James, R. E., 1965, "An accurate equation for the computation of the friction factor for smooth pipes for the Reynolds number," J. Appl. Mech., 32, p. 443.

[234] Zhou, F., and Catton, I., "Numerical investigation on turbulent flow and heat transfer of rectangular channels with elliptic scale-roughened walls," Proc. ASME 2012 International Mechanical Engineering Congress and Exposition, IMECE 2012, November 9, 2012 - November 15, 2012, American Society of Mechanical Engineers, pp. 3221-3229.

[235] Sieder, E. N., and Tate, G. E., 1936, "Heat transfer and pressure drop of liquids in tubes," Industrial and Engineering Chemistry, 28, pp. 1429-1435.

[236] Gungor, K. E., and Winterton, R. H. S., 1986, "A general correlation for flow boiling in tubes and annuli," International Journal of Heat and Mass Transfer, 29(3), pp. 351-358.

[237] Beavers, G. S., Sparrow, E. M., and Lloyd, J. R., 1971, "Low Reynolds number turbulent flow in large aspect ratio rectangular ducts," Trans. ASME, D, J. Basic Eng., 93(2), pp. 296-299299.

[238] Geb, D., Zhou, F., DeMoulin, G., and Catton, I., 2013, "Genetic Algorithm Optimization of a Finned-Tube Heat Exchanger Modeled With Volume-Averaging Theory," Journal of Heat Transfer, 135(8), pp. 082602-082602.

[239] Geb, D., Zhou, F., DeMoulin, G., and Catton, I., "Genetic algorithm optimization of a compact heat exchanger modeled using volume averaging theory," Proc. ASME 2012 Heat Transfer Summer Conference Collocated with the ASME 2012 Fluids Engineering Div. Summer Meeting and the ASME 2012 10th Int. Conf. on Nanochannels,

Microchannels and Minichannels, HT 2012, July 8, 2012 - July 12, 2012, American Society of Mechanical Engineers, pp. 907-915.

[240] Geb, D., 2013, "Hierarchical Modeling for Population-Based Heat Exchanger Design," Ph.D., University of California, Los Angeles.

[241] Zhou, F., DeMoulin, G. W., Geb, D. J., and Catton, I., "Modeling of pin fin heat sinks based on volume averaging theory," Proc. ASME-JSME-KSME 2011 Joint Fluids Engineering Conference, AJK 2011, July 24, 2011 - July 29, 2011, American Society of Mechanical Engineers, pp. 1357-1365.

[242] Hansen, N., Catton, I., and Zhou, F., "Heat sink optimization; A multi-parameter optimization problem," Proc. 2010 14th International Heat Transfer Conference, IHTC14, August 8, 2010 - August 13, 2010, American Society of Mechanical Engineers, pp. 649-655.

[243] Zhou, F., DeMoulin, G., Geb, D., and Catton, I., 2012, "Closure for a plane fin heat sink with scale-roughened surfaces for volume averaging theory (VAT) based modeling," International Journal of Heat and Mass Transfer, 55(25–26), pp. 7677-7685.

[244] Geb, D., and Catton, I., 2014, "Nonlocal modeling and swarm-based design of heat sinks," Journal of Heat Transfer, 136(1).

[245] Geb, D., Demoulin, G., and Catton, I., "Population-based optimization for heat sink design in electronics cooling applications," Proc. 29th Annual IEEE Semiconductor Thermal Measurement and Management Symposium, SEMI-THERM 2013, March 17, 2013 - March 21, 2013, Institute of Electrical and Electronics Engineers Inc., pp. 173-180.

[246] Zhou, F., and Catton, I., 2011, "Numerical evaluation of flow and heat transfer in plate-pin fin heat sinks with various pin cross-sections," Numerical Heat Transfer, Part A: Applications, 60(2), pp. 107-128.

[247] Zhou, F., Geb, D., and Catton, I., "Cooling performance comparisons of five different plate-pin compound heat sinks based on two different length scale," Proc. ASME 2011 Pacific Rim Technical Conference and Exhibition on Packaging and Integration of Electronic and Photonic Systems, InterPACK 2011, July 6, 2011 - July 8, 2011, American Society of Mechanical Engineers, pp. 47-57.

[248] Zhou, F., Hansen, N., and Catton, I., "Numerical predictions of thermal and hydraulic performances of heat sinks with enhanced heat transfer capability," Proc. ASME/JSME 2011 8th Thermal Engineering Joint Conference, AJTEC 2011, March 13, 2011 - March 17, 2011, American Society of Mechanical Engineers, pp. American Society of Mechanical Engineers, Heat Transfer Division; Japan Soc. Mech. Eng., Therm. Eng. Div.

[249] Zhou, F., Hansen, N., and Catton, I., "VAT based modeling of plate-pin fin heat sink and obtaining closure from CFD solution," Proc. ASME/JSME 2011 8th Thermal Engineering Joint Conference, AJTEC 2011, March 13, 2011 - March 17, 2011, American Society of Mechanical Engineers, pp. American Society of Mechanical Engineers, Heat Transfer Division; Japan Soc. Mech. Eng., Therm. Eng. Div.

[250] Yu, X. L., Feng, Q. K., and Liu, Q. P., 2003, "Research on the heat transfer and flow performance of a composite heat sink," J Xi'an Jiaotong Univ 37(4), pp. 670-673.

[251] Yu, X. L., Feng, Q. K., and Feng, J. M., 2004, "Research on thermal performance of plate-pin fin heat sink," J Xi'an Jiaotong Univ 38(11), pp. 1114-1118.

[252] Yu, X., Feng, J., Feng, Q., and Wang, Q., 2005, "Development of a plate-pin fin heat sink and its performance comparisons with a plate fin heat sink," Applied Thermal Engineering, 25(2-3), pp. 173-182.

[253] Yang, Y.-T., and Peng, H.-S., 2009, "Numerical Study of Thermal and Hydraulic Performance of Compound Heat Sink," Numerical Heat Transfer, Part A: Applications: An International Journal of Computation and Methodology, 55(5), pp. 432 - 447.

[254] Yang, Y.-T., and Peng, H.-S., 2009, "Investigation of planted pin fins for heat transfer enhancement in plate fin heat sink," Microelectronics Reliability, 49(2), pp. 163-169.

[255] Jacobs, N. E., 1931, "Tests of six symmetrical airfoils in the variable density wind tunnel," Washington, DC.

[256] Jacobs, N. E., Ward, K. E., and Pinkerton, R. M., 1933, "The characteristics of 78 related airfoil sections from tests in the variable-density wind tunnel," Washington, DC.

[257] Moran, J., 2003, An introduction to theoretical and computational aerodynamics, Dover Publications

[258] Deb, K., Pratap, A., Agarwal, S., and Meyarivan, T., 2002, "A fast and elitist multiobjective genetic algorithm: NSGA-II," IEEE Transactions on Evolutionary Computation, 6(Compendex), pp. 182-197.

[259] Nakayama, A., and Kuwahara, F., 2008, "A general bioheat transfer model based on the theory of porous media," International Journal of Heat and Mass Transfer, 51(11–12), pp. 3190-3199.

[260] Kuwahara, F., Sano, Y., Liu, J., and Nakayama, A., 2009, "A Porous Media Approach for Bifurcating Flow and Mass Transfer in a Human Lung," Journal of Heat Transfer, 131(10), p. 101013.

[261] Nakayama, A., Kuwahara, F., and Liu, W., 2009, "A macroscopic model for countercurrent bioheat transfer in a circulatory system," Journal of Porous Media, 12(4), pp. 289-300.

[262] Nakayama, A., Kuwahara, F., and Liu, W., 2010, "A General Set of Bioheat Transfer Equations Based on the Volume Averaging Theory," Porous Media: Applications in Biological Systems and Biotechnology, K. Vafai, ed., pp. 1-44.

[263] Nakayama, A., Sano, Y., and Yoshikawa, K., 2010, "A rigorous derivation of the bioheat equation for local tissue heat transfer based on a volume averaging theory," Heat and Mass Transfer, 46(7), pp. 739-746.

[264] Sano, Y., Iwase, S., and Nakayama, A., 2012, "A Local Thermal Nonequilibrium Analysis of Silicon Carbide Ceramic Foam as a Solar Volumetric Receiver," Journal of Solar Energy Engineering, 134(2), p. 021006.

[265] Kreith, F., 2000, "The CRC Handbook of Thermal Engineering," CRC Press LLC.

[266] Boyd, S., and Vandenberghe, L., 2004, Convex Optimization, Cambridge University Press.

[267] Fletcher, R., 2000, Practical methods of optimization, Wiley.

[268] Devi, S. P., Manivannan, S., and Rao, K. S., 2012, "Comparison of nongradient methods with hybrid Taguchi-based epsilon constraint method for multiobjective optimization of cylindrical fin heat sink," Int J Adv Manuf Technol, 63(9-12), pp. 1081-1094.

[269] Guinta, A. A., 1997, "Aircraft multidisciplinary design optimization using design of experimental theory and response surface modeling methods," PhD, Virginia Polytechnic Institute and State University, Virginia.

[270] Myers, R. H., and Montgomery, D. C., 1995, Response Surface Methodology: Process and Product Optimization Using Designed Experiments, John Wiley & Sons, New York, NY.

[271] Chou, C.-C., Liu, N.-M., Horng, J.-T., and Chiang, K.-T., 2009, "Designing parameter optimization of a Parallel-Plain Fin heat sink using the grey-based fuzzy algorithm with the orthogonal arrays," International Journal of Thermal Sciences, 48(12), pp. 2271-2279.

[272] Chiang, K.-T., 2007, "Modeling and optimization of designing parameters for a parallel-plain fin heat sink with confined impinging jet using the response surface methodology," Applied Thermal Engineering, 27(14–15), pp. 2473-2482.

[273] Chiang, K.-T., Chou, C.-C., and Liu, N.-M., 2009, "Application of response surface methodology in describing the thermal performances of a pin-fin heat sink," International Journal of Thermal Sciences, 48(6), pp. 1196-1205.

[274] Sahin, B., 2007, "A Taguchi approach for determination of optimum design parameters for a heat exchanger having circular-cross sectional pin fins," Heat and Mass Transfer, 43(5), pp. 493-502.

[275] Sahin, B., Yakut, K., Kotcioglu, I., and Celik, C., 2005, "Optimum design parameters of a heat exchanger," Applied Energy, 82(1), pp. 90-106.

[276] Kota, K., Burton, L., and Joshi, Y., 2013, "Performance of an Air-Cooled Heat Sink Channel With Microscale Dimples Under Transitional Flow Conditions," Journal of Heat Transfer, 135(11), pp. 111005-111005.

[277] Manivannan, S., Devi, S. P., Arumugam, R., and Sudharsan, N. M., 2011, "Multi-objective optimization of flat plate heat sink using Taguchi-based Grey relational analysis," Int J Adv Manuf Technol, 52(5-8), pp. 739-749.

[278] Jang, D., Yu, S.-H., and Lee, K.-S., 2012, "Multidisciplinary optimization of a pin-fin radial heat sink for LED lighting applications," International Journal of Heat and Mass Transfer, 55(4), pp. 515-521.

[279] Abdullah, M. K., Ismail, N. C., Abdul Mujeebu, M., Abdullah, M. Z., Ahmad, K. A., Husaini, M., and Hamid, M. N. A., 2012, "Optimum tip gap and orientation of multi-piezofan for heat transfer enhancement of finned heat sink in microelectronic cooling," International Journal of Heat and Mass Transfer, 55(21–22), pp. 5514-5525.

[280] Park, K., and Moon, S., 2005, "Optimal design of heat exchangers using the progressive quadratic response surface model," International Journal of Heat and Mass Transfer, 48(11), pp. 2126-2139.

[281] Kim, H.-M., and Kim, K.-Y., 2006, "Shape optimization of three-dimensional channel roughened by angled ribs with RANS analysis of turbulent heat transfer," International Journal of Heat and Mass Transfer, 49(21-22), pp. 4013-4022.

[282] Park, K., Oh, P.-K., and Lim, H.-J., 2006, "The application of the CFD and Kriging method to an optimization of heat sink," International Journal of Heat and Mass Transfer, 49(19-20), pp. 3439-3447.

[283] Husain, A., and Kwang-Yong, K., 2008, "Shape Optimization of Micro-Channel Heat Sink for Micro-Electronic Cooling," Components and Packaging Technologies, IEEE Transactions on, 31(2), pp. 322-330.

[284] Srisomporn, S., and Bureerat, S., 2008, "Geometrical Design of Plate-Fin Heat Sinks Using Hybridization of MOEA and RSM," Components and Packaging Technologies, IEEE Transactions on, 31(2), pp. 351-360.

[285] Chen, H.-T., Horng, J.-T., Chen, P.-L., and Hung, Y.-H., 2004, "Optimal Design for PPF Heat Sinks in Electronics Cooling Applications," Journal of Electronic Packaging, 126(4), pp. 410-422.

[286] Chen, H.-T., Hung, Y.-H., Chen, P.-L., and Horng, J.-T., 2004, "Design Optimization for Pin-Fin Heat Sinks," Journal of Electronic Packaging, 127(4), pp. 397-406.